Integrability Breaking and Bound States in Google's Decorated XXZ Circuits

Ana Hudomal[1,2] Ryan Smith,[1] Andrew Hallam,[1] and Zlatko Papić[1,*]

[1]*School of Physics and Astronomy, University of Leeds, Leeds LS2 9JT, United Kingdom*
[2]*Institute of Physics Belgrade, University of Belgrade, Belgrade 11080, Serbia*

Recent quantum simulation by Google [Nature **612**, 240 (2022)] has demonstrated the formation of bound states of interacting photons in a quantum-circuit version of the XXZ spin chain. While such bound states are protected by integrability in a one-dimensional chain, the experiment found the bound states to be unexpectedly robust when integrability was broken by decorating the circuit with additional qubits, at least for small numbers of qubits (≤ 24) within the experimental capability. Here we scrutinize this result by state-of-the-art classical simulations, which greatly exceed the experimental system sizes and provide a benchmark for future studies in larger circuits. We find that the bound states consisting of a *finite* number of photons are indeed robust in the nonintegrable regime, even after scaling to the infinite-time and infinite-system size limit. Moreover, we show that such systems possess unusual spectral properties, with level statistics that deviates from the random matrix theory expectation. On the other hand, for low but finite density of photons, we find a much faster onset of thermalization and significantly weaker signatures of bound states, suggesting that anomalous dynamics may only be a property of dilute systems with *zero* density of photons in the thermodynamic limit. The robustness of the bound states is also influenced by the number of decoration qubits and, to a lesser degree, by the regularity of their spatial arrangement.

I. INTRODUCTION

Recent advances in quantum simulators based on ultracold atoms, trapped ions, and superconducting circuits [1–8] have opened a window to studying far-from-equilibrium dynamics and thermalization in isolated many-body systems [9–12]. The behavior of generic thermalizing systems is described by the eigenstate thermalization hypothesis (ETH) [13–15], which seeks to explain the process of thermalization at the level of the system's energy eigenstates. In certain systems, the ETH can break down, allowing for new types of dynamical behavior and phases of matter to emerge [16]. One of the most striking manifestations of ergodicity breakdown occurs in finely tuned one-dimensional systems [17], which fail to thermalize due to their rich symmetry structure known as quantum integrability [18,19].

A paradigmatic quantum integrable system is the spin-1/2 XXZ model, which describes the low-energy physics of certain ferromagnetic materials [20]. In one spatial dimension, the model's *tour de force* analytic solution in the isotropic limit was presented by Bethe in the 1930s [21]. One remarkable consequence of that solution was a special class of eigenstates that can be viewed as bound states of magnons—the elementary quasiparticle excitations, whose signatures were observed in spectroscopic experiments [22–24]. However, due to the challenges of probing bound states via conventional techniques such as inelastic neutron scattering, it has been proposed [25] that local quenches [26–32] may provide deeper insight into the physics of bound states [33–39]. Dynamical signatures of bound states were indeed observed in systems of ^{87}Rb atoms in an optical lattice, realizing an effective Heisenberg model [40].

While previous studies mostly focused on systems with continuous dynamics governed by a static Hamiltonian, it is also possible to construct equivalent Floquet models defined as a product of unitary matrices. Such models, whose quantum dynamics is intrinsically discrete, are better suited for quantum devices, which operate as a sequence of unitary gates. Quantum circuit models that correspond to the spin-1/2 Heisenberg model in the high-frequency limit were studied in Refs. [41,42]. Remarkably, the Floquet circuit realization was shown to be integrable for arbitrary parameters and not only in the small time-step limit where it reduces via Troterrization to the Hamiltonian model [41–43].

The Floquet XXZ model was recently experimentally realized using a ring of superconducting qubits connected by high-fidelity fSim quantum logic gates [44]. These qubits interact with each other by superconducting currents and can host excitations in the form of trapped photons. This setup has allowed for the preparation and observation of bound states of a few interacting photons, which were predicted and analytically studied in Ref. [45]. One of the advantages was the possibility of controllably breaking the integrability by attaching extra qubits to the main chain and thus changing the geometry of the system. In contrast with the expectation that the bound states are protected by integrability, it was experimentally observed that these states survive even in the non-integrable regime, as previously suggested for the Hamiltonian version of the model [25]. However, the robustness of the bound states was not studied in detail and the question of which mechanism protects it in the nonintegrable case remains open.

In this work, we use classical simulations, based on exact diagonalization (ED) and matrix product states (MPS), to gain understanding of the experiment in Ref. [44]. Specifically, we study the statistical properties of the Floquet spectrum in order to detect the transition from the integrable to the nonintegrable regime. We also employ time-evolving block decimation (TEBD) simulations to investigate the evolution of bound states and their robustness. In this way, we are able to reach far larger system sizes, photon numbers, and timescales compared to the quantum hardware [44]. In contrast to the experiment, which has limitations due to the unwanted leakage of photons, the photon number is conserved in our study. We find that sectors with *small but fixed* photon number have nonthermalizing spectral properties, which affect both their level statistics and quantum dynamics. Additionally, we confirm the experimental finding that the bound states in these sectors persist beyond the integrable regime. While this effect is pronounced in dilute systems containing small photon numbers, it appears to be restricted to *zero density* of excitations in the thermodynamic limit. By contrast, sectors with small but finite excitation density are found to thermalize rapidly as the photon number is increased, in parallel with the fast decay of bound states.

The remainder of this paper is organized as follows. In Sec. II we introduce the Floquet XXZ model that will be the main object of our study. In Sec. III we identify anomalous properties in the statistics of the Floquet quasienergy levels, including the average ratio of consecutive gaps and the density of states. These results are complemented by the spectral form factor, which captures the signatures of anomalous spectral features at an intermediate Thouless time scale, relevant to transport. In Sec. IV we study the evolution of bound states and their robustness to integrability breaking. We perform extrapolations to infinite system size and compare the data against the diagonal ensemble predictions, which provides information about

the *infinite-time* limit. In Sec. V we discuss several cases beyond those studied in experiment, in particular systems with a constant filling factor and different decoration patterns, including nonsymmetric ones. We summarize our results and discuss their implications in Sec. VI. Appendices provide more details about the corresponding continuous XXZ model, effects of different parameters, the origin of peaks in the density of states, and the properties of Floquet modes, such as their localization in the Fock space.

II. MODEL

The experiment in Ref. [44] realized a decorated ring of superconducting qubits, schematically illustrated in Fig. 1(a). If the occupancy is limited to zero or one photon per qubit, the photons can be modeled as hard-core bosons. Since we are considering a ring of qubits, we will impose periodic boundary conditions (PBCs) in our ED calculations, unless stated otherwise. The fundamental building block of the circuit is a two-qubit fSim gate acting on pairs of adjacent qubits,

$$\text{fSim}(\theta, \phi, \beta) = \begin{pmatrix} 1 & 0 & 0 & 0 \\ 0 & \cos\theta & ie^{i\beta}\sin\theta & 0 \\ 0 & ie^{-i\beta}\sin\theta & \cos\theta & 0 \\ 0 & 0 & 0 & e^{i\phi} \end{pmatrix}, \quad (1)$$

where θ and β determine the nearest-neighbor hopping amplitude and phase, while ϕ represents the strength of interactions between neighboring qubits. The parameter β mimics the external magnetic flux threading the ring. In the following, we will primarily consider the case $\text{fSim}(\theta, \phi, \beta = 0) = \text{fSim}(\theta, \phi)$.

Figure 1(a) is a sketch of the model with decorations attached to every other site as in Ref. [44]. The number of photons will be denoted by N and the total number of sites by $L = L_{\text{sites}} + L_{\text{decor}}$, which includes both the sites
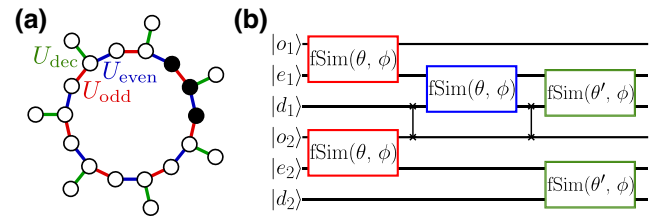

FIG. 1. (a) Sketch of the XXZ circuit model with $L = 14 + 7$ sites (7 unit cells). Filled dots denote a bound state of $N = 3$ photons. Here, the integrability-breaking decorations are attached to every other site. (b) An example of the corresponding quantum circuit with $L = 4 + 2$ sites. The circuit consists of fSim (boxes) and SWAP gates (vertical lines). The alternating layers of gates acting on even or odd bonds and decorations are denoted by blue, red, and green color, respectively, matching the unitaries U_{even}, U_{odd}, and U_{dec} in (a). Our classical MPS simulations in iTensor [46] follow this diagram and assume open boundary conditions.

on the ring L_{sites} and the extra sites L_{decor}. The sketch also depicts a state with $N = 3$ adjacent photons, which will typically be used as the initial state in our simulations. Note that there is another, similar configuration of three adjacent photons, that is simply shifted by one lattice site. This configuration is inequivalent to the one in Fig. 1(a) because it is connected to two decorations instead of one. As specified below, we will occasionally find it useful to average the results over these two initial states. In addition to the layout shown here, in Sec. V we will also consider other decoration patterns. In general, we find the dynamical properties are highly sensitive to the number of photons and the decoration pattern.

Figure 1(b) shows the corresponding quantum circuit, which consists of fSim and SWAP gates. The states of the even, odd, and decoration qubits are denoted by $|e_i\rangle$, $|o_i\rangle$, and $|d_i\rangle$, respectively. Our classical TEBD simulations follow the layout in Fig. 1(b) and, for convenience, assume open boundary conditions (OBCs). We emphasize that the results below are insensitive to the choice of boundary conditions, as we will demonstrate good agreement between TEBD with OBCs and ED with PBCs. The circuit is defined by first applying fSim gates across all odd bonds, then across all even bonds. Since the even and odd bonds are thus not equivalent, the system is invariant to translation by two lattice sites of the main chain. Additional gates which couple to the integrability-breaking extra sites $|d_i\rangle$ are subsequently applied, which can further reduce the symmetry of the full system depending on the pattern of arrangement of the extra sites. The coupling parameter θ' is used to tune between the integrable and nonintegrable regimes, while the interaction strength $\phi = \phi'$ is the same, both along the main chain and between the chain and the decorations. The one-cycle unitary operator is then

$$\hat{U}_F = \underbrace{\prod_{\text{extra bonds}} \text{fSim}(\theta', \phi)}_{\hat{U}_{\text{dec}}}$$

$$\times \underbrace{\prod_{\text{even bonds}} \text{fSim}(\theta, \phi)}_{\hat{U}_{\text{even}}} \underbrace{\prod_{\text{odd bonds}} \text{fSim}(\theta, \phi)}_{\hat{U}_{\text{odd}}}. \quad (2)$$

As shown in Appendix A, the Hamiltonian of the XXZ model corresponds to the Trotter-Suzuki expansion of this unitary in the $\phi, \theta, \theta' \to 0$ limit.

The isotropic XXX version of the model in Eq. (2) was first proposed in Ref. [41], while the Floquet XXZ model was formulated in Ref. [42] and analytically studied in detail in Ref. [45]. The latter used the Bethe ansatz to derive the dispersion of bound states containing an arbitrary number of photons. These bound states are formed by stable magnon quasiparticles, and there are two different phases depending on the ratio of θ and ϕ: (1) gapped phase

$\phi > 2\theta$, where bound states of any photon number exist for any momentum, and (2) gapless phase $\phi < 2\theta$ where the bound states are only present for a finite range of momenta. The maximal group velocity was found to decrease with the number of photons in the bound state. Quantum simulations [44] have later confirmed the analytical relations between the velocity of quasiparticles and their momentum. However, analytical solutions are not available for the nonintegrable case, where the integrability is broken either by adding certain perturbations or by changing the geometry of the system. We will use classical simulations to numerically study this regime.

A. Circular orthogonal ensemble

Before we analyze in detail the Floquet spectrum of Eq. (2), we must understand the relevant symmetries of the model as they affect the random matrix theory ensemble describing the spectrum after breaking the integrability [47]. For example, the undecorated model with PBCs is invariant under translation by two sites, due to the even and odd layers of fSim gates being applied separately. Such a circuit is also invariant under spatial inversion. However, attaching extra qubits to some of the sites reduces the symmetry of the full system. Regular patterns with decorations on every nth site will preserve some form of translation invariance, although with a larger unit cell. Furthermore, the system can be inversion symmetric only if the decoration pattern itself is also inversion symmetric. However, in some cases, such as that with decorations on every other site, the inversion of the decorations can be incompatible with the inversion of the main ring due to different reflection axes, so the full system only has translation symmetry, even though the decoration pattern is still inversion-symmetric. This will be discussed in more detail in Sec. V B.

For a general unitary matrix $\hat{U}_F$, the level statistics is expected to conform with the circular unitary ensemble (CUE). However, as will be apparent in Secs. III A and V B, in most cases studied here we obtain the circular orthogonal ensemble (COE) statistics instead. COE would trivially ensue if $\hat{U}_F = \hat{U}_F^T$, however this is not the case here for any arrangement of decorations. Our calculations show that the necessary conditions for COE level statistics are an inversion-symmetric decoration pattern and equal parameters for the fSim gates on the even and odd bonds along the ring, as defined in Eq. (2). Additionally, the mirror axis for inversion needs to be centered on a site, not on a bond between two sites. If $\hat{R}$ is the inversion-symmetry operator, which reflects the qubits along this axis, we then have $\hat{R}\hat{U}_{\text{odd}}\hat{R} = \hat{U}_{\text{even}}$, $\hat{R}\hat{U}_{\text{even}}\hat{R} = \hat{U}_{\text{odd}}$, and $\hat{R}\hat{U}_{\text{dec}}\hat{R} = \hat{U}_{\text{dec}}$. For simplicity, we define a modified one-cycle unitary operator

$$\hat{U}_F' = \sqrt{\hat{U}_{\text{dec}}}\, \hat{U}_{\text{even}} \hat{U}_{\text{odd}} \sqrt{\hat{U}_{\text{dec}}}. \quad (3)$$

The operators $\hat{U}_F$ and $\hat{U}'_F$ have the same spectrum, since they differ only by a time shift. It is now easy to see that $\hat{U}'_F = \hat{R}\hat{U}'^T_F\hat{R}$. This can be understood as an additional symmetry, which relates the evolution operator and its transpose, resulting in COE level statistics. Our situation is reminiscent of Ref. [48], where the Floquet spectrum was shown to have COE instead of CUE statistics if there is a transformation which connects the two steps of the Floquet unitary.

Another possibility is when the mirror axis is between two adjacent sites, leading to $\hat{R}\hat{U}_{\mathrm{odd}}\hat{R} = \hat{U}_{\mathrm{odd}}$ and $\hat{R}\hat{U}_{\mathrm{even}}\hat{R} = \hat{U}_{\mathrm{even}}$. We then have $\hat{U}'_F = \hat{R}\hat{U}'^T_F\hat{R}$, meaning that $\hat{R}$ is simply another symmetry of $\hat{U}'_F$ which needs to be resolved. The level statistics in the sector where $\hat{R}$ has eigenvalue $+1$ is then CUE. The only deviations from this expectation are found for small numbers of decorations such as two or four adjacent decorations, where the level statistics after resolving the $\hat{R}$ symmetry is somewhere between COE and CUE. However, it seems to increase towards CUE as the density of decorations or the number of photons is increased. There are also special cases, which are inversion symmetric in respect to both types of mirror axes, such as the pattern with decorations on every third site. In those cases, the level statistics stays COE even after resolving the $\hat{R}$ symmetry. In contrast, all nonsymmetric decoration arrangements were found to exhibit CUE level statistics.

III. SPECTRAL PROPERTIES

In this section we analyze the spectrum of our unitary circuit model in Eq. (2). This model does not have a Hamiltonian representation in general, since the mapping to the XXZ model (Appendix A) is only valid in the $dt \rightarrow 0$ limit. As a consequence, the system does not have eigenstates in the usual sense. However, we can instead compute the eigenstates of the one-cycle evolution operator $\hat{U}_F$ Eq. (2), which are known as the Floquet modes. The corresponding Floquet quasienergy spectrum is periodic, with periodicity $2\pi/T$, where T is the time length of one cycle. We set the units such that $T = 1$. We will investigate properties of the Floquet modes and quasienergies by studying their level statistics and the density of states, which tell us about the behavior of the system at very late time scales corresponding to the Heisenberg time. We follow these results by studying the spectral form factor, which reveals similar information at the intermediate Thouless time, relevant for transport.

A. Level statistics

In order to determine whether our model Eq. (2) is integrable or chaotic, we study the statistics of its quasienergy levels ϵ_n. In particular, we examine the level statistics ratio, $r = \min(s_n, s_{n+1})/\max(s_n, s_{n+1})$, characterizing the
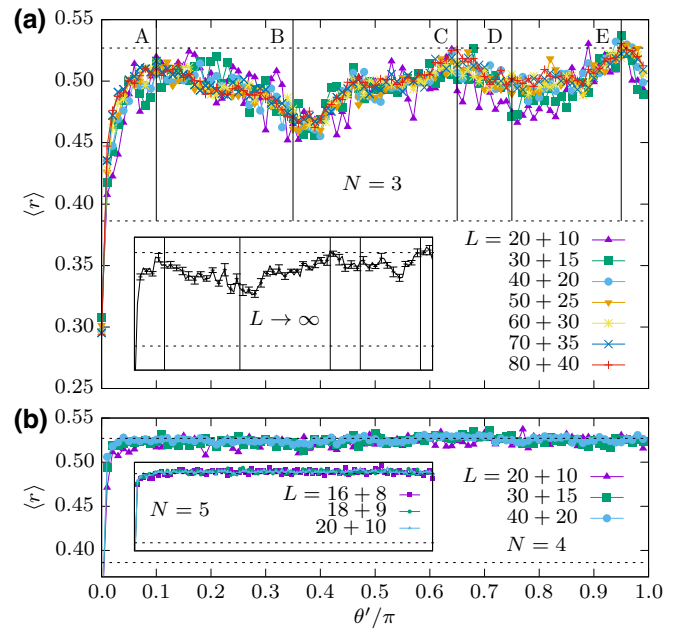

FIG. 2. Statistics of the Floquet quasienergies. Average ratio of consecutive energy gaps $\langle r \rangle$ for different values of θ' with fixed $\theta = \pi/6$, $\phi = 2\pi/3$, $\beta = 0$. The horizontal dashed lines are $\langle r \rangle_{\mathrm{P}} \approx 0.386$ and $\langle r \rangle_{\mathrm{COE}} \approx 0.527$. (a) $N = 3$ photons for different system sizes indicated in the legend. The relevant Hilbert-space dimensions range from $\dim_{L=20+10} = 406$ to $\dim_{L=80+40} = 7021$. The vertical lines A, B, C, D, and E mark several values of θ'/π (0.10, 0.35, 0.65, 0.75, and 0.95, respectively) that will be studied later in more detail. Inset: linear extrapolation to $L\rightarrow\infty$. (b) The case of $N = 4$ photons and $N = 5$ photons (inset), with the largest Hilbert-space dimensions $\dim_{L=40+20} = 24405$ and $\dim_{L=20+10} = 14253$, respectively. In all the plots, we resolve the translation symmetry and consider only the $k = 0$ momentum sector.

spacing of adjacent quasienergy gaps $s_n = \epsilon_{n+1} - \epsilon_n$ [49]. When computing $\langle r \rangle$, we omit any exact degeneracies, although such degeneracies are typically absent as long as $\theta' \neq 0$. An integrable system is expected to follow the Poisson distribution with the average value $\langle r \rangle_{\mathrm{P}} \approx 0.386$, while in the chaotic regime the expected distribution for our case, as explained in Sec. II A above, is the circular orthogonal ensemble (COE) with $\langle r \rangle_{\mathrm{COE}} \approx 0.527$ [47,50]. We vary the hopping amplitude θ' between the main chain and the extra sites from 0 to π and plot the corresponding $\langle r \rangle (\theta')$. Figure 2(a) shows the results for $N = 3$ photons for various chain lengths, while the extrapolation to an infinitely large system $L\rightarrow\infty$ is plotted in the inset. This result should be contrasted against the results for $N = 4$ and $N = 5$ photons in Fig. 2(b).

Turning on the coupling to the decorations is expected to break integrability, which can indeed be observed in Fig. 2, where the value of $\langle r \rangle (\theta')$ rapidly jumps towards $\langle r \rangle_{\mathrm{COE}}$ as soon as $\theta' \neq 0$. For $N \geq 4$ photons, as soon as $\theta' \gtrsim 0.05\pi$, the level statistics remains pinned to the COE value, in agreement with the usual expectation for

integrability breaking in Hamiltonian systems [51]. However, the case with $N = 3$ photons shows a visible departure from these expectations, exhibiting pronounced dips towards the Poisson value at special values of θ'—see Fig. 2(a). Furthermore, we find that the positions of the dips in $\langle r \rangle$ depend on the main chain hopping amplitude θ, but not on the interaction strength ϕ or the flux through the ring β, see Appendix C. No emergent symmetry, which would explain the dips at certain values of θ', could be identified. Instead, below we will relate the presence of dips with special structures in the density of states of the quasienergy spectrum.

We note that in all cases plotted in Fig. 2, the value of $\langle r \rangle(0)$ lies below the Poisson line, even though the model is known to be integrable at $\theta' = 0$. This is simply due to a large number of degeneracies that arise in the Floquet spectrum due to the disconnected decorations, which produces a strong peak in the probability distribution at zero level spacing. Namely, even though there is no hopping to the extra sites when $\theta' = 0$, there are still states where one or more photons are frozen in these additional sites. A state with all photons outside the main chain has zero energy, as do some states with two separate photons on the main chain and all other photons outside. We found that completely removing the extra sites brings $\langle r \rangle(0)$ closer to $\langle r \rangle_P$, as expected. We also note that, while the hopping amplitudes inside the main chain and between the chain and the extra sites are different, $\theta \neq \theta'$, the nearest-neighbor interaction strength is equal in both cases $\phi = \phi'$. This means that the photons frozen in the decorations can still interact with other photons.

The intriguing features in the level statistics observed in Fig. 2(a) can be understood from the density of states (DOS). The intuition is that sharp peaks in DOS signal a large number of degeneracies in the spectrum, which can decrease the value of $\langle r \rangle$. In Fig. 3(a), we plot the normalized DOS curves for $N = 3$ and $N = 5$ photons at several values of θ' that were marked by A–E in Fig. 2(a). Both photon numbers exhibit a peak at $\epsilon = 0$ when $\theta' = 0$, which is explained by the previously discussed large number of zero modes due to the extra sites. This zero-energy peak is much more prominent for $N = 3$ and its relative height decreases with N. The results for $N = 4$ (not shown) are in between those for $N = 3$ and $N = 5$, with more peaks than $N = 5$, but still overall flatter than $N = 3$. As θ' is increased, the DOS curves become more flat. However, several other notable peaks are present for $N = 3$. Although these peaks are visible at all θ', they are particularly sharp at those values where $\langle r \rangle$ deviates from $\langle r \rangle_{COE}$ (e.g., $\theta' \in [0.25\pi, 0.45\pi]$ and $\theta' \in [0.75\pi, 0.85\pi]$), see Figs. 2(a) and 3(a), signaling high nonuniformity in the quasienergy spectrum. The peaks in DOS are not present for the nonsymmetric patterns of extra sites, such as a single or three decorations, which will be discussed in Sec. V B.
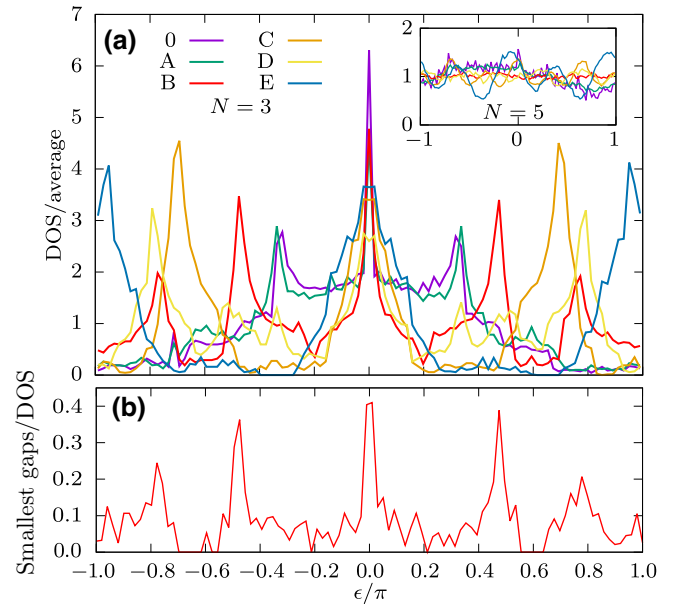

FIG. 3. (a) Density of states (DOS) for different values of θ', normalized by the average over the entire quasienergy spectrum [the labels A–E are defined in Fig. 2(a), while 0 denotes the integrable case $\theta' = 0$]. The main panel corresponds to $N = 3$ photons in a system size $L = 80 + 40$, while the inset shows $N = 5$ in $L = 20 + 10$. In both cases, $\theta = \pi/6$, $\phi = 2\pi/3$. (b) Distribution of the 1000 smallest quasienergy gaps (i.e., about 15% of all levels) throughout the Floquet spectrum, normalized by the local DOS. Data is for $N = 3$ photons in system size $L = 80 + 40$ at $\theta = \pi/6$, $\phi = 2\pi/3$, $\theta' = 0.35\pi$, i.e., for the point labeled B in (a).

At $\theta' = 0$, the peaks in DOS correspond to exact and near degeneracies in the spectrum. Since DOS is probing aggregated features of the spectrum, at finite θ' the peaks do not necessarily demonstrate the presence of near degeneracies between neighboring energy levels that are required for $\langle r \rangle$ to anomalously reduce. However, we find that the smallest gaps between quasienergies are indeed disproportionately concentrated in the towers. In Fig. 3(b), we see that the 1000 smallest quasienergy gaps (normalized by the local DOS) at point B align closely with the location of the towers. Further discussion of the origin of peaks in DOS based on the quasiparticle dispersion relation can be found in Appendix B.

B. Spectral form factor

The level statistics quantities considered above derive from the properties of eigenvalues of the Floquet unitary, hence they describe the behavior of the system at late times. In order to gain information about intermediate times, we study the spectral form factor (SFF) [52]:

$$K(t) = \sum_{m,n} e^{it(\epsilon_n - \epsilon_m)}, \qquad (4)$$

which is defined in terms of two-point correlations between the Floquet quasienergies, ϵ_n. As we set the time period of one unitary cycle to $T = 1$, the time in the above equation is equal to the number of cycles, $t = n_c$.

SFF is known to exhibit starkly different behavior in integrable and chaotic systems, see Refs. [53–56] for some recent examples. In both cases, the SFF at short times is governed by microscopic details of the system and therefore it is nonuniversal. After this initial transient, in integrable systems (Poisson ensemble) the SFF stays approximately constant $K_P(t) \approx \mathcal{H}$, around the value equal to the Hilbert space dimension $\mathcal{H}$. In nonintegrable systems, SFF first reaches a global minimum and, around the Thouless time t_{Th}, it starts to grow approximately linearly, according to the predictions of random matrix theory, until it saturates by the Heisenberg time $t_H \sim \mathcal{H}$. The level statistics and the DOS studied above naturally pertain to the times of order t_H, where the discreteness of the Floquet quasienergy spectrum is resolved.

SFF is typically noisy and suffers from a lack of self-averaging [57,58]. In order to smoothen its time dependence, we chose to average it over the flux through the ring β. This parameter does not qualitatively affect the level statistics, as confirmed in Appendix C. Additionally, after averaging over 100 values of $\beta \in [0, \pi]$, we also compute the moving average at each time point by taking into account the nearest 60 points, which finally results in relatively smooth curves. The averaged SFFs for $N = 3$ photons, $L = 60 + 30$ sites and different values of θ' are shown in the inset of Fig. 4(a). After an initial period

of nonuniversal behavior, the SFF for $\theta' = 0$ assumes an approximately constant value, confirming that the system is integrable. In contrast, a clear linear ramp followed by saturation emerges for all studied values of $\theta' > 0$, consistent with broken integrability. We note that the SFF for $\theta' = 0$ saturates at a higher value than $\theta' > 0$, where the plateau is exactly as expected at $\mathcal{H}$. The reason for this is a large number n_0 of zero modes in the integrable case, which increases the late-time value of the SFF to $\mathcal{H} + n_0^2$ (at $\theta' = 0$).

Furthermore, the Thouless time t_{Th} can be extracted from the SFF data. This time gives us the onset of the linear ramp, i.e., the universal behavior described by the random matrix theory. The COE prediction for SFF in the time window $0 < t < \mathcal{H}$ is [47]

$$K_{COE}(t) = 2t - t\ln(1 + 2t/\mathcal{H}), \quad (5)$$

as shown by the dashed black curve in Fig. 4. In principle, the Thouless time could be defined as the smallest time for which $K(t) = K_{COE}(t)$. However, since $K(t)$ is typically not smooth enough even after averaging, in practice we use the following criterion to determine the Thouless time [59]:

$$\ln(K(t_{Th})/K_{COE}(t_{Th})) = 0.4. \quad (6)$$

The precise value of the filtering parameter 0.4 is unimportant, as long as it is finite but not too small. In Fig. 4, we plot the extracted Thouless time together with the
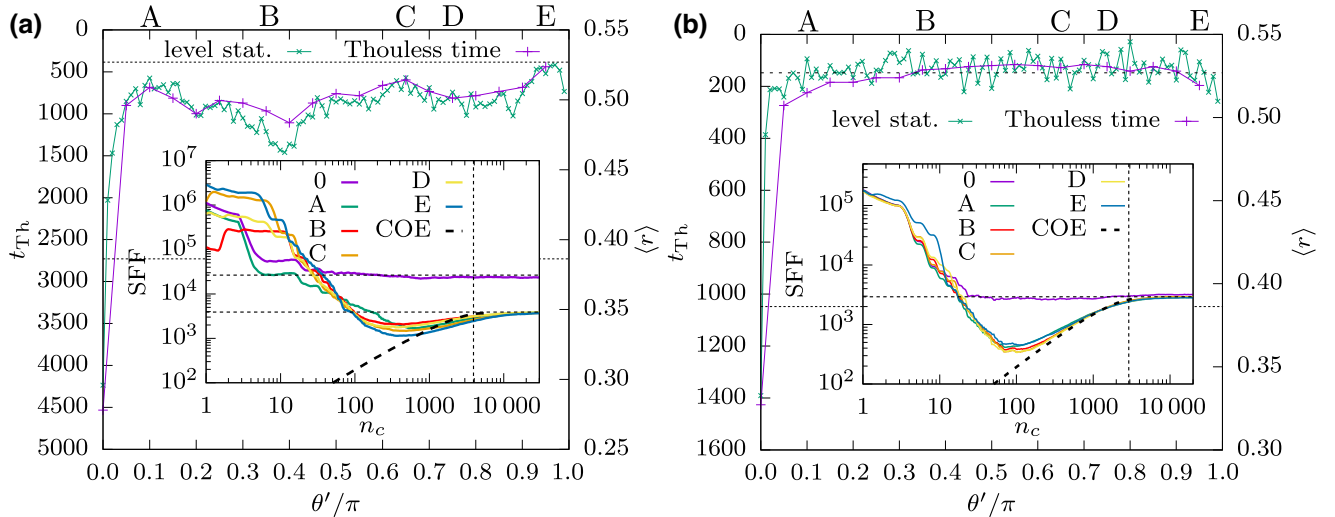

FIG. 4. (a) Comparison of the level statistics ratio $\langle r \rangle$ and the Thouless time extracted from the spectral form factor (SFF) for $N = 3$ photons, $L = 60 + 30$. The labels A, B, C, D, and E mark the special values of θ' from Fig. 2. Inset: SFF time series for several values of θ' indicated in the main panel. The data was averaged over β and smoothened by a moving average (see text). Note the logarithmic scale on both the x and y axis. The horizontal dashed lines mark the saturation values, $\mathcal{H}$ and $\mathcal{H} + n_0^2$, while the vertical line at $n_c = \mathcal{H}$ is the Heisenberg time. The dashed black curve is the COE prediction for the linear ramp. The agreement with COE becomes better as N increases. (b) Same as panel (a) but for $N = 5$ and $L = 14 + 7$, which shows a much clearer linear ramp in the SFF and better agreement with the random matrix theory at late times.

average level-spacing ratio $\langle r \rangle$ for $N = 3$ and varying θ'. Interestingly, the two curves exhibit very similar features, which means that the previously observed deviations in the level statistics for $N = 3$ leave an imprint on the transport properties. The latter—as defined by the Thouless time—occurs later in systems that are farther away from the nonintegrable case, as defined by $\langle r \rangle$.

The agreement of SFF with the random matrix-theory prediction K_{COE} is not particularly good for $N = 3$ photons. This supports our previous observation that the energy spectra in small photon-number sectors have special properties, e.g., as seen in fluctuations of the level statistics and the nonmonotonic DOS. The agreement with COE becomes better as the number of photons N increases, as can be seen for $N = 5$ in Fig. 4(b). The number of zero modes at $\theta' = 0$ is now much smaller than the Hilbert-space dimension, so the dashed horizontal lines at $\mathcal{H}$ and $\mathcal{H} + n_0^2$ are visually indistinguishable. There is also less variance in $K(t)$ curves for different values of $\theta' > 0$, which is reflected in the almost constant value of the extracted Thouless time, as shown in the same figure. This is in line with the level-spacing ratio $\langle r \rangle$, which shows no oscillation with θ' for this photon number but instead remains approximately constant around $\langle r \rangle_{\mathrm{COE}}$.

C. Summary

In this section, we have studied the spectral properties of the Floquet unitary in Eq. (2). We confirmed that integrability is generally broken by $\theta' \neq 0$ in large system sizes. However, at special values of θ', for $N = 3$ photons we also observed a pronounced tendency towards restoration of the Poisson level statistics, see Fig. 2(a). We have related these features in the level statistics to the peaks in the DOS in Fig. 3(a), resulting from an interplay between the geometry of the decorations and the small photon clusters forming the bound states. As these properties derive from the quasienergy spectrum of the Floquet operator, they implicitly relate to the behavior of the system at the very late Heisenberg time. Nevertheless, the study of the SFF showed that similar signatures at these special values of θ' can also be observed at the intermediate Thouless time. A natural question, addressed next, is how these features relate to the dynamics from the special subset of initial conditions associated with bound states of photons.

IV. DYNAMICS OF BOUND STATES

Thus far, we have focused on generic aspects of thermalization at the level of the entire Floquet spectrum of the decorated XXZ circuit in Eq. (2). However, one of the motivations behind the experiment [44] to study this particular model is the fact that its integrable version hosts a special class of ballistically propagating bound states. While such bound states are here protected by integrability, they represent only a fraction of all eigenstates and

therefore it is not hard to imagine that they may persist, due to some other protective mechanism, after integrability is broken. We now examine in detail the stability of such states after decorating the circuit to break its integrability.

In the Ising limit of the Hamiltonian version of the XXZ model, $J_z \gg J$, an N-particle bound state corresponds to N adjacent spins being flipped [25],

$$|000.. \underbrace{1 \cdots 1}_{N} ..000 \rangle. \tag{7}$$

Even far from the Ising limit when $J_z \geq J$, the behavior of an N-particle bound state can be understood by starting from such an initial state, which is no longer an eigenstate. The same is true for the Floquet XXZ circuit, with the Hamiltonian Ising limit corresponding to $\phi \gg \theta$.

Starting from the initial state (7), the "bound-state probability" (BSP) after n_c cycles is given by

$$\mathcal{B} = \frac{n_T}{n_T + n_S}, \tag{8}$$

where $n_T = \langle \psi(n_c)| \sum_j \prod_{i=j}^{j+(N-1)} \hat{n}_i |\psi(n_c) \rangle$ is the probability of finding photons in N adjacent sites, where the indices i and j label the sites on the main chain. Conversely, the probability of any other N-photon configuration was denoted n_S.

The BSP was experimentally measured in Ref. [44] and found to gradually decay over time even at $\theta' = 0$. This decay was due to experimental imperfections rather than an intrinsic property of the model. For an ideal implementation of the XXZ circuit, the BSP drops rapidly before fluctuating around a steady finite value, as will be shown below. However, once integrability breaking terms are introduced into the circuit, there is no requirement for the N-photon bound states to continue to be stable at late times. Below, we focus on understanding the effect of integrability breaking on BSP dynamics using TEBD simulations implemented in iTensor [46].

The BSP dynamics for $N = 3$, 4, and 5 photon bound states is presented in Figs. 5(a)–5(c) for various strengths of the integrability breaking θ'. By increasing θ' from 0 to $\pi/2$, the decorations become more strongly coupled to the main chain and the bound states are eventually destroyed. However, at intermediate θ' the BSP does not decay to zero, even after many cycles. This is true even when θ' is comparable in size to the natural energy scale along the chain, $\theta' \approx \theta$. For larger bound states, θ' introduces large, slow oscillations into the BSP that are independent of system size. The origin of these oscillations will be explained in Appendix F.

Typically, an infinitesimally small perturbation is sufficient to destroy integrability in the thermodynamic limit $L \rightarrow \infty$ and infinite time limit $t \rightarrow \infty$. We access these limits by extrapolating the numerical data for the BSP via
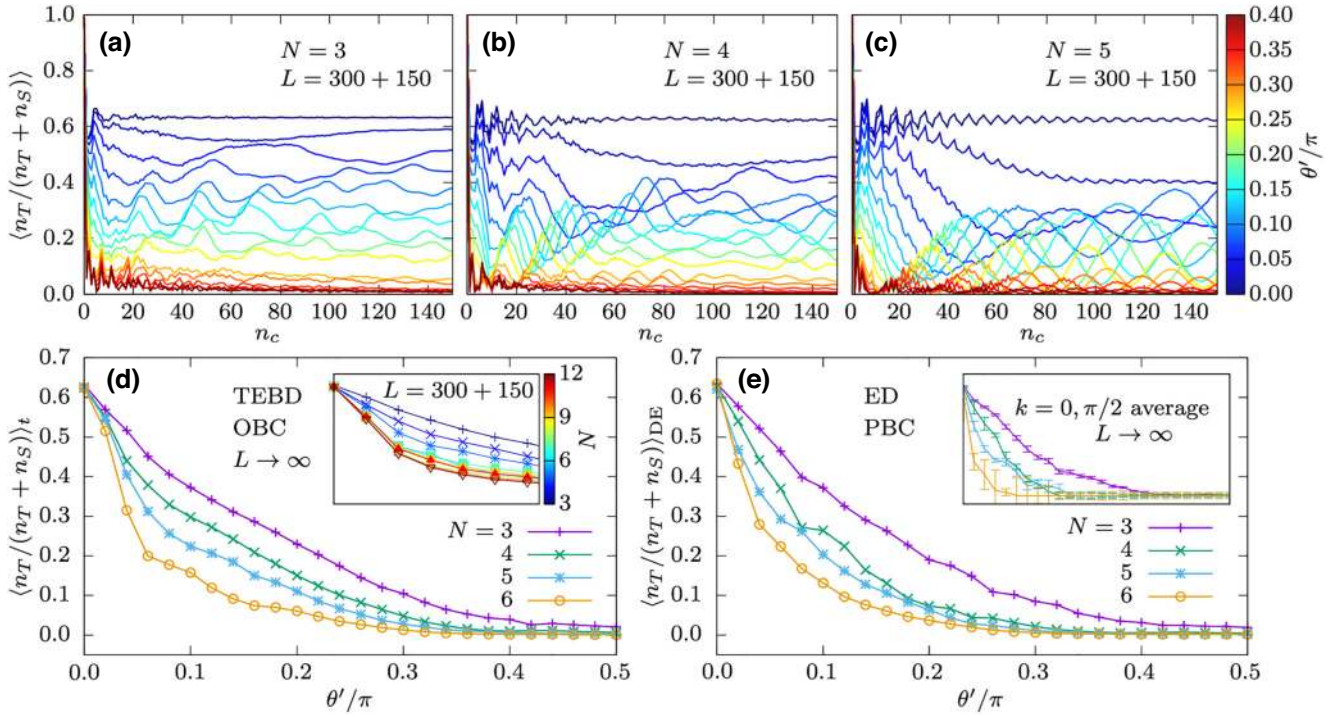
FIG. 5. (a)–(c) Dynamics of the bound-state probability (BSP) with $\theta = \pi/6$, $\phi = 2\pi/3$, for $N = 3$ photons (a), $N = 4$ (b), and $N = 5$ (c), at fixed system size $L = 300 + 150$. Data is obtained using TEBD with bond dimension $\chi = 256$ and open boundary conditions. (d) Time average of the BSP over 100 cycles using TEBD and extrapolated to $L \to \infty$. We also averaged over two inequivalent initial states (7). The extrapolation errors are smaller than the size of the symbols in the plot. Inset: average BSP for different photon numbers N at fixed $L = 300 + 150$. Data was averaged over 150 cycles and obtained using TEBD with bond dimension $\chi = 320$ for $3 \le N \le 12$, $\theta = \pi/6$, $\phi = 2\pi/3$ and varying θ'. (e) Diagonal ensemble prediction for the probability to remain in a bound state, averaged over two possible initial configurations. Data in this panel is obtained using ED with PBCs, on system sizes $N = 3$, $L = 30 + 15$ (with Hilbert-space dimension dim $= 14189$); $N = 4$, $L = 20 + 10$ (dim $= 27404$); $N = 5$, $L = 14 + 7$ (dim $= 20348$); $N = 6$, $L = 12 + 6$ (dim $= 18563$). Inset: extrapolation to infinite system size for translation invariant initial configurations, averaged over states with $k = 0$ and $k = \pi/2$ momenta.

two methods: time averaging the TEBD results and evaluating the diagonal ensemble predictions from ED data. The latter directly takes the $t \to \infty$ limit by assuming that the off-diagonal elements of the density matrix average out to zero [15,50]. These two methods have different advantages and limitations. While the TEBD method allows us to study dynamics in very large systems, these simulations become computationally more expensive as the evolution time increases, which limits the total number of cycles. On the other hand, the diagonal ensemble prediction provides information about the BSP at infinite time. This avoids the problems associated with long time scales for decay, which have been observed in quenches involving low density of quasiparticle excitations [60]. However, the diagonal ensemble requires a computation of the complete eigenspectrum using ED, which limits the maximal system size. The total Hilbert-space size is constrained by the amount of RAM available for diagonalization, while our implementation relies on 128-bit integers to represent basis configurations, which limits the maximal number of sites $L \le 128$, irrespective of the photon number N.

In principle, the latter restriction can be lifted using a more flexible encoding of the basis states, at the cost of sacrificing some of the computation efficiency.

For the TEBD time average of the BSP, we consider 100 cycles between cycle $n_c = 20$ and cycle $n_c = 120$ for a variety of system sizes ranging from $L = 20 + 10$ to $L = 300 + 150$. In this way, we exclude the data at very short times, which may be impacted by nonuniversal effects. By fitting the average BSP at each system size according to $\mathrm{BSP}(L, \theta') = \alpha(1/L) + \mathrm{BSP}_\infty$ we extrapolate to $L \to \infty$ and obtain the result plotted in Fig. 5(d). This procedure was repeated for several photon numbers N. In each case, the initial state was chosen according to Eq. (7), which is not translation invariant. As discussed in Sec. II, there are two such inequivalent configurations and our results are averaged over both. We find that the bound states are robust for a finite range of θ', which decreases as the size of the bound states increases.

We also address how the robustness changes as the bound states increase in size, but continue to be dilute relative to the total system size, $N/L \ll 1$. We calculate the

BSP for bound states between sizes $N = 3$ and $N = 12$, averaged over $n_c = 150$ cycles, to find BSP(N, θ'). The results for a fixed number of sites $L = 300 + 150$ are plotted in the inset of Fig. 5(d), where it can be seen that the BSP(N, θ') curves are starting to converge for larger values of N. These results suggest that large but dilute bound states continue to be robust.

The diagonal ensemble results, which directly access the infinite time limit $t \to \infty$ of the BSP, can be seen in Fig. 5(e). These results are consistent with the extrapolated TEBD results, suggesting small bound states are robust for a finite range of θ'. In particular, the $N = 3$ bound states appear to be robust up to values of the integrability breaking that are comparable to the on-chain hopping terms. As N becomes larger the bound states appear to become less robust, however, both Figs. 5(e) and 5(d) suggest the $N = 4$, $N = 5$, and $N = 6$ bound states are robust for a finite range of θ'.

For our diagonal ensemble calculations in Fig. 5(e) we also averaged over two inequivalent initial configurations (7). Since these states break translation invariance, we have to work in the full Hilbert space and therefore cannot obtain enough data points for reliable system-size scaling. However, if we form a translation-invariant initial state, we can restrict to a particular momentum sector and reach much larger system sizes. This allows us to extrapolate the diagonal ensemble value for BSP to $L \to \infty$, as shown in the inset of Fig. 5(e), where we have averaged over the $k = 0$ and $k = \pi/2$ sectors. We chose these two values of momenta because we found that they capture the extremal behavior of BSP at small θ': the latter is particularly robust for $k = 0$ and decays most rapidly for $k = \pi/2$, hence their average qualitatively captures the behavior of BSP obtained by averaging over all momentum sectors in the main panel of Fig. 5(e). We emphasize that the observed sensitivity to the momentum sector at $N = 3$ is found to rapidly diminish in larger photon sectors.

In summary, we have shown that the regular decoration pattern, chosen in Ref. [44], gives rise to robust signatures of bound states beyond the integrable regime of the XXZ circuit for photon numbers $N \leq 5$. At long but finite times, these signatures are well converged in system size, as confirmed by TEBD simulations. Moreover, similar conclusions are obtained by considering finite-size scaling of the diagonal ensemble results, pertaining to infinite time, that can be accessed in ED simulations. In Appendix E we show that other observables can reveal a signature of bound states by probing the memory of the initial configuration in Eq. (7) as the system evolves in time. Furthermore, the dynamics of BSP studied above is also reflected in the properties of Floquet eigenstates, in particular their localization in the Fock space and their overlap on the initial state in Eq. (7), which is discussed in Appendix F.

V. FINITE DENSITY OF EXCITATIONS AND OTHER DECORATION PATTERNS

Up to this point, we have mostly focused on the experimental setup of Ref. [44], restricting to the case with integrability-breaking decorations on every other site and small numbers of photons $N \leq 6$. In this section, we consider other cases that were not studied previously. In particular, we will now fix the filling factor instead of fixing the total photon number, which will allow us to investigate convergence to the thermodynamic limit by growing both the system size and the number of excitations, as conventionally done in the literature. Moreover, we will explore other decoration patterns, including those with decorations on every nth site where the system still retains translational invariance, as well as completely random patterns, which break all the symmetries.

A. Fixed filling factor

When we extrapolate systems with small but fixed photon numbers to the infinite number of sites, they become infinitely dilute. By contrast, the thermodynamic limit is conventionally taken by keeping the *density* constant. Thus, we introduce the filling factor $\nu = N/L_{\text{sites}}$ and study properties of our circuit as both N and L_{sites} are simultaneously increased such that ν remains constant.

As done previously for fixed N, we average the BSP (8) over a certain number of cycles and investigate its dependence on θ'. In particular, the averaging was done between cycles $n_c = 100$ to $n_c = 200$, after the initial drop in bound state survival. The time-averaged value is then extrapolated to the thermodynamic limit, while keeping ν fixed, using a quadratic fit in $1/L$, see Fig. 6. Here we set the filling factor to $\nu = 1/10$, but the results for other ν values
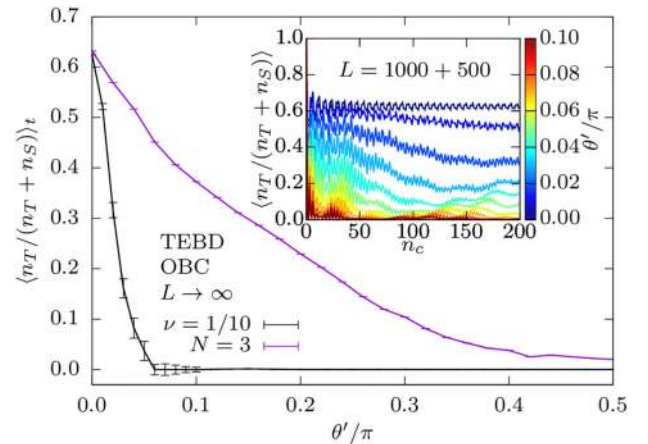

FIG. 6. Time-averaged BSP extrapolated to infinite system size. Filling factor is fixed to $\nu = N/L_{\text{sites}} = 1/10$. For comparison, we also replotted the case of fixed $N = 3$ from Fig. 5. Inset: BSP dynamics for $L = 1000 + 500$ and $N = 100$. All data is obtained by TEBD with bond dimension $\chi = 256$.

are similar. In contrast to dilute systems with fixed photon numbers, the average BSP now drops to very small values already at $\theta' \approx 0.05\pi$. Due to a very slow decay rate of the BSP for very weak integrability breaking $\theta' \lesssim 0.05\pi$, we expect Fig. 6 to provide only an upper bound, as the extrapolated value of the BSP would likely be smaller with an access to a longer time window. However, the TEBD calculations become significantly more time consuming with increasing number of cycles, which is a limiting factor in very large systems.

In the inset of Fig. 6 we show the evolution of BSP for $N = 100$ photons in system size $L = 1000 + 500$, and several values of θ' obtained using TEBD. Unlike the case of fixed but small photon numbers, the large-N bound states are less resilient to integrability breaking by coupling to the extra sites. The BSP quickly decreases with the number of cycles, as can be seen in the inset, where we show only the relatively small coupling strengths $\theta' \in [0, 0.1\pi]$. The extrapolated values in Fig. 6 point to the conclusion that very small photon-number sectors we studied up to this point have unconventional properties, which are not shared by thermodynamically large sectors with nonzero filling factor ν.

B. Other decoration patterns

In this section, we consider the level statistics and BSP dynamics for different patterns of decorations. In Fig. 7 we show the average level-spacing ratio $\langle r \rangle(\theta')$ for $N = 3$ photons and five different types of decoration arrangements. The first one [Fig. 7(a)] is only a single decoration, while the second one [Fig. 7(b)] consists of three decorations attached to sites 2, 4, and 6. Both of these patterns break translation symmetry, which limits the system sizes we can reach. Unlike the level statistics in Fig. 2(a), where $\langle r \rangle$ was oscillatory for $N = 3$, here we observe no such oscillations. Instead, $\langle r \rangle$ first increases to the COE value and then starts to decrease around $\theta' \approx 0.3\pi$. The decrease is not present in larger photon numbers, with the $\langle r \rangle(\theta')$ curve becoming flat already at $N = 4$. Thus, we conclude that $N = 3$ displays anomalous level statistics properties, irrespective of the decoration pattern.

We have also examined the DOS for the patterns of extra sites in Figs. 7(a) and 7(b). The DOS distribution in these cases differs from Fig. 3(a) in that it loses the sharp peaks, but the overall shape stays approximately the same and becomes flatter with increasing number of photons (data not shown). The peaks likely disappear because the new decoration pattern is no longer translation invariant, and the eigenstates, which were previously degenerate are no longer related by symmetry, hence they generally have different energies.

Note that the $\langle r \rangle$ plateau is more pronounced and closer to the COE value for three decorations compared to a single decoration. This trend continues as we add more
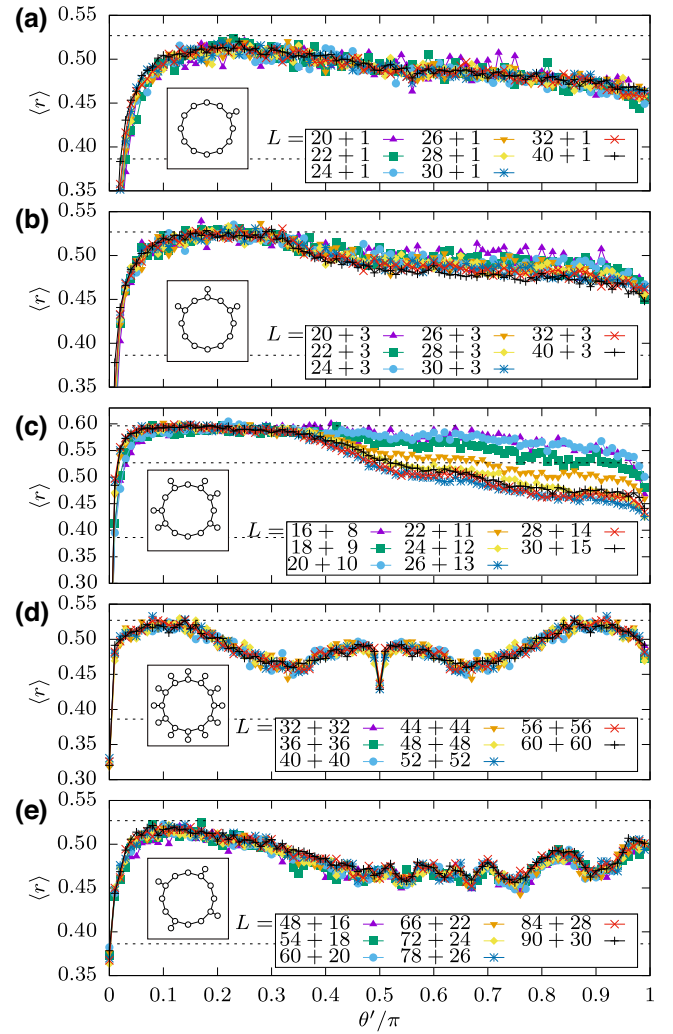

FIG. 7. Level statistics for different decoration patterns (both translation symmetric and nonsymmetric). Data is for $N = 3$ photons, $\theta = \pi/6$, $\phi = 2\pi/3$, and various system sizes specified in legends. The horizontal dashed lines are expectations for the relevant ensembles, $\langle r \rangle_{\text{P}} \approx 0.386$, $\langle r \rangle_{\text{COE}} \approx 0.527$, and $\langle r \rangle_{\text{CUE}} \approx 0.597$. (a) One decoration on site 2. (b) Three decorations on sites 2, 4, and 6. (c) Random nonsymmetric patterns. (d) Decorations on every site, in the momentum $k = 0$ and inversion-symmetric $I = +1$ sector. (e) Decorations on every third site, $k = 0$, $I = +1$ sector.

decorations. In Fig. 7(c) we show several random patterns where the number of extra sites is equal to half the number of sites inside the ring. We again observe similar behavior, with an initial plateau followed by a decrease in $\langle r \rangle$. However, the plateau is now at the CUE value $\langle r \rangle_{\text{CUE}} \approx 0.597$ instead of $\langle r \rangle_{\text{COE}} \approx 0.527$. As explained in Sec. II A, this is due to all of the studied random patterns breaking inversion symmetry, unlike the previous cases of one and three decorations. It might seem surprising that $\langle r \rangle$ is nonmonotonic with system size in Fig. 7(c), but this is simply due to choosing completely different patterns for each system size and could be avoided by averaging over several random

patterns for each L. The DOS distribution for the cases in Fig. 7(c) again has no peaks for $\theta' \neq 0$ and is noticeably flatter than the previously considered patterns.

We have also considered two examples of periodic patterns, one with decorations attached to every site of the main ring [Fig. 7(d)] and the other with decorations on every third site [Fig. 7(e)]. The first case is invariant to translations by two sites and inversion, which swaps the ith site (decoration) with $(L_{\mathrm{sites}} - i)$th $[(L_{\mathrm{decor}} - i)$th], so these symmetries must be resolved in order to obtain the correct level statistics. We note that the full system is not inversion symmetric for the usual periodic pattern with decorations on every other site, even though the arrangement of decorations itself is. This is due to first applying the fSim gates on odd bonds and then on even bonds, Eq. (2). There is no reflection axis, which simultaneously preserves both the decoration pattern and the order of even and odd fSim gate layers. Similar to previous results in Fig. 2(a), for $N = 3$ we again observe deviations from $\langle r \rangle_{\mathrm{COE}}$ at certain values of θ'. However, the $\langle r \rangle(\theta')$ curve is now symmetric around $\theta' = \pi/2$ with an integrable point in the middle. This is similar to the case in Fig. 12(a) in Appendix C, where $\langle r \rangle(\theta')$ is symmetric around $\theta = \pi/2$. As can be seen from Eq. (1), this value of the hopping amplitude corresponds to a photon moving to the neighboring site with probability 1, so it is not surprising that this is a special case.

For the second periodic pattern [Fig. 7(e)], the symmetries of the full system are translation by six sites and inversion, which preserves this arrangement of decorations. In this case, we also observe oscillations in $\langle r \rangle(\theta')$, but the local minima and maxima are at different values of θ' compared to the other patterns. As before, all oscillations disappear for $N = 4$ or more photons. For all studied periodic patterns with decorations on every nth site, the DOS still exhibits pronounced peaks for $N = 3$ and to some extent for $N = 4$.

In summary, none of the considered patterns that break translation invariance exhibit oscillations in $\langle r \rangle(\theta')$ that were visible in Fig. 2(a). Instead, $\langle r \rangle$ first reaches a plateau and then starts to slowly decay at larger values of θ'. The plateau is at $\langle r \rangle_{\mathrm{COE}}$ for inversion-symmetric patterns and at $\langle r \rangle_{\mathrm{CUE}}$ for nonsymmetric ones. For the patterns, which preserve some form of translation symmetry, the level statistics shows similar properties to the experimental case of decorations on every other site, with deviations from $\langle r \rangle_{\mathrm{COE}}$ for $N = 3$, albeit with minima and maxima in $\langle r \rangle$ at different locations. Any observed anomalies disappear in larger numbers of photons $N \geq 4$.

Finally, we have also investigated the robustness of bound states for various decoration patterns. In Fig. 8 we plot the averaged BSP for $N = 3$ photons, $L_{\mathrm{sites}} = 300$ sites on the main chain averaged over $n_c = 100$ cycles between cycles $n_c = 50$ and $n_c = 150$. For a decoration on every second site we average over the two possible $N = 3$ photon initial states around the center of the chain.
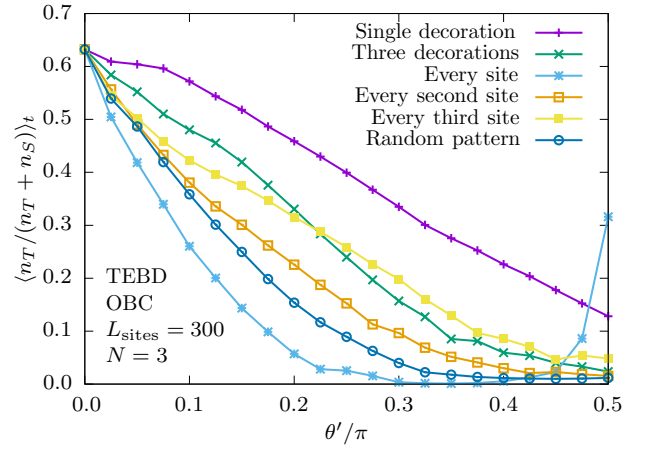

FIG. 8.   Time-averaged BSP over 100 cycles for different decoration patterns in the $N = 3$ excitation sector for $L_{\mathrm{sites}} = 300$. The fixed parameters are $\theta = \pi/6$, $\phi = 2\pi/3$, and $\chi = 256$. In the case of decorations on every second (third) site the results were averaged over two (three) nonequivalent initial bound-state configurations. The random pattern results were averaged over five different patterns with decorations on half of the sites, $L_{\mathrm{decor}}/L_{\mathrm{sites}} = 1/2$.

We perform a similar averaging over the three possible initial states for the case of a decoration on every third site. For randomly allocated decorations we instead average over five different random patterns with the initial bound state at the center of the chain. These results suggest the robustness of the bound states is more dependent on the density of decorations $L_{\mathrm{decor}}/L_{\mathrm{sites}}$ than on the actual pattern. The bound states survive for larger values of θ' when the number of decorations is smaller. The average BSP decays over a similar range of θ' for random patterns with $L_{\mathrm{decor}}/L_{\mathrm{sites}} = 1/2$ and for the periodic case of the same site density. For the case of decorations on every site there is a peak at $\theta' = \pi/2$, which corresponds to the near integrable point as seen in Fig. 7(d). As before, the bound states become increasingly less robust as the number of photons grows.

VI. CONCLUSIONS AND DISCUSSION

We have performed systematic classical simulations of the Floquet XXZ circuit on a 1D chain with integrability breaking decorations. This study was motivated by the recent Google experiment [44], which realized the same model on a ring of superconducting qubits and investigated the dynamics of its bound states. Surprisingly, the bound states were observed to be resilient to integrability-breaking perturbations in the form of extra qubits attached to the ring. We have analyzed the level statistics of this model and simulated the dynamics of bound states, confirming that some of these states indeed survive in certain parts of the nonintegrable regime, even for an infinite number of qubits and at infinite time. In

contrast to much previous work, the focus of Ref. [44] and our own was on dilute systems containing *few* excitations. Such models have been studied in the context of "weak" quenches [60,61], the onset of quantum chaos in few-body systems [62], and meson bound states [63–69]. As we have demonstrated, the latter are amenable to classical simulations in large numbers of qubits, providing useful benchmarks for future studies on improved quantum hardware.

One of our most significant findings is that small but fixed photon-number sectors show unusual properties in several respects. In particular, the robustness of bound states depends on the photon number, with larger states decaying more rapidly as the coupling to the integrability-breaking extra sites is increased. Moreover, the energy spectrum for $N = 3$ photons has unusual level statistics, which deviates from the expectation for a chaotic system even for strong couplings to the integrability-breaking decorations. As discussed in more detail in Appendices B and D, this can be attributed to the presence of special eigenstates in the energy spectrum. These eigenstates have a relatively simple structure, which is related to one-photon and two-photon states, while the rest of the photons are located in the decorations. The proportion of such states is large enough only in sufficiently dilute systems. When the decoration pattern is periodic, some of these eigenstates are related by translation and are therefore degenerate in energy, which results in prominent peaks in the DOS and affects the level statistics. The deviations in level statistics were shown to leave an imprint in the dynamics of bound states by slowing down the thermalization.

Additionally, we have investigated systems with constant filling factors and their extrapolation to the thermodynamic limit. Such systems are no longer dilute and our findings indicate that they do not support stable bound states when integrability is broken. This is in stark contrast with the bound states in very dilute systems with small photon numbers, such as the one studied in experiment [44]. Moreover, we have explored other decoration patterns, including both periodic and nonperiodic ones. A brief summary of all considered systems is given in Table I. Our calculations suggest that the peaks in the density of states disappear when the pattern is not periodic, which destroys the translation symmetry of the full system. This is likely a consequence of certain eigenstates no longer being degenerate. We also find that the inversion symmetry of the decoration patterns (or lack of it) influences the level statistics. In particular, inversion-symmetric patterns are consistent with COE and nonsymmetric with CUE statistics in the chaotic regime. Deviations from these values were observed only for $N = 3$ photons and were found to diminish as the number of photons is increased. However, our results do not indicate a link between the irregularities in the level statistics and the robustness of bound states, although both properties are most prominent in dilute systems. For example, nonperiodic decoration patterns result in level-spacing ratios consistent with random matrix theory, implying that the integrability is indeed fully broken, while the few-photon bound states remain robust in that regime.

One advantage of the classical simulations performed in this work is direct access to the system's properties at finite energy densities. Thus, the model considered here would

TABLE I.   Brief summary of different systems studied in this work. N is the number of photons, L_{sites} is the number of sites on the main chain, and L_{decor} the number of decorations, while $\nu = N/L_{\text{sites}}$ is the filling factor. Periodic patterns are those with decorations on every single, second, third, fourth, or fifth site.

N	$L_{\text{decor}}/L_{\text{sites}}$	pattern	robust bound states	level statistics	DOS	Figs.
3	1 1/2 1/3 1/4 1/5	periodic	✓	oscillating $\langle r \rangle(\theta)$	sharp peaks	7(d) 2(a), 3 7(e)
3	single decoration three decorations	non-periodic	✓	$\langle r \rangle_{\text{COE}}$ plateau then decrease	no peaks	7(a) 7(b)
3	1/2	random	✓	$\langle r \rangle_{\text{CUE}}$ plateau then decrease	no peaks	7(c)
4 and 5	1 1/2 1/3	periodic	✓	$\langle r \rangle_{\text{COE}}$ for $\theta' \gtrsim 0.05\pi$	relatively flat	2(b), 3(a)
4 and 5	single decoration three decorations	non-periodic	✓	$\langle r \rangle_{\text{COE}}$ for $\theta' \gtrsim 0.05\pi$	relatively flat	not shown
4 and 5	1/2	random	✓	$\langle r \rangle_{\text{CUE}}$ for $\theta' \gtrsim 0.05\pi$	relatively flat	not shown
$\nu = 1/10$	1/2	periodic	✗	not computed	not computed	6

be useful for benchmarking quantum algorithms that target states at a finite energy density [70]. Moreover, it would be interesting to explore other models that host bound states, e.g., the chiral Hubbard model [45], and investigate if such models exhibit similar behavior in relation to the density of excitations and integrability breaking by changing the geometry of the system, as described in this work.

ACKNOWLEDGMENTS

Note added.—Recently, we became aware of Ref. [71], which also studied the stability of bound eigenstates in the special case of $N = 3$ photons and decorations on every second qubit. Based on perturbative arguments and the scaling of inverse participation ratio, Ref. [71] concluded that $N = 3$ eigenstates slowly lose their bound-state character in the $L \to \infty$ limit. Our finite-size scaling analysis above suggests that the bound state probability remains finite in this limit for $N = 3$, however this cannot rule out the possibility of a much larger length scale, at which all dynamical signatures of bound states would ultimately disappear at infinite time.

APPENDIX A: CONTINUOUS MODEL

For simplicity, here we assume a decoration pattern where one extra site is attached to every even site of the main ring with PBCs. The continuous XXZ Hamiltonian, which corresponds to the unitary circuit from Eqs. (1) and (2) in the $dt \to 0$ limit is

$$
\begin{aligned}
H_{\text{XXZ}} = &\sum_{i=1}^{L_{\text{sites}}} J(e^{i\beta}\sigma_+^i \sigma_-^{i+1} + e^{-i\beta}\sigma_-^i \sigma_+^{i+1}) + J_z(\sigma_z^i \sigma_z^{i+1}) \\
&+ \sum_{i=1}^{L_{\text{decor}}} J'(e^{i\beta}\sigma_+^{2i}\sigma_-^{e_i} + e^{-i\beta}\sigma_-^{2i}\sigma_+^{e_i}) + J_z'(\sigma_z^{2i}\sigma_z^{e_i}) \\
&+ \sum_{i=1}^{L_{\text{sites}}} h_z(i)\sigma_z^i + \sum_{i=1}^{L_{\text{decor}}} h_z^e \sigma_z^{e_i}, \qquad (A1)
\end{aligned}
$$

where e_i are the integrability-breaking extra sites attached to even sites $2i$. The local field is $h_z(2i + 1) = -2J_z$ on odd sites, $h_z(2i) = -3J_z$ on even sites and $h_z^e = -J_z$ on extra sites. Additionally, if we impose OBCs and an even number of sites, the local field is $h_z(1) = -J_z$ on the first site and $h_z(L) = -2J_z$ on the last site. The corresponding unitary circuit parameters are $\theta = 2Jdt$, $\phi = 2J_z dt$, $\theta' = 2J'dt$, and $\phi' = 2J_z'dt$. This continuous model can be easily generalized to an arbitrary decoration pattern by changing the local fields.

APPENDIX B: ORIGIN OF PEAKS IN THE DENSITY OF STATES

The sharp peaks in DOS can be attributed to the existence of special eigenstates with a relatively simple structure obtained by combining single-photon and two-photon states. Analytical expressions for the dispersions of a single photon or N-bound photons in the integrable (nondecorated) circuit are known [45]. Adding the decorations with $\theta' = 0$ results in an additional zero-energy band in the single-photon dispersion, since all the photons in the extra sites are frozen. This means that, for example, single-photon and two-photon eigenstates are still present in the three-photon spectrum at $\theta' = 0$, since we can just move the remaining photons to the decorations, where they will have zero energy.

In Fig. 9(a), we compare the actual two-photon Floquet spectrum (dots) with the states constructed from two single-photon states (crosses). The color scale represents the deviation from the nearest analytically constructed state. The agreement is remarkably good, which is not surprising given that the system is very dilute and only nearest-neighbor interactions are present. The two bands at the bottom of the plot are two-photon bound states, which are also in agreement with analytical expressions from Ref. [45]. Figure 9(a) is for the integrable case with no extra sites. Adding the decorations leads to the appearance of two additional bands, see Fig. 9(b) and compare with (a). The first one is a bound-state band, which corresponds to one photon in the main chain and another in adjacent decoration and is completely flat. The second one is a wider band of single-photon states corresponding to one photon inside and the other in a nonadjacent decoration. This wider band is centered around zero and has high DOS on its edges, which coincides with the peaks around $\pm\pi/3$ in three-photon DOS from Fig. 3(a). Another smaller peak in DOS around -0.75π comes from the flat band of two bound photons.

We can conclude from the previous discussion that the three-photon DOS is strongly influenced by special single- and two-photon eigenstates. This effect is not so prominent in DOS for four or more photons. This is because the number of special states is much smaller compared to the total
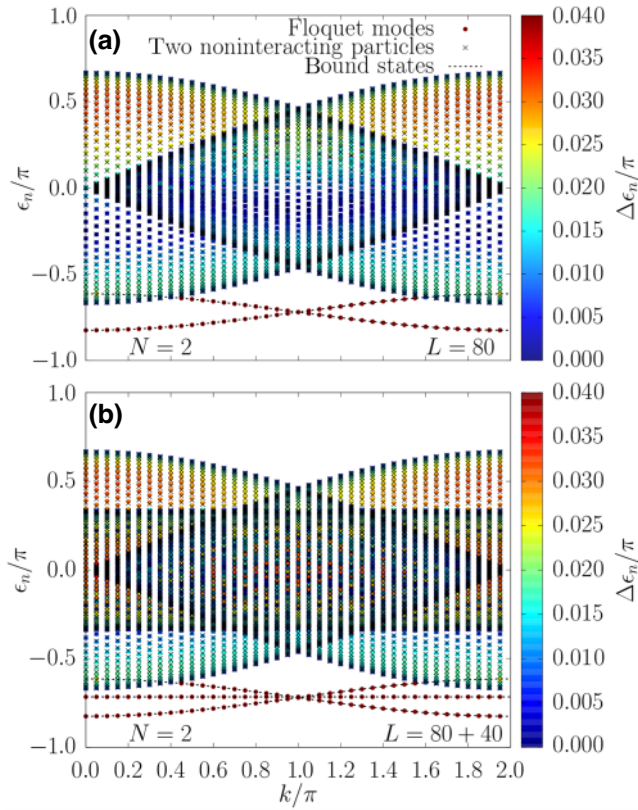
FIG. 9. (a) Comparison of the actual dispersion of two-photon states for the integrable case $\theta' = 0$ with no extra sites (dots) and the theoretical prediction for two separate noninteracting photons (crosses) and two bound photons (dashed lines). The color scale corresponds to the deviation between each dot and the closest cross. (b) Same as (a) but with added extra sites, while $\theta' = 0$.

Hilbert-space size but also due to the special states becoming more uniformly distributed through the quasienergy spectrum. In Appendix D we quantify this and show that the proportion of special states for a fixed photon number N becomes asymptotically independent of the system size L. However, the saturation value still strongly depends on N, e.g., the special states comprise as many as 70% of all states for $N = 3$ but only 1% for $N = 8$.

This previous analysis can now be extended to finite values of θ'. Analytical expressions for the single-photon dispersion are not available in this case, but can be easily numerically computed for different coupling strengths θ'. There are still three different bands, since each unit cell contains three sites. We then construct three-photon bands by taking combinations of the single-particle bands, neglecting the interactions between the particles. This is a good approximation in a dilute system, even with nonzero interaction strength. For three photons we obtain ten different bands, one for each combination of the three bands. We label the combination in which all photons come from the first band 111, two photons in first and one in second 112, one photon in the first, second, and third 123, etc. The
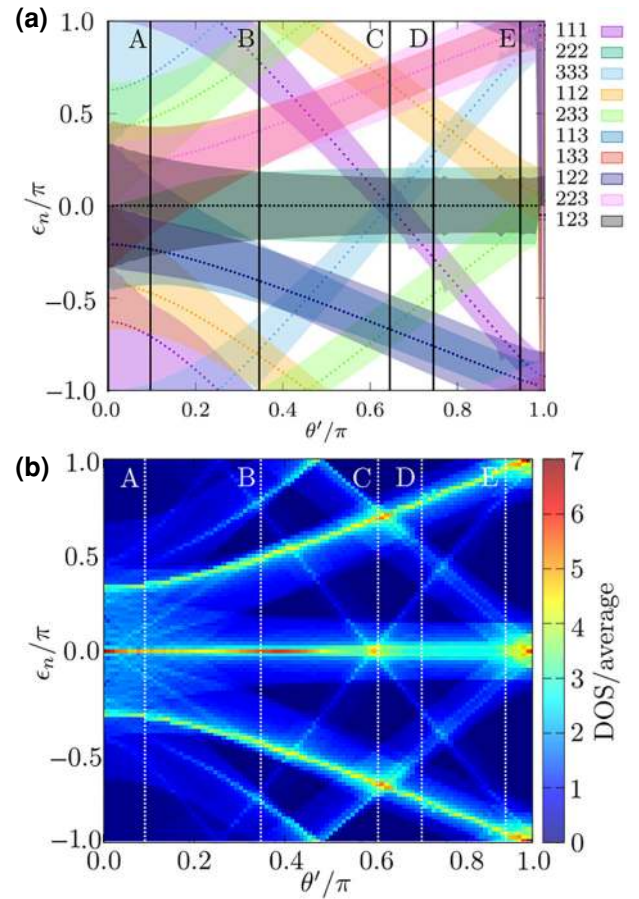

FIG. 10. (a) Bands of special states constructed by taking linear combinations of numerically obtained single-photon bands for $\theta' \in [0, \pi]$. Here we consider the case of $N = 3$ separate photons. The bands are labeled by three numbers, stating if each photon is in the first (1), second (2), and third (3) single-photon band. (b) Corresponding DOS. The bright regions can be related to the peaks in Fig. 3. The vertical lines A, B, C, D, and E mark special values of θ' from Fig. 2.

dependence of these bands of special states on θ' is shown in Fig. 10(a). As θ' is increased, the bands move and cross each other.

The DOS is typically higher near the edges of the bands, so we expect the DOS to be amplified when two bands cross. The edges of 222 and 123 bands overlap around $\theta' = 0.35\pi$, which is where the level-spacing ratio deviates the most from $\langle r \rangle_{\text{COE}}$. Several other bands also overlap around this point. The DOS plot for the special bands shown in Fig. 10(b) roughly corresponds to the peaks in Fig. 3(a). Therefore, as in the $\theta' = 0$ case, the peaks in DOS at $\theta' \neq 0$ are also explained by the special states, which comprise a large proportion of the Hilbert space in systems with smaller numbers of photons, such as $N = 3$. However, it is not obvious from Fig. 10(b) in which θ' regions the level statistics deviates the most from the value expected in

chaotic systems. In particular, there are three very prominent peaks around $\theta' = 0.65\pi$, where the level-spacing distribution is actually very close to COE. We conjecture that these peaks are not narrow enough to lead to a sufficient number of degeneracies that could affect the level statistics. One might expect that the specially constructed states are a better approximation for a noninteracting system and that the $\langle r \rangle(\theta')$ dependence would look different at smaller values of the interaction strength ϕ. This, however, is not the case, as shown in Appendix C, where it can be observed that the level statistics barely changes with ϕ.

APPENDIX C: EFFECT OF PARAMETERS θ, ϕ, AND β

Throughout this paper, we have mostly considered the parameters $\theta = \pi/6$, $\phi = 2\pi/3$, and $\beta = 0$, which were used in the experiment from Ref. [44]. In this Appendix, we explore the effects of changing these parameters. First we perform a scan of the parameter space over a range of interaction strengths ϕ and couplings to the extra sites θ' while keeping the hopping amplitude inside the ring fixed to $\pi/6$. The BSP for an initial state of $N = 3$ bound photons, Eq. (7), averaged over the first $n_c = 50$ unitary cycles, is shown in Fig. 11. Here we also average over two nonequivalent initial configurations, although the plot looks very similar without averaging. The results are symmetric to reflection around the $\phi = \pi$ and $\theta' = \pi$ axes, which is unsurprising as these reflections result only in minus signs in certain matrix elements from Eq. (1) [$\sin(2\pi - \theta') = -\sin(\theta')$ and $e^{i(2\pi - \phi)} = e^{-i\phi}$].

The region of interest is the bottom part of this figure, with intermediate ϕ and small θ'. There is a minimal value of interaction strength required for the survival of

bound states, $\phi_{\min} \approx \pi/3 \approx 2\theta$. This is in line with previous analytical results, which state that the bound states exist for any momentum in the gapped regime $\phi > 2\theta$ [45]. The maximal decoration coupling, which supports the bound states, is around $\theta' = \pi/3$ and does not significantly depend on ϕ. There are also additional regions where the bound states remain stable, such as around $\phi = \pi/3$ and $\theta' = \pi$. However, the $\theta' = \pi$ line is a special case since there is no hopping from the main chain to the extra sites, see Eq. (1). We therefore did not focus on these regions of the phase diagram. We have also investigated the cases of $N = 4$ or more photons in the initial bound state and these plots show similar features to $N = 3$. The main difference is that the region with robust bound states shrinks in the θ' direction with increasing N, which is consistent with our results from Figs. 5(d) and 5(e).

In Fig. 12 we plot the average level-spacing ratio $\langle r \rangle(\theta')$ for several values of the parameters θ, ϕ, and β. As can be observed in Fig. 12(a), the oscillations in $\langle r \rangle(\theta')$ are visible for all values of the hopping amplitude θ, but the exact positions of the local minima and maxima depend on θ. The most distinctive case is $\theta = \pi/2$, where the level statistics is close to Poisson for most values of θ'. According to Eq. (1), this is a special case where the hopping probability on the main chain is 1 in each cycle. Additionally, we note that the $\langle r \rangle(\theta')$ curve is the same for θ and $\pi - \theta$.
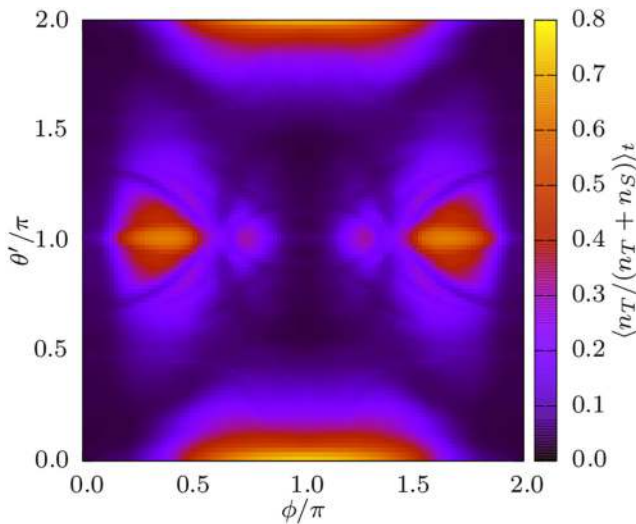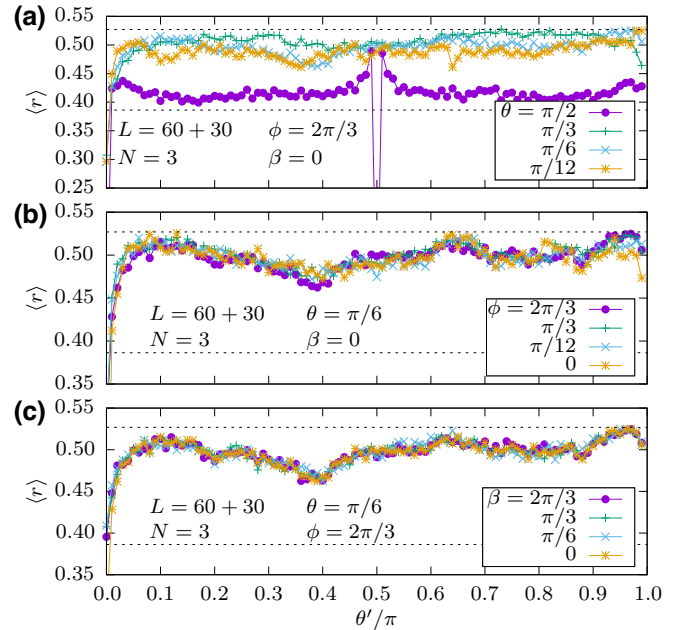

FIG. 11. Bound-state probability averaged over $n_c = 50$ cycles and two different initial configurations. $L = 40 + 20$, $N = 3$, $\theta = \pi/6$, $\beta = 0$, $\theta' \in [0, 2\pi]$, and $\phi \in [0, 2\pi]$.

FIG. 12. Level statistics for different values of parameter θ (a), ϕ (b), and β (c). The only parameter that significantly affects the results is the hopping amplitude θ. We note that $\theta = \pi/2$ is a special case where the probability of hopping to the neighboring site is 1 in each cycle, see Eq. (1). It is therefore not surprising that this case is close to being integrable.

In contrast to θ, the other two parameters ϕ and β have almost no effect on the level statistics. The dependence on the nearest-neighbor interaction strength ϕ is shown in Fig. 12(b). This further supports the conclusion that the deviations from $\langle r \rangle_{\text{COE}}$ are mainly a consequence of three separate photon states whose energies do not depend on ϕ. The magnetic flux through the ring β has even less influence on the results, see Fig. 12(c). However, it does change the actual energy levels. For this reason, the parameter β was very useful for averaging the spectral form factor in Sec. IV.

APPENDIX D: DENSITY OF EXCITATIONS

We have previously attributed the deviations from the chaotic level statistics and sharp peaks in DOS to the existence of special eigenstates in Sec. B. These features were more pronounced for small photon numbers such as $N = 3$. In Fig. 13 we show the proportion of some simple basis configurations in total Hilbert spaces of systems with different fixed numbers of photons N and increasing number of sites L. In particular, these are the configurations with all photons outside the main chain, just one photon inside, two separate photons inside, and two bound photons inside. The special eigenstates that affect the spectral statistics are superpositions of such configurations. They are highly degenerate in energy, due to diluteness of the system and large number of possible configurations of photons in the extra sites, which results in peaks in DOS and deviations in the average ratio of consecutive energy gaps.

For all photon numbers considered, the proportion saturates at some constant value as the size increases and the system becomes sufficiently dilute. Indeed, the saturation
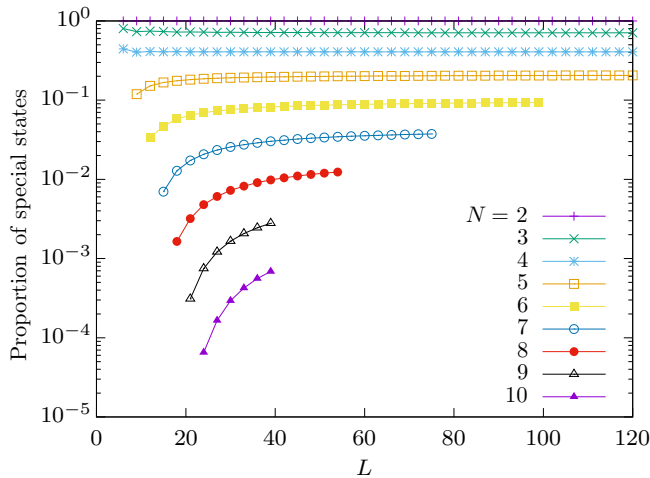
value is much larger for $N = 3$ (approximately 70%) than it is in cases of more photons (e.g., around 1% for $N = 8$). This explains why the special states have much stronger effects on the spectra of systems with small photon numbers. Such states are still present in large-N systems, but their proportion is negligible and thus has practically no influence on the energy spectrum. We note that the proportion of special states depends on the ratio between the number of decorations and the number of sites $L_{\text{decor}}/L_{\text{sites}}$, which is equal to $1/2$ in the case shown here. More decorations would result in a larger proportion of these states.

APPENDIX E: MEMORY OF THE INITIAL STATE

The BSP is not the only local observable that reveals the unusual behavior of the bound initial states at finite θ'. Persistent nonthermalizing behavior can also be seen in the site occupation, $n_i = \langle \hat{n}_i \rangle$. Since the integrability breaking decorations make up one third of the total sites on the chain, we would expect a third of the photons to be located on them after a short time when the system has sufficiently thermalized. Instead, we find that this is only true at larger $\theta' \gtrsim \pi/3$. The fraction of photons located on the decorations as θ' is varied shows very similar behavior for bound states of different sizes.

In the integrable case, larger bound states propagate more slowly due to their small group velocity [44,45]. This behavior appears to persist in the nonintegrable model. A large fraction of photons in the bound state remain in the vicinity of their initial sites even after many cycles. In
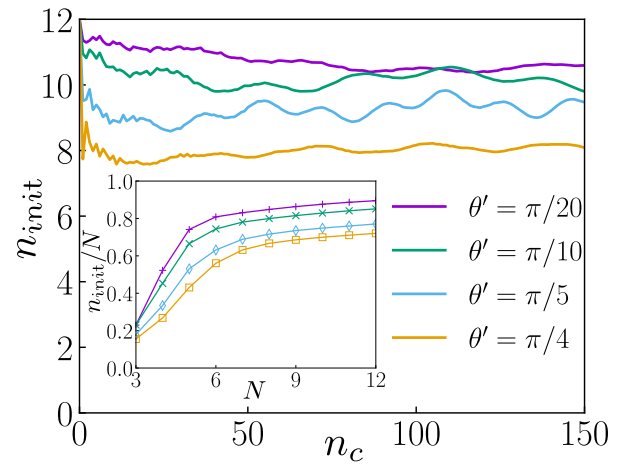

FIG. 13. Proportion of special configurations for different photon numbers N and system sizes $L = L_{\text{sites}} + L_{\text{decor}}$. The decorations are on every other site. These simple states can be constructed by combining single-photon and two-photon configurations with photons in the extra sites.

FIG. 14. Continued occupation of sites initially occupied by an $N = 12$ photon bound state after n_c cycles. Data is obtained by TEBD for a system size $L = 300 + 150$, bond dimension $\chi = 320$ for $\theta = \pi/6$, $\phi = 2\pi/3$ and a few values of θ' indicated in the legend. Inset: n_{init}/N for bound states of sizes $N = 3$ to $N = 12$ at different values of θ'. Data is obtained by TEBD for 150 cycles and the same parameters as in the main plot.

Fig. 14, we show $n_{\text{init}} = \sum_{i \in \text{initial sites}} n_i$ for an $N = 12$ photon bound state for different θ', demonstrating this robust nonthermalizing behavior. The average of n_{init} for different size bound states can be seen in the inset of Fig. 14. From this perspective, the bound states appear to grow more robust as they increase in size. This at first seems to be in contradiction with the BSP results from Fig. 5. However, the BSP measures the overlap with the N-photon bound state as a whole, while n_{init} also captures the case when the bound state loses photons from the edges while its core stays robust and does not move away significantly from its initial position. This is precisely what happens for large-N bound states. Since we are considering hardcore bosons, the photons from the middle of the bound state can only hop to the decorations and back, while the photons at the edge can move further away along the chain and become detached from the rest.

APPENDIX F: PROPERTIES OF FLOQUET MODES

In Sec. IV, we demonstrated the robustness of the bound states in the dynamics. These results are naturally reflected in the anomalous properties of special eigenstates associated with bound states, which we investigate in detail in this Appendix. As a generic measure of eigenstate localization in the Fock space, it is customary to study the inverse participation ratio (IPR). For a (normalized) eigenstate $|\psi_{i,k}\rangle$ of the Floquet unitary $\hat{U}_F$ with momentum k, we define the IPR as

$$\text{IPR}_k = \sum_n |\langle \psi_{i,k}|k_n\rangle|^4, \qquad (\text{F1})$$

where, for convenience, we take $|k_n\rangle$ to be the momentum basis states. For sufficiently small θ', the eigenstates with largest support on the bound state can be uniquely identified with the aid of the BSP in Eq. (8). In a fixed momentum sector, there are four bound eigenstates corresponding to the largest BSP: two which have all the excitations on the main chain, and two where one of the excitations is on a decoration. A natural question is how localized these eigenstates are in the Fock space, e.g., whether their IPR asymptotically converges to a constant or decays as a power law, $L_{\text{sites}}^{-\alpha}$, in the limit $L_{\text{sites}} \to \infty$.

In Fig. 15 we plot the averaged IPR of the four bound eigenstates for $\theta' = 0.1\pi$ and different system sizes in the $N = 3$ sector. We find the IPR has strong fluctuations between different system sizes, even after averaging over the four bound states in the given momentum sector. Contrasting the linear plot against the log-log plot shown in the inset of Fig. 15, it is difficult to ascertain the asymptotic behavior of IPR, in particular for larger values of θ' such as 0.3π, where power-law decay remains a possibility. For
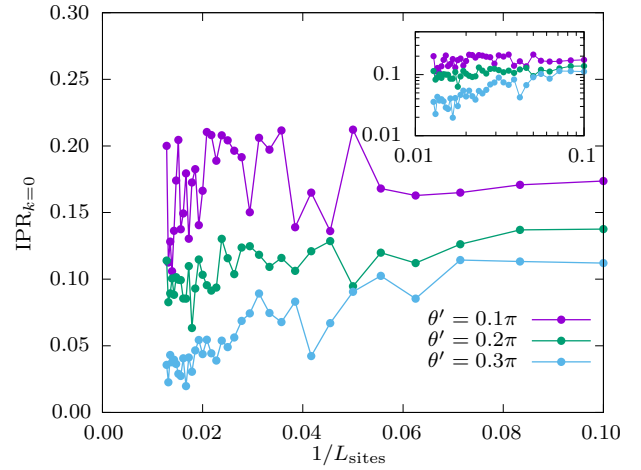

FIG. 15. Finite-size scaling of IPR, Eq. (F1), for three values of θ'. We plot the average IPR for the four bound eigenstates in $k = 0$ momentum sector. Inset shows the same data on a log-log scale.

this reason, in the main text we focused on the dynamical properties, which show smoother convergence while (at finite times) are also readily accessible in experiment.

A finer characterization of the Floquet modes is obtained by plotting their overlap with the bound initial state (7), against the number of pairs of neighboring occupied sites on the main chain, $\langle \psi | \sum_i \hat{n}_i \hat{n}_{i+1} | \psi \rangle$, in each Floquet mode. This is shown in Figs. 16(a) and 16(b), for the case of $N = 3$ photons, contrasting the integrable case with that of $\theta' = 0.2\pi$. For $N = 3$, the number of neighboring occupied sites can be at most 2, corresponding to a three-photon bound state. Alternatively, the value 1 corresponds to two neighboring and one separate photon, while 0 implies three separate photons. The integrable case, $\theta' = 0$, in Fig. 16(a) displays three separate sectors, one of which contains the bound states (red points). The energies of these sectors overlap, but there is no mixing between the states. The overlapping energies are a consequence of the periodic Floquet spectrum, while in the Hamiltonian XXZ model these sectors are separated by energy gaps. As θ' is increased, the system becomes nonintegrable and the sectors start to mix. At $\theta' = 0.2\pi$, Fig. 16(b), the bound states have almost merged with the bulk, but still remain visible. This is no longer the case after $\theta' = 0.3\pi$, which is consistent with the results of Figs. 5(d) and 5(e) where it was shown that the bound states are robust only up to this point.

The overlap plots for larger numbers of photons display similar features to $N = 3$. At $\theta' = 0$, there are N separate sectors, which are defined by the number of pairs of adjacent photons. The bound Floquet modes slowly mix with the other sectors as the coupling to the decorations in increased. The case of $N = 5$ and $\theta' = 0.1\pi$ is shown in Fig. 16(c). Here we see three prominent towers of states, which are related to the oscillations in the BSP in Fig. 5(c).
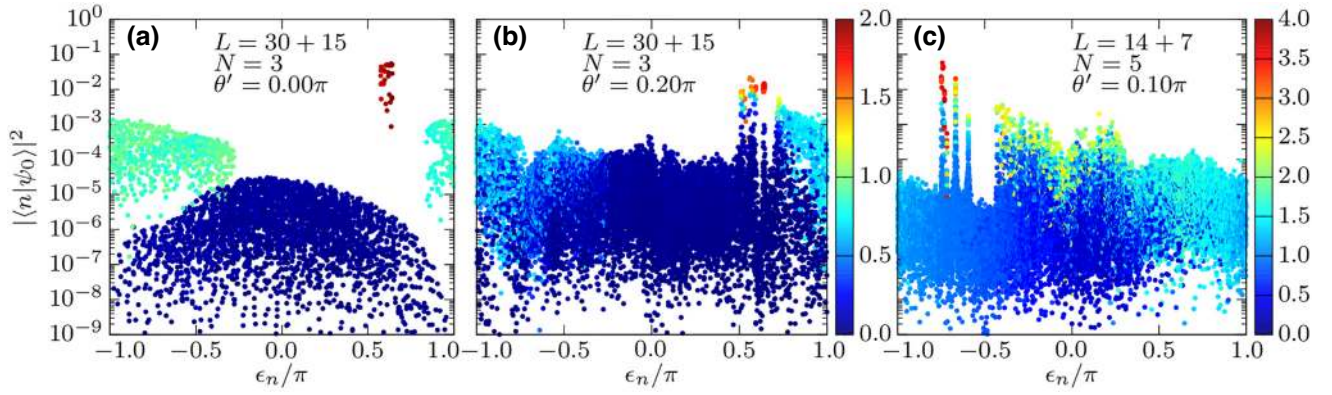
FIG. 16.   Overlap of the initial state with the eigenstates of the one-cycle evolution operator. (a),(b) $N = 3$ photons in system size $L = 30 + 15$ for $\theta' = 0$ and $\theta' = 0.2\pi$, respectively. (c) $N = 5$ photons in system size $L = 14 + 7$ with $\theta' = 0.1\pi$. The color scale is the number of pairs of adjacent occupied sites on the main chain (see text).

These oscillations can be attributed to photons from the bound-state hopping onto the extra sites and back. The towers appear as soon as $\theta' \neq 0$ and persist until approximately $\theta' \approx 0.3\pi$. The distance between the towers and therefore the oscillation frequency depends approximately linearly on θ'. Moreover, the shape and height of the towers depend on the number of decorations attached to the initially occupied sites.

Intriguingly, we find that the towers are more prominent for the five-photon initial bound state with two decorations on the second and fourth site [Fig. 16(c)] than for the state with three decorations on the first, third, and fifth site. Upon closer inspection, some towers of high-overlap states can also be discerned for $N = 3$ in Fig. 16(b). However, they are not as well differentiated as for $N = 5$, and do not appear to be equally spaced in energy, which is the reason why the oscillations in BSP at $\theta' = 0.2\pi$ are irregular, see Fig. 5(a). Interestingly, the towers do not become better resolved with increasing the photon number and the case of $N = 5$ actually features the sharpest towers and corresponding oscillations in BSP and various local observables, such as the number of photons in the extra sites. As a side note, similar looking towers of states are often found in systems that host "quantum many-body scars" [72–74], however, it is not clear whether similar physics occurs in the present case.

———————

[1] I. Bloch, J. Dalibard, and W. Zwerger, Many-body physics with ultracold gases, Rev. Mod. Phys. **80**, 885 (2008).

[2] I. Bloch, J. Dalibard, and S. Nascimbène, Quantum simulations with ultracold quantum gases, Nat. Phys. **8**, 267 (2012).

[3] I. M. Georgescu, S. Ashhab, and F. Nori, Quantum simulation, Rev. Mod. Phys. **86**, 153 (2014).

[4] M. Kjaergaard, M. E. Schwartz, J. Braumüller, P. Krantz, J. I.-J. Wang, S. Gustavsson, and W. D. Oliver, Superconducting qubits: Current state of play, Annu. Rev. Condens. Matter Phys. **11**, 369 (2020).

[5] R. Blatt and C. F. Roos, Quantum simulations with trapped ions, Nat. Phys. **8**, 277 (2012).

[6] A. A. Houck, H. E. Türeci, and J. Koch, On-chip quantum simulation with superconducting circuits, Nat. Phys. **8**, 292 (2012).

[7] C. Monroe, W. C. Campbell, L.-M. Duan, Z.-X. Gong, A. V. Gorshkov, P. W. Hess, R. Islam, K. Kim, N. M. Linke, G. Pagano, P. Richerme, C. Senko, and N. Y. Yao, Programmable quantum simulations of spin systems with trapped ions, Rev. Mod. Phys. **93**, 025001 (2021).

[8] A. Browaeys and T. Lahaye, Many-body physics with individually controlled Rydberg atoms, Nat. Phys. **16**, 132 (2020).

[9] A. Polkovnikov, K. Sengupta, A. Silva, and M. Vengalattore, *Colloquium*: Nonequilibrium dynamics of closed interacting quantum systems, Rev. Mod. Phys. **83**, 863 (2011).

[10] C. Gogolin and J. Eisert, Equilibration, thermalisation, and the emergence of statistical mechanics in closed quantum systems, Rep. Prog. Phys. **79**, 056001 (2016).

[11] L. D'Alessio, Y. Kafri, A. Polkovnikov, and M. Rigol, From quantum chaos and eigenstate thermalization to statistical mechanics and thermodynamics, Adv. Phys. **65**, 239 (2016).

[12] M. Ueda, Quantum equilibration, thermalization and prethermalization in ultracold atoms, Nat. Rev. Phys. **2**, 669 (2020).

[13] J. M. Deutsch, Quantum statistical mechanics in a closed system, Phys. Rev. A **43**, 2046 (1991).

[14] M. Srednicki, Chaos and quantum thermalization, Phys. Rev. E **50**, 888 (1994).

[15] M. Rigol, V. Dunjko, and M. Olshanii, Thermalization and its mechanism for generic isolated quantum systems, Nature **452**, 854 (2008).

[16] R. Nandkishore and D. A. Huse, Many-body localization and thermalization in quantum statistical mechanics, Annu. Rev. Condens. Matter Phys. **6**, 15 (2015).

[17] T. Kinoshita, T. Wenger, and D. S. Weiss, A quantum Newton's cradle, Nature **440**, 900 (2006).

[18] B. Sutherland, *Beautiful Models: 70 Years of Exactly Solved Quantum Many-Body Problems* (World Scientific, Singapore, 2004).

[19] B. Bertini, F. Heidrich-Meisner, C. Karrasch, T. Prosen, R. Steinigeweg, and M. Žnidarič, Finite-temperature transport in one-dimensional quantum lattice models, Rev. Mod. Phys. **93**, 025003 (2021).

[20] D. Mattis, *The Theory of Magnetism Made Simple: An Introduction to Physical Concepts and to Some Useful Mathematical Methods, The Theory of Magnetism Made Simple: An Introduction to Physical Concepts and to Some Useful Mathematical Methods* (World Scientific, Singapore, 2006).

[21] H. Bethe, Zur theorie der metalle, Z. Phys. **71**, 205 (1931).

[22] M. Date and M. Motokawa, Spin-cluster resonance in $CoCl_2 \cdot 2H_2O$, Phys. Rev. Lett. **16**, 1111 (1966).

[23] J. B. Torrance and M. Tinkham, Excitation of multiple-magnon bound states in $CoCl_2 \cdot 2H_2O$, Phys. Rev. **187**, 595 (1969).

[24] R. Hoogerbeets, A. J. van Duyneveldt, A. C. Phaff, C. H. W. Swuste, and W. J. M. de Jonge, Evidence for magnon bound-state excitations in the quantum chain system (C6H11N3)CuCl3, J. Phys. C: Solid State Phys. **17**, 2595 (1984).

[25] M. Ganahl, E. Rabel, F. H. L. Essler, and H. G. Evertz, Observation of complex bound states in the spin-1/2 Heisenberg *XXZ* chain using local quantum quenches, Phys. Rev. Lett. **108**, 077206 (2012).

[26] D. Gobert, C. Kollath, U. Schollwöck, and G. Schütz, Real-time dynamics in spin-$\frac{1}{2}$ chains with adaptive time-dependent density matrix renormalization group, Phys. Rev. E **71**, 036102 (2005).

[27] D. Petrosyan, B. Schmidt, J. R. Anglin, and M. Fleischhauer, Quantum liquid of repulsively bound pairs of particles in a lattice, Phys. Rev. A **76**, 033606 (2007).

[28] S. Langer, F. Heidrich-Meisner, J. Gemmer, I. P. McCulloch, and U. Schollwöck, Real-time study of diffusive and ballistic transport in spin-$\frac{1}{2}$ chains using the adaptive time-dependent density matrix renormalization group method, Phys. Rev. B **79**, 214409 (2009).

[29] J. Ren and S. Zhu, Quench dynamics of entanglement in an open anisotropic spin-$\frac{1}{2}$ Heisenberg chain, Phys. Rev. A **81**, 014302 (2010).

[30] L. F. Santos and A. Mitra, Domain wall dynamics in integrable and chaotic spin-1/2 chains, Phys. Rev. E **84**, 016206 (2011).

[31] R. Steinigeweg, S. Langer, F. Heidrich-Meisner, I. P. McCulloch, and W. Brenig, Coherent spin-current oscillations in transverse magnetic fields, Phys. Rev. Lett. **106**, 160602 (2011).

[32] S. Langer, M. Heyl, I. P. McCulloch, and F. Heidrich-Meisner, Real-time energy dynamics in spin-$\frac{1}{2}$ Heisenberg chains, Phys. Rev. B **84**, 205115 (2011).

[33] R. G. Pereira, S. R. White, and I. Affleck, Exact edge singularities and dynamical correlations in spin-1/2 chains, Phys. Rev. Lett. **100**, 027206 (2008).

[34] R. G. Pereira, S. R. White, and I. Affleck, Spectral function of spinless fermions on a one-dimensional lattice, Phys. Rev. B **79**, 165113 (2009).

[35] J.-S. Caux and J. M. Maillet, Computation of dynamical correlation functions of Heisenberg chains in a magnetic field, Phys. Rev. Lett. **95**, 077201 (2005).

[36] J.-S. Caux, R. Hagemans, and J. M. Maillet, Computation of dynamical correlation functions of Heisenberg chains: The gapless anisotropic regime, J. Stat. Mech.: Theory Exp. **2005**, P09003 (2005).

[37] M. Kohno, Dynamically dominant excitations of string solutions in the spin-1/2 antiferromagnetic Heisenberg chain in a magnetic field, Phys. Rev. Lett. **102**, 037203 (2009).

[38] A. Shashi, L. I. Glazman, J.-S. Caux, and A. Imambekov, Nonuniversal prefactors in the correlation functions of one-dimensional quantum liquids, Phys. Rev. B **84**, 045408 (2011).

[39] A. Imambekov, T. L. Schmidt, and L. I. Glazman, One-dimensional quantum liquids: Beyond the Luttinger liquid paradigm, Rev. Mod. Phys. **84**, 1253 (2012).

[40] T. Fukuhara, P. Schauß, M. Endres, S. Hild, M. Cheneau, I. Bloch, and C. Gross, Microscopic observation of magnon bound states and their dynamics, Nature **502**, 76 (2013).

[41] M. Vanicat, L. Zadnik, and T. Prosen, Integrable Trotterization: Local conservation laws and boundary driving, Phys. Rev. Lett. **121**, 030606 (2018).

[42] M. Ljubotina, L. Zadnik, and T. Prosen, Ballistic spin transport in a periodically driven integrable quantum system, Phys. Rev. Lett. **122**, 150605 (2019).

[43] P. W. Claeys, J. Herzog-Arbeitman, and A. Lamacraft, Correlations and commuting transfer matrices in integrable unitary circuits, SciPost Phys. **12**, 007 (2022).

[44] Google Quantum AI and Collaborators, Formation of robust bound states of interacting photons, Nature (London) **612**, 240 (2022).

[45] I. L. Aleiner, Bethe ansatz solutions for certain periodic quantum circuits, Ann. Phys. **433**, 168593 (2021).

[46] M. Fishman, S. R. White, and E. M. Stoudenmire, The ITensor Software Library for tensor network calculations, SciPost Phys. Codebases, 4 (2022).

[47] M. L. Mehta, *Random Matrices* (Elsevier, Amsterdam, 2004), Vol. 142.

[48] N. Regnault and R. Nandkishore, Floquet thermalization: Symmetries and random matrix ensembles, Phys. Rev. B **93**, 104203 (2016).

[49] V. Oganesyan and D. A. Huse, Localization of interacting fermions at high temperature, Phys. Rev. B **75**, 155111 (2007).

[50] L. D'Alessio and M. Rigol, Long-time behavior of isolated periodically driven interacting lattice systems, Phys. Rev. X **4**, 041048 (2014).

[51] L. F. Santos and M. Rigol, Localization and the effects of symmetries in the thermalization properties of one-dimensional quantum systems, Phys. Rev. E **82**, 031130 (2010).

[52] F. Haake, *Quantum Signatures of Chaos*, Physics and astronomy online library (Springer, Heidelberg, 2001).

[53] E. J. Torres-Herrera and L. F. Santos, Dynamical manifestations of quantum chaos: correlation hole and bulge, Philos. Trans. R. Soc. London, Series A **375**, 20160434 (2017).

[54] B. Bertini, P. Kos, and T. Prosen, Exact spectral form factor in a minimal model of many-body quantum chaos, Phys. Rev. Lett. **121**, 264101 (2018).

[55] A. Chan, A. De Luca, and J. T. Chalker, Solution of a minimal model for many-body quantum chaos, Phys. Rev. X **8**, 041019 (2018).

[56] J. Šuntajs, J. Bonča, T. c. v. Prosen, and L. Vidmar, Quantum chaos challenges many-body localization, Phys. Rev. E **102**, 062144 (2020).

[57] R. E. Prange, The spectral form factor is not self-averaging, Phys. Rev. Lett. **78**, 2280 (1997).

[58] M. Schiulaz, E. J. Torres-Herrera, F. Pérez-Bernal, and L. F. Santos, Self-averaging in many-body quantum systems out of equilibrium: Chaotic systems, Phys. Rev. B **101**, 174312 (2020).

[59] L. Colmenarez, D. J. Luitz, I. M. Khaymovich, and G. De Tomasi, Subdiffusive Thouless time scaling in the Anderson model on random regular graphs, Phys. Rev. B **105**, 174207 (2022).

[60] J. H. Robertson, R. Senese, and F. H. L. Essler, Decay of long-lived oscillations after quantum quenches in gapped interacting quantum systems, arXiv e-prints arXiv:2307.04466 [cond-mat.stat-mech] (2023).

[61] S. Scopa, P. Calabrese, and A. Bastianello, Entanglement dynamics in confining spin chains, Phys. Rev. B **105**, 125413 (2022).

[62] G. Zisling, L. F. Santos, and Y. B. Lev, How many particles make up a chaotic many-body quantum system?, SciPost Phys. **10**, 088 (2021).

[63] M. Kormos, M. Collura, G. Takács, and P. Calabrese, Real-time confinement following a quantum quench to a non-integrable model, Nat. Phys. **13**, 246 (2017).

[64] C.-J. Lin and O. I. Motrunich, Quasiparticle explanation of the weak-thermalization regime under quench in a nonintegrable quantum spin chain, Phys. Rev. A **95**, 023621 (2017).

[65] K. Hódsági, M. Kormos, and G. Takács, Quench dynamics of the Ising field theory in a magnetic field, SciPost Phys. **5**, 027 (2018).

[66] A. J. A. James, R. M. Konik, and N. J. Robinson, Nonthermal states arising from confinement in one and two dimensions, Phys. Rev. Lett. **122**, 130603 (2019).

[67] N. J. Robinson, A. J. A. James, and R. M. Konik, Signatures of rare states and thermalization in a theory with confinement, Phys. Rev. B **99**, 195108 (2019).

[68] S. Birnkammer, A. Bastianello, and M. Knap, Prethermalization in one-dimensional quantum many-body systems with confinement, Nat. Commun. **13**, 7663 (2022).

[69] J. Vovrosh, R. Mukherjee, A. Bastianello, and J. Knolle, Dynamical hadron formation in long-range interacting quantum spin chains, PRX Quantum **3**, 040309 (2022).

[70] S. Lu, M. C. Bañuls, and J. I. Cirac, Algorithms for quantum simulation at finite energies, PRX Quantum **2**, 020321 (2021).

[71] F. M. Surace and O. Motrunich, Robustness and eventual slow decay of bound states of interacting microwave photons in the Google Quantum AI experiment, PRX Quantum **5**, 010317 (2024).

[72] M. Serbyn, D. A. Abanin, and Z. Papić, Quantum many-body scars and weak breaking of ergodicity, Nat. Phys. **17**, 675 (2021).

[73] S. Moudgalya, B. A. Bernevig, and N. Regnault, Quantum many-body scars and Hilbert space fragmentation: A review of exact results, Rep. Prog. Phys. **85**, 086501 (2022).

[74] A. Chandran, T. Iadecola, V. Khemani, and R. Moessner, Quantum many-body scars: A quasiparticle perspective, Annu. Rev. Condens. Matter Phys. **14**, 443 (2023).

Bridging quantum criticality via many-body scarring

Aiden Daniel [●],[1] Andrew Hallam,[1] Jean-Yves Desaules [●],[1] Ana Hudomal [●],[1,2] Guo-Xian Su [●],[3,4,5]
Jad C. Halimeh [●],[6,7] and Zlatko Papić [●][1]

[1]*School of Physics and Astronomy, University of Leeds, Leeds LS2 9JT, United Kingdom*
[2]*Institute of Physics Belgrade, University of Belgrade, 11080 Belgrade, Serbia*
[3]*Hefei National Laboratory for Physical Sciences at Microscale and Department of Modern Physics,
University of Science and Technology of China, Hefei, Anhui 230026, China*
[4]*Physikalisches Institut, Ruprecht-Karls-Universität Heidelberg, Im Neuenheimer Feld 226, 69120 Heidelberg, Germany*
[5]*CAS Center for Excellence and Synergetic Innovation Center in Quantum Information and Quantum Physics,
University of Science and Technology of China, Hefei, Anhui 230026, China*
[6]*Department of Physics and Arnold Sommerfeld Center for Theoretical Physics (ASC), Ludwig-Maximilians-Universität München,
Theresienstraße 37, D-80333 München, Germany*
[7]*Munich Center for Quantum Science and Technology (MCQST), Schellingstraße 4, D-80799 München, Germany*

Quantum dynamics in certain kinetically-constrained systems can display a strong sensitivity to the initial condition, wherein some initial states give rise to persistent quantum revivals—a type of weak ergodicity breaking known as "quantum many-body scarring" (QMBS). Recent work [Yao, Pan, Liu, and Zhai, Phys. Rev. B **105**, 125123 (2022)] pointed out that QMBS gets destroyed by tuning the system to a quantum critical point, echoing the disappearance of long-range order in the system's ground state at equilibrium. Here we show that this picture can be much richer in systems that display QMBS dynamics from a continuous family of initial conditions: As the system is tuned across the critical point while at the same time deforming the initial state, the dynamical signatures of QMBS at intermediate times can undergo an apparently smooth evolution across the equilibrium phase transition point. We demonstrate this using the PXP model—a paradigmatic model of QMBS that has recently been realized in Rydberg atom arrays as well as ultracold bosonic atoms in a tilted optical lattice. Using exact diagonalization and matrix product state methods, we map out the dynamical phase diagram of the PXP model with the quenched chemical potential. We demonstrate the existence of a continuous family of initial states that give rise to QMBS and formulate a ramping protocol that can be used to prepare such states in experiment. Our results show the ubiquity of scarring in the PXP model and highlight its intriguing interplay with quantum criticality.

I. INTRODUCTION

Quantum many-body scarring (QMBS) is a form of weak ergodicity breaking in which a small number of states retain memory of their initial wavefunction despite the rest of the system thermalizing (see recent reviews [1–4]). The set of models hosting QMBS states has rapidly expanded in recent years [5–20], including experimental realizations in several cold atom platforms [21–25]. At the same time, the underlying origin of memory-retaining initial states remains the subject of ongoing work. Some recently identified mechanisms giving rise to such phenomena include proximity to an integrable model [19,26,27], dynamical symmetry [5,28–32], and eigenstate embedding constructions [33].

Signatures of QMBS were initially observed in experiments on Rydberg atom arrays [21], where energy cost due to

van der Waals interactions strongly disfavors two neighboring atoms occupying excited states—a form of kinetic constraint called the Rydberg blockade [34]. When the Rydberg blockade is strong, the atoms are described by an effective "PXP" model [35,36]. This is a one-dimensional (1D) chain of spin-1/2 degrees of freedom, where the spin-up state $|1\rangle$ corresponds to a Rydberg atom occupying an excited state (and, similarly, for the spin-down state $|0\rangle$, which denotes an atom in the ground state). Thus, the number of up spins translates into the number of Rydberg excitations, and we will use such nomenclature interchangeably. The PXP Hamiltonian for N atoms takes the form (in units $\hbar = 1$)

$$H_{\text{PXP}}(\mu) = \Omega \sum_{j=0}^{N-1} P_{j-1} X_j P_{j+1} + \mu \sum_{j=0}^{N-1} Q_j, \qquad (1)$$

where $X = |1\rangle \langle 0| + |0\rangle \langle 1|$ is the Pauli-X operator describing the Rabi flipping of each atom. Below we will set the Rabi frequency to $\Omega = 1$. The projector $P = |0\rangle \langle 0|$ implements the constraint by preventing the Rabi flip from generating any neighboring excitations. The complementary projector, $Q = 1 - P = |1\rangle \langle 1|$, counts the number of excitations in the

---

system and thus defines the chemical potential term μ. We will consider two types of boundary conditions for the Hamiltonian in Eq. (1): For analytical considerations and exact diagonalization simulations, we will use periodic boundary conditions (PBCs), which are implicit in Eq. (1) after identifying site $j + N \equiv j$. For matrix product state simulations in large systems, we will instead use open boundary conditions (OBCs), where the first and the last flip term are taken to be $X_0 P_1$ and $P_{N-2} X_{N-1}$, respectively.

In the absence of chemical potential ($\mu = 0$), the PXP model displays nonthermalizing dynamics when initialized in the Néel state, $|\psi(0)\rangle = |\mathbb{Z}_2\rangle \equiv |1010...10\rangle$ [21]. Evolving this state with the Hamiltonian in Eq. (1), one observes that the return probability periodically reaches values close to unity [6]. By contrast, other initial states exhibit fast equilibration, as expected in a chaotic system. Conversely, this atypical dynamics is also reflected in ergodicity breaking amongst a subset of eigenstates of the PXP model [27,37,38], even in the presence of perturbations [39,40] or in energy transport at infinite temperature [41].

The chemical potential term plays a central role in this paper. When the chemical potential is tuned to $\mu_c \approx -1.31$, the PXP ground state undergoes an Ising phase transition [35,42], associated with a spontaneous breaking of $\mathbb{Z}_2$ symmetry [43–46]. The signatures of this transition have been observed in programmable Rydberg atom quantum simulators [47]. This equilibrium phase transition (referred to as "EPT" throughout this paper) is in the same universality class as the one induced by varying the quark mass in the Schwinger model of quantum electrodynamics in $(1 + 1)$-dimension [48]. The lattice formulation of the latter, known as the U(1) quantum link model, exactly maps to the PXP model in Eq. (1) for the case of spin-1/2 degrees of freedom [49].

The effect of chemical potential on scarring in the PXP model has also been the subject of much attention. On the one hand, Ref. [37] studied the effect of μ on the revivals of $|\mathbb{Z}_2\rangle$ state, finding that $\mu \neq 0$ restores thermalizing behavior. On the other hand, suitable periodic modulations of μ can enhance scarring and have been studied extensively [50–56]. In particular, a recent study [24] has found that new QMBS regimes can emerge for $\mu > 0$, even in the absence of a periodic drive. One example is the polarized state, $|0\rangle = |000....0\rangle$. While in the absence of chemical potential the $|0\rangle$ state is believed to thermalize [21], at moderate values of the chemical potential, it starts to revive, much like the Néel state. This raises the question about the existence of a larger family of scarred initial states in the PXP model in the presence of a chemical potential.

Another natural question concerns the interplay between criticality and QMBS. While the EPT has a profound effect on the low-energy physics of the PXP model, it is not obvious that it should directly impact QMBS, which manifests in the quench dynamics at infinite temperature. Nevertheless, Ref. [57] recently argued that there is a link between this EPT and QMBS. Namely, when tracing the eigenstates responsible for the quantum revival of the $|\mathbb{Z}_2\rangle$ state, Ref. [57] found that these states merge with the thermal bulk of the energy spectrum as the EPT is approached. On the contrary, upon moving away from the EPT towards $\mu \to -\infty$, the degenerate ground states acquire high overlap with the $|\mathbb{Z}_2\rangle$ state and its partner

translated by one site, $|\bar{\mathbb{Z}}_2\rangle \equiv |0101...\rangle$. Thus, the $|\mathbb{Z}_2\rangle$ state can only thermalize as one approaches the EPT, suggesting a connection between QMBS and criticality. This was also demonstrated experimentally in the Bose-Hubbard quantum simulator [58]. Moreover, by investigating the quantum Ising model in transverse and longitudinal fields, Ref. [59] argued that QMBS from the $|\mathbb{Z}_2\rangle$ state is smoothly connected to integrability by continuously turning off the constraint, induced by the longitudinal field.

In this paper, we map out the dynamical phase diagram of the PXP model corresponding to global quenches of the chemical potential from some initial value μ_i to an arbitrary final value μ_f. This provides a means of probing out-of-equilibrium dynamics from more complex initial states beyond $|\mathbb{Z}_2\rangle$ or $|0\rangle$, which had been accessed in previous experiments by taking the limits $\mu_i \to \pm\infty$. We identify QMBS regimes in the dynamical phase diagram based on signatures of ergodicity breaking, such as the deviation of observable expectation values from the canonical ensemble predictions and the presence of quantum revivals. Our results show that the previously known scarring regimes, associated with $|\mathbb{Z}_2\rangle$ and $|0\rangle$ states, indeed break down when approaching the EPT, either via $\mu_i \to \mu_c$ or $\mu_f \to \mu_c$, in agreement with Refs. [57,58]. However, we also find a new QMBS regime corresponding to the initial state being the ground state near the EPT. Using the time-dependent variational principle (TDVP) framework for QMBS, developed in Ref. [60], we identify a semiclassical picture behind QMBS dynamics. Across much of the phase diagram away from the EPT point, the QMBS dynamics can be understood in terms of a periodic trajectory that passes through the $|0\rangle$ state, with the radius of the trajectory controlled by the chemical potential. Allowing for a continuous family of initial states—the ground states of $H_{\mathrm{PXP}}(\mu_i)$—we find surprisingly robust QMBS signatures at intermediate times that smoothly bridge across the EPT. We work out a ramping protocol for the preparation of such states, providing a recipe for probing the dynamical phase diagram in experiment.

The remainder of this paper is organized as follows. We start by presenting the results of numerical simulations of the dynamical phase diagram of the PXP model for global quenches of the chemical potential in Sec. II. In Secs. III–V we analyze in detail the various regimes of this phase diagram. Section III contains a brief introduction to the TDVP formalism that will be useful for the semiclassical interpretation of the results. In Sec. IV we focus on QMBS regimes of the phase diagram, while Sec. V discusses the special case when the system is initialized in the ground state near the EPT. In Sec. VI, we show how the dynamical phase diagram can be probed in experiment by preparing the desired ground states using a ramping protocol. Our conclusions are presented in Sec. VII, while Appendices contain details of the TDVP formalism, finite-size scaling analysis, and additional characterizations of the phase diagram.

II. DYNAMICAL PHASE DIAGRAM OF THE PXP MODEL

In this paper we are interested in the following out-of-equilibrium probe of the PXP model in Eq. (1): start from the ground state of $H_{\mathrm{PXP}}(\mu_i)$ and then evolve with the same

Hamiltonian but generally different chemical potential value $H_{PXP}(\mu_f)$. We assume a closed system evolving under unitary Schrödinger dynamics. Since the energy level spacings in the PXP model are expected to obey the Wigner-Dyson distribution for all values of μ [6,35], the nonequilibrium dynamics induced by quenching μ should be described by random matrix theory [62]. In particular, quenching the chemical potential by a large amount $\sim O(1)$ should initialize the system in a generic high-temperature state, which is expected to lead to rapid thermalization according to the eigenstate thermalization hypothesis (ETH) [63–65]. This means that the expectation value of any local observable should converge towards the value predicted by the canonical ensemble within any symmetry-resolved sector of the many-body Hilbert space. Deviation from this prediction, i.e., ergodicity breaking, can be detected through a number of probes, two of which we utilize.

One probe of ergodicity breaking, convenient in the context of QMBS, is quantum fidelity or return probability of the wavefunction to its initial value,

$$\mathcal{F}(t) = |\langle \psi(0)|\psi(t)\rangle|^2. \tag{2}$$

For a thermalizing initial state, $\mathcal{F}(t)$ rapidly drops to a value close to zero and remains exponentially small in system size at late times. Therefore, if the average fidelity over a time interval $\gg \Omega^{-1}$ is much larger than $\sim O(\exp(-N))$, we expect nonergodic behavior. However, one should exclude trivial cases such as $\mu_i \approx \mu_f$ when the ground state of $H_{PXP}(\mu_i)$ is approximately an eigenstate of $H_{PXP}(\mu_f)$, as this would lead to the system getting "stuck" in an eigenstate, with fidelity $\mathcal{F}(t) \approx 1$ and potentially never decaying. To avoid such cases, we compute the difference $\delta\mathcal{F}$ between minimal fidelity and maximal fidelity over a time window $t \in [t_0, t_1]$, with $t_0 = 1$ and $t_1 = 20$. This window is large enough to exceed the initial relaxation on the scale $\gtrsim \Omega^{-1}$ (thus excluding the high fidelity near $t = 0$), yet small enough ($t_1 \lesssim N/\Omega$) to be free of the boundary effects. The obtained $\delta\mathcal{F}$ in the $\mu_i - \mu_f$ plane is shown in Fig. 1(a). The fidelity has been evaluated in a system of $N = 51$ atoms using matrix product state (MPS) [66] simulations based on the algorithm in Ref. [61], and we have checked that the results agree closely with exact diagonalization for systems with $N < 30$ atoms. We note that $t_0 = 1$ in Fig. 1(a) was chosen to be just slightly longer than the initial relaxation period, as modulating μ alters the period of the fidelity revivals. Setting $t_0 > 1$ results in a qualitatively similar phase diagram, but with a reduced overall scale for $\delta\mathcal{F}$, as the window with larger t_0 may miss the first (and typically the largest) revival peak.

Before we comment on the interesting regimes of the phase diagram, we note that we have also computed the deviation of an observable expectation value from the thermal ensemble prediction, shown in Fig. 1(b). This provides a complementary probe of ergodicity breaking that is more amenable to experimental measurements. For the observable, we chose the density of excitations in the system, $n = (1/N)\sum_{j=1}^{N} Q_j$, which is readily available in existing experimental setups [21,24]. After quenching the system, we compute the integrated mean-square deviation of the excitation density from the thermal value over the time window between $t_0 = 10$ and
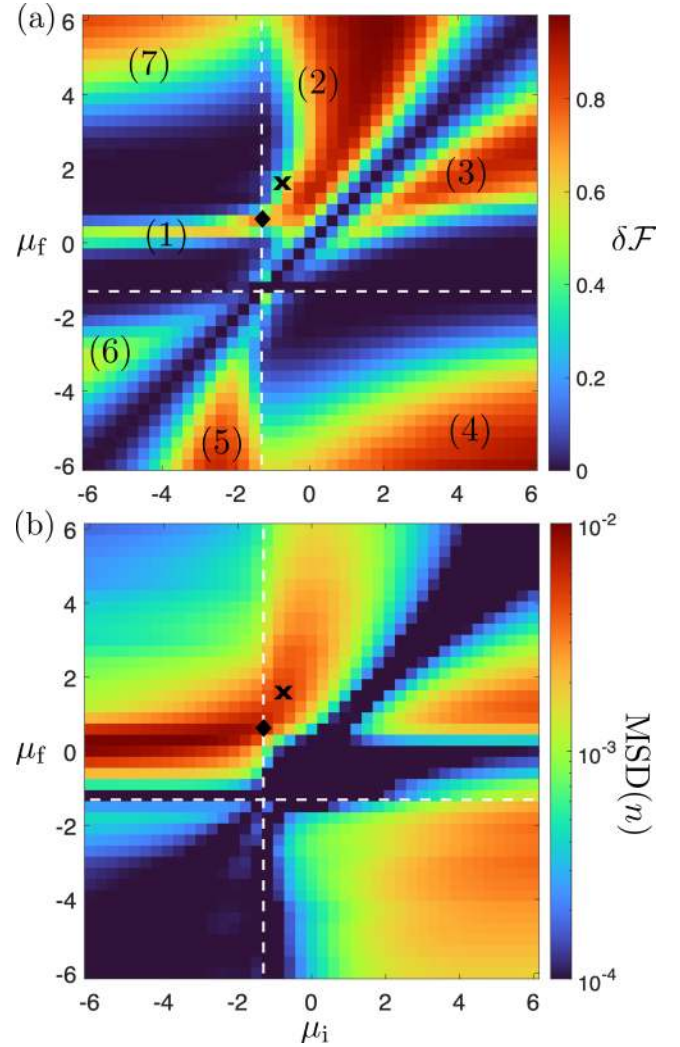

FIG. 1. Dynamical phase diagram for global quenches starting in the ground state of $H_{PXP}(\mu_i)$ and evolving with $H_{PXP}(\mu_f)$. (a) The difference between maximal and minimal revival fidelity $\delta\mathcal{F}$ over time interval $1 \leqslant t \leqslant 20$ following the quench. Regions with strong fidelity revivals have been enumerated (see the text for details). (b) Same as (a) but the color bar showing the deviation of the excitation density from the thermal value, Eq. (3). Data is obtained using MPS simulations [61] for a chain of $N = 51$ atoms with OBCs, maximum bond dimension $\chi = 128$ and time step $\delta t = 0.025$. Dashed lines mark the EPT at $\mu_c \approx -1.31$. In both plots, the cross marks the point ($\mu_i = -0.76$, $\mu_f = 1.60$) that will be analyzed in Sec. IV. The diamond marks the optimal reviving point in the $\mu_i = \mu_c$ plane, which will be discussed in Sec. V.

$t_1 = 20$,

$$\text{MSD}(n) = \frac{1}{t_1 - t_0} \int_{t_0}^{t_1} |\langle \psi(t)|n|\psi(t)\rangle - n_{th}|^2 \, dt. \tag{3}$$

The thermal value is defined as

$$n_{th} = \text{Tr}(\rho_{th} n), \tag{4}$$

where the thermal density matrix is given by the usual Boltzmann-Gibbs expression, $\rho_{th} = \exp(-\beta H)/\mathcal{Z}$, with the partition function $\mathcal{Z} = \text{Tr}\exp(-\beta H)$ and the inverse

temperature β determined from the condition

$$\langle \psi(0)|H_{\text{PXP}}(\mu_{\text{f}})|\psi(0)\rangle = \text{Tr}(\rho_{th}H_{\text{PXP}}). \qquad (5)$$

The plot of MSD(n) is shown in Fig. 1(b), where the bright nonergodic regions match those of high fidelity in Fig. 1(a). The color contrast is stronger in the fidelity plot due to the exponential sensitivity of that quantity. A few distinct regimes where fidelity displays large-amplitude oscillations have been marked by (1)–(7) in Fig. 1(a). These regions will be analyzed in detail in the subsequent sections. There, we will argue that regions (1), (2), and (3) can be identified as QMBS regimes. Regions (1) and (3) fall under the "universality class" of $|\mathbb{Z}_2\rangle$ and $|0\rangle$ QMBS behavior, as we explain in Sec. III. On the other hand, while the dynamics in region (2) has some similarities with regions (1) and (3), in Sec. IV we will highlight the distinctions of this QMBS regime. As it turns out, regions (4), (5), (6), and (7) have a simple origin, which will be explained briefly in Appendix A.

A few comments are in order. The QMBS fidelity appears to vary smoothly between regions (1) and (2) in Fig. 1(a), while they are separated by the EPT (indicated by the dashed line). In fact, we find the most robust revivals correspond to the ground state precisely at the EPT point (highlighted by the diamond in Fig. 1). That is to say, although $\delta\mathcal{F}$ may be smaller than other regions, the revivals decay more slowly over time, and this behavior persists with increasing N. This intriguing case will be addressed in detail in Sec. V. Here we note that we have confirmed the existence of QMBS across the critical point in much larger systems ($N \leqslant 400$ spins) using MPS numerics. This is in contrast to the $\mu_{\text{f}} = \mu_{\text{c}}$ case, where we see no ergodicity breaking in Fig. 1(a), as also expected from Refs. [57,58].

III. TIME-DEPENDENT VARIATIONAL PRINCIPLE AND PERIODIC ORBITS FOR MANY-BODY SCARRING

Without chemical potential, quantum dynamics from the $|\mathbb{Z}_2\rangle$ state in the PXP model can be visualized as a classical periodic orbit [60,67,68]. This is accomplished in the framework of the time-dependent variational principle (TDVP) [69–71], which we briefly review in this section. TDVP establishes a parallel between many-body dynamics in the PXP model and the analogous dynamical phenomena of a single particle in a stadium billiard, in which the wavepackets are anomalously long-lived when prepared along the periodic orbits of the corresponding classical billiard [72,73]. TDVP will provide a natural semiclassical language for interpreting the essential features of the dynamical phase diagram in Fig. 1.

A. A brief overview of TDVP formalism

The starting point of TDVP is to specify a variational manifold of states $\mathcal{M}$, parameterized by some continuous variable, and then project the Schrödinger dynamics into that manifold in a way that manifestly conserves the energy. The nature of states belonging to $\mathcal{M}$ determines to what extent we can interpret the dynamics as "semiclassical". For example, it would be simplest to consider a manifold spanned by tensor products of spin-coherent states. This would yield a "mean-field" description for the dynamics, where each atom

processes independently. However, the Rydberg blockade intrinsically builds in local correlations into the system, due to the fact that any neighboring excitations, $|\dots 11 \dots\rangle$, are projected out of the Hilbert space. Ordinary spin-coherent states clearly violate this blockade condition.

Another way of defining a manifold, which naturally accommodates the Rydberg blockade constraint, is to take the span over MPS states with bond dimension χ controlling the amount of correlations necessary to capture the projected dynamics [71]. To simplify matters as much as possible, we will consider the dynamics to be spatially periodic with a (infinitely repeated) unit cell of size K (below we will be primarily interested in small unit cells with $K = 1, 2$). For a 1D chain of size N, the resulting MPS ansatz is given by

$$|\psi_{\text{MPS}}(\{\mathbf{x}\})\rangle = \sum_{\{\sigma\}} \text{Tr}\left(\prod_{m=0}^{N/K-1} A^{\sigma_{1+Km}}(\mathbf{x}_1)A^{\sigma_{2+Km}}(\mathbf{x}_2) \right.$$
$$\left. \times A^{\sigma_{K+Km}}(\mathbf{x}_K) \right)|\sigma_1\sigma_2\sigma_3\cdots\sigma_N\rangle. \qquad (6)$$

Here $A^\sigma(\mathbf{x_i})$ are $(\chi \times \chi)$-dimensional matrices that depend on variational parameters $\mathbf{x_i} = (\theta_i, \phi_i)$, where the angles θ_i, ϕ_i are akin to the Bloch sphere angles of each spin in the unit cell. The physical degree of freedom $\sigma_i = 0, 1$ labels the basis states of a single spin. Following Refs. [60,74], in order to make things analytically tractable, we will restrict to $\chi = 2$ and chose

$$A^1(\theta_i, \phi_i) = \begin{pmatrix} 0 & e^{-i\phi_i} \\ 0 & 0 \end{pmatrix}, \quad A^0(\theta_i, \phi_i) = \begin{pmatrix} \cos\theta_i & 0 \\ \sin\theta_i & 0 \end{pmatrix}. \quad (7)$$

Due to $A^1A^1 = 0$, this ansatz ensures that configurations with neighboring spin-up are forbidden, thus our manifold $\mathcal{M} = \text{span}\{|\psi_{\text{MPS}}(\mathbf{x})\rangle \,|\forall\mathbf{x}\}$ is consistent with the Rydberg blockade.

With the choice of ansatz in Eqs. (6) and (7) and setting $K = 1$, we are left with only two variational degrees of freedom, (θ, ϕ). Choosing (0,0) recovers the state $|0\rangle \equiv |000\dots\rangle$, while $(\pi/2, \pi/2)$ corresponds to the equal-weight superposition of the two Néel states,

$$|\mathbb{Z}^+\rangle \equiv \frac{1}{\sqrt{2}}(|\mathbb{Z}_2\rangle + |\bar{\mathbb{Z}}_2\rangle). \qquad (8)$$

Note that with $K = 1$ unit-cell periodicity, the states $|\mathbb{Z}_2\rangle$, $|\bar{\mathbb{Z}}_2\rangle$ do not individually belong to the manifold. Instead, if we extend the ansatz to $K = 2$, then $(\theta_1, \theta_2) = (0, \pi/2)$ recovers the $|\mathbb{Z}_2\rangle$ state. Thus, our manifold with bond dimension $\chi = 2$ captures the initial product states that we expect to play an important role for QMBS dynamics in the PXP model.

After defining the manifold, the next step is to minimize the difference between exact Hamiltonian dynamics and its projection to the manifold,

$$\min_{\{\mathbf{x}\}} \left\| i\hbar\frac{\partial}{\partial t}|\psi_{\text{MPS}}(\{\mathbf{x}\})\rangle - H|\psi_{\text{MPS}}(\{\mathbf{x}\})\rangle \right\|. \qquad (9)$$

This results in the Euler-Lagrange equations of motion for the classical variables $\mathbf{x}$ [71]. In the case of the PXP model, this step can be performed analytically in the limit of $N \to \infty$ to obtain the equations of motions for the θ and ϕ angles, see Appendix B for $K = 1$ and Refs. [60,74] for some $K = 2$ and $K = 3$ examples. Integrating this system of differential
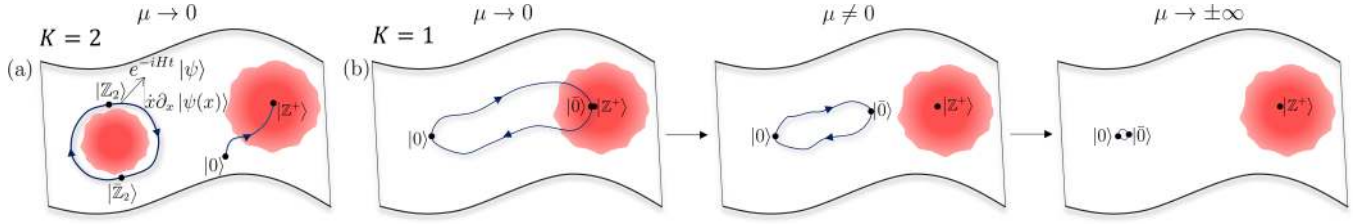
FIG. 2. Sketch of the TDVP manifold $\mathcal{M}$ for the PXP model with chemical potential μ. Red regions represent areas of high leakage where the TDVP approximation breaks down, as quantified by Eq. (10). The Néel state is denoted by $|\mathbb{Z}_2\rangle \equiv |1010\ldots\rangle$ and its translated partner—the anti-Néel state is $|\bar{\mathbb{Z}}_2\rangle \equiv |0101\ldots\rangle$, while $|\mathbb{Z}^+\rangle = (|\mathbb{Z}_2\rangle + |\bar{\mathbb{Z}}_2\rangle)/\sqrt{2}$. The polarized state is $|0\rangle \equiv |0000\ldots\rangle$. (a) For a two-site unit cell $K = 2$ and $\mu = 0$, the $|\mathbb{Z}_2\rangle$ state lies on a periodic trajectory identified in Ref. [60]. We also illustrate the trajectory of the $|0\rangle$ state, which is predicted by TDVP to evolve to $|\mathbb{Z}^+\rangle$; however, this point lies within a region of high leakage where the TDVP dynamics does not accurately describe the quantum evolution. This is consistent with the $|0\rangle$ state thermalizing at $\mu = 0$. (b) Taking $K = 1$ we focus on the evolution of the $|0\rangle$ state trajectory as μ is varied. For $\mu = 0$, the trajectory is periodic but passes through a region of high leakage. When $\mu \neq 0$, the trajectory shrinks, whilst gradually exiting the high leakage area, and QMBS dynamics starts to emerge in the full system. In this regime, the QMBS dynamics can be seen as an oscillation between $|0\rangle$ and a new state $|\bar{0}(\mu)\rangle$ defined in Eq. (11). Finally, in the extreme $\mu \to \pm\infty$ limit, the orbit shrinks to a point.

equations yields the trajectory in $\mathcal{M}$ taken by $|\psi_{\text{MPS}}(\{\boldsymbol{\theta}, \boldsymbol{\phi}\})\rangle$ during the course of quantum evolution. Figure 2 shows a pictorial representation of the manifold and the projection of exact dynamics into it, for the cases of interest in the PXP model perturbed by the chemical potential.

Importantly, beyond equations of motion, it is possible to estimate "quantum leakage": the difference between exact quantum evolution and its projection into the manifold [60]. Quantum leakage γ is defined as the instantaneous rate at which the exact wave function leaves $\mathcal{M}$,

$$\gamma^2 = \lim_{N \to \infty} \frac{1}{N} \left\| iH \,|\psi_{\text{MPS}}(\mathbf{x})\rangle + \sum_j \dot{x}_j \partial_{x_j} |\psi_{\text{MPS}}(\mathbf{x})\rangle \right\|^2. \quad (10)$$

Red regions in Fig. 2 indicate areas of large γ^2. In these high-leakage regions, the instantaneous TDVP dynamics is expected to poorly capture the exact dynamics. Consequently, trajectories passing through such regions will generally be of limited accuracy. On the other hand, as first noted in Ref. [60], the special property of the PXP phase space is that it has regions of remarkably *low* leakage, such as the region traversed by the semiclassical orbit associated with the $|\mathbb{Z}_2\rangle$ state. This is depicted in Fig. 2(a) where the orbit is sketched, lying within a region of low leakage. Note that, in general, there can exist *multiple* periodic orbits within the same manifold [67].

B. TDVP interpretation of the dynamical phase diagram

Much of the PXP dynamical phase diagram in Fig. 1 can be understood by considering the trajectory of the polarized state in the TDVP manifold introduced above. Figure 2(b) sketches this trajectory for three different values of the chemical potential μ. Within TDVP, a periodic orbit exists even for $\mu = 0$. However, the orbit passes through the superposition of the two Néel states $|\mathbb{Z}^+\rangle$, which is located in the high-leakage region. The TDVP dynamics is therefore not a good approximation in this case, which accounts for the absence of revivals observed in the full quantum dynamics.

The addition of a finite chemical potential μ contracts the trajectory and pushes it into a low-leakage region, as shown in

the middle panel of Fig. 2(b), effectively allowing the revivals from the polarized state to emerge. As we will explain in Sec. IV, in this intermediate range of μ, the ground state of $H_{\text{PXP}}(\mu')$ (where $\mu \neq \mu'$) occupies an antipodal position on the orbit, corresponding to a chemical-potential dependent state we label $|\bar{0}(\mu)\rangle$, given by Eq. (7) for unit-cell size $K = 1$,

$$|\bar{0}(\mu)\rangle = |\psi_{\text{MPS}}(\theta_{\max}, \phi_{\max})\rangle, \quad (11)$$

with angles $(\theta_{\max}, \phi_{\max})$ denoting the antipodal point in the TDVP orbit of the initial polarized state, see Fig. 2(b). As μ has the effect of deforming the trajectory, the antipodal angles also depend on μ, as will be specified in Eq. (16) below. Note that the sign of μ has no effect on the deformation of the particular orbit discussed here, as we explain in Appendix C. Finally, in the extreme limit $\mu \to \pm\infty$, the trajectory is restricted to the vicinity of the initial state and the dynamics is effectively frozen, as shown in the right panel of Fig. 2(b).

IV. SCARRING IN GAPPED REGIMES OF THE PHASE DIAGRAM

In this section we focus on regions (1), (2), and (3) of the phase diagram in Fig. 1, in particular for the values of the chemical potential away from the EPT. Based on the discussion of TDVP in Sec. III and Fig. 2, the origin of regions (1) and (3) can be understood by examining the form of the PXP ground state in the presence of chemical potential. When $\mu_i \to -\infty$, excitations are favored and the ground state is (for PBCs) a superposition of the two Néel states $|\mathbb{Z}^+\rangle$ in Eq. (8). By contrast, $\mu_i \to \infty$ penalizes excitations, therefore the ground state is the polarized state $|0\rangle$. The superposition state $|\mathbb{Z}^+\rangle$ is known to display revivals when quenched to $\mu_f = 0$ [37], while the polarized state revives when quenched with $\mu_f \neq 0$ as shown more recently in Refs. [24,55]. By continuity, these limiting cases explain the mechanism behind revivals in regions (1) and (3) of Fig. 1. In the remainder of this section, we focus on the more interesting region (2) where the prequench initial state is an entangled state with low overlap on both $|0\rangle$ and $|\mathbb{Z}_2\rangle$ states.
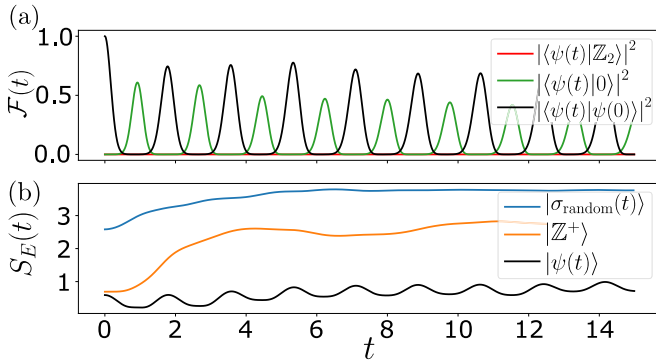
FIG. 3. Dynamics of quantum fidelity and entanglement entropy, following a global quench of the chemical potential, $\mu_i^* = -0.76 \rightarrow \mu_f^* = 1.6$, corresponding to the point marked by the cross in Fig. 1(a). Quantum fidelity for the initial state $|\psi(0)\rangle$ defined as the ground state of the PXP model with μ_i^*. Also shown is the projection of the time-evolved state on the $|\mathbb{Z}_2\rangle$ and $|0\rangle$ states. While the overlap with the $|\mathbb{Z}_2\rangle$ state is low throughout the evolution, the overlap with $|0\rangle$ reaches relatively high values between the main revival peaks. (b) Growth of entanglement entropy $S_E(t)$ for the same initial state $|\psi(0)\rangle$ as in (a), as well as for a random state $|\sigma_{\text{Random}}\rangle$ and $|\mathbb{Z}^+\rangle$ state. The initial state $|\psi(0)\rangle$ has strongly suppressed entanglement growth compared to the other cases. Data is for system size $N = 28$ obtained using exact diagonalization with PBCs.

A. Scarring in region (2) of the phase diagram

We focus on region (2) of the phase diagram in Fig. 1 and pick $(\mu_i^*, \mu_f^*) = (-0.76, 1.60)$ as an illustrative point in this region, marked by the cross in Figs. 1(a) and 1(b). QMBS dynamics at this point was first noted in Ref. [24] and here we will characterize it in detail and explain its origin. The evolution of fidelity and overlap with the polarized and Néel state are shown in Fig. 3(a), where persistent fidelity revivals can be observed while the overlap with $|\mathbb{Z}_2\rangle$ remains negligible throughout the evolution. Curiously, while the initial state at μ_i^* has low overlap with $|0\rangle$, the evolved state does develop a relatively high overlap with $|0\rangle$ state, approximately half way between the main revival peaks—see the green line in Fig. 3(a). This is reminiscent of the $|\mathbb{Z}_2\rangle$ state, which in the pure PXP model undergoes state transfer to $|\bar{\mathbb{Z}}_2\rangle$ at half the revival period [60], implying that the ground state of $H_{\text{PXP}}(\mu_i^*)$ is related to the polarized state.

Another tell-tale signature of QMBS is a slower growth of entanglement entropy $S_E(t)$ for special initial states. The entanglement entropy is defined as the von Neumann entropy of the reduced density matrix, $\rho_A = \text{Tr}_B |\psi(t)\rangle\langle\psi(t)|$, obtained by tracing out degrees of freedom belonging to one half of the chain (denoted B). We plot the dynamics of $S_E(t)$ in Fig. 3(b). Compared to both $|\mathbb{Z}^+\rangle$ and a random state in the constrained Hilbert space $|\sigma_{\text{Random}}\rangle$, the entropy growth from the ground state of $H_{\text{PXP}}(\mu_i^*)$ is strongly suppressed. Moreover, for the latter state, we observe clear oscillations in the time series of $S_E(t)$, reminiscent of entropy dynamics in the PXP model in the absence of chemical potential [6].

We emphasize that the special point (μ_i^*, μ_f^*) is representative of the entire region (2) in the phase diagram, where similar QMBS phenomenology is numerically observed. In the remainder of this section, we use TDVP to garner a further

understanding of this QMBS regime from a semiclassical point of view.

B. TDVP analysis of scarring in region (2)

Before we apply TDVP to extract the semiclassical description of the dynamics in Fig. 3, we need to make sure that the PXP ground state in the presence of chemical potential is represented within the manifold spanned by states in Eq. (6). In a recent paper [75], a method of "optimal steering" has been devised to smoothly prepare a class of PXP ground states based on the minimization of quantum leakage along the trajectory. To show that the detuned PXP ground states are captured in the TDVP manifold, here we follow a simpler approach of optimizing the overlap $|\langle\psi_{\text{MPS}}(\{\mathbf{x}\})|\psi(\mu_i)\rangle|^2$, where $|\psi(\mu_i)\rangle$ is the ground state of the PXP model in Eq. (1). For a unit cell size $K = 1$, we performed exhaustive numerical sampling at system size $N = 20$ and found that most states belonging to the TDVP manifold ($>90\%$ of them) can be approximated with better than 98% accuracy by a ground state of Eq. (1). Conversely, we numerically find that PXP ground states with nonzero μ can be well captured by low bond dimension MPS states. Intuitively, this is expected due to the area-law entanglement scaling of the gapped PXP ground state. As a side note, we mention that in order to prepare the states in the TDVP manifold with unit cell $K \geqslant 2$, we need to make two modifications to the preparation procedure: (i) we need to allow chemical potential to be different for different atoms within the unit cell; (ii) we need to include a unit-cell modulated pulse in the z direction. As explained in Appendix D, after these generalizations, one can also successfully prepare TDVP states with $K \geqslant 2$. While we do not have a general proof, this provides a numerical confirmation of the representability of the ground states of the PXP model with a suitably-defined generalization of the chemical potential within the TDVP manifold.

Having established that our prequench ground state at arbitrary μ_i can be approximately mapped to an MPS state in the $K = 1$ TDVP manifold for some variational parameters (θ, ϕ), we now proceed to describe the dynamics from this initial state using the classical dynamical system defined by $(\theta(t), \phi(t))$. From Eq. (9), one can derive the TDVP equations of motion for $K = 1$ and arbitrary chemical potential μ (see Appendix B for details),

$$\dot{\theta} = -\cos\theta\cos\phi(1 + \sin^2\theta), \qquad (12)$$

$$\dot{\phi} = \mu + \frac{\sin\phi}{\sin\theta}(1 - 4\sin^2\theta - \sin^4\theta). \qquad (13)$$

Unlike the special case $\mu = 0$, where ϕ variables can be set to zero in the flow-invariant subspace [60], for general values of μ one must consider both θ and ϕ variables simultaneously [67].

Integrating Eqs. (12) and (13), we plot the phase space θ, ϕ portrait for the chemical potential value $\mu_f = 1.6$ in Fig. 4(a). The grayscale background indicates the quantum leakage at any given point in the manifold,

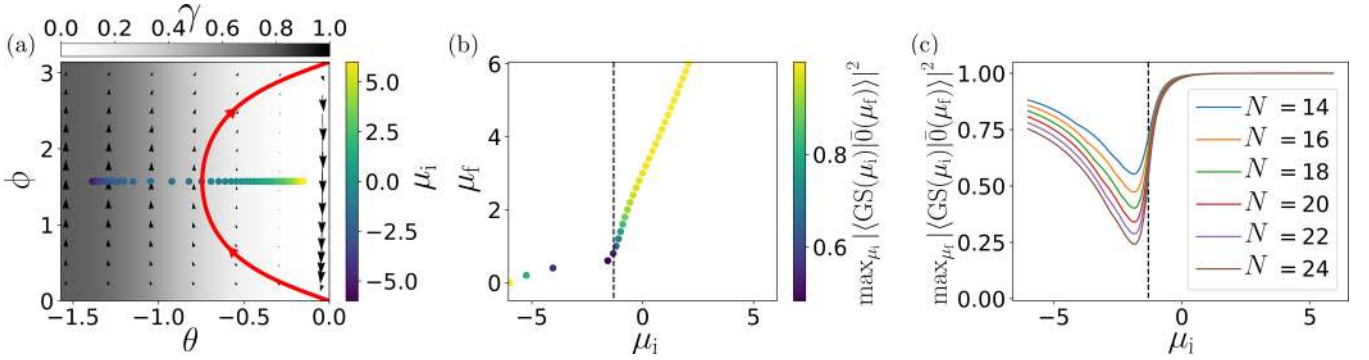$$\gamma^2 = \frac{\sin^6\theta}{1 + \sin^2\theta}, \qquad (14)$$

FIG. 4. (a) Phase space portrait of quantum dynamics within the $K = 1$ TDVP manifold for the PXP model with $\mu_f = 1.6$. Grey shading indicates quantum leakage (darker regions represent larger leakage). The trajectory of the $|0\rangle$ state for the given value of μ_f is highlighted in red, while colored symbols indicate the location of the PXP ground states corresponding to various μ_i indicated on the color bar. The ground states with $\mu_i \approx -0.76$ can be seen to lie close to the point, which is antipodal to the $|0\rangle$ state in its trajectory. With changing μ_f, this trajectory either expands or compresses, meaning all ground states will lie on this antipodal point for some μ_f. (b) In region (2) of the phase diagram, for a given μ_f, $|\bar{0}(\mu_f)\rangle$ state is well approximated by a detuned PXP ground state with some μ_i. Color bar shows the highest overlap between the $|\bar{0}(\mu_f)\rangle$ state, given by Eq. (16) for a range of fixed $\mu_f \in [-5, 5]$, and the family of ground states of $H_{PXP}(\mu_i)$. Dashed lines denote the EPT. For negative chemical potentials, especially relevant for region (1) of the phase diagram, the mapping requires an additional phase pulse, as described in Appendix D. (c) Matching the detuned PXP ground state with a $|\bar{0}\rangle$ state becomes progressively more difficult at the critical point (dashed line) as system size N is increased. In contrast to panel (b), here we fix the PXP ground state at μ_i and vary μ_f to find the optimal $|\bar{0}(\mu_f)\rangle$ state with the highest overlap. All plots are obtained using exact diagonalization with PBCs and system size $N = 20$ in panels (a) and (b).

which only depends on θ variable (see Appendix B). By integrating the equations of motion for $\mu_f = 1.6$, starting from the polarized state $|\psi_{MPS}(0, 0)\rangle$, we obtain the trajectory plotted in red color in Fig. 4(a). Generally, for any $|\mu_f| \neq 0$, the polarized state has a periodic orbit within TDVP. When μ_f is large, the orbit is pinned around $\theta = 0$. Decreasing $|\mu_f|$ stretches the orbit until the maximal point in the trajectory eventually tends towards the $|\mathbb{Z}^+\rangle$ superposition state, $(\theta, \phi) \equiv (\pi/2, \pi/2)$. Due to the quantum leakage gradient, the $|\mathbb{Z}^+\rangle$ point is not reached for any finite time, consistent with the lack of revivals from the polarized state in the full quantum dynamics for sufficiently small values of μ_f. Thus, we conclude that the orbit corresponding to the cross in Fig. 1(a) is a compromise between two competing effects: the orbit is sufficiently stretched so that it has nontrivial dynamics, while at the same time, by being not stretched too much, it can avoid the large leakage in the vicinity of $|\mathbb{Z}^+\rangle$ state.

To verify this picture across the entire region (2), we study the projection of the PXP ground state at μ_i, $|GS(\mu_i)\rangle$, to the TDVP manifold. We numerically maximize the overlap $|\langle \psi_{MPS}(\theta, \phi)|GS(\mu_i)\rangle|^2$, with the MPS state given in Eq. (6). We plot the resulting (θ, ϕ) phase space coordinates for a variety of μ_i in Fig. 4(a), where the colored dots correspond to the ground states from our phase diagram in Fig. 1(a). As expected, some of the ground states are "distant" from $|\mathbb{Z}^+\rangle$ or $|0\rangle$ but tend towards either in their respective limits. All successfully optimized ground states lie on the same ϕ plane in Fig. 1(a), such that the deformation of the trajectory means they will correspond to some maximum point μ_f on the polarized state trajectory, denoted by the state $|\bar{0}\rangle$. By analogy with the Néel state, whose translation partner—the anti-Néel state—displays identical scarring behavior [19], here we have a similar relation between $|0\rangle$ and $|\bar{0}(\mu_f)\rangle$ states. The main difference with the anti-Néel state is that $|\bar{0}\rangle$ state depends on the value of μ_f.

To substantiate this further, we analytically derive the phase-space coordinates corresponding to $|\bar{0}(\mu_f)\rangle$. Using Eq. (12), we see that the turning point in the gradient of θ along the trajectory is governed by $\cos \phi$. A sign flip therefore must occur when $\phi = \pm \pi/2$. Because energy is exactly conserved along a TDVP trajectory, $|\bar{0}(\mu_f)\rangle$ must have the same energy as the polarized state. For states belonging to $K = 1$ TDVP manifold, the energy density is given by

$$E(\theta, \phi)/N = \frac{\sin \theta}{1 + \sin^2 \theta}(\mu_f \sin \theta + 2 \cos^2 \theta \sin \phi). \quad (15)$$

For the polarized state, $E(0, 0) = 0$ and, setting $\phi_{max} = \pi/2$, allows us to determine the θ_{max} coordinate of the $|\bar{0}(\mu_f)\rangle$ turning point,

$$\sin \theta_{max} = \left(|\mu_f| - \sqrt{\mu_f^2 + 16}\right)/4. \quad (16)$$

In Fig. 4(b) we test the overlap of the state $|\bar{0}(\mu_f)\rangle$, with the MPS angles given by Eq. (16), against the family of ground states of $H_{PXP}(\mu_i)$. We scan through a set of values $\mu_f \in [-5, 5]$ and, for each μ_f, plot the maximum overlap obtained by maximizing over μ_i. Although $\mu_f < 0$ is not particularly relevant for region (2), we note that the optimization fails there. This, however, can be fixed by including an additional phase pulse, as explained in Appendix D. Comparing Fig. 4(b) to Fig. 1(a), we see a striking correspondence between the successful optimization and region (2) in the phase diagram, which confirms that the QMBS phenomena in region (2) are indeed associated with $|\bar{0}(\mu_f)\rangle$ state.

Finally, in Fig. 4(c) we study the system size scaling of the mapping between the PXP ground state with chemical potential and states in the TDVP manifold. We scan for the maximal overlap of the ground state at some μ_i with the set of all $|\bar{0}(\mu_f)\rangle$ states in the interval $\mu_f \in [-20, 20]$. Remarkably, for the vast majority of region (2) when $\mu_i > 0$, we see a

near perfect overlap between the ground state and $|\bar{0}(\mu_f)\rangle$, independent of system size—suggesting that the TDVP state captures well the PXP ground state in region (2). Nevertheless, in Fig. 4(c) we also observe a breakdown of the mapping at the EPT point $\mu_i = \mu_c$. This is expected since the ground state at the critical point develops a diverging entanglement entropy and the $\chi = 2$ MPS approximation must deteriorate as system size is increased, since an area-law state cannot capture the critical ground state in the thermodynamic limit. This naturally leads to the question: Is the observed scarring in the critical ground state an artefact of finite size and what is its origin?

V. INTERPLAY BETWEEN SCARRING AND CRITICALITY

We now focus on the nature of QMBS regime when quenching from the critical ground state at $\mu_i = \mu_c$. Despite the complexity of this state, we find robust signatures of ergodicity breaking. Long-time memory retention from states in energy close to an EPT has previously been observed in the LMG model [76,77]. We find similar behavior between regions (1) and (2) in Fig. 1(a). For example, by fixing $\mu_i = \mu_c$ and scanning μ_f to determine the largest $\delta\mathcal{F}$, we find the most robust revivals occur at $\mu_f = 0.633$—a point marked by the diamond in Fig. 1. This turns out to be one of the best reviving points in all of regions (1), (2), and (3), including the $|\mathbb{Z}_2\rangle$ and $|0\rangle$ initial states. As discussed above, the TDVP semiclassical formalism is not well suited for describing this case as it cannot capture the diverging entanglement entropy of the initial state. This immediately raises the question if the observed QMBS behavior is a finite-size effect and whether one should rather expect a sharp boundary between regions (1) and (2) in Fig. 1 in the thermodynamic limit.

To probe the robustness of QMBS revivals in the thermodynamic limit, we simulated the quench $\mu_i = -1.31 \rightarrow \mu_f = 0.6$ in large systems up to $N = 401$ using MPS in Fig. 5. The fidelity, plotted in Fig. 5(a), demonstrates that revivals exist in all accessible system sizes. The fidelity is not an intensive quantity, therefore it is generically expected to decay in the $N \rightarrow \infty$ limit, as indeed can be observed in Fig. 5(a). Thus, to compare different system sizes, we take the fidelity at the first revival peak $\mathcal{F}_1$ and plot its density $-\log(\mathcal{F}_1)/N$ against $1/N$, in the inset of Fig. 5(a). This serves as an indicator of ergodicity breaking at a finite time that can be properly scaled to the thermodynamic limit. For a random state in the constrained Hilbert space of the PXP model, whose dimension grows asymptotically as $\sim\phi^N$, where $\phi = (1 + \sqrt{5})/2$ is the *golden ratio* [36], the fidelity density at late times asymptotically approaches the value $\log\phi \approx 0.48$, with $O(1/N^2)$ corrections. Contrary to this expectation, the fidelity density in Fig. 5(a) continues to decrease as $N \rightarrow \infty$ and extrapolates to a value smaller than 0.01, signaling nonergodicity in the thermodynamic limit at a finite time scale $t \sim 5/\Omega$, which is well beyond the initial relaxation.

In Fig. 5(b) we observe a slow growth of entanglement entropy following the same quench. In contrast to previous QMBS cases in the literature, where the system was initialized in a product with zero entropy, here we start from a critical ground state whose entropy is expected to diverge logarithmically with system size according to the Cardy-Calabrese
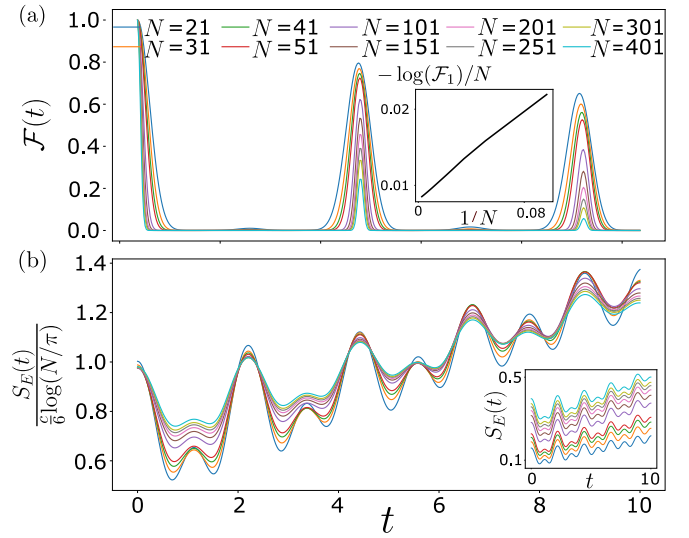

FIG. 5. Fidelity and entanglement entropy dynamics for the quench from the critical ground state with $\mu_i = -1.31$ to $\mu_f = 0.6$. (a) Fidelity revivals persist up to the largest system size $N = 401$. While the fidelity decays with N, the fidelity *density* of the first revival peak $-\log(\mathcal{F}_1)/N$, plotted against inverse system size $1/N$, extrapolates to a value close to 0 (inset), indicating nonergodic behavior in the thermodynamic limit at a finite time. (b) Dynamics of the half-chain entanglement entropy $S_E(t)$ for the same quench. We scale the entropy by the critical value given by the Cardy-Calabrese formula with central charge $c = 1/2$ [78], which collapses the data to 1 at $t = 0$ (inset shows the unscaled entropy). The growth of entropy is seen to be linear, with pronounced oscillations. Data is obtained by MPS simulations with OBCs, bond dimension $\chi = 300$, and time step $\delta t = 0.025$.

formula, $S_{crit} = (c/6)\log(N/\pi)$ [78]. The universal prefactor is determined by the central charge c of the conformal field theory, which is $c = 1/2$ for our critical point in the Ising universality class. Scaling the data by S_{crit} indeed yields a good collapse at time $t = 0$. At later times, the entropy grows linearly with time. On top of linear growth, we observe prominent oscillations that are typically found in QMBS systems, e.g., the $|\mathbb{Z}_2\rangle$ initial state in the PXP model [6]. The amplitude of these oscillations is roughly independent of system size, as can be seen in the inset of Fig. 5(b). At much later times, which are inaccessible to MPS methods, we expect the entropy to saturate to a value proportional to the volume of the subsystem. Apart from the diverging entropy of the initial state, the overall picture from Fig. 5 is broadly similar to previous studies of QMBS dynamics [1]. What remains to be explained is why the critical ground state is poised towards QMBS-like dynamics.

To identify the microscopic origin of this robust ergodicity breaking in the vicinity of $\mu_f = 0.633$, we plot the overlap of the initial critical ground state with the eigenstates of the postquench Hamiltonian in Fig. 6. The overlap exhibits clear towers of eigenstates, which are emblematic of QMBS. While these features are present throughout the spectrum, the dominant contributions to the initial state come from low-energy eigenstates. In order to approximate their characteristics, we can treat them as magnons with a given momentum k on top
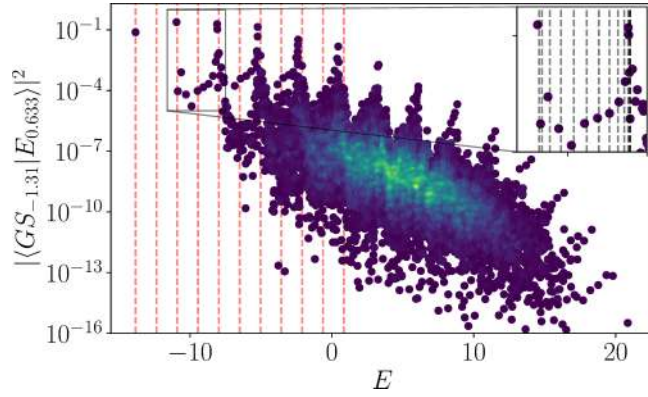
FIG. 6. Overlap between the ground state at the critical point $\mu_i = \mu_c = -1.31$ and the eigenstates of the PXP model with $\mu_f = 0.633$. The color indicates the density of datapoints. The red dashed lines indicate multiples of the energy of a $k = \pi$ excitation on top of the ground state. This matches well with the scarred towers in the relevant part of the spectrum. The inset shows the first set of excited states, with the grey dashed lines indicating the expected energy for noninteracting pairs of excitations with momenta k and $-k$. Due to the flatness of the band near $k = \pi$ and $k = 0$, the lines are denser near the scarred states, leading to sharper towers and better revivals (see further analysis of the magnon dispersion in Fig. 7 below). Data is obtained by exact diagonalization for system size $N = 28$ with PBCs.

of the ground state. For $\mu_f = 0$, this has been shown to give a good approximation of scarred states even at relatively high energies when using magnons with momentum $k = \pi$ [79]. Similarly, we find this to be true in our case near $\mu_f = 0.6$, where much of the low-energy spectrum can be approximately reconstructed from pairs of noninteracting magnons with momenta k and $-k$, see the dashed lines in Fig. 6 and inset. Note that the PXP model is gapped for $\mu_f = 0.633$, hence the ground state and the first tower in Fig. 6 are separated by a finite energy that is independent of N in sufficiently large systems.

A detailed analysis of the magnon dispersion as a function of chemical potential is presented in Fig. 7. The dispersion relation for several values of μ_f is shown in Fig. 7(a). For $\mu_f < 0.6$, the single-magnon band merges with the two-magnon continuum, causing the downward slope near $k = 0$. Near $\mu_f = 0.6$, the band becomes remarkably flat for small k, coinciding with the one-magnon and two-magnon bands barely touching. At that point, the energies of the first excited states at $k = 0$ are well approximated by twice the energies of the single-magnon states, indicating that they correspond to a pair of two noninteracting magnons with momentum k and $-k$. This is illustrated in Fig. 7(b) and the inset of Fig. 7(a). This simple picture of noninteracting excitations allows us to predict the energies of the low-energy excited states based solely on the dispersion relation of the single-magnon states. In particular, the flatness of the band near $k = 0$ and $k = \pi$ means that the eigenstates near the scarred ones have approximately the same energy. This implies that tower of states will be sharper, and that the effective energy spacing, which determines the dynamics at intermediate times, is the spacing between the towers. In turn, the fact that magnons are very weakly inter-
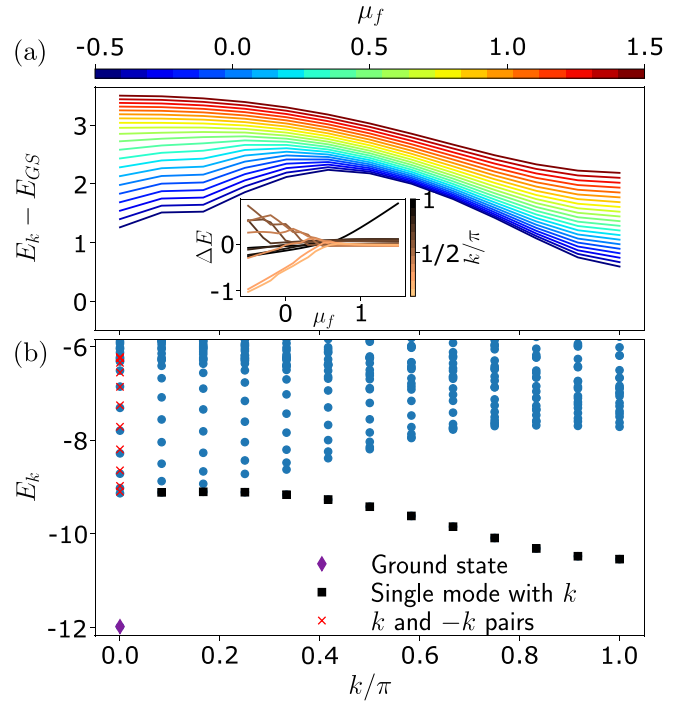

FIG. 7. (a) Dispersion relation of the low-lying excitations of the PXP model for several values of the chemical potential μ_f, shown in different colors. When $\mu_f \approx 0.6$, the dispersion becomes visibly flat near both $k = 0$ and $k = \pi$ momenta. Inset shows the difference between the actual energies of the first excited states in the spectrum and their approximation by a pair of two noninteracting excitations. For all momenta k, the best agreement between the approximation and exact energy is attained at $\mu_f \approx 0.6$. (b) Low-energy spectrum of the PXP model with $\mu_f = 0.6$ – the value with the best revivals when quenching from the critical ground state. The ground state and first excited states are indicated, along with energies corresponding to a noninteracting pair of excitations with momenta k and $-k$. In this instance, we see the approximate excitations and exact energy levels lie close to each other. Data is obtained by exact diagonalization for system size $N = 24$ with PBCs.

acting means that the spacing between these towers will be approximately equal.

In summary, we showed that QMBS in the critical initial state can persist due to (i) the postquench Hamiltonian $H_{\text{PXP}}(\mu_f)$ having a gapped spectrum with a sufficiently flat band of the low-lying magnon excitations and (ii) the magnons are weakly interacting and their multiplets give rise to regularly spaced QMBS-like towers in the spectrum. While this scenario is reminiscent of Ref. [80], where quantum revivals in some nonintegrable models were related to the low-lying quasiparticle states, in our case the chemical potential needs to be finely tuned to a value $\mu_f \approx 0.6$ to meet the conditions (i) and (ii). Indeed, as seen in Fig. 1, varying μ_f around this value leads to a sharp decay of QMBS revivals. In contrast to the PXP model with $\mu_i = 0$ and the $|\mathbb{Z}_2\rangle$ initial state, the QMBS eigenstates in the $\mu_i = \mu_c$ case are clearly skewed towards the low-energy part of the spectrum; however, this allows the QMBS revivals to persist in large systems, despite the highly entangled initial state.

VI. EXPERIMENTAL PROTOCOL

Finally, in this section we address the experimental observation of the phase diagram in Fig. 1. The key step is the preparation of the PXP ground state in Eq. (1). The protocol below is directly applicable to Rydberg atom arrays [22]; however, it can also be adapted to ultracold bosons in a tilted optical lattice, where the chemical potential μ maps to the energy mismatch between the Hubbard interaction and electric field, which induces a tilt potential [24].

Ground-state preparation is accomplished via a "ramping" procedure utilized in related experiments [21,45,47,81,82]. This assumes fine control of the chemical potential that is varied in time, $\mu = \mu(t)$. Taking the chemical potential very large, $\mu \to \pm\infty$, one can prepare $|0\rangle$ and $|\mathbb{Z}_2\rangle$ states. Starting in one of these states, one can then ramp to a desired ground state in the interior of our phase diagram in Fig. 1 by evolving with a time-dependent PXP Hamiltonian $H_{PXP}(\mu(t))$, where $\mu(t)$ is appropriately parameterized for adiabatic evolution, as specified below. The adiabaticity implies that the ramping will not be able to prepare the critical ground state after a finite time in the thermodynamic limit. Therefore, with finite resources, we can only hope to approach the critical point from different gapped regions of the phase diagram. We start the ramp either in $|\mathbb{Z}_2\rangle$ or $|0\rangle$, depending on whether we are in a ordered ($\mu < \mu_c$) or disordered ($\mu > \mu_c$) phase, respectively.

Specifically, we make use of the following ramp:

$$\mu(t) = \frac{A}{(t-B)^2} - \frac{A}{(t-C)^2} + \mu_c, \qquad (17)$$

where A, B, and C are tunable parameters. One particularly successful choice was found to be $A = \mp 40$, when ramping from $|0\rangle$ or $|\mathbb{Z}_2\rangle$, respectively, $B = 30$, and $C = -0.1$. An example of this ramping curve is plotted in the inset of Fig. 8(b). We include μ_c due to the need for a much slower ramp as the gap between the ground state and first excited state closes in the vicinity of the EPT.

After specifying the ramp and the initial state, we evolve by the PXP Hamiltonian in the presence of chemical potential, Eq. (17), until some time t. The evolution time is determined by numerically minimizing $1 - |\langle\psi(t)|\,GS(\mu_{target})\rangle|^2$, where $|GS(\mu_{target})\rangle$ is the state we are trying to prepare. Figure 8(a) illustrates the success of the ramping procedure. For system sizes ranging from $N = 6$ to $N = 14$, we have ramped to prepare the ground states from $\mu = \pm 6$, in increments $\delta\mu = 0.5$, towards the critical point, $\mu_c = -1.31$. Figure 8(b) shows the time that the ramp took for each ground state. We see the ramp time is insensitive to system size in gapped regions of the phase diagram, while it sharply increases near μ_c and exhibits strong fluctuations with N. For fixed ramp parameters, we expect it will take an infinite amount of time to prepare the critical ground state in the $N \to \infty$ limit.

Finally, to verify our preparation scheme in large systems, we repeated the preparation of the detuned PXP ground states for system sizes of $N = 51, 75$, and 101 using MPS simulations with bond dimension $\chi = 128$ and the ramping protocol in Eq. (17), with the same A, B, C parameters. The inset of Fig. 8(a) demonstrates that the ramping continues to successfully reproduce the desired ground state with high
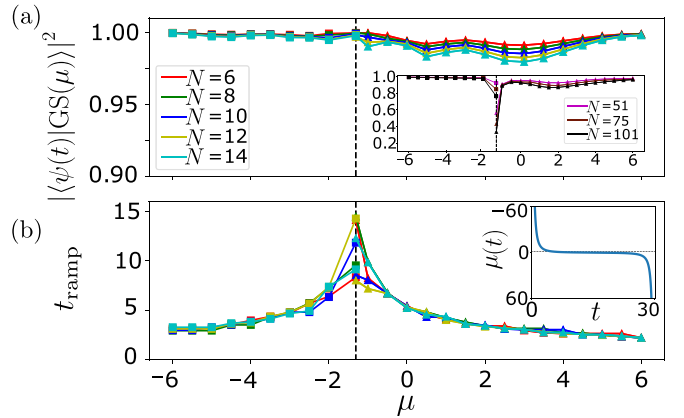

FIG. 8. (a) The success of preparing the PXP ground state at chemical potential μ by ramping the chemical potential according to Eq. (17). The total ramp time is varied for each point to maximize the overlap, which is plotted on the y axis. For $\mu > \mu_c$, the initial state is $|0\rangle$ (square symbols), while for $\mu < \mu_c$ we start the ramp in the $|\mathbb{Z}_2\rangle$ state (triangles). Separate optimizations were performed for different system sizes N, shown in the same plot. Black dashed line (in all the panels) denotes the critical point μ_c. Inset: Using the optimal parameters and average ramping time determined in smaller sizes in the main panel, we prepare the ground states for the same values of μ in much larger system sizes $N = 51, 75, 101$. The preparation in this case was done using the MPS method with time step $\delta t = 0.025$ and maximum bond dimension $\chi = 128$. While in the gapped phases the preparation remains successful, there is a visible drop near the critical point. (b) Total ramp time t_{ramp} returned by the optimizations in the main panel (a). Inset shows the ramping curve $\mu(t)$ in Eq. (17). We observe an increase of the ramp time and strong finite-size fluctuations at the critical point. The data in the main panels (a) and (b) was computed using exact diagonalization in $k = 0$ momentum and $p = +1$ inversion symmetry sector with PBCs.

fidelity, with the exception of the critical point where we see a clear drop in overlap with the target state. This suggests the ramping procedure is a viable method for generating desired ground states even in large systems. With this in hand, along with the already existing capabilities to quench with a detuned PXP Hamiltonian and conduct measurements of local observables [21,22], all the tools are, in principle, available to reconstruct the dynamical phase diagram in Fig. 1. In particular, local fidelity measurements [24] can be used to approximate the numerically computed global fidelity in Fig. 1(a). This would allow to experimentally verify the persistence of QMBS across the phase diagram and its robustness near the critical point.

VII. CONCLUSIONS AND DISCUSSION

We have mapped out the dynamical phase diagram of the PXP model, based on ergodicity breaking in its dynamics following the global quench of the chemical potential. We have demonstrated the existence of extended regions, which harbor QMBS phenomena, either associated with the previously studied initial conditions, such as $|\mathbb{Z}_2\rangle$ and $|0\rangle$, or with new entangled states such as $|\bar{0}(\mu)\rangle$. The mechanisms giving rise to these QMBS phenomena, in particular the

underlying periodic trajectories, were identified within the TDVP framework. We have analyzed in detail the robustness of QMBS when the system is tuned to the EPT point, arguing that this is not an obstacle for QMBS, provided that the postquench Hamiltonian is tuned in such a way that the low-lying quasiparticle excitations are weakly interacting and possess a flat energy-momentum dispersion. This enables different QMBS regions in the dynamical phase diagram to connect smoothly, bridging across the EPT. Finally, we have also outlined an adiabatic preparation scheme that allows to map out the same phase diagram in experiments on Rydberg atoms and ultracold bosons in tilted optical lattices, both of which have recently realized the PXP model in the presence of a tunable chemical potential. In light of these experiments, our discussion of the phase diagram above was restricted to finite times; however, in Appendix F we discuss the corresponding phase diagram for time $t \to \infty$. We note that the existence of a continuous family of QMBS states, tunable by the chemical potential, is of independent interest in quantum-enhanced metrology, for which QMBS states were shown to be advantageous [83–85].

One motivation behind this work is the open problem of identifying all initial conditions associated with QMBS. For the pure PXP model it had originally appeared that only the $|\mathbb{Z}_2\rangle$ and $|\mathbb{Z}_3\rangle = |100100...100\rangle$ states are special in this regard [21]; however, more recent explorations of the chemical potential [24] have revealed that the latter can also stabilize QMBS from a different initial state $|0\rangle$. In this paper, we have shown that these two product states share the semiclassical description and belong to a larger family, which also includes some other weakly-entangled states such as $|\bar{0}(\mu)\rangle$ state. While we have numerically related these initial states and their quench dynamics, it is not obvious how to relate them at the level of a spectrum-generating su(2) algebra, which has provided an elegant description of revivals from the $|\mathbb{Z}_2\rangle$ state in the pure PXP model [29]. Moreover, our investigation focused on the dynamics with periodicity $K = 1$ and it would be interesting to extend it to $K \geqslant 2$. For example, it is known that $|\mathbb{Z}_3\rangle = |100100100 \ldots 100\rangle$ state also exhibits revivals in the pure PXP model model [37]. However, this state necessitates a TDVP description with $K = 3$ unit cell, which already gives rise to an intricate phase space at the semiclassical level [67]. It would be interesting to understand the dynamical phase diagram associated with such states that have larger unit cells, either in the PXP model or analogous models for larger Rydberg blockade radii.

Finally, our results for the initial state at the critical point suggest that QMBS dynamics is not necessarily associated with preparing the system in a product state or even an area-law entangled state, but in principle allows for highly-entangled initial states. In this case, QMBS dynamics is more strongly temperature dependent, as the initial state has dominant support on the relatively low-lying energy eigenstates of the postquench Hamiltonian. The key ingredient for making this work was to suppress the interaction between quasiparticles and flatten their energy dispersion. It would be interesting to understand how to engineer such conditions in other models and thereby realize similar dynamics from highly-entangled initial states.

APPENDIX A: OTHER REGIONS OF THE PHASE DIAGRAM

Several regions of the phase diagram in Fig. 1 exhibit fidelity revivals that have a simple origin that can be understood without invoking QMBS. Here we explain in more detail these regions labeled (4), (5), (6), and (7). It is useful to consider the inverse participation ratio (IPR), one of the traditional measures of ergodicity of the eigenfunctions introduced in the context of Anderson localization [86]. The IPR is defined as

$$\mathrm{IPR} = \frac{1}{\sum_E |\langle E|\psi\rangle|^4}, \tag{A1}$$

and it intuitively tells us about how many basis states $|E\rangle$ the state $|\psi\rangle$ has support on. For example, if $|\psi\rangle$ is a basis state, its IPR will be 1, while if $|\psi\rangle$ is homogeneously spread over the entire Hilbert space, the IPR will be equal to the Hilbert space dimension. Note that IPR is a basis-dependent quantity and, in our case, we have a natural choice of eigenstates $|E\rangle$ of $H_{\mathrm{PXP}}(\mu_{\mathrm{f}})$ as the basis states.

The logarithm of IPR for μ_{i} ground states with respect to μ_{f} eigenstates is plotted in Fig. 9. This allows us to further distinguish between different regions. For conventional $|\mathbb{Z}_2\rangle$ scarring we expect the IPR to be on the order of system size N, since the $|\mathbb{Z}_2\rangle$ state has high overlap with a band of $N + 1$ scarred eigenstates of $H_{\mathrm{PXP}}(0)$ but low overlap with the rest. This is evidenced in region (1) of Fig. 9. On the other hand, the band of scarred eigenstates associated with $|0\rangle$ state in the detuned PXP model is "tilted" to one edge of the spectrum, so we expect the IPR to be smaller. In general, the regions with high IPR are expected to be ergodic, while the least interesting regimes are characterized by very low IPR, such as around the $\mu_{\mathrm{i}} = \mu_{\mathrm{f}}$ diagonal and in regions (5) and (6). The IPR is not as low in parts of regions (4) and (7) visible in this figure, but it decreases with increasing $|\mu_{\mathrm{i}}|$ and $|\mu_{\mathrm{f}}|$ as the ground state of $H_{\mathrm{PXP}}(\mu_{\mathrm{i}})$ approaches an eigenstate of $H_{\mathrm{PXP}}(\mu_{\mathrm{f}})$.
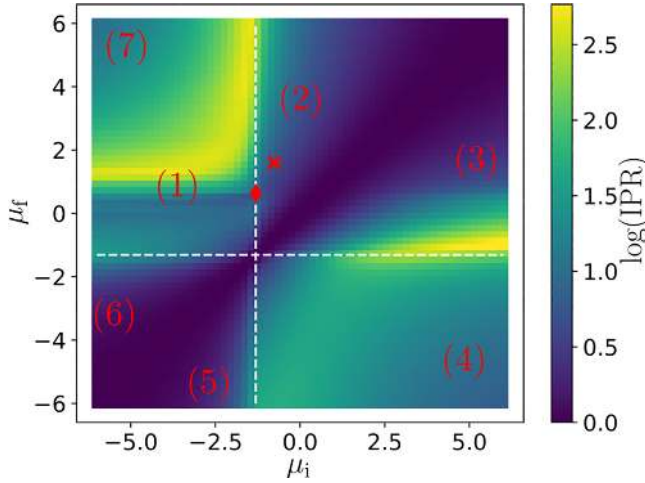
FIG. 9. Logarithm (base 10) of the IPR of the ground state of $H_{PXP}(\mu_i)$ with respect to the eigenstates of $H_{PXP}(\mu_f)$. All the labels have the same meaning as in Fig. 1. Data is obtained using exact diagonalization in the sector with $k = 0$ momentum and $p = +1$ inversion symmetry for size $N = 26$ with PBCs.

Large $|\mu_f|$ leads to the number of excitations in the system becoming effectively conserved, splitting the Hamiltonian into several sectors with an energy difference proportional to $|\mu_f|$. The dynamics in these sectors also becomes more regular, and even integrable at $|\mu_f| \to \infty$ [35]. Additionally, initial states with a number of excitations close to the minimum (maximum) effectively have overlap with very few eigenstates in the low (high) energy spectrum, leading to oscillations. For example, region (4) [i.e., $\mu_i > 0$, $-\mu_f \gg 1$] roughly corresponds to the polarized state in the strongly detuned regime, since the initial ground state has significant overlap with $|0\rangle$ for $\mu_i > 0$. In the $\mu_i \to \infty$ limit, it is expected to become the exact mirror image of region (3), given that the polarized state has the same dynamics for $\pm \mu_f$ (see Appendix C). Similarly, region (7) [$\mu_i < 0$, $\mu_f \gg 1$] has a simple explanation in terms of $|\mathbb{Z}^+\rangle$ state in the strongly detuned regime.

The origin of revivals in region (5) [$\mu_f < \mu_i < -1.3$] is perhaps not immediately obvious, since the initial state in that case does not have high overlap with one of the previously studied states such as $|0\rangle$ or $|\mathbb{Z}^+\rangle$. We now briefly investigate this region. The fidelity and the average number of excitations after quenching from $\mu_i = -2.5$ to $\mu_f = -6$ can be seen in Figs. 10(a) and 10(b). The quenched state maintains high overlap with the $|\mathbb{Z}^+\rangle$ state, with peaks in the middle between the fidelity revivals, see Fig. 10(a). This situation is reminiscent of the $|\bar{0}\rangle$ state in region (2), which periodically evolves to $|0\rangle$ and back. Although it oscillates, the overlap with $|\mathbb{Z}^+\rangle$ never drops to zero. In contrast, the overlap with $|0\rangle$ is constantly zero. In Fig. 10(b) we also see that the average occupation is remarkably stable, fluctuating only slightly around ≈ 0.47. As explained above for regions (4) and (7), such behavior arises due to the fact that in the large-μ limit states with near-extremal number of excitations only have support on a small number of eigenstates at the edge of the spectrum. This can be seen in Fig. 10(c), which shows the overlap of the initial state and the eigenstates. The splitting of eigenstates into sectors, effective conservation of
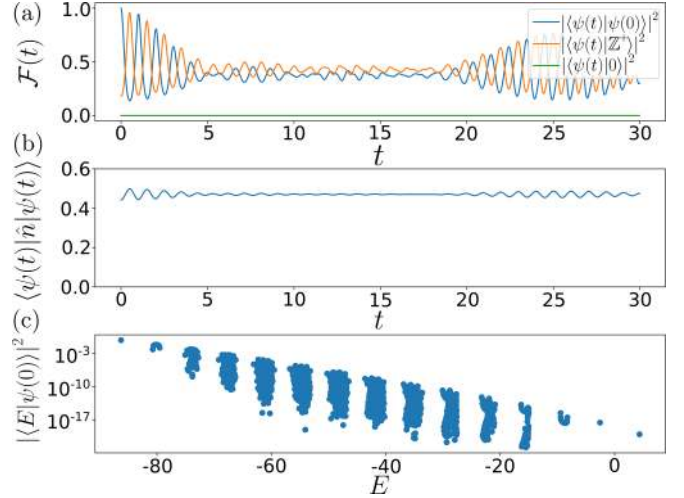

FIG. 10. Dynamics and eigenstate properties of the PXP model quenched from $\mu_i = -2.5$ to $\mu_f = -6$, corresponding to region (5) of the phase diagram in Fig. 1. (a) Fidelity of the initial state $|\psi(0)\rangle$, i.e., the ground state of $H_{PXP}(-2.5)$, as well as the overlap with both the polarized state $|0\rangle$, and superposition state $|\mathbb{Z}^+\rangle$. (b) The average number of excitations remains nearly constant in time. (c) The overlap of the initial state with eigenstates of $H_{PXP}(-6)$ reveals that the latter split into sectors based on the value of $\hat{n}$, leading to $|\psi(0)\rangle$ only having support on the low-energy spectrum. Data obtained by exact diagonalization for $N = 28$ with PBCs.

$\hat{n}$ and high overlap with the ground state are all apparent. Further evidence comes from the inverse participation ratio (IPR), which we find to be very low in this region, indicating overlap with only a small number of eigenstates, as will be shown below. Finally, region (6) [$\mu_i < \mu_f < -1.3$] has a similar phenomenology to its mirroring region (5).

In summary, we have argued that regions (4), (7), and part of (5) correspond to regimes where μ_f has a large absolute value, leading to a simple oscillatory dynamics due to Hilbert space becoming disconnected, while in regions (5) and (6), $\mu_f \approx \mu_i$ causes the initial state to be close to an eigenstate of the postquench Hamiltonian.

APPENDIX B: DERIVATION OF TDVP EQUATIONS OF MOTION AND QUANTUM LEAKAGE

In this section we first derive the TDVP equations of motion and then compute the instantaneous leakage rate. These derivations follow Appendices A and C of Ref. [67].

1. Equations of motion

The TDVP equations of motion can be derived as the saddle point equations for the following Lagrangian [69,71]:

$$\mathcal{L} = \frac{i}{2}(\langle \psi_{MPS} | \dot{\psi}_{MPS} \rangle - \langle \dot{\psi}_{MPS} | \psi_{MPS} \rangle) - \langle \psi_{MPS} | H | \psi_{MPS} \rangle, \tag{B1}$$

where it will be convenient to split our Hamiltonian into two terms, $H = H_{PXP} + H_\mu$. Unlike Ref. [67], we restrict to $K = 1$, which greatly simplifies the calculation. Throughout this section we will consider mixed MPS transfer matrices,

denoted by

$$T_C^B = \sum_\sigma \bar{B}^\sigma \otimes C^\sigma, \tag{B2}$$

where B and C are arbitrary MPS tensors. The MPS transfer matrix for the PXP ansatz chosen in the main text takes the form

$$T_A^A = T = \begin{pmatrix} \cos^2\theta & 0 & 0 & 1 \\ \cos\theta\sin\theta & 0 & 0 & 0 \\ \cos\theta\sin\theta & 0 & 0 & 0 \\ \sin^2\theta & 0 & 0 & 0 \end{pmatrix}. \tag{B3}$$

The dominant left and right eigenvalues of the transfer matrix are equal to 1, and the corresponding eigenvectors are

$$|R) = \begin{pmatrix} 1 \\ \cos\theta\sin\theta \\ \cos\theta\sin\theta \\ \sin^2\theta \end{pmatrix}, \quad (L| = (1 \quad 0 \quad 0 \quad 1), \tag{B4}$$

which obey $(L|R) = 1 + \sin^2\theta$. We also introduce the following shorthand for a three-site local Hamiltonian term contracted with MPS tensors on every site:

$$\mathcal{H} = \mathcal{H}_{A,A,A}^{A,A,A} = \sum_{\sigma_i} \bar{A}^{\sigma_1}\bar{A}^{\sigma_2}\bar{A}^{\sigma_3} h_{\sigma_4,\sigma_5,\sigma_6}^{\sigma_1,\sigma_2,\sigma_3} A^{\sigma_4}A^{\sigma_5}A^{\sigma_6}. \tag{B5}$$

Using the mixed transfer matrix expression, it is straightforward to compute

$$f = -iN \frac{(L|T_A^{\partial_\phi A}|R)}{(L|R)} = N \frac{2\sin^2\theta}{\cos 2\theta - 3}, \tag{B6}$$

$$\text{with } T_A^{\partial_\phi A} = \begin{pmatrix} 0 & 0 & 0 & -i \\ 0 & 0 & 0 & 0 \\ 0 & 0 & 0 & 0 \\ 0 & 0 & 0 & 0 \end{pmatrix}. \tag{B7}$$

Next we compute the expectation value of the Hamiltonian. We find the two terms are

$$\langle\psi|H_{\text{PXP}}|\psi\rangle = N \frac{(L|H_{\text{PXP}}|R)}{(L|R)} = N \frac{2\cos^2\theta\sin\theta\sin\phi}{1 + \sin^2\theta}, \tag{B8}$$

and

$$\langle\psi|H_\mu|\psi\rangle = N \frac{(L|H_\mu|R)}{(L|R)} = N\mu \frac{\sin^2\theta}{1 + \sin^2\theta}. \tag{B9}$$

The total expectation value is given by $\langle\psi|H|\psi\rangle = \langle\psi|H_{\text{PXP}}|\psi\rangle + \langle\psi|H_\mu|\psi\rangle$, which yields the energy density, Eq. (15) in the main text.

To get the equations of motion for θ and ϕ, we need to compute

$$\eta = \partial_\theta f = -4N \frac{\sin 2\theta}{(\cos^2\theta - 3)^2}. \tag{B10}$$

From there the equations of motion are given by

$$\dot{\theta} = \frac{1}{\eta}\partial_\phi\langle\psi|H|\psi\rangle, \quad \dot{\phi} = -\frac{1}{\eta}\partial_\theta\langle\psi|H|\psi\rangle, \tag{B11}$$

which lead to Eqs. (12) and (13) in the main text.

2. Instantaneous leakage

The instantaneous leakage is given by

$$\begin{aligned}\Lambda^2(\theta) &= \||\dot{\psi}\rangle - iH|\psi\rangle\|^2 \\ &= \langle\psi|H^2|\psi\rangle_c - 2\dot{\theta}\,\text{Im}\,(\langle\partial_\theta\psi|H\,|\,\psi\rangle_c) \\ &\quad + (\dot{\theta})^2\,\text{Re}\,(\langle\partial_\theta\psi\,|\,\partial_\theta\psi\rangle_c) - 2\dot{\phi}\,\text{Im}(\langle\partial_\phi\psi|H\,|\,\psi\rangle_c) \\ &\quad + (\dot{\phi})^2\,\text{Re}(\langle\partial_\phi\psi\,|\,\partial_\phi\psi\rangle_c) + 2\dot{\phi}\dot{\theta}\,\text{Re}(\langle\partial_\phi\psi\,|\,\partial_\theta\psi\rangle_c). \end{aligned} \tag{B12}$$

Due to the gauge choice, the leakage depends on connected correlators defined as

$$\langle\partial_\theta\psi|\partial_\theta\psi\rangle_c = \langle\partial_\theta\psi|\partial_\theta\psi\rangle - \langle\partial_\theta\psi|\psi\rangle\langle\psi|\partial_\theta\psi\rangle.$$

In order to evaluate these connected correlators, we introduce the projector on the dominant subspace, $\mathcal{P} = |R)(L|/(L|R)$, and its complement $\mathcal{Q} = \mathbf{1} - \mathcal{P}$. We also introduce $\mathcal{T}$, which is obtained by re-summing the contribution of the nondominant subspace of T in $\sum_{q=0}^\infty T^q$ and is defined from $\mathcal{T}^{-1} = \mathcal{Q}(\mathbf{1} - \mathcal{Q}T\mathcal{Q})^{-1}\mathcal{Q}$.

Let us now evaluate the various terms involved in the instantaneous leakage. Taking each term one by one, we find that

$$\begin{aligned}\langle\partial_\theta\psi\,|\,\partial_\theta\psi\rangle_c &= \frac{N}{(L\,|\,R)}\big(L\,\big|\,T_{\partial_\theta A}^{\partial_\theta A} + T_{\partial_\theta A}^A\mathcal{T}^{-1}T_A^{\partial_\theta A} \\ &\quad + T_A^{\partial_\theta A}\mathcal{T}^{-1}T_{\partial_\theta A}^A - T_{\partial_\theta A}^A\mathcal{P}T_A^{\partial_\theta A}\,\big|\,R\big), \end{aligned} \tag{B13}$$

which after a straightforward calculation evaluates to

$$\langle\partial_\theta\psi|\partial_\theta\psi\rangle_c = \frac{N}{1 + \sin^2\theta}. \tag{B14}$$

Turning our attention to the term $\langle\partial_\theta\psi|H|\psi\rangle_c$, we find that this evaluates to

$$\frac{N}{(L\,|\,R)}\big(L\big|\mathcal{H}_{\partial_\theta A} + \mathcal{H}\mathcal{T}^{-1}T_A^A + T_{\partial_\theta A}^A\mathcal{T}^{-1}\mathcal{H} - 3\mathcal{H}\mathcal{P}T_{\partial_\theta A}^A\big|R\big). \tag{B15}$$

This yields

$$\langle\partial_\theta\psi|H|\psi\rangle_c = -iN\cos\theta\cos\phi + N \frac{\cos\theta\sin\theta}{(1 + \sin^2\theta)^2}\dot{\phi}. \tag{B16}$$

As we are only interested in the imaginary part, we can discard the second term and are left with

$$\text{Im}\,(\langle\partial_\theta\psi|H|\psi\rangle_c) = -N\cos\theta\cos\phi = \frac{N}{1 + \sin^2\theta}\dot{\theta}. \tag{B17}$$

The expressions containing the derivatives with respect to ϕ can be calculated similarly. Starting with $\langle\partial_\phi\psi|\partial_\phi\psi\rangle_c$ which we compute as

$$\begin{aligned}\frac{N}{(L\,|\,R)}\big(L\big|T_{\partial_\phi A}^{\partial_\phi A} + T_{\partial_\phi A}^A\mathcal{T}^{-1}T_A^{\partial_\phi A} \\ + T_A^{\partial_\phi A}\mathcal{T}^{-1}T_{\partial_\phi A}^A - T_{\partial_\phi A}^A\mathcal{P}T_A^{\partial_\phi A}\big|R\big). \end{aligned} \tag{B18}$$

Evaluating this term, we find

$$\langle\partial_\phi\psi|\partial_\phi\psi\rangle_c = N \frac{\cos^2\theta\sin^2\theta}{(1 + \sin^2\theta)^3}. \tag{B19}$$

The next term to compute is the cross term

$$\langle \partial_\phi \psi | \partial_\theta \psi \rangle_c = \frac{N}{(L \mid R)} \left(L \big| T_{\partial_\theta A}^{\partial_\phi A} + T_{\partial_\theta A}^A \mathcal{T}^{-1} T_A^{\partial_\phi A} \right.$$
$$\left. + T^{\partial_\phi A} \mathcal{T}^{-1} T_{\partial_\theta A} - T_{\partial_\theta A} \mathcal{P} T^{\partial_\phi A} \big| R \right). \quad \text{(B20)}$$

The result after evaluating Eq. (B20) is

$$\langle \partial_\phi \psi | \partial_\theta \psi \rangle_c = -iN \frac{\cos\theta \sin\theta}{(1 + \sin^2\theta)^2}; \quad \text{(B21)}$$

however, because its real part is identically zero, we get no contribution from this term. We now compute $\langle \partial_\phi \psi | H | \psi \rangle_c$ as

$$\langle \partial_\phi \psi | H | \psi \rangle_c = \frac{N}{(L \mid R)} \left(L \big| \mathcal{H}_{\partial_\phi A} + \mathcal{H} \mathcal{T}^{-1} T_{A \partial_\phi A}^A \right.$$
$$\left. + T_{\partial_\phi A}^A \mathcal{T}^{-1} \mathcal{H} - 3 \mathcal{H} \mathcal{P} T_{\partial_\phi A} \big| R \right). \quad \text{(B22)}$$

We find this can be expressed as

$$\langle \partial_\phi \psi | H | \psi \rangle_c = N \cos\theta \cos\phi + iN \frac{\cos^2\theta \sin^2\theta}{(1 + \sin^2\theta)^3} \dot\phi. \quad \text{(B23)}$$

We now move onto the terms involving the square of the Hamiltonian, H^2. The connected correlator in this case is

$$\langle \psi | H^2 | \psi \rangle_c = N \frac{(L | \mathcal{H}^{(2)} + 2\mathcal{H} \mathcal{T}^{-1} \mathcal{H} - 5 \mathcal{H} \mathcal{P} \mathcal{H} | R)}{(L \mid R)}, \quad \text{(B24)}$$

where $\mathcal{H}^{(2)}$ is the product of two overlapping local Hamiltonian terms. As the local Hamiltonian spans three sites, the two terms will both act upon one, two, or three shared sites. Evaluating this expression, we obtain

$$\langle \psi | H^2 | \psi \rangle_c = \frac{N \sin^6\theta}{1 + \sin^2\theta} + \frac{N \cos^2\theta \sin^2\theta (\dot\phi)^2}{(1 + \sin^2\theta)^3}$$
$$+ \frac{N(\dot\theta)^2}{1 + \sin^2\theta}. \quad \text{(B25)}$$

Substituting each of these into the equation for the leakage, we finally arrive at

$$\Lambda^2 = N \frac{\sin^6\theta}{1 + \sin^2\theta}.$$

Rescaling this by the system size yields the intensive expression for the leakage γ^2, Eq. (14), quoted in the main text.

APPENDIX C: RELATION BETWEEN μ AND $-\mu$

It is interesting to note that for μ and $-\mu$ the eigenstates are simply related by the application of the operator $\Pi = \prod_{j=1}^N Z_j$, with $Z = Q - P$. The same operator maps a state with energy E to $-E$. This can be easily seen by considering an eigenstate $|E\rangle$ of $H_{\text{PXP}}(\mu)$ with energy E. First let us consider the commutation relation between H_{PXP} and Π. As Z commutes with P and Q but anticommutes with X, it means that

$$\Pi H_{\text{PXP}}(\mu) = -H_{\text{PXP}}(-\mu)\Pi. \quad \text{(C1)}$$

As a consequence

$$H_{\text{PXP}}(-\mu)(\Pi |E\rangle) = -\Pi H_{\text{PXP}}(\mu) |E\rangle = -E(\Pi |E\rangle), \quad \text{(C2)}$$

showing that $\Pi |E\rangle$ is an eigenstate of $H_{\text{PXP}}(-\mu)$ with energy $-E$. This means that the spectral properties are the same for

$\pm\mu$ and that the ceiling state of $H_{\text{PXP}}(\mu)$ becomes symmetry-breaking for $\mu > 1.31$.

Similarly, it is important to further note the relation between μ and $-\mu$ with respect to the TDVP equations of motion, Eqs. (12) and (13). In general, flipping the sign of μ may not result in identical dynamics; however, this is not the case when considering the dynamics of the polarized state. As $|0\rangle$ has TDVP angles $(0,0)$, at this point $\dot\phi = \mu$. On the other hand, $\dot\theta$ has no μ dependence and so is unaffected by the a sign flip and the only dependence on ϕ comes from the $\cos(\phi)$ term, which has the property $\cos(\phi) = \cos(-\phi)$. Because of this, a sign flip of μ does not affect the dynamics of θ and simply flips Eq. (13). This means that the dynamics of $|0\rangle$ are symmetric under the sign flip and the shrinking of the orbit in Fig. 2 occurs for both $\pm\mu$.

APPENDIX D: PREPARATION OF STATES IN THE TDVP MANIFOLD

Here we demonstrate that the states belonging to the TDVP manifold with $K = 1, 2$ unit cell can be represented as ground states of the PXP model with a suitably generalized chemical potential term. To show this correspondence, we numerically optimize the overlap $|\langle \psi_{\text{MPS}}(\{\mathbf{x}\}) | \Psi(\mathbf{w}) \rangle|^2$, where $|\Psi(\mathbf{w})\rangle$ is the ground state of the PXP model with a K-site periodic density modulation,

$$H(\mathbf{w}) = \sum_{j=0}^{N-1} P_{j-1} X_j P_{j+1} + \sum_{j=0}^{N-1} w_j Q_j, \quad \text{(D1)}$$

where $\mathbf{w} = (w_1, w_2, \dots, w_K)$ is a generalization of the chemical potential term that is periodic (with period K) but takes different values for different atoms within the unit cell. The Hamiltonian $H(\mathbf{w})$ reduces to the PXP Hamiltonian with uniform chemical potential in Eq. (1) for $K = 1$.

Furthermore, in order to prepare the states in larger TDVP manifolds with unit cells $K \geqslant 2$, we found it necessary to act on the ground state of Eq. (D1) with a unit-cell modulated phase pulse,

$$\Theta(\boldsymbol{\gamma}) = \prod_{j=0}^{N/K-1} e^{-i\gamma_K Z_{Kj+(K-1)}} \cdots e^{-i\gamma_2 Z_{Kj+1}} e^{-i\gamma_1 Z_{Kj}}, \quad \text{(D2)}$$

where Z_i denotes the usual Pauli-Z matrix on site i and $\gamma_1, \dots, \gamma_K$ are variational parameters in addition to $\mathbf{w}$.

Our extensive numerical sampling in system sizes $N \leqslant 18$ confirms that the ansatz in Eqs. (D1) and (D2) allows for an accurate approximation of states in the TDVP manifold after optimizing for $(\mathbf{w}, \boldsymbol{\gamma})$. As this is performed at relatively small system sizes, here we verify that these results can be extended to larger systems. As a test case, we choose a particularly interesting TDVP trajectory, which starts at $(\theta_1, \theta_2, \phi_1, \phi_2) = (1.25\pi, 2.985, 0.166, 0.188)$. This trajectory was derived in Ref. [67] within a $K = 2$ TDVP ansatz and it belongs to a regular region of the manifold, giving rise to fidelity oscillations in the full quantum dynamics. We choose this trajectory to show that the ansatz can capture trajectories of interest in larger manifolds. We optimize for 30 states evenly spaced along this TDVP trajectory between time $t = 0$ and $t = 6$ in system sizes ranging from $N = 6$ to $N = 18$. The optimization
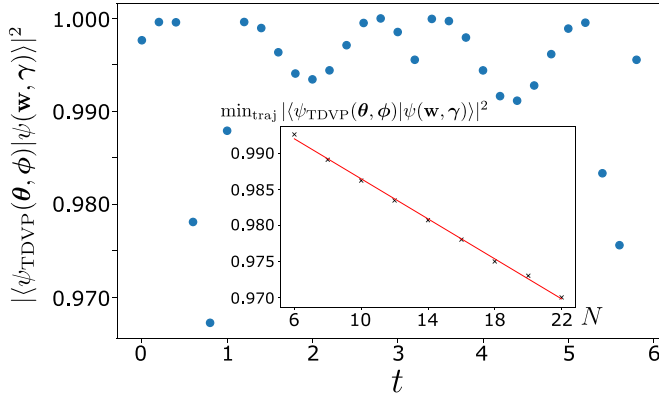
FIG. 11. Preparing the states along a particular $K = 2$ TDVP trajectory (defined in the text) using the ansatz in Eqs. (D1) and (D2). A set of states on the trajectory up to time $t = 6$ are variationally approximated in system sizes $N = 6 - 18$, finding the optimal parameters $\mathbf{w}$, $\boldsymbol{\gamma}$. The optimized parameters are then extrapolated to size $N = 22$ and the resulting overlap with the TDVP states is plotted, illustrating the success of the optimization (overlap is $>97\%$ along the entire trajectory). Inset shows the scaling of the overlap for the most poorly approximated point on the trajectory as a function of system size N. The overlap decays slowly and its extrapolation yields high overlap for this point even in large systems (e.g., overlap $\sim 90\%$ at size $N \sim 50$).

yields an overlap close to 1 for all the points on the trajectory and yields a set of optimal (w_1, w_2) and (γ_1, γ_2) for different N. Over the range of N, we found $\boldsymbol{\gamma}$ changes little so we do not re-optimize this in larger N but simply take the average from smaller sizes. On the other hand, we find $\mathbf{w}$ for different values of N fits well the empirical formula $w_j = ae^{bN+c} + d$, where a, b, c, and d are fitting parameters depending on w_1 and w_2. With this information, we can calculate (w_1, w_2), (γ_1, γ_2) for larger system sizes via extrapolation. The resulting overlap in system size $N = 22$ is shown in Fig. 11. We see that the ansatz successfully captures the entire trajectory (up to 97% overlap in this system size). In the inset of Fig. 11 the minimum overlap found along the trajectory is plotted as a function of system size, showing that it decays very slowly and allows to prepare the TDVP states on the trajectory with accuracy of 90% or better in large systems $N \sim 50$.

APPENDIX E: SINGLE MODE APPROXIMATION

In Sec. V we have discussed the revivals from the critical ground state based on the structure of the low energy spectrum at $\mu_{\mathrm{f}} = 0.633$. In this section we provide more details of this analysis, in particular on the range of μ that it can be applied to. Ref. [79] showed that for $\mu_{\mathrm{f}} = 0$, the scarred states throughout the spectrum could be well approximated as a collection of magnons with momentum π. Here, we show that this analysis also holds for $\mu_{\mathrm{f}} \approx 0.6$, especially in the low-energy part of the spectrum. In turn, the ground state at $\mu_{\mathrm{i}} = \mu_{\mathrm{c}} = -1.31$ can be understood as mainly being a superposition of these multimagnon states.

In Fig. 12 one can see the low-energy spectrum resolved by momentum for three different values of μ_{f}. The data for the overlap of the same eigenstates with the ground state at $\mu_{\mathrm{f}} =$
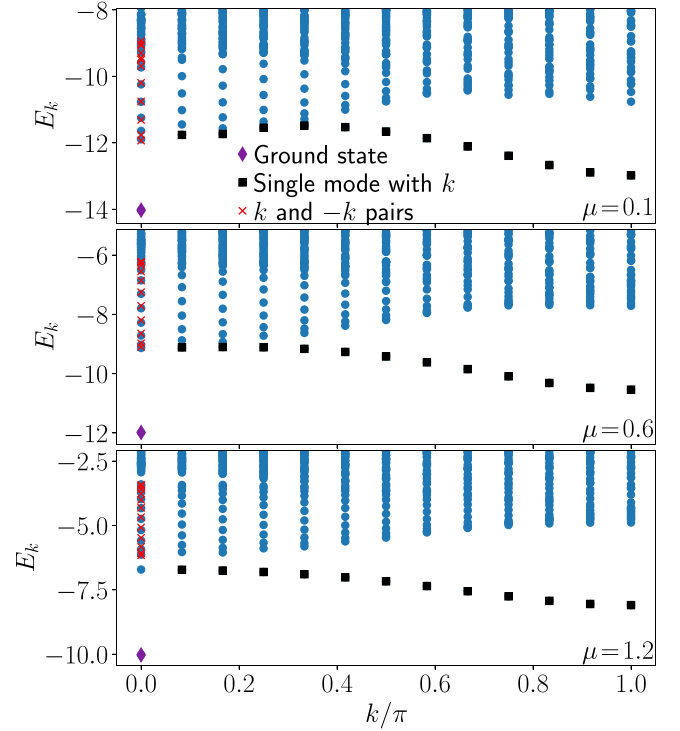

FIG. 12. Low-energy spectrum of the PXP model for three values of μ. The red crosses correspond to the energies of a noninteracting pair of excitations with momenta k and $-k$. For $\mu = 0.1$, the first band merges with the two-magnon continuum. For $\mu = 1.2$, the first excited state with $k = 0$ has an energy that differs from that of two noninteracting magnons. Data is for system size $N = 24$ with PBCs.

$\mu_{\mathrm{c}} = -1.31$ is also plotted in Fig. 13. Note that, as this ground state has $k = 0$, only the eigenstates with the same momentum value will have a nonzero overlap. For too small values of μ, the one-magnon states merge into the two-magnon continuum
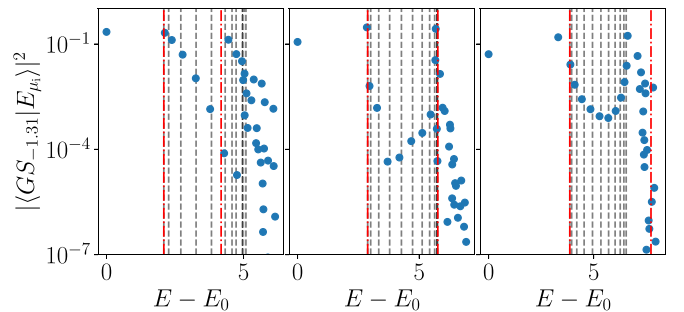
FIG. 13. Overlap between the ground state at $\mu_{\mathrm{i}} = \mu_{\mathrm{c}} = -1.31$ and the low-energy eigenstates of the PXP model with various values of μ for $N = 24$ and PBCs. The states are the same as in Fig. 12 with $k = 0$, and panels correspond to $\mu_{\mathrm{f}} = 0.1$, 0.6, and 1.2 respectively (from left to right). The red lines correspond to the expected energy of two and four magnons with momentum π on top of the ground state. The grey line correspond to the expected energy of two magnons with momentum k and $-k$ on top of the ground state. Due to the flatness of the band and the weak interactions between magnons, the towers of states are sharper around $\mu = 0.633$.

near $k = 0$, causing the band to bend downwards. As a consequence, the noninteracting magnon pairs approximation is less accurate for $k \neq \pi$, and the critical ground state has increased overlap with them. On top of this, the band being far from flat at the edges means that the towers of states are not sharp, i.e., states near the top of the towers have a non-negligible energy difference. As their energy separation from the ground state is roughly twice that of a single-magnon with momentum k, the flatter the band the more similar in energy the states will be.

For $\mu_f \approx 0.6$, the single-magnon band barely touches the two-magnon continuum. The magnon-pair approximation now holds well for all values of k. Consequently, one can see that the overlap of the critical ground state with two-magnon states built out of magnons with momentum $k \neq \pi$ is very low. Among these, the states with the highest overlap are the ones made from magnons with momentum close to 0 or π. As the band is flat near these points, they have approximately the same energy as the scarred states and so do not lead to dephasing until late times.

Finally, when μ_f becomes too large, the nature of the excitations changes and the π magnons no longer describe the elementary excitations in the system. Indeed, for $\mu_f \gg 1$, the ground state is simply the polarized state and the excitations are just a single flipped 1 on top of the background of 0. So the first excited state with $k = 0$ is simply a symmetric superposition of the state $|100 \cdots 0\rangle$ and its translations. As any kind of excitation with $k = \pi$ will need at least one 1 site, adding two of them that are noninteracting will never lead to the correct excited state at $k = 0$. This can already be seen for $\mu_f = 1.2$ in the bottom panel of Fig. 12, as the lowest red cross—corresponding to the expected energy of two noninteracting magnons—is far above the actual first excited state with $k = 0$. This again impacts the sharpness of the towers of states, especially the spacing between the first and second excited state, which grows with μ_f.

APPENDIX F: DYNAMICAL PHASE DIAGRAM IN THE INFINITE-TIME LIMIT

In the main text, we explored the dynamical phase diagram using two probes based on the dynamics at intermediate time scales: fidelity revivals and the deviation of average density of excitations from its thermal value. Here we directly address the long-time behavior of the system using the latter quantity. We study the average density of excitations evaluated in the diagonal ensemble,

$$\bar{n} = \lim_{T \to \infty} \frac{1}{T} \int_0^T \langle \psi(t)|n|\psi(t)\rangle dt = \sum_j |c_j|^2 n_{j,j}, \quad \text{(F1)}$$

where $c_j = \langle E_j||\psi(0)\rangle$ and $n_{j,k} = \langle E_j| n |E_k\rangle$. The initial state $|\psi(0)\rangle$ is the PXP ground state at some μ_i, while E_j, $|E_j\rangle$ are the eigenvalues and eigenstates of the quench Hamiltonian $H_{\text{PXP}}(\mu_f)$. In the second equality of Eq. (F1), we have assumed that the off-diagonal elements average out to zero in the infinite-T limit. This is true in the absence of spectral degeneracies, as integrating off-diagonal contributions over time corresponds to integrating e^{-irt} with $r \neq 0$ being essentially a random number. Thus, each contribution will give a finite number that will go to zero as it is multiplied by $1/T$
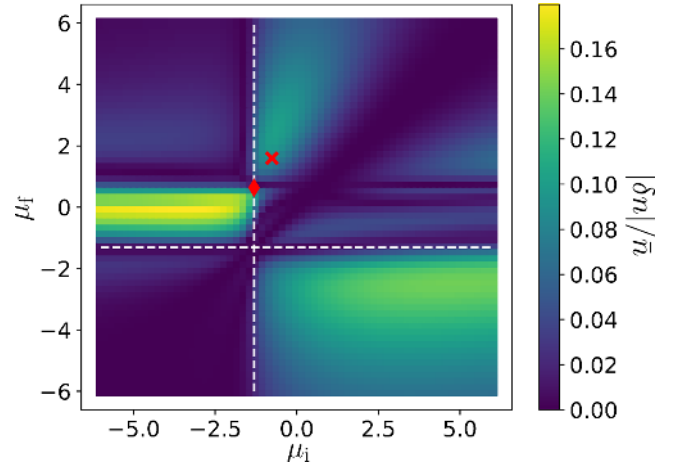
FIG. 14. The norm of the scaled difference of the number of excitations between the diagonal and canonical ensembles when quenching the initial ground state of $H_{\text{PXP}}(\mu_i)$ to $H_{\text{PXP}}(\mu_f)$. All the labels are the same as in Fig. 1. Data is obtained using exact diagonalization in the momentum $k = 0$ and $p = +1$ inversion symmetry sector for system size $N = 28$ with PBCs.

and the limit $T \to \infty$ is taken. The quench Hamiltonian is generally nondegenerate after resolving the momentum and inversion symmetries (our calculations are mostly performed in the sector with $k = 0$ and $p = +1$). An exception to this occurs at $\mu_f = 0$ where the spectrum contains an extensive number of "zero modes" [37,87]. In that case, the off-diagonal
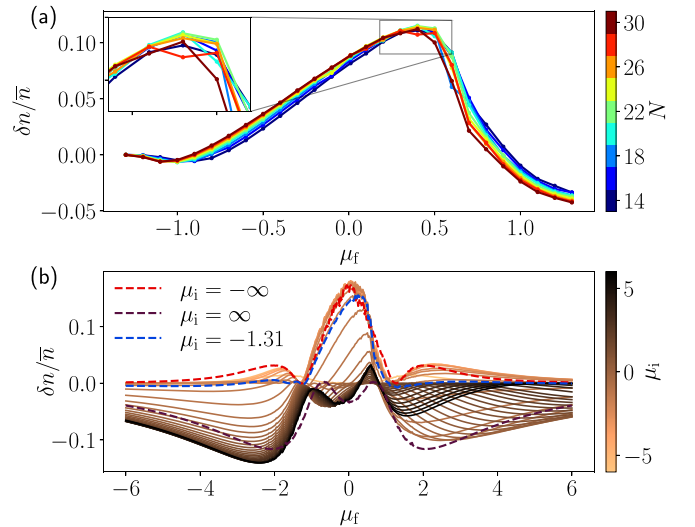
FIG. 15. Scaled difference of the expectation values between the diagonal and canonical ensembles. (a) For $\mu_i = \mu_c = -1.31$, there is a large difference around $\mu_f = 0.5$ that does not vary much with system size. Notably, we also see that to the left of that point the difference between the ensembles increases with system size. (b) Cross cuts through the phase diagram with a fixed value of μ_i indicated on the color bar. The middle peak corresponds to region (1), while the two negative peaks on the bottom right correspond to regions (2) and (3), from left to right respectively. Data is obtained by exact diagonalization for system size $N = 26$ with PBCs.

contributions between all eigenstates with $E = 0$ must also be counted.

After evaluating $\bar{n}$, we compute the difference between the diagonal and canonical ensembles, $\delta n = \bar{n} - n_{th}$, where n_{th} was defined in Eq. (4). This allows to quantify ergodicity breaking via the deviation from the thermal value in the infinite-time limit, as shown in Fig. 14. Comparing this with the original phase diagram in Fig. 1, we see that the main regions (1), (2), and (3) associated with QMBS still show visible signatures. In other regions, such as region (5), the diagonal and canonical ensemble averages happen to be equal but this does not imply thermalization—rather, the difference between ensembles is small because the dynamics is reduced to a superposition of only a few eigenstates. Similarly, we notice that region (2) and region (3) are intersected by a flat line where $|\delta n| \ll \bar{n}$, which is completely insensitive to the initial state (i.e., independent of μ_i). This line passes through the vicinity of the diamond point, discussed in Sec. V, where we emphasized that the relevant dynamics occurs at lower effective temperatures than the other parts of region (1) and (2). Consequently, we expect $|\delta n|/\bar{n}$ to be suppressed. Indeed,

as we discuss in Fig. 15 below, this apparent discontinuity between regions (1) and (2) is related to the fact that δn takes opposite signs in the two regions, thus it crosses zero at their interface.

Figure 15(a) shows that at the critical point there is still a sizable difference between the two ensembles in various system sizes. The maximum difference is closer to $\mu_f = 0.5$ than to the fidelity maximum of 0.633. The latter is a compromise between the flatness of the band and the level of interactions of the magnons. As the long-time behavior should not depend on the spacings of the towers, it is not surprising that the optimal μ_f is much closer to 0.5, where the level of interactions of the magnons seems the lowest. Figure 15(b) shows a cut through the phase diagram at fixed μ_i values shown on the color bar. The change of sign between region (1) versus regions (2) and (3) is clearly visible, hence there has to be a point where δn passes through zero. This crossing appears to be unrelated to thermalization as the deviation from the canonical ensemble is still pronounced on either side of the crossing. This could be caused by the particular choice of the observable, and it is possible that other observables may not exhibit such a behavior.

---

[1] M. Serbyn, D. A. Abanin, and Z. Papić, Quantum many-body scars and weak breaking of ergodicity, Nat. Phys. **17**, 675 (2021).

[2] S. Moudgalya, B. A. Bernevig, and N. Regnault, Quantum many-body scars and Hilbert space fragmentation: A review of exact results, Rep. Prog. Phys. **85**, 086501 (2022).

[3] Z. Papić, Weak ergodicity breaking through the lens of quantum entanglement, in *Entanglement in Spin Chains: From Theory to Quantum Technology Applications*, edited by A. Bayat, S. Bose, and H. Johannesson (Springer International Publishing, Cham, 2022), pp. 341–395.

[4] A. Chandran, T. Iadecola, V. Khemani, and R. Moessner, Quantum many-body scars: A quasiparticle perspective, Ann. Rev. Condens. Matter Phys. **14**, 443 (2023).

[5] S. Moudgalya, N. Regnault, and B. A. Bernevig, Entanglement of exact excited states of Affleck-Kennedy-Lieb-Tasaki models: Exact results, many-body scars, and violation of the strong eigenstate thermalization hypothesis, Phys. Rev. B **98**, 235156 (2018).

[6] C. J. Turner, A. A. Michailidis, D. A. Abanin, M. Serbyn, and Z. Papic, Weak ergodicity breaking from quantum many-body scars, Nat. Phys. **14**, 745 (2018).

[7] M. Schecter and T. Iadecola, Weak Ergodicity Breaking and Quantum Many-Body Scars in Spin-1 XY Magnets, Phys. Rev. Lett. **123**, 147201 (2019).

[8] S. Moudgalya, B. A. Bernevig, and N. Regnault, Quantum many-body scars in a Landau level on a thin torus, Phys. Rev. B **102**, 195150 (2020).

[9] S. Ok, K. Choo, C. Mudry, C. Castelnovo, C. Chamon, and T. Neupert, Topological many-body scar states in dimensions one, two, and three, Phys. Rev. Res. **1**, 033144 (2019).

[10] K. Bull, I. Martin, and Z. Papić, Systematic Construction of Scarred Many-Body Dynamics in 1D Lattice Models, Phys. Rev. Lett. **123**, 030601 (2019).

[11] A. Hudomal, I. Vasić, N. Regnault, and Z. Papić, Quantum scars of bosons with correlated hopping, Commun. Phys. **3**, 99 (2020).

[12] H. Zhao, J. Vovrosh, F. Mintert, and J. Knolle, Quantum Many-Body Scars in Optical Lattices, Phys. Rev. Lett. **124**, 160604 (2020).

[13] N. Shibata, N. Yoshioka, and H. Katsura, Onsager's Scars in Disordered Spin Chains, Phys. Rev. Lett. **124**, 180604 (2020).

[14] N. O'Dea, F. Burnell, A. Chandran, and V. Khemani, From tunnels to towers: Quantum scars from Lie algebras and q-deformed Lie algebras, Phys. Rev. Res. **2**, 043305 (2020).

[15] S. Moudgalya, E. O'Brien, B. A. Bernevig, P. Fendley, and N. Regnault, Large classes of quantum scarred Hamiltonians from matrix product states, Phys. Rev. B **102**, 085120 (2020).

[16] J.-Y. Desaules, A. Hudomal, C. J. Turner, and Z. Papić, Proposal for Realizing Quantum Scars in the Tilted 1D Fermi-Hubbard Model, Phys. Rev. Lett. **126**, 210601 (2021).

[17] J.-Y. Desaules, A. Hudomal, D. Banerjee, A. Sen, Z. Papić, and J. C. Halimeh, Prominent quantum many-body scars in a truncated Schwinger model, Phys. Rev. B **107**, 205112 (2023).

[18] J.-Y. Desaules, D. Banerjee, A. Hudomal, Z. Papić, A. Sen, and J. C. Halimeh, Weak ergodicity breaking in the Schwinger model, Phys. Rev. B **107**, L201105 (2023).

[19] J.-Y. Desaules, K. Bull, A. Daniel, and Z. Papić, Hypergrid subgraphs and the origin of scarred quantum walks in many-body Hilbert space, Phys. Rev. B **105**, 245137 (2022).

[20] C. M. Langlett, Z.-C. Yang, J. Wildeboer, A. V. Gorshkov, T. Iadecola, and S. Xu, Rainbow scars: From area to volume law, Phys. Rev. B **105**, L060301 (2022).

[21] H. Bernien, S. Schwartz, A. Keesling, H. Levine, A. Omran, H. Pichler, S. Choi, A. S. Zibrov, M. Endres, M. Greiner *et al.*, Probing many-body dynamics on a 51-atom quantum simulator, Nature (London) **551**, 579 (2017).

[22] D. Bluvstein, A. Omran, H. Levine, A. Keesling, G. Semeghini, S. Ebadi, T. T. Wang, A. A. Michailidis, N. Maskara, W. W.

Ho *et al.*, Controlling quantum many-body dynamics in driven Rydberg atom arrays, Science **371**, 1355 (2021).

[23] P. N. Jepsen, Y. K. E. Lee, H. Lin, I. Dimitrova, Y. Margalit, W. W. Ho, and W. Ketterle, Long-lived phantom helix states in Heisenberg quantum magnets, Nat. Phys. **18**, 899 (2022).

[24] G.-X. Su, H. Sun, A. Hudomal, J.-Y. Desaules, Z.-Y. Zhou, B. Yang, J. C. Halimeh, Z.-S. Yuan, Z. Papić, and J.-W. Pan, Observation of unconventional many-body scarring in a quantum simulator, Phys. Rev. Res. **5**, 023010 (2023).

[25] P. Zhang, H. Dong, Y. Gao, L. Zhao, J. Hao, J.-Y. Desaules, Q. Guo, J. Chen, J. Deng, B. Liu *et al.*, Many-body Hilbert space scarring on a superconducting processor, Nat. Phys. **19**, 120 (2023).

[26] V. Khemani, C. R. Laumann, and A. Chandran, Signatures of integrability in the dynamics of Rydberg-blockaded chains, Phys. Rev. B **99**, 161101(R) (2019).

[27] K. Omiya and M. Müller, Quantum many-body scars in bipartite Rydberg arrays originate from hidden projector embedding, Phys. Rev. A **107**, 023318 (2023).

[28] D. K. Mark, C.-J. Lin, and O. I. Motrunich, Unified structure for exact towers of scar states in the Affleck-Kennedy-Lieb-Tasaki and other models, Phys. Rev. B **101**, 195131 (2020).

[29] S. Choi, C. J. Turner, H. Pichler, W. W. Ho, A. A. Michailidis, Z. Papić, M. Serbyn, M. D. Lukin, and D. A. Abanin, Emergent SU(2) Dynamics and Perfect Quantum Many-Body Scars, Phys. Rev. Lett. **122**, 220603 (2019).

[30] B. Buča, J. Tindall, and D. Jaksch, Non-stationary coherent quantum many-body dynamics through dissipation, Nat. Commun. **10**, 1730 (2019).

[31] M. Medenjak, B. Buča, and D. Jaksch, Isolated Heisenberg magnet as a quantum time crystal, Phys. Rev. B **102**, 041117(R) (2020).

[32] K. Bull, J.-Y. Desaules, and Z. Papić, Quantum scars as embeddings of weakly broken Lie algebra representations, Phys. Rev. B **101**, 165139 (2020).

[33] N. Shiraishi and T. Mori, Systematic Construction of Counterexamples to the Eigenstate Thermalization Hypothesis, Phys. Rev. Lett. **119**, 030601 (2017).

[34] H. Labuhn, D. Barredo, S. Ravets, S. de Léséleuc, T. Macrì, T. Lahaye, and A. Browaeys, Tunable two-dimensional arrays of single Rydberg atoms for realizing quantum Ising models, Nature (London) **534**, 667 (2016).

[35] P. Fendley, K. Sengupta, and S. Sachdev, Competing density-wave orders in a one-dimensional hard-boson model, Phys. Rev. B **69**, 075106 (2004).

[36] I. Lesanovsky and H. Katsura, Interacting Fibonacci anyons in a Rydberg gas, Phys. Rev. A **86**, 041601(R) (2012).

[37] C. J. Turner, A. A. Michailidis, D. A. Abanin, M. Serbyn, and Z. Papić, Quantum scarred eigenstates in a Rydberg atom chain: Entanglement, breakdown of thermalization, and stability to perturbations, Phys. Rev. B **98**, 155134 (2018).

[38] C.-J. Lin and O. I. Motrunich, Exact Quantum Many-Body Scar States in the Rydberg-Blockaded Atom Chain, Phys. Rev. Lett. **122**, 173401 (2019).

[39] C.-J. Lin, A. Chandran, and O. I. Motrunich, Slow thermalization of exact quantum many-body scar states under perturbations, Phys. Rev. Res. **2**, 033044 (2020).

[40] I. Mondragon-Shem, M. G. Vavilov, and I. Martin, Fate of Quantum Many-Body Scars in the Presence of Disorder, PRX Quantum **2**, 030349 (2021).

[41] M. Ljubotina, J.-Y. Desaules, M. Serbyn, and Z. Papić, Superdiffusive Energy Transport in Kinetically Constrained Models, Phys. Rev. X **13**, 011033 (2023).

[42] S. Sachdev, K. Sengupta, and S. M. Girvin, Mott insulators in strong electric fields, Phys. Rev. B **66**, 075128 (2002).

[43] T. M. R. Byrnes, P. Sriganesh, R. J. Bursill, and C. J. Hamer, Density matrix renormalization group approach to the massive Schwinger model, Phys. Rev. D **66**, 013002 (2002).

[44] E. Rico, T. Pichler, M. Dalmonte, P. Zoller, and S. Montangero, Tensor Networks for Lattice Gauge Theories and Atomic Quantum Simulation, Phys. Rev. Lett. **112**, 201601 (2014).

[45] B. Yang, H. Sun, R. Ott, H.-Y. Wang, T. V. Zache, J. C. Halimeh, Z.-S. Yuan, P. Hauke, and J.-W. Pan, Observation of gauge invariance in a 71-site Bose–Hubbard quantum simulator, Nature (London) **587**, 392 (2020).

[46] M. Van Damme, J. C. Halimeh, and P. Hauke, Gauge-symmetry violation quantum phase transition in lattice gauge theories, arXiv:2010.07338.

[47] A. Keesling, A. Omran, H. Levine, H. Bernien, H. Pichler, S. Choi, R. Samajdar, S. Schwartz, P. Silvi, S. Sachdev *et al.*, Quantum Kibble-Zurek mechanism and critical dynamics on a programmable Rydberg simulator, Nature (London) **568**, 207 (2019).

[48] S. Coleman, More about the massive Schwinger model, Ann. Phys. **101**, 239 (1976).

[49] F. M. Surace, P. P. Mazza, G. Giudici, A. Lerose, A. Gambassi, and M. Dalmonte, Lattice Gauge Theories and String Dynamics in Rydberg Atom Quantum Simulators, Phys. Rev. X **10**, 021041 (2020).

[50] S. Sugiura, T. Kuwahara, and K. Saito, Many-body scar state intrinsic to periodically driven system, Phys. Rev. Res. **3**, L012010 (2021).

[51] B. Mukherjee, S. Nandy, A. Sen, D. Sen, and K. Sengupta, Collapse and revival of quantum many-body scars via Floquet engineering, Phys. Rev. B **101**, 245107 (2020).

[52] B. Mukherjee, A. Sen, D. Sen, and K. Sengupta, Dynamics of the vacuum state in a periodically driven Rydberg chain, Phys. Rev. B **102**, 075123 (2020).

[53] K. Mizuta, K. Takasan, and N. Kawakami, Exact Floquet quantum many-body scars under Rydberg blockade, Phys. Rev. Res. **2**, 033284 (2020).

[54] N. Maskara, A. A. Michailidis, W. W. Ho, D. Bluvstein, S. Choi, M. D. Lukin, and M. Serbyn, Discrete Time-Crystalline Order Enabled by Quantum Many-Body Scars: Entanglement Steering via Periodic Driving, Phys. Rev. Lett. **127**, 090602 (2021).

[55] A. Hudomal, J.-Y. Desaules, B. Mukherjee, G.-X. Su, J. C. Halimeh, and Z. Papić, Driving quantum many-body scars in the PXP model, Phys. Rev. B **106**, 104302 (2022).

[56] P.-G. Rozon, M. J. Gullans, and K. Agarwal, Constructing quantum many-body scar Hamiltonians from Floquet automata, Phys. Rev. B **106**, 184304 (2022).

[57] Z. Yao, L. Pan, S. Liu, and H. Zhai, Quantum many-body scars and quantum criticality, Phys. Rev. B **105**, 125123 (2022).

[58] H.-Y. Wang, W.-Y. Zhang, Z.-Y. Yao, Y. Liu, Z.-H. Zhu, Y.-G. Zheng, X.-K. Wang, H. Zhai, Z.-S. Yuan, and J.-W. Pan, Interrelated thermalization and quantum criticality in a lattice gauge simulator, arXiv:2210.17032.

[59] C. Peng and X. Cui, Bridging quantum many-body scars and quantum integrability in Ising chains with trans-

verse and longitudinal fields, Phys. Rev. B **106**, 214311 (2022).

[60] W. W. Ho, S. Choi, H. Pichler, and M. D. Lukin, Periodic Orbits, Entanglement, and Quantum Many-Body Scars in Constrained Models: Matrix Product State Approach, Phys. Rev. Lett. **122**, 040603 (2019).

[61] J. Haegeman, C. Lubich, I. Oseledets, B. Vandereycken, and F. Verstraete, Unifying time evolution and optimization with matrix product states, Phys. Rev. B **94**, 165116 (2016).

[62] M. L. Mehta, *Random Matrices* (Elsevier, Amsterdam, 2004), Vol. 142.

[63] J. M. Deutsch, Quantum statistical mechanics in a closed system, Phys. Rev. A **43**, 2046 (1991).

[64] M. Srednicki, Chaos and quantum thermalization, Phys. Rev. E **50**, 888 (1994).

[65] L. D'Alessio, Y. Kafri, A. Polkovnikov, and M. Rigol, From quantum chaos and eigenstate thermalization to statistical mechanics and thermodynamics, Adv. Phys. **65**, 239 (2016).

[66] D. Pérez-García, F. Verstraete, M. M. Wolf, and J. I. Cirac, Matrix product state representations, Quantum Inf. Comput. **7**, 401 (2007).

[67] A. A. Michailidis, C. J. Turner, Z. Papić, D. A. Abanin, and M. Serbyn, Slow Quantum Thermalization and Many-Body Revivals from Mixed Phase Space, Phys. Rev. X **10**, 011055 (2020).

[68] C. J. Turner, J.-Y. Desaules, K. Bull, and Z. Papić, Correspondence Principle for Many-Body Scars in Ultracold Rydberg Atoms, Phys. Rev. X **11**, 021021 (2021).

[69] P. A. M. Dirac, Note on exchange phenomena in the Thomas atom, Math. Proc. Camb. Philos. Soc. **26**, 376 (1930).

[70] P. Kramer and M. Saraceno, *Geometry of the Time-Dependent Variational Principle in Quantum Mechanics*, Lecture Notes in Physics (Springer, Berlin, 1981).

[71] J. Haegeman, J. I. Cirac, T. J. Osborne, I. Pižorn, H. Verschelde, and F. Verstraete, Time-Dependent Variational Principle for Quantum Lattices, Phys. Rev. Lett. **107**, 070601 (2011).

[72] E. J. Heller, Bound-State Eigenfunctions of Classically Chaotic Hamiltonian Systems: Scars of Periodic Orbits, Phys. Rev. Lett. **53**, 1515 (1984).

[73] E. J. Heller, Wavepacket dynamics and quantum chaology, in *Chaos and Quantum Physics* (North-Holland, Amsterdam, 1991), Vol. 52.

[74] A. A. Michailidis, M. Žnidarič, M. Medvedyeva, D. A. Abanin, T. Prosen, and Z. Papić, Slow dynamics in translation-invariant quantum lattice models, Phys. Rev. B **97**, 104307 (2018).

[75] M. Ljubotina, B. Roos, D. A. Abanin, and M. Serbyn, Optimal steering of matrix product states and quantum many-body scars, PRX Quantum **3**, 030343 (2022).

[76] S. P. Kelly, E. Timmermans, and S.-W. Tsai, Thermalization and its breakdown for a large nonlinear spin, Phys. Rev. A **102**, 052210 (2020).

[77] M. R. Lambert, S.-W. Tsai, and S. P. Kelly, Quantum memory at an eigenstate phase transition in a weakly chaotic model, Phys. Rev. A **106**, 012206 (2022).

[78] P. Calabrese and J. Cardy, Entanglement entropy and quantum field theory, J. Stat. Mech.: Theory Exp. (2004) P06002.

[79] T. Iadecola, M. Schecter, and S. Xu, Quantum many-body scars from magnon condensation, Phys. Rev. B **100**, 184312 (2019).

[80] C.-J. Lin and O. I. Motrunich, Quasiparticle explanation of the weak-thermalization regime under quench in a nonintegrable quantum spin chain, Phys. Rev. A **95**, 023621 (2017).

[81] Z.-Y. Zhou, G.-X. Su, J. C. Halimeh, R. Ott, H. Sun, P. Hauke, B. Yang, Z.-S. Yuan, J. Berges, and J.-W. Pan, Thermalization dynamics of a gauge theory on a quantum simulator, Science **377**, 311 (2022).

[82] J. C. Halimeh, I. P. McCulloch, B. Yang, and P. Hauke, Tuning the topological θ-angle in cold-atom quantum simulators of gauge theories, PRX Quantum **3**, 040316 (2022).

[83] S. Dooley, Robust quantum sensing in strongly interacting systems with many-body scars, PRX Quantum **2**, 020330 (2021).

[84] J.-Y. Desaules, F. Pietracaprina, Z. Papić, J. Goold, and S. Pappalardi, Extensive Multipartite Entanglement from SU(2) Quantum Many-Body Scars, Phys. Rev. Lett. **129**, 020601 (2022).

[85] S. Dooley, S. Pappalardi, and J. Goold, Entanglement enhanced metrology with quantum many-body scars, Phys. Rev. B **107**, 035123 (2023).

[86] B. Kramer and A. MacKinnon, Localization: Theory and experiment, Rep. Prog. Phys. **56**, 1469 (1993).

[87] M. Schecter and T. Iadecola, Many-body spectral reflection symmetry and protected infinite-temperature degeneracy, Phys. Rev. B **98**, 035139 (2018).

Weak ergodicity breaking in the Schwinger model

Jean-Yves Desaules [ID],[1] Debasish Banerjee [ID],[2,3] Ana Hudomal [ID],[1,4] Zlatko Papić [ID],[1] Arnab Sen [ID],[5] and Jad C. Halimeh [ID],[6,7,*]

[1]*School of Physics and Astronomy, University of Leeds, Leeds LS2 9JT, United Kingdom*
[2]*Theory Division, Saha Institute of Nuclear Physics, 1/AF Bidhan Nagar, Kolkata 700064, India*
[3]*Homi Bhabha National Institute, Training School Complex, Anushaktinagar, Mumbai 400094, India*
[4]*Institute of Physics Belgrade, University of Belgrade, 11080 Belgrade, Serbia*
[5]*School of Physical Sciences, Indian Association for the Cultivation of Science, Kolkata 700032, India*
[6]*Department of Physics and Arnold Sommerfeld Center for Theoretical Physics (ASC), Ludwig-Maximilians-Universität München,*
Theresienstraße 37, D-80333 München, Germany
[7]*Munich Center for Quantum Science and Technology (MCQST), Schellingstraße 4, D-80799 München, Germany*

As a paradigm of weak ergodicity breaking in disorder-free nonintegrable models, quantum many-body scars (QMBS) can offer deep insights into the thermalization dynamics of gauge theories. Having been first discovered in a spin-$\frac{1}{2}$ quantum link formulation of the Schwinger model, it is a fundamental question as to whether QMBS persist for $S > \frac{1}{2}$ since such theories converge to the lattice Schwinger model in the large-S limit, which is the appropriate version of lattice QED in one spatial dimension. In this work, we address this question by exploring QMBS in spin-S U(1) quantum link models (QLMs) with staggered fermions. We find that QMBS persist at $S > \frac{1}{2}$, with the resonant scarring regime, which occurs for a zero-mass quench, arising from simple high-energy gauge-invariant initial product states. We furthermore find evidence of detuned scarring regimes, which occur for finite-mass quenches starting in the physical vacua and the charge-proliferated state. Our results conclusively show that QMBS exist in a wide class of lattice gauge theories in one spatial dimension represented by spin-S QLMs coupled to dynamical fermions, and our findings can be tested on near-term cold-atom quantum simulators of these models.

Introduction. Quantum many-body scars (QMBS) form an intriguing paradigm of ergodicity breaking in interacting systems that are typically expected to thermalize due to their nonintegrability and spatial homogeneity [1–8]. QMBS comprise eigenstates of low entanglement entropy [9,10], many of which reside in the middle of the spectrum, and are often separated roughly equally in energy [11,12]. These eigenstates are nonthermal, forming a "cold" subspace that is weakly connected to the rest of the Hilbert space. Consequently, quenches starting in initial states with high overlap with these nonthermal states do not show typical thermalization, but instead exhibit long-lived coherent dynamics [13,14]. This behavior is of particular interest to fundamental investigations of the eigenstate thermalization hypothesis (ETH) [15–20], as it has been linked to novel mechanisms for avoiding thermalization in closed quantum systems based on spectrum generating algebras [21–24] and embedding of nonthermal eigenstates [25] (see recent reviews [26,27]). Moreover, given that QMBS constitute high- or even infinite-temperature states, when the system is initially prepared in them it will not dephase its

information, which is pertinent to applications in quantum memory and information processing [28–31].

QMBS are also relevant to gauge theories [32–36], which describe the interactions of elementary particles mediated by gauge bosons through an extensive set of local constraints [37–39]. A paradigmatic example of the latter is Gauss's law in quantum electrodynamics (QED), where the distribution of charged matter strictly specifies the allowed configurations of the surrounding electromagnetic field [40]. Recently, a concerted experimental effort has emerged for the implementation of gauge theories in synthetic quantum matter (SQM) devices [41–51]. This has been facilitated in large part due to the great progress achieved in the precision and control of SQM setups [52,53], making the quantum simulation of gauge theories a realistic endeavor [54–60]. Due to the complexity of these experiments, the implementations often focus on quantum link formulations of gauge theories, where spin-S operators model the gauge fields, which in QED span an infinite-dimensional Hilbert space [61]. This has allowed the first large-scale realization of the spin-$\frac{1}{2}$ U(1) quantum link model (QLM) in $1 + 1$ dimensions [$(1 + 1)$D] using ultracold atoms [50,51].

The first experimental observation of QMBS was achieved in a Rydberg-atom setup implementing the PXP model [1], a paradigm of QMBS which maps to the spin-$\frac{1}{2}$ U(1) QLM [33]. Such a mapping breaks down at $S > \frac{1}{2}$, and it remains an open question whether QMBS persist at larger link spin lengths in the QLM formulation of QED, and, if they do, what their form will be. In this Letter, we show that QMBS are ubiquitous in

lattice gauge theories for all values of spin $S \leqslant \frac{5}{2}$ accessible in numerical simulations. For a zero-mass quench, QMBS arise when the system is prepared in the *extreme vacua* of the spin-S U(1) QLM, which are the most highly excited vacuum states of lattice QED. Furthermore, we find that preparing the system in the physical (least excited) vacua or in the charge-proliferated state can still lead to *detuned* scarring behavior for certain massive quenches, similar to the case of $S = \frac{1}{2}$ that has recently been demonstrated experimentally in a tilted Bose-Hubbard optical lattice [7]. The nonthermalizing dynamics due to QMBS provides a useful benchmark for the upcoming realizations of larger-S lattice gauge theories in cold-atom quantum simulators and the exploration of their out-of-equilibrium properties [48,57].

U(1) quantum link model. The Schwinger model, or QED in $1 + 1$ dimensions, is possibly the simplest gauge theory with dynamical matter that shows nontrivial phenomena like confinement [62,63]. A discrete version of the Schwinger Hamiltonian on a lattice is provided by the Kogut-Susskind formulation, which is also reached in the large-S limit of the QLMs being studied here. The $(1 + 1)$D spin-S U(1) QLM is given by the Hamiltonian [64,65]

$$\hat{H} = \sum_{j=1}^{L} \left[\frac{J}{2a\sqrt{S(S+1)}} (\hat{\sigma}_j^+ \hat{s}_{j,j+1}^+ \hat{\sigma}_{j+1}^- + \text{H.c.}) \right.$$
$$\left. + \frac{\mu}{2}(-1)^j \hat{\sigma}_j^z + \frac{g^2 a}{2} \left(\hat{s}_{j,j+1}^z \right)^2 \right]. \quad (1)$$

Here, $J = 1$ sets the energy scale, μ is the fermionic mass, and g^2 is the gauge coupling strength. Throughout this work, we will set the lattice spacing to $a = 1$ and employ periodic boundary conditions, with L denoting the number of lattice sites. The matter field on site j is represented by the Pauli operator $\hat{\sigma}_j^z$, and the electric (gauge) field at the link between sites j and $j + 1$ is represented by the spin-S operator $\hat{s}_{j,j+1}^{z(+)}$. The generator of the U(1) gauge symmetry of Hamiltonian (1) is

$$\hat{G}_j = \frac{\hat{\sigma}_j^z + (-1)^j}{2} + \hat{s}_{j-1,j}^z - \hat{s}_{j,j+1}^z, \quad (2)$$

which can be interpreted as a discretized version of Gauss's law relating the matter occupation on site j to the electric-field configuration on its neighboring links. We will work in the *physical* sector of Gauss's law: $\hat{G}_j |\phi\rangle = 0, \ \forall \ j$.

Due to the gauge symmetry imposed by the generator (2), one can integrate out the matter fields in the Hamiltonian (1), resulting in a constrained spin system. For $S = \frac{1}{2}$, this corresponds to the PXP model [33]. For larger S, the resulting model differs from generalizations of the PXP model already explored in the literature [13,66]. In the companion article [67], we derive the relevant constrained spin-S model corresponding to the spin-S U(1) QLM for any value of S [68]. Exact diagonalization (ED) techniques resolving the translation and spatial-inversion symmetries have been employed to study the eigenstates of these models. Time-evolution results are obtained either directly from the ED results or by time evolving the initial state using sparse matrix exponential techniques.
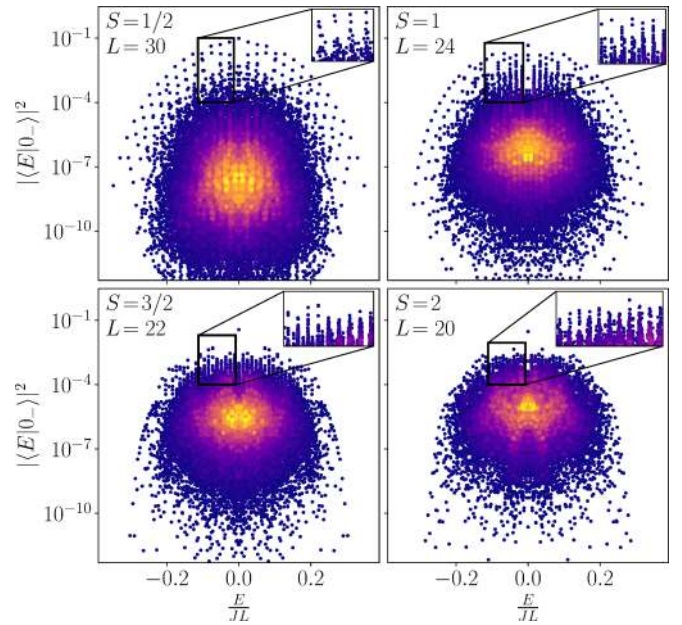

FIG. 1. Quantum many-body scars in the spin-S U(1) QLM: Overlap of the *extreme vacuum* $|0_-\rangle$ with the eigenstates of the quench spin-S U(1) QLM Hamiltonian (1) at $\mu = g = 0$. At all considered values of S, distinctive towers of eigenstates arise that are equally spaced in energy (see insets). These are a hallmark of quantum many-body scars. These results are obtained by exact diagonalization calculations, where L denotes the number of matter sites, and periodic boundary conditions are employed. The color indicates the density of data points, with yellow color representing higher density. In all cases, the Hilbert space has more than 4×10^5 states, with at least 2.5×10^4 states belonging to the relevant symmetry sectors of the extreme vacua.

Resonant scarring. The *physical vacuum* of $\hat{H}$ is its ground state at $\mu \to \infty$ and $g^2 > 0$. In the case of half-integer S, there are two doubly degenerate physical vacua. These can be defined on a two-site two-link unit cell using as quantum numbers the eigenvalues σ_j^z and $s_{j,j+1}^z$ of the matter and electric field operators $\hat{\sigma}_j^z$ and $\hat{s}_{j,j+1}^z$, respectively, explicitly reading as $|\sigma_1^z, s_{1,2}^z, \sigma_2^z, s_{2,3}^z\rangle = |+1, \pm\frac{1}{2}, -1, \pm\frac{1}{2}\rangle$. For integer S, the physical vacuum is nondegenerate, and reads as $|\sigma_1^z, s_{1,2}^z, \sigma_2^z, s_{2,3}^z\rangle = |+1, 0, -1, 0\rangle$. Henceforth, we will denote $|0_+\rangle = |+1, +\frac{1}{2}, -1, +\frac{1}{2}\rangle$ for half-integer S and $|0_+\rangle = |+1, 0, -1, 0\rangle$ for integer S, with the subscript denoting the sign of g^2.

On the other hand, the *extreme vacua* of $\hat{H}$ are high-energy states that can be realized as doubly degenerate ground states of Eq. (1) at $\mu \to \infty$ and $g^2 < 0$: $|\sigma_1^z, s_{1,2}^z, \sigma_2^z, s_{2,3}^z\rangle = |+1, \pm S, -1, \pm S\rangle$. Henceforth, we will denote $|0_-\rangle = |+1, +S, -1, +S\rangle$, with the subscript again indicating the sign of g^2.

We will further consider the charge-proliferated state, which is the ground state of Eq. (1) at $\mu \to -\infty$ and $g^2 > 0$. For half-integer S, it is nondegenerate and reads as $|\text{CP}\rangle = |-1, -\frac{1}{2}, +1, +\frac{1}{2}\rangle$. For integer S, we obtain two doubly degenerate ground states: $|\text{CP}\rangle = |-1, -1, +1, 0\rangle$ and $|-1, 0, +1, +1\rangle$.
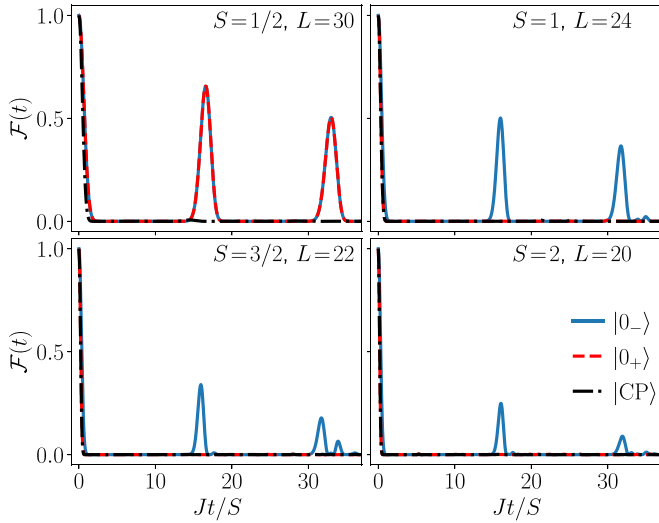
FIG. 2. Dynamics of the fidelity in the wake of a quench by the spin-S U(1) QLM (1) at $\mu = g = 0$ starting in either the extreme vacuum $|0_-\rangle$ (solid blue curve), the physical vacuum $|0_+\rangle$ (dashed red curve), or the charge-proliferated state $|\mathrm{CP}\rangle$ (dashed-dotted black curve). The qualitative conclusion is that regardless of the value of S, prominent revivals appear in the fidelity dynamics only when the initial state is the extreme vacuum, whereas for other states the dynamics is thermal. Note that for $S = \frac{1}{2}$, the physical and extreme vacua are identical.

With respect to the eigenstates of Hamiltonian (1) at $\mu = g = 0$, we find through ED that only $|0_-\rangle$ exhibits the overlap behavior indicative of scarring for general S (see Fig. 1). Just as in the known case of $S = \frac{1}{2}$, we also see at other values of S signatures of $2SL + 1$ towers equally spaced in energy (see insets), exhibiting large overlap with $|0_-\rangle$, particularly in the middle of the spectrum. The overlap of the top band of states can be further enhanced by considering a truncated version of the QED gauge field [67]. Note how for all values of S that we consider, there is a prominent zero-energy mode with the largest overlap. The presence of these eigenstates is evidence of weak ergodicity breaking in the model. Due to the scaling term $1/\sqrt{S(S+1)}$, the ground-state energy E_0 is approximately independent of S at $\mu = g^2 = 0$, and we find numerically that $E_0 \approx -0.32L$. As the spectrum is symmetric around zero, we can use this along with the number of towers to get the approximate energy spacing between towers as $\Delta E \approx -2E_0/(2SL) \approx 0.32/S$. We note that the various approximation schemes for scarred eigenstates in the PXP model also show good results for QLMs with larger S [67].

The presence of scarred eigenstates can be detected using the global quench: the system is prepared in some initial state $|\psi(0)\rangle$ and let to evolve under unitary dynamics, $|\psi(t)\rangle = e^{-i\hat{H}t} |\psi(0)\rangle$, generated by the Hamiltonian $\hat{H}$. The state $|\psi(0)\rangle$ is a highly nonequilibrium state, i.e., it is a superposition of a large number of eigenstates of $\hat{H}$, resulting in complex dynamics that we characterize using the fidelity, $\mathcal{F}(t) = |\langle\psi(0)|\psi(t)\rangle|^2$. In the case of $S = \frac{1}{2}$, $|0_+\rangle = |0_-\rangle$, as the last term of Eq. (1) is an inconsequential energy constant since $(\hat{s}_{j,j+1}^z)^2 = \mathbb{1}$. Quenching this vacuum state with $\hat{H}$ at $\mu = 0$ is known to lead to scarring behavior for $S = \frac{1}{2}$ [1,33], and this is exhibited in the revivals of the fidelity, shown in the
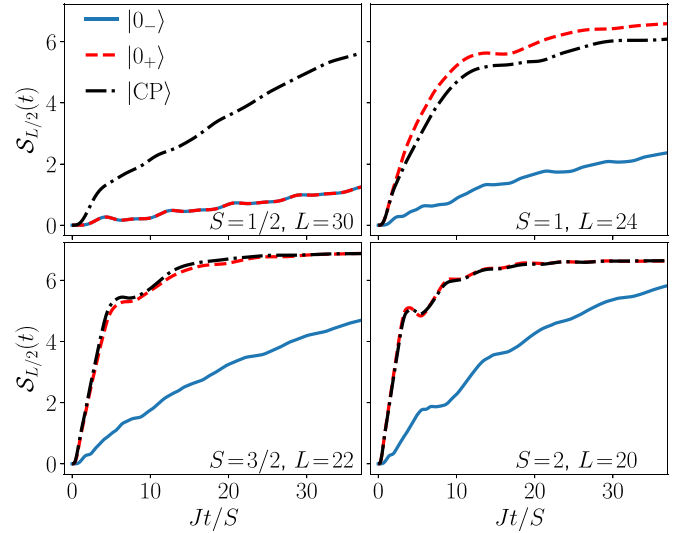

FIG. 3. Dynamics of the mid-chain entanglement entropy for the same quench and initial states considered in Fig. 2. For all considered values of the link spin length S, an anomalously low and slowly growing entanglement entropy arises when the initial state is the extreme vacuum. Preparing the system in the charge-proliferated state or the physical vacuum leads to a fast growth in the entanglement entropy except for the case of $S = \frac{1}{2}$, where the physical and extreme vacua are the same.

top left panel of Fig. 2. For comparison, we have included the fidelity dynamics for $|\psi(0)\rangle = |\mathrm{CP}\rangle$, which shows no revivals, in agreement with what is established in the literature for this quench when $S = \frac{1}{2}$ [26].

However, once the link spin length is $S > \frac{1}{2}$, we find that the fidelity dynamics exhibits revivals only when the system is initialized in the extreme vacuum $|\psi(0)\rangle = |0_-\rangle$, whereas neither the physical vacuum $|0_+\rangle$ nor the charge-proliferated state $|\mathrm{CP}\rangle$ give rise to scarring behavior; see Fig. 2 for $S = 1, \frac{3}{2}, 2$. We have checked that the other vacua $|\sigma_1^z, s_{1,2}^z, \sigma_2^z, s_{2,3}^z\rangle = |+1, \pm M, -1, \pm M\rangle$ with $\frac{1}{2} < M < S$ and higher-energy charge-proliferated states are also not scarred states [67]. From the previous estimate of the energies of scarred towers, we expect the revival period to be $T \approx 6.25\pi S$. However, in practice the energy spacing between towers varies throughout the spectrum. So the relevant energy spacing is the one near $E = 0$, where the scarred states have the higher overlap with $|0_-\rangle$. This provides an estimate of $T \approx 5.13\pi S$, which agrees much more accurately with the numerical data.

We explore the effect of scarring on the dynamics of the mid-chain entanglement entropy $\mathcal{S}_{L/2}(t)$, shown in Fig. 3 for $S = \frac{1}{2}$ to 2. $\mathcal{S}_{L/2}$ is defined as the von Neumann entropy for the reduced density matrix describing one half of the chain. In all cases, starting in the extreme vacuum leads to an anomalously low $\mathcal{S}_{L/2}(t)$ exhibiting significantly slower growth, whereas preparing the system in the charge-proliferated state leads to a rapid increase of the entanglement entropy. Except for the case of $S = \frac{1}{2}$ where the extreme and physical vacua are the same, starting in the physical vacuum leads to qualitatively similar behavior to that of the charge-proliferated state, with a rapid growth in $\mathcal{S}_{L/2}(t)$. These findings are consistent with
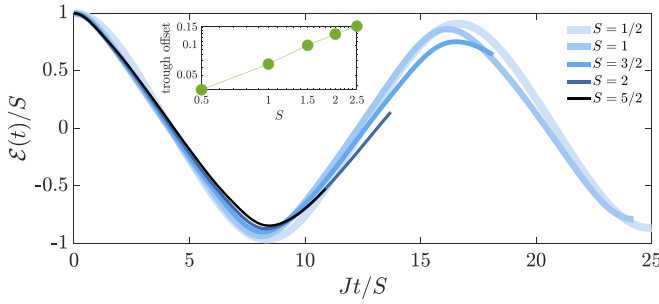
FIG. 4. Dynamics of the electric flux (3) in the TL for a resonant quench ($\mu = g = 0$) starting in the extreme vacuum for different values of S. Inset shows the difference between -1 and the first minimum of the normalized electric flux, plotted as a function of S.

nonthermal scarred dynamics only when the initial state is prepared in the extreme vacuum.

We now investigate the fate of scarring in the thermodynamic limit (TL). Using infinite matrix product states [69], which work directly in the TL, we calculate the dynamics of the electric flux

$$\mathcal{E}(t) = \frac{1}{L} \sum_{j=1}^{L} \langle \psi(t) | \hat{s}_{j,j+1}^z | \psi(t) \rangle, \tag{3}$$

which is an order parameter associated with the global $\mathbb{Z}_2$ symmetry of the Hamiltonian (1). The corresponding results are shown in Fig. 4. Due to the computational cost of these simulations, where convergence is achieved at a maximal bond dimension of 550 and a time step of $0.0005/J$, we can only reach relatively short times. Nevertheless, scarred revivals in $\mathcal{E}(t)$ are clearly visible in Fig. 4 at all accessible values of S.

To quantify ergodicity breaking, in the inset to Fig. 4 we plot the deviation of the first minimum in $\mathcal{E}(t)$ from -1 as a function of S. For sufficiently large S, we expect the data to saturate to some well-defined value between 0 (perfect scarring) and 1 (full thermalization). While the available values remain far from 1, the deviation clearly grows with S, indicating a weakening of scarring towards the Kogut-Susskind limit $S \to \infty$. At the same time, there is no convergence of the data with respect to S, implying that larger values of S are needed in order to reach a reliable conclusion about the existence of ergodicity breaking in the $S \to \infty$ limit.

As such, we have demonstrated that for a quench at $\mu = g = 0$, the spin-S U(1) QLM (1) exhibits scarring behavior when the system is initially prepared in an *extreme vacuum*. The underlying scarring mechanism is precession of a "large" spin of magnitude SL [70]. The relation between scarring and the Hilbert space constraint can be firmed up by studying the structure of the adjacency graph of the Hamiltonian [67]. These extreme vacua are product states that can be naturally explored in SQM experiments [50,51] even though they are otherwise inaccessible in lattice QED.

Detuned scarring. In a recent study [7], it has been shown theoretically and demonstrated experimentally that there are scarring regimes beyond the resonant one discussed above. This was demonstrated in the spin-$\frac{1}{2}$ U(1) QLM by starting
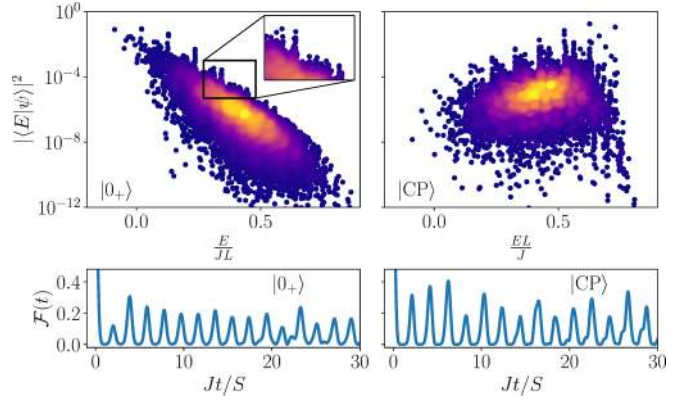

FIG. 5. The spin-S U(1) QLM also exhibits detuned scarring [7], where the physical vacuum $|0_+\rangle$ and the charge-proliferated state $|CP\rangle$ can lead to scarred dynamics when quenched by Hamiltonian (1) at small nonzero values of μ and g^2. Here, we set $\mu = 0.486J$ and $g^2 = 0.6J$, and the overlap of each of $|0_+\rangle$ and $|CP\rangle$ with the corresponding eigenstates of Hamiltonian (1) are shown for $L = 20$ and $S = \frac{3}{2}$. Towers of eigenstates equally spaced in energy emerge, indicating the presence of QMBS. We confirm this picture by calculating the dynamics of the fidelity in the wake of this quench. For all accessible evolution times, we find consistent revivals in the fidelity, strongly indicative of scarred dynamics. The color indicates the density of data points, with yellow color representing higher density.

in the charge-proliferated state and performing a quench at finite mass (detuning).

Motivated by the question as to whether QMBS persist in lattice QED for physically relevant initial states, we explore these *detuned* scarring regimes in the spin-$\frac{3}{2}$ U(1) QLM starting in either the physical vacuum $|0_+\rangle$ or the charge-proliferated state $|CP\rangle$. As shown in Fig. 5, the overlap of these initial states with the eigenstates of the quench Hamiltonian (1) at $\mu = 0.486J$ and $g^2 = 0.6J$ shows distinctive towers equally spaced in energy, similar to the known case of $S = \frac{1}{2}$ [7]. Also displayed in Fig. 5 is the fidelity dynamics for each of $|0_+\rangle$ and $|CP\rangle$ upon quenching them with this Hamiltonian, where we see persistent revivals up to all considered evolution times. We also arrive at a similar picture for other values of S, and in fact we find a wide range of values of (μ, g^2) over which scarring behavior emerges [67].

Given that $|0_+\rangle$ and $|CP\rangle$ are both physically relevant in lattice QED in one spatial dimension, and since the latter has been shown to be achieved at relatively small values of S both in [68,71,72] and out of equilibrium [73], our results suggest that QMBS may play a role for understanding dynamics in physically interesting regimes as well.

Summary. In conclusion, we have demonstrated an abundance of QMBS in the paradigmatic spin-S U(1) QLM, a staple of modern SQM experiments on lattice gauge theories. We have shown that the regime of resonant scarring for quenches at zero mass, prevalent in the literature in the case of $S = \frac{1}{2}$, is also present in the case of $S > \frac{1}{2}$ when the system is initially prepared in an *extreme vacuum*, where the local electric field takes on its largest possible eigenvalue. This has been demonstrated by ergodicity-breaking properties of many-body eigenstates, obtained using ED, as well as by showing the existence of quantum revivals in local observables in the TL

using infinite matrix product state method. The extreme vacua associated are not physical as ground states in lattice QED, but they are product states easily implementable in SQM experiments [48,57]. These experiments, in particular, could provide key insight into the persistence of ergodicity breaking upon approaching the limit $S \to \infty$, which our classical simulations cannot reliably access.

We have also presented evidence of detuned scarring in the spin-S U(1) QLM arising from quenches at small nonzero mass and electric-field coupling, when the system is initially prepared in either the physical vacuum, where the local electric field takes on its lowest possible eigenvalue, or the charge-proliferated state. While the scarring phenomenology is similar to the resonant case, the initial states associated with detuned scarring are physically relevant as low-energy states in lattice QED. Given that recent works have shown convergence to the latter limit in and out of equilibrium already at $S \gtrsim \frac{3}{2}$, our results suggest that this detuned scarring regime may already exist in lattice QED.

---

[1] H. Bernien, S. Schwartz, A. Keesling, H. Levine, A. Omran, H. Pichler, S. Choi, A. S. Zibrov, M. Endres, M. Greiner, V. Vuletić, and M. D. Lukin, Probing many-body dynamics on a 51-atom quantum simulator, Nature (London) **551**, 579 (2017).

[2] S. Moudgalya, S. Rachel, B. A. Bernevig, and N. Regnault, Exact excited states of nonintegrable models, Phys. Rev. B **98**, 235155 (2018).

[3] H. Zhao, J. Vovrosh, F. Mintert, and J. Knolle, Quantum Many-Body Scars in Optical Lattices, Phys. Rev. Lett. **124**, 160604 (2020).

[4] H. Zhao, A. Smith, F. Mintert, and J. Knolle, Orthogonal Quantum Many-Body Scars, Phys. Rev. Lett. **127**, 150601 (2021).

[5] D. Bluvstein, A. Omran, H. Levine, A. Keesling, G. Semeghini, S. Ebadi, T. T. Wang, A. A. Michailidis, N. Maskara, W. W. Ho, S. Choi, M. Serbyn, M. Greiner, V. Vuletić, and M. D. Lukin, Controlling quantum many-body dynamics in driven Rydberg atom arrays, Science **371**, 1355 (2021).

[6] P. N. Jepsen, Y. K.-E. Lee, H. Lin, I. Dimitrova, Y. Margalit, W. W. Ho, and W. Ketterle, Long-lived phantom helix states in Heisenberg quantum magnets, Nat. Phys. **18**, 899 (2022).

[7] G.-X. Su, H. Sun, A. Hudomal, J.-Y. Desaules, Z.-Y. Zhou, B. Yang, J. C. Halimeh, Z.-S. Yuan, Z. Papić, and J.-W. Pan, Observation of many-body scarring in a Bose-Hubbard quantum simulator, Phys. Rev. Res. **5**, 023010 (2023).

[8] P. Zhang, H. Dong, Y. Gao, L. Zhao, J. Hao, J.-Y. Desaules, Q. Guo, J. Chen, J. Deng, B. Liu, W. Ren, Y. Yao, X. Zhang, S. Xu, K. Wang, F. Jin, X. Zhu, B. Zhang, H. Li, C. Song *et al.*, Many-body Hilbert space scarring on a superconducting processor, Nat. Phys. **19**, 120 (2022).

[9] S. Moudgalya, N. Regnault, and B. A. Bernevig, Entanglement of exact excited states of Affleck-Kennedy-Lieb-Tasaki models: Exact results, many-body scars, and violation of the strong eigenstate thermalization hypothesis, Phys. Rev. B **98**, 235156 (2018).

[10] C.-J. Lin and O. I. Motrunich, Exact Quantum Many-Body Scar States in the Rydberg-Blockaded Atom Chain, Phys. Rev. Lett. **122**, 173401 (2019).

[11] C. J. Turner, A. A. Michailidis, D. A. Abanin, M. Serbyn, and Z. Papić, Weak ergodicity breaking from quantum many-body scars, Nat. Phys. **14**, 745 (2018).

[12] M. Schecter and T. Iadecola, Weak Ergodicity Breaking and Quantum many-body Scars in Spin-1 XY Magnets, Phys. Rev. Lett. **123**, 147201 (2019).

[13] W. W. Ho, S. Choi, H. Pichler, and M. D. Lukin, Periodic Orbits, Entanglement, and Quantum Many-Body Scars in Constrained Models: Matrix Product State Approach, Phys. Rev. Lett. **122**, 040603 (2019).

[14] C. J. Turner, A. A. Michailidis, D. A. Abanin, M. Serbyn, and Z. Papić, Quantum scarred eigenstates in a Rydberg atom chain: Entanglement, breakdown of thermalization, and stability to perturbations, Phys. Rev. B **98**, 155134 (2018).

[15] M. Srednicki, Chaos and quantum thermalization, Phys. Rev. E **50**, 888 (1994).

[16] J. M. Deutsch, Quantum statistical mechanics in a closed system, Phys. Rev. A **43**, 2046 (1991).

[17] M. Rigol, V. Dunjko, and M. Olshanii, Thermalization and its mechanism for generic isolated quantum systems, Nature (London) **452**, 854 (2008).

[18] J. Eisert, M. Friesdorf, and C. Gogolin, Quantum many-body systems out of equilibrium, Nat. Phys. **11**, 124 (2015).

[19] L. D'Alessio, Y. Kafri, A. Polkovnikov, and M. Rigol, From quantum chaos and eigenstate thermalization to statistical mechanics and thermodynamics, Adv. Phys. **65**, 239 (2016).

[20] J. M. Deutsch, Eigenstate thermalization hypothesis, Rep. Prog. Phys. **81**, 082001 (2018).

[21] D. K. Mark, C.-J. Lin, and O. I. Motrunich, Unified structure for exact towers of scar states in the Affleck-Kennedy-Lieb-Tasaki and other models, Phys. Rev. B **101**, 195131 (2020).

[22] S. Moudgalya, N. Regnault, and B. A. Bernevig, η-pairing in Hubbard models: From spectrum generating algebras to quantum many-body scars, Phys. Rev. B **102**, 085140 (2020).

[23] N. O'Dea, F. Burnell, A. Chandran, and V. Khemani, From tunnels to towers: Quantum scars from Lie algebras and q-deformed Lie algebras, Phys. Rev. Res. **2**, 043305 (2020).

[24] K. Pakrouski, P. N. Pallegar, F. K. Popov, and I. R. Klebanov, Many-Body Scars as a Group Invariant Sector of Hilbert Space, Phys. Rev. Lett. **125**, 230602 (2020).

[25] N. Shiraishi and T. Mori, Systematic Construction of Counterexamples to the Eigenstate Thermalization Hypothesis, Phys. Rev. Lett. **119**, 030601 (2017).

[26] M. Serbyn, D. A. Abanin, and Z. Papić, Quantum many-body scars and weak breaking of ergodicity, Nat. Phys. **17**, 675 (2021).

[27] S. Moudgalya, B. A. Bernevig, and N. Regnault, Quantum many-body scars and Hilbert space fragmentation: A review of exact results, Rep. Prog. Phys. **85**, 086501 (2022).

[28] A. Omran, H. Levine, A. Keesling, G. Semeghini, T. T. Wang, S. Ebadi, H. Bernien, A. S. Zibrov, H. Pichler, S. Choi, J. Cui, M. Rossignolo, P. Rembold, S. Montangero, T. Calarco, M. Endres, M. Greiner, V. Vuletić, and M. D. Lukin, Generation and manipulation of Schrödinger cat states in Rydberg atom arrays, Science **365**, 570 (2019).

[29] S. Dooley, Robust quantum sensing in strongly interacting systems with many-body scars, PRX Quantum **2**, 020330 (2021).

[30] J.-Y. Desaules, F. Pietracaprina, Z. Papić, J. Goold, and S. Pappalardi, Extensive Multipartite Entanglement from su(2) Quantum Many-Body Scars, Phys. Rev. Lett. **129**, 020601 (2022).

[31] S. Dooley, S. Pappalardi, and J. Goold, Entanglement enhanced metrology with quantum many-body scars, Phys. Rev. B **107**, 035123 (2023).

[32] M. Brenes, M. Dalmonte, M. Heyl, and A. Scardicchio, Many-Body Localization Dynamics from Gauge Invariance, Phys. Rev. Lett. **120**, 030601 (2018).

[33] F. M. Surace, P. P. Mazza, G. Giudici, A. Lerose, A. Gambassi, and M. Dalmonte, Lattice Gauge Theories and String Dynamics in Rydberg Atom Quantum Simulators, Phys. Rev. X **10**, 021041 (2020).

[34] D. Banerjee and A. Sen, Quantum Scars from Zero Modes in an Abelian Lattice Gauge Theory on Ladders, Phys. Rev. Lett. **126**, 220601 (2021).

[35] A. S. Aramthottil, U. Bhattacharya, D. González-Cuadra, M. Lewenstein, L. Barbiero, and J. Zakrzewski, Scar states in deconfined $\mathbb{Z}_2$ lattice gauge theories, Phys. Rev. B **106**, L041101 (2022).

[36] S. Biswas, D. Banerjee, and A. Sen, Scars from protected zero modes and beyond in U(1) quantum link and quantum dimer models, SciPost Phys. **12**, 148 (2022).

[37] S. Weinberg, *The Quantum Theory of Fields*, Vol. 2: Modern Applications (Cambridge University Press, Cambridge, 1995).

[38] C. Gattringer and C. Lang, *Quantum Chromodynamics on the Lattice: An Introductory Presentation*, Lecture Notes in Physics (Springer, Berlin, 2009).

[39] A. Zee, *Quantum Field Theory in a Nutshell* (Princeton University Press, Princeton, NJ, 2003).

[40] R. P. Feynman and P. Cziffra, *Quantum Electrodynamics*, A Lecture Note and Reprint Series (Basic Books, New York, 1962).

[41] E. A. Martinez, C. A. Muschik, P. Schindler, D. Nigg, A. Erhard, M. Heyl, P. Hauke, M. Dalmonte, T. Monz, P. Zoller, and R. Blatt, Real-time dynamics of lattice gauge theories with a few-qubit quantum computer, Nature (London) **534**, 516 (2016).

[42] C. Muschik, M. Heyl, E. Martinez, T. Monz, P. Schindler, B. Vogell, M. Dalmonte, P. Hauke, R. Blatt, and P. Zoller, U(1) Wilson lattice gauge theories in digital quantum simulators, New J. Phys. **19**, 103020 (2017).

[43] N. Klco, E. F. Dumitrescu, A. J. McCaskey, T. D. Morris, R. C. Pooser, M. Sanz, E. Solano, P. Lougovski, and M. J. Savage, Quantum-classical computation of Schwinger model dynamics using quantum computers, Phys. Rev. A **98**, 032331 (2018).

[44] A. Keesling, A. Omran, H. Levine, H. Bernien, H. Pichler, S. Choi, R. Samajdar, S. Schwartz, P. Silvi, S. Sachdev, P. Zoller, M. Endres, M. Greiner, V. Vuletić, and M. D. Lukin, Quantum Kibble–Zurek mechanism and critical dynamics on a programmable Rydberg simulator, Nature (London) **568**, 207 (2019).

[45] C. Kokail, C. Maier, R. van Bijnen, T. Brydges, M. K. Joshi, P. Jurcevic, C. A. Muschik, P. Silvi, R. Blatt, C. F. Roos, and P. Zoller, Self-verifying variational quantum simulation of lattice models, Nature (London) **569**, 355 (2019).

[46] F. Görg, K. Sandholzer, J. Minguzzi, R. Desbuquois, M. Messer, and T. Esslinger, Realization of density-dependent Peierls phases to engineer quantized gauge fields coupled to ultracold matter, Nat. Phys. **15**, 1161 (2019).

[47] C. Schweizer, F. Grusdt, M. Berngruber, L. Barbiero, E. Demler, N. Goldman, I. Bloch, and M. Aidelsburger, Floquet approach to $\mathbb{Z}2$ lattice gauge theories with ultracold atoms in optical lattices, Nat. Phys. **15**, 1168 (2019).

[48] A. Mil, T. V. Zache, A. Hegde, A. Xia, R. P. Bhatt, M. K. Oberthaler, P. Hauke, J. Berges, and F. Jendrzejewski, A scalable realization of local U(1) gauge invariance in cold atomic mixtures, Science **367**, 1128 (2020).

[49] N. Klco, M. J. Savage, and J. R. Stryker, SU(2) non-Abelian gauge field theory in one dimension on digital quantum computers, Phys. Rev. D **101**, 074512 (2020).

[50] B. Yang, H. Sun, R. Ott, H.-Y. Wang, T. V. Zache, J. C. Halimeh, Z.-S. Yuan, P. Hauke, and J.-W. Pan, Observation of gauge invariance in a 71-site Bose–Hubbard quantum simulator, Nature (London) **587**, 392 (2020).

[51] Z.-Y. Zhou, G.-X. Su, J. C. Halimeh, R. Ott, H. Sun, P. Hauke, B. Yang, Z.-S. Yuan, J. Berges, and J.-W. Pan, Thermalization dynamics of a gauge theory on a quantum simulator, Science **377**, 311 (2022).

[52] I. Bloch, J. Dalibard, and W. Zwerger, Many-body physics with ultracold gases, Rev. Mod. Phys. **80**, 885 (2008).

[53] W. S. Bakr, J. I. Gillen, A. Peng, S. Fölling, and M. Greiner, A quantum gas microscope for detecting single atoms in a Hubbard-regime optical lattice, Nature (London) **462**, 74 (2009).

[54] U.-J. Wiese, Ultracold quantum gases and lattice systems: Quantum simulation of lattice gauge theories, Ann. Phys. (Berlin) **525**, 777 (2013).

[55] M. C. Bañuls, R. Blatt, J. Catani, A. Celi, J. I. Cirac, M. Dalmonte, L. Fallani, K. Jansen, M. Lewenstein, S.

Montangero, C. A. Muschik, B. Reznik, E. Rico, L. Tagliacozzo, K. Van Acoleyen, F. Verstraete, U.-J. Wiese, M. Wingate, J. Zakrzewski, and P. Zoller, Simulating lattice gauge theories within quantum technologies, Eur. Phys. J. D **74**, 165 (2020).

[56] Y. Alexeev, D. Bacon, K. R. Brown, R. Calderbank, L. D. Carr, F. T. Chong, B. DeMarco, D. Englund, E. Farhi, B. Fefferman, A. V. Gorshkov, A. Houck, J. Kim, S. Kimmel, M. Lange, S. Lloyd, M. D. Lukin, D. Maslov, P. Maunz, C. Monroe *et al.*, Quantum computer systems for scientific discovery, PRX Quantum **2**, 017001 (2021).

[57] M. Aidelsburger, L. Barbiero, A. Bermudez, T. Chanda, A. Dauphin, D. González-Cuadra, P. R. Grzybowski, S. Hands, F. Jendrzejewski, J. Jünemann, G. Juzeliūnas, V. Kasper, A. Piga, S.-J. Ran, M. Rizzi, G. Sierra, L. Tagliacozzo, E. Tirrito, T. V. Zache, J. Zakrzewski *et al.*, Cold atoms meet lattice gauge theory, Philos. Trans. R. Soc. A **380**, 20210064 (2022).

[58] E. Zohar, Quantum simulation of lattice gauge theories in more than one space dimension: Requirements, challenges and methods, Philos. Trans. R. Soc. A **380**, 20210069 (2022).

[59] N. Klco, A. Roggero, and M. J. Savage, Standard model physics and the digital quantum revolution: Thoughts about the interface, Rep. Prog. Phys. **85**, 064301 (2022).

[60] L. Homeier, C. Schweizer, M. Aidelsburger, A. Fedorov, and F. Grusdt, $\mathbb{Z}_2$ lattice gauge theories and Kitaev's toric code: A scheme for analog quantum simulation, Phys. Rev. B **104**, 085138 (2021).

[61] S Chandrasekharan and U.-J Wiese, Quantum link models: A discrete approach to gauge theories, Nucl. Phys. B **492**, 455 (1997).

[62] J. Schwinger, Gauge invariance and mass. II, Phys. Rev. **128**, 2425 (1962).

[63] S. Coleman, R. Jackiw, and L. Susskind, Charge shielding and quark confinement in the massive Schwinger model, Ann. Phys. **93**, 267 (1975).

[64] D. Banerjee, M. Dalmonte, M. Müller, E. Rico, P. Stebler, U.-J. Wiese, and P. Zoller, Atomic Quantum Simulation of Dynamical Gauge Fields Coupled to Fermionic Matter: From String Breaking to Evolution after a Quench, Phys. Rev. Lett. **109**, 175302 (2012).

[65] V. Kasper, F. Hebenstreit, F. Jendrzejewski, M. K. Oberthaler, and J. Berges, Implementing quantum electrodynamics with ultracold atomic systems, New J. Phys. **19**, 023030 (2017).

[66] B. Mukherjee, Z. Cai, and W. V. Liu, Constraint-induced breaking and restoration of ergodicity in spin-1 PXP models, Phys. Rev. Res. **3**, 033201 (2021).

[67] J.-Y. Desaules, A. Hudomal, D. Banerjee, A. Sen, Z. Papić, and J. C. Halimeh, Prominent quantum many-body scars in a truncated Schwinger model, Phys. Rev. B **107**, 205112 (2023).

[68] T. V. Zache, M. V. Damme, J. C. Halimeh, P. Hauke, and D. Banerjee, Toward the continuum limit of a (1+1)D quantum link Schwinger model, Phys. Rev. D **106**, L091502 (2022).

[69] U. Schollwöck, The density-matrix renormalization group in the age of matrix product states, Ann. Phys. **326**, 96 (2011).

[70] S. Choi, C. J. Turner, H. Pichler, W. W. Ho, A. A. Michailidis, Z. Papić, M. Serbyn, M. D. Lukin, and D. A. Abanin, Emergent SU(2) Dynamics and Perfect Quantum Many-Body Scars, Phys. Rev. Lett. **122**, 220603 (2019).

[71] B. Buyens, S. Montangero, J. Haegeman, F. Verstraete, and K. Van Acoleyen, Finite-representation approximation of lattice gauge theories at the continuum limit with tensor networks, Phys. Rev. D **95**, 094509 (2017).

[72] M. C. Bañuls and K. Cichy, Review on novel methods for lattice gauge theories, Rep. Prog. Phys. **83**, 024401 (2020).

[73] J. C. Halimeh, M. V. Damme, T. V. Zache, D. Banerjee, and P. Hauke, Achieving the quantum field theory limit in far-from-equilibrium quantum link models, Quantum **6**, 878 (2021).

Editors' Suggestion

Prominent quantum many-body scars in a truncated Schwinger model

Jean-Yves Desaules [ID],[1] Ana Hudomal [ID],[1,2] Debasish Banerjee [ID],[3,4] Arnab Sen [ID],[5] Zlatko Papić [ID],[1] and Jad C. Halimeh [ID][6,7,*]

[1]*School of Physics and Astronomy, University of Leeds, Leeds LS2 9JT, United Kingdom*
[2]*Institute of Physics Belgrade, University of Belgrade, 11080 Belgrade, Serbia*
[3]*Theory Division, Saha Institute of Nuclear Physics, 1/AF Bidhan Nagar, Kolkata 700064, India*
[4]*Homi Bhabha National Institute, Training School Complex, Anushaktinagar, Mumbai 400094, India*
[5]*School of Physical Sciences, Indian Association for the Cultivation of Science, Kolkata 700032, India*
[6]*Department of Physics and Arnold Sommerfeld Center for Theoretical Physics (ASC),*
Ludwig-Maximilians-Universität München, Theresienstraße 37, D-80333 München, Germany
[7]*Munich Center for Quantum Science and Technology (MCQST), Schellingstraße 4, D-80799 München, Germany*

The high level of control and precision achievable in current synthetic quantum matter setups has enabled first attempts at quantum-simulating various intriguing phenomena in condensed matter physics, including those probing thermalization or its absence in closed quantum systems. In the companion Letter to this article [J.-Y. Desaules *et al.*, Phys. Rev. B **107**, L201105 (2023)], we have shown that quantum many-body scars, special low-entropy eigenstates that weakly break ergodicity in nonintegrable systems, arise in spin-S quantum link models that converge to $(1 + 1)$-dimensional lattice quantum electrodynamics (Schwinger model) in the Kogut-Susskind limit $S \to \infty$. In this work, we further demonstrate that quantum many-body scars exist in a truncated version of the Schwinger model, and are qualitatively more prominent than their counterparts in spin-S quantum link models. We illustrate this by, among other things, performing a finite-S scaling analysis that strongly suggests that scarring persists in the truncated Schwinger model in the limit $S \to \infty$. Although it does not asymptotically converge to the Schwinger model, the truncated formulation is relevant to synthetic quantum matter experiments, and also provides fundamental insight into the nature of quantum many-body scars, their connection to lattice gauge theories, and the thermalization dynamics of the latter. Our conclusions can be readily tested in current cold-atom setups.

I. INTRODUCTION

Recent advances in the development of synthetic quantum matter platforms that possess high levels of control and precision at the single-atom level [1] have revolutionized the study of exotic quantum phenomena [2,3]. There is a major ongoing effort in the scientific community to utilize this technological advancement to address various problems on analog and digital quantum simulators [4–7]. Of particular interest in this endeavor are quantum simulations probing the eigenstate thermalization hypothesis (ETH) that shed light on the nature of thermalization or lack thereof in closed quantum systems [8–13]. This has led to experimental observations of (pre)thermalization and out-of-equilibrium phase transitions in nonintegrable quantum many-body models [14–19].

Paradigms of strong ergodicity breaking such as many-body localization (MBL) [20–22] have also received major

experimental attention in recent years [23–30]. In MBL systems, sufficiently strong quenched disorder leads to localization in the dynamics of observables over all practically relevant evolution times. This disorder-induced MBL violates ETH in a way not so different from integrable models [31]. The strong disorder in the system gives rise to an extensive number of local integrals of motion [32,33], which can indefinitely delay thermalization. However, strong ergodicity breaking can also occur without any disorder, for example, when a constant electric field is introduced in a chain of interacting spinless fermions [34]. This Stark MBL has recently been demonstrated experimentally [35]. Moreover, it has recently been shown that in Stark-MBL systems there exist quasilocalized dynamical l-bits, which are exponentially stable in time and prohibit thermalization [36]. Yet another example of strong ergodicity breaking has appeared in the context of gauge theories [37–46], where quenches from an initial state forming a superposition over an extensive number of gauge superselection sectors lead to localized dynamics. This disorder-free localization is caused by an effective disorder emerging over the different background charges of the underlying superselection sectors.

More recently, a new concept of *weak* ergodicity breaking, dubbed quantum many-body scars, has received much attention [47,48]. Scarring involves the presence of special

nonthermal eigenstates existing at equal energy intervals over the entire spectrum of a nonintegrable, usually disorder-free, interacting model [49–55]. A characteristic signature of scarred eigenstates is their anomalously low bipartite entanglement entropy, even when they exist in the middle of the spectrum [56,57]. As such, these eigenstates span a "cold" subspace, weakly connected to the rest of the Hilbert space [51]. When a system is prepared in this cold subspace and subsequently quenched, the dynamics will take significantly longer to "leak out" into the rest of the Hilbert space, thus delaying the thermalization of the system. This manifests as persistent oscillations in certain local observables, reminiscent of single-particle chaotic systems [58]. Scarred dynamics was first observed in a Rydberg-atom system [59,60]. More recently, various signatures of weak ergodicity breaking have also been observed in several other ultracold-atom platforms [61–64].

Interestingly, the Ising-type quantum spin model realized in the experiment of Ref. [59] was later shown to map onto the spin-$\frac{1}{2}$ U(1) quantum link model (QLM), which is a quantum link formulation [65,66] of (1+1)-dimensional [(1 + 1)D] quantum electrodynamics on a lattice, known as the lattice Schwinger model. This, along with other works proving the existence of quantum many-body scars in various discrete lattice gauge theories [67–69] and the necessity of gauge-symmetry stability for their robustness [70], has led to the natural question of whether scars are an inherent feature of "standard" lattice gauge theories with a continuous configuration space. In the companion Letter to this article [71], we have shown that quantum many-body scars persist at larger link spin lengths $S > \frac{1}{2}$ in the spin-S U(1) QLM in the form of *resonant scarring* when the initial state is an extreme vacuum, defined as the most highly excited vacuum state. We have additionally presented evidence of *detuned scarring*, recently demonstrated experimentally for $S = \frac{1}{2}$ [64], also for $S > \frac{1}{2}$ when starting in the physical vacuum or the charge-proliferated state. This all indicates that scarring behavior in the U(1) QLM is quite rich also beyond $S = \frac{1}{2}$. But is this richness directly related to the specific quantum link formulation that begets the U(1) QLM from the lattice Schwinger model, or can other, perhaps cruder, representations of the latter also yield equally rich scarring behavior?

In this work, we address the previous question by contrasting the spin-S U(1) QLM with the spin-S *truncated Schwinger model* (TSM), in which the gauge field is a crude truncation of its counterpart in the lattice Schwinger model. We show that the TSM exhibits qualitatively more pronounced scarring behavior than the spin-S U(1) QLM. Furthermore, through a finite-S scaling analysis, we argue that scarring in the TSM is likely to persist in the Kogut-Susskind limit $S \to \infty$. The QLM, on the other hand, is shown to exhibit scarring signatures for any $S \leqslant 4$ amenable to numerical analysis. At the same time, the QLM also exhibits much stronger finite-size fluctuations compared to the TSM, which ultimately preclude a reliable extrapolation to $S \to \infty$.

The rest of the paper is organized as follows: In Sec. II, we first present the mappings used to obtain the two constrained spin models [the spin-S U(1) QLM and TSM] that we investigate in this work from the lattice Schwinger model, and we showcase their scarring behavior. In Sec. III, we show how

these models differ from the generalized PXP model studied in Ref. [58], and that they have a different semiclassical limit. In Sec. IV, we investigate the fate of scarring in the limit $S \to \infty$, and contrast the TSM and QLM results. Finally, in Sec. V, we summarize our findings and discuss their implications. The Appendixes contain further information and (numerical and analytical) details supporting the main results of the paper.

II. SPIN-*S* U(1) QUANTUM LINK MODEL AND TRUNCATED SCHWINGER MODEL

We now consider the spin-S U(1) QLM and the TSM, both of which are directly relevant to modern experiments probing quantum electrodynamics in synthetic quantum matter. The lattice Schwinger model, which is quantum electrodynamics in $(1 + 1)$ dimensions, includes gauge fields with an infinite-dimensional local Hilbert space. Whereas the spin-S U(1) QLM substitutes these operators with spin-S matrices, retrieving the lattice Schwinger model asymptotically in the limit $S \to \infty$, the TSM involves explicitly truncating these operators. In contrast to the case of the QLM, this forbids an asymptotic approach to the lattice Schwinger model as $S \to \infty$ in the case of the TSM. Nevertheless, both the QLM and TSM are lattice gauge theories, and can therefore provide deep insights into the connection between the underlying gauge symmetry and the corresponding scarring behavior.

A. Mapping to a constrained spin model

Let us now take advantage of the gauge symmetry of the spin-S U(1) QLM and the TSM in order to map them into spin models that are invariant under translation. To achieve this, we follow a procedure similar to the one used in Ref. [72] to map to the PXP model. We start in the lattice Schwinger model, described by the Hamiltonian

$$\hat{H} = \frac{J}{2a} \sum_{j=1}^{L} (\hat{\phi}_j^\dagger \hat{U}_{j,j+1} \hat{\phi}_{j+1} + \text{H.c.})$$
$$+ \mu \sum_{j=1}^{L} (-1)^j \hat{\phi}_j^\dagger \hat{\phi}_j + \frac{a}{2} \sum_{j=1}^{L} (\hat{E}_{j,j+1})^2, \quad (1)$$

where a is the lattice spacing and μ is the fermionic mass. We henceforth set $a = 1$ throughout this work. Matter fields are represented by the staggered fermionic operators $\hat{\phi}_j^{(\dagger)}$ at lattice site j, while the gauge and electric fields $\hat{U}_{j,j+1}$ and $\hat{E}_{j,j+1}$ reside on the link between lattice sites j and $j + 1$, and satisfy the commutation relations

$$[\hat{U}_{j,j+1}, \hat{U}_{l,l+1}^\dagger] = 0, \quad (2a)$$

$$[\hat{E}_{j,j+1}, \hat{U}_{l,l+1}] = g\delta_{j,l}\hat{U}_{j,j+1}. \quad (2b)$$

The lattice Schwinger model is a U(1) gauge theory, and Gauss's law is given by $\hat{G}_j |\text{phys}\rangle = 0$, $\forall j$, where $|\text{phys}\rangle$ is a physical state and the local gauge-symmetry generator is

$$\hat{G}_j = \hat{E}_{j,j+1} - \hat{E}_{j-1,j} - g \left[\hat{\phi}_j^\dagger \hat{\phi}_j - \frac{1 - (-1)^j}{2} \right], \quad (3)$$

and g is the gauge coupling.

In the quantum link formulation, the gauge and electric fields are represented by finite-dimensional spin-S operators:

$$\hat{U}_{j,j+1} \rightarrow \frac{\hat{s}^+_{j,j+1}}{\sqrt{S(S+1)}}, \tag{4a}$$

$$\hat{E}_{j,j+1} \rightarrow g\hat{s}^z_{j,j+1}, \tag{4b}$$

where the factor $1/\sqrt{S(S+1)}$ ensures the correct scaling with S [73]. This can be checked by substituting (4) into the commutation relations (2) to get

$$[\hat{U}_{j,j+1}, \hat{U}^\dagger_{l,l+1}] \rightarrow \frac{1}{S(S+1)}[\hat{s}^+_{j,j+1}, \hat{s}^-_{l,l+1}]$$

$$= \frac{2\delta_{j,l}}{S(S+1)}\hat{s}^z_{j,j+1}, \tag{5a}$$

$$[\hat{E}_{j,j+1}, \hat{U}_{l,l+1}] \rightarrow \frac{g}{\sqrt{S(S+1)}}[\hat{s}^z_{j,j+1}, \hat{s}^+_{j,j+1}]$$

$$= g\delta_{j,l}\frac{\hat{s}^+_{j,j+1}}{\sqrt{S(S+1)}}. \tag{5b}$$

Whereas Eq. (2b) is automatically satisfied at any S through Eq. (5b), we find that Eq. (2a) is achieved through Eq. (5a) asymptotically in the limit $S \rightarrow \infty$.

In order to obtain a Hamiltonian that is invariant under translation, we directly incorporate the particle-hole transformation

$$\hat{\phi}_j \rightarrow \frac{1+(-1)^j}{2}\hat{\phi}_j + \frac{1-(-1)^j}{2}\hat{\phi}^\dagger_j. \tag{6}$$

This has the consequence of taking

$$\hat{\phi}^\dagger_j\hat{\phi}_j \rightarrow \frac{1-(-1)^j}{2} + (-1)^j\hat{\phi}^\dagger_j\hat{\phi}_j, \tag{7}$$

due to the fermionic anticommutation relations. For our field operators, this particle-hole transformation takes the form

$$\hat{U}_{j,j+1} \rightarrow \frac{1-(-1)^j}{2\sqrt{S(S+1)}}\hat{s}^+_{j,j+1} + \frac{1+(-1)^j}{2\sqrt{S(S+1)}}\hat{s}^-_{j,j+1}, \tag{8a}$$

$$\hat{E}_{j,j+1} \rightarrow g(-1)^{j+1}\hat{s}^z_{j,j+1}, \tag{8b}$$

rendering Hamiltonian (1) in the form

$$\hat{H} = \frac{J}{2\sqrt{S(S+1)}}\sum_{j=1}^L (\hat{\phi}_j\hat{s}^+_{j,j+1}\hat{\phi}_{j+1} + \text{H.c.})$$

$$+ \mu\sum_{j=1}^L \hat{\phi}^\dagger_j\hat{\phi}_j + \frac{g^2}{2}\sum_{j=1}^L \left(\hat{s}^z_{j,j+1}\right)^2. \tag{9}$$

The generator of Gauss's law can now be rewritten in the simple form

$$\hat{G}_j = (-1)^{j+1}g\left(\hat{s}^z_{j,j+1} + \hat{s}^z_{j-1,j} + \hat{\phi}^\dagger_j\hat{\phi}_j\right). \tag{10}$$

As $\hat{\phi}^\dagger_j\hat{\phi}_j$ can only be equal to zero or $\mathbb{1}$, this means that $\hat{s}^z_{j,j+1} + \hat{s}^z_{j-1,j}$ must always be equal to zero or $-\mathbb{1}$, respectively, in the physical sector $\hat{G}_j|\text{phys}\rangle = 0$, $\forall j$. Restricting to this sector and employing periodic boundary conditions (PBC), we can therefore replace the mass term by $-\mu\sum_j (\hat{s}^z_{j,j+1} + \hat{s}^z_{j-1,j}) = -2\mu\sum_j \hat{s}^z_{j,j+1}$. By then integrating out the fermionic degrees of freedom, we end up with the translation-invariant Hamiltonian

$$\hat{H}_{\text{QLM}} = J_S\,\hat{\mathcal{P}}\left(\sum_j \hat{s}^x_j\right)\hat{\mathcal{P}} - 2\mu\sum_j \hat{s}^z_j + \frac{g^2}{2}\sum_j \left(\hat{s}^z_j\right)^2, \tag{11}$$

where $\hat{\mathcal{P}}$ is a projector that annihilates all states outside of the physical sector, and $J_S = J/\sqrt{S(S+1)}$.

However, this is not the only way to obtain a finite-dimensional model for which we recover the lattice Schwinger model at infinite S. One can also replace $\hat{U}_{j,j+1}$ in Eq. (1) not by a spin-S operator but by the $[(2S+1) \times (2S+1)]$-dimensional operator $\hat{\tau}^+_{j,j+1}$. This operator has the same structure as the $\hat{s}^+_{j,j+1}$, with the exception that each of the latter's nonzero matrix elements is replaced by 1. In other words, $\hat{\tau}^+_{j,j+1}$ is merely the $[(2S+1) \times (2S+1)]$-dimensional truncated version of $\hat{U}_{j,j+1}$ at its center. The field operator can then be represented by the matrix $\hat{\tau}^z_{j,j+1} = \hat{s}^z_{j,j+1}$, and we thus identify our fields as

$$\hat{U}_{j,j+1} \rightarrow \hat{\tau}^+_{j,j+1}, \tag{12a}$$

$$\hat{E}_{j,j+1} \rightarrow g\hat{\tau}^z_{j,j+1}. \tag{12b}$$

The commutation relations (2) then become

$$[\hat{U}_{j,j+1}, \hat{U}^\dagger_{l,l+1}] \rightarrow [\hat{\tau}^+_{j,j+1}, \hat{\tau}^-_{l,l+1}] = \delta_{j,l}\hat{\Sigma}_{j,j+1} = \delta_{j,l}\begin{pmatrix} 1 & 0 & \cdots & 0 & 0 \\ 0 & & & & 0 \\ \vdots & & \mathbf{0} & & \vdots \\ 0 & & & & 0 \\ 0 & 0 & \cdots & 0 & -1 \end{pmatrix}_{j,j+1}, \tag{13a}$$

$$[\hat{E}_{j,j+1}, \hat{U}_{l,l+1}] \rightarrow g[\hat{\tau}^z_{j,j+1}, \hat{\tau}^+_{j,j+1}] = g\delta_{j,l}\hat{\tau}^+_{j,j+1}. \tag{13b}$$

Similarly to the case of the QLM, the commutation relation (2b) is satisfied through Eq. (13b) for any S. However, Eq. (2a) is satisfied through Eq. (13a) only strictly at infinite S, rather than approach it asymptotically as in the case of the QLM. Indeed, the commutation relation (13a) is always equal to $\hat{\Sigma}_{j,j+1}$, which is a $(2S+1) \times (2S+1)$ matrix with zeros everywhere except in entries $(1,1)$ and $(2S+1, 2S+1)$, which are, respectively, plus and minus unity.

By employing the particle-hole transformations (7) to set

$$\hat{U}_{j,j+1} \rightarrow \frac{1-(-1)^j}{2}\hat{\tau}^+_{j,j+1} + \frac{1+(-1)^j}{2}\hat{\tau}^-_{j,j+1}, \tag{14a}$$

$$\hat{E}_{j,j+1} \rightarrow g(-1)^{j+1}\hat{\tau}^z_{j,j+1}, \tag{14b}$$

and utilizing Gauss's law to integrate out the fermionic degrees of freedom as done before in the case of the QLM, we

obtain

$$\hat{H}_{\mathrm{TSM}} = \hat{\mathcal{P}} \left(\sum_j \hat{\tau}_j^x \right) \hat{\mathcal{P}} - 2\mu \sum_j \hat{\tau}_j^z + \frac{g^2}{2} \sum_j \left(\hat{\tau}_j^z \right)^2, \quad (15)$$

where $\hat{\tau}_j^x = (\hat{\tau}_j^+ + \hat{\tau}_j^-)/2$ is the tridiagonal matrix with entries of 0 along the principal diagonal and entries of $\frac{1}{2}$ along both the subdiagonal and superdiagonal. Note that as $\hat{\tau}_{j,j+1}^z = \hat{s}_{j,j+1}^z$, Gauss's law goes through the same transformation as for the QLM, and the global projector $\hat{\mathcal{P}}$ is the same in the two models. As a consequence, the Hilbert space is also the same. However, due to the difference in the matrix elements of the Hamiltonian, the two models are only equivalent (up to an overall multiplicative factor) for $S = \frac{1}{2}$ and $S = 1$, which are the only cases where the spin operator $\hat{s}_j^x$ has equal matrix elements.

The difference on how the TSM and QLM approach the Kogut-Susskind limit ($S \to \infty$) can be highlighted by looking at the 2-norms of the commutators (5a) and (13a). As both operators are diagonal, the 2-norm is simply the largest absolute value of any diagonal entry. In the case of the TSM, the commutator in Eq. (13a) will always have a 2-norm of unity for any finite S no matter how large S is. In the case of the QLM, the commutator of Eq. (5a) has a 2-norm of $2/(S+1)$. Consequently, the QLM asymptotically approaches the lattice Schwinger model as $S \to \infty$, while the TSM does not. We emphasize that this result does not depend on the choice of the norm. As an example, even if we choose the Frobenius norm we get in the case of the TSM a norm of $\sqrt{2}$ at any S, while in the case of the QLM it is equal to $2\sqrt{(2S+1)/[3S(S+1)]}$. This is the main reason why from a gauge-theory perspective the QLM is favored over the TSM, as one can employ the QLM and controllably study the approach to the Kogut-Susskind limit of quantum electrodynamics. Nevertheless, it is important to emphasize that here we are interested in scarring behavior, and as we will show in this work, the TSM has more prominent scars than the QLM. Therefore, from a quantum many-body scars perspective and given its experimental feasibility, the TSM is fundamentally as relevant for our purposes as the QLM is.

For $S = \frac{1}{2}$, both Eqs. (11) and (15) reduce to the well-known PXP model [74,75] (although with a slightly different prefactor in front). However, we stress that for $S > \frac{1}{2}$ these models are different from the generalized spin-S PXP model in Ref. [58], and we address these differences in Sec. III.

Before delving into the properties of the QLM and TSM, we mention a few states that have physical significance for any value of S. The first one is the vacuum state (i.e., with no matter present in the Schwinger model), with the highest possible value of the electric field, which we shall henceforth refer to as the *extreme vacuum*. This state corresponds to the ground state of the TSM or QLM with $\mu \to \infty$ and $g^2 < 0$. Correspondingly, we will denote it by $|0_-\rangle$, with the subscript denoting the fact that g^2 is negative. This state is doubly degenerate for any value of S, and, working in the basis of the $\hat{s}^z$, we set $|0_-\rangle = |S, -S, \ldots, S, -S\rangle$ and $|0'_-\rangle = |-S, S, \ldots, -S, S\rangle$. For a more physical set of parameters, we can have the ground state at $\mu \to \infty$ but with g^2 positive. We call this state the *physical vacuum* and denote it by $|0_+\rangle$. The physical vacuum state is $|0_+\rangle = |0, 0 \ldots 0, 0, 0\rangle$ for integer

S. For half-integer S, it is doubly degenerate and given by $|0_+\rangle = |\frac{1}{2}, -\frac{1}{2}, \ldots, \frac{1}{2}, -\frac{1}{2}\rangle$ and $|0'_+\rangle = |-\frac{1}{2}, \frac{1}{2}, \ldots, -\frac{1}{2}, \frac{1}{2}\rangle$. In this formulation, it is immediately clear that for the PXP case (i.e., $S = \frac{1}{2}$) the extreme and physical vacua are identical, which is expected as the electric field coupling term is just an inconsequential energetic constant. We also are interested in the ground state of the TSM and QLM for $\mu \to -\infty$ and g^2 positive. In that case the presence of fermions is energetically favorable, and so the ground state is the *charge-proliferated state* with the maximal matter occupation, which we denote by $|CP\rangle$. For integer S, this state is doubly degenerate with the two states being $|CP\rangle = |0, -1, \ldots, 0, -1\rangle$ and $|CP'\rangle = |-1, 0, \ldots - 1, 0\rangle$. For half-integer S, it is nondegenerate and given by $|CP\rangle = |-\frac{1}{2}, -\frac{1}{2}, \ldots, -\frac{1}{2}, -\frac{1}{2}\rangle$. This state corresponds to the polarized state in the PXP model.

To probe dynamics, below we study the system's response to a global quench: we prepare the system in the ground state for some values of μ and g^2, and then suddenly quench these parameters to different values. The initial state is no longer the ground state, or even an eigenstate, of the post-quench Hamiltonian. Instead, it is a highly excited state and we are effectively probing the out-of-equilibrium dynamics. Note that any small perturbation would lift the degeneracy of the ground-state manifold, hence, we always select a single state in that manifold instead of a superposition of all of them.

To obtain the eigenstates and eigenenergies of the post-quench Hamiltonian, below we make use of the standard exact diagonalization method, implementing the symmetries of the system as well as the kinetic constraint due to Gauss's law. To simulate time evolution, we resort to sparse matrix techniques which allows us to access dynamics in system sizes for which full diagonalization is not possible. Specifically, we use the algorithm developed in Ref. [76] as implemented in the function `expm_multiply` of the Python package SCIPY to compute the action of e^{-iHt} on a pure state.

B. Resonant scarring: Quenches to $\mu = g = 0$

In the spin-$\frac{1}{2}$ QLM, the scarred states are the two vacua $|0_-\rangle = |0_+\rangle$ and $|0'_-\rangle = |0'_+\rangle$ for the quench Hamiltonian with $\mu = g = 0$ (resonant scarring). Numerical simulations show that for any $S > \frac{1}{2}$ only the extreme vacua $|0_-\rangle$ and $|0'_-\rangle$ exhibit scarring [71] (see Appendix A for results on the physical vacuum $|0_+\rangle$). A typical signature of scarring is high overlap of the scarred state with a small set of eigenstates that are approximately equally spaced in energy. We have demonstrated this for the spin-S U(1) QLM in Ref. [71] for the extreme vacua. However, this can be seen even more clearly for the TSM, as shown in the top panels of Fig. 1 for the overlap of the extreme vacuum with the eigenstates of the TSM at $\mu = g = 0$ for $S = \frac{3}{2}$ and 2. A top band with $2SL + 1$ states is well separated from the bulk of states. Note that for $S = \frac{1}{2}$ and 1, the TSM and QLM are identical, which is why we do not show results for these values of S as they can already be found in Ref. [71].

The band of high-overlap eigenstates defines the set of nonthermal eigenstates that lead to scarring when an initial state is prepared in their subspace. These eigenstates are expected to exhibit nonthermal properties such as anomalously
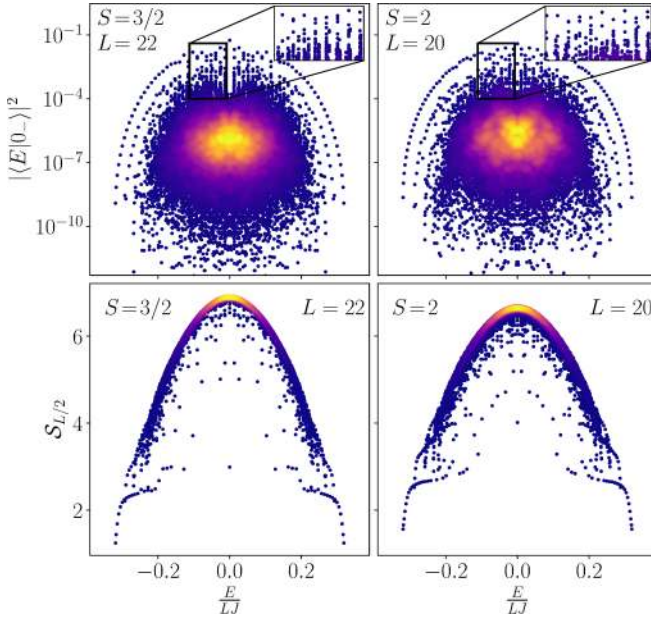
FIG. 1. Overlap between the extreme vacuum $|0_-\rangle$ and the energy eigenstates $|E\rangle$ (top) and entanglement entropy of the eigenstates $\mathcal{S}_{L/2}$ (bottom) in the spin-S TSM at $\mu = g = 0$. The top band of scarred eigenstates is clearly visible for all S, and the states in it have anomalously low entanglement entropy. The color indicates the density of data points, where yellow color implies higher density. In all cases, the Hilbert space has more than 4×10^5 states, with at least 2.5×10^4 states belonging to the relevant symmetry sector of the extreme vacua.
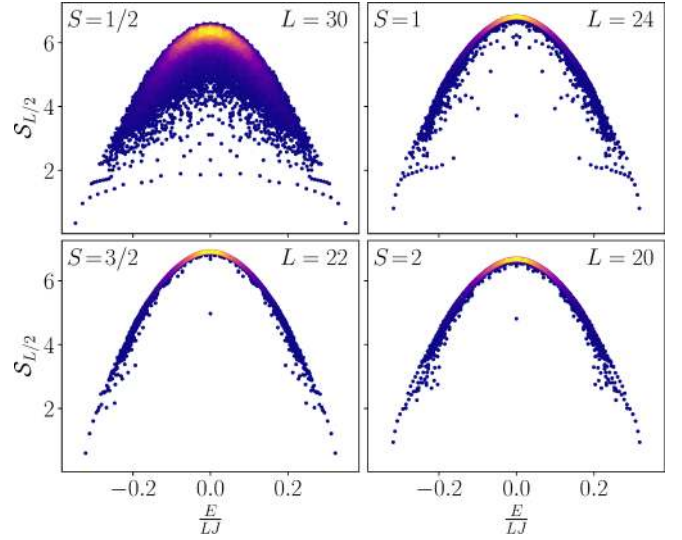

FIG. 2. Entanglement entropy of the eigenstates of the QLM for $S = \frac{1}{2}$ to $S = 2$. In contrast to the TSM, the scarred eigenstates away from the edges of the spectrum have high entanglement entropy in this case, close to that of the eigenstates belonging to the bulk of the spectrum, except for a single outlier with energy $E = 0$. The color indicates the density of data points, where yellow color implies higher density.

low bipartite entanglement entropy. For a pure state $|\psi\rangle$, the entanglement entropy is defined as the von Neumann entropy

$$\mathcal{S}_{L/2} = -\mathrm{tr}\rho_{L/2} \ln \rho_{L/2}, \qquad (16)$$

of the reduced density matrix $\rho_{L/2} = \mathrm{tr}_{L/2+1,...,L}|\psi\rangle\langle\psi|$, obtained by partitioning the chain in the middle and tracing out one half of it (denoted by $\mathrm{tr}_{L/2+1,...,L}$). The bottom panels of Fig. 1 show the entanglement entropy $\mathcal{S}_{L/2}$ evaluated for each eigenstate in the spectrum of the TSM with $S = \frac{3}{2}$ and $S = 2$. The distribution of entanglement entropies in Fig. 1 is unusually broad for a thermalizing system, with some states possessing much lower entropy than other states at roughly the same energy density, even near the middle of the spectrum. This is reminiscent of previous examples of quantum many-body scars in the literature, including the PXP model [77] and constrained quantum clock models [78]. In contrast, for the QLM at $S > 1$, the distribution of entanglement entropies is much narrower (see Fig. 2) and resembles that of the Affleck-Kennedy-Lieb-Tasaki model, which also hosts scarred states [50]. In this case, the outliers with anomalous low entropy are not clearly visible, apart from a single eigenstate with energy $E = 0$.

We attribute the difference in the distribution of the entanglement entropy of eigenstates in the TSM and QLM models to the "dilution" of scarring among a larger number of eigenstates in the second model. Indeed, the overlap between $|0_-\rangle$ and the eigenstates of the QLM does not show a single well-separated band of states with high overlap, but rather a

set of $2SL + 1$ towers rising above the bulk of states [71]. Thus, instead of having one scarred eigenstate per tower with highly atypical behavior, we have a larger number of eigenstates sharing this atypicality. This is similar to what is observed in the PXP model in the largest numerically accessible system sizes [77], where certain scarred eigenstates were observed to hybridize with their neighbors belonging to the same tower. Due to hybridization, the entropy of the top scarred eigenstate is typically increased, as the state becomes slightly more "thermal," while the other state involved in the hybridization becomes slightly more "atypical." As a result of this, near the middle of the spectrum in the QLM there is no single eigenstate with very low entanglement entropy. Instead, there are several outliers just below the band of thermal states. Similar phenomenology has been observed in other models where scars are not protected by an exact dynamical symmetry [79,80]. As S is increased, the towers seem to get denser, without any clear state at the top even relatively close to the edges of the spectrum. As a consequence, the outliers with low entanglement entropy get pulled increasingly closer to the thermal states in the case of the QLM. This is in contrast with the TSM, where both in the overlap and entanglement entropy, the scarred eigenstates remain clearly separated from their thermal counterparts up to the largest system sizes accessible numerically. The only exception for the QLM is the presence of a single low-entangled state with energy $E = 0$. This energy has a macroscopic degeneracy due to an interplay of the symmetries of the model, similar to Ref. [77]. It is therefore expected that some low-entropy states can be obtained by forming appropriate linear combinations of degenerate states, as demonstrated in Refs. [67,81].
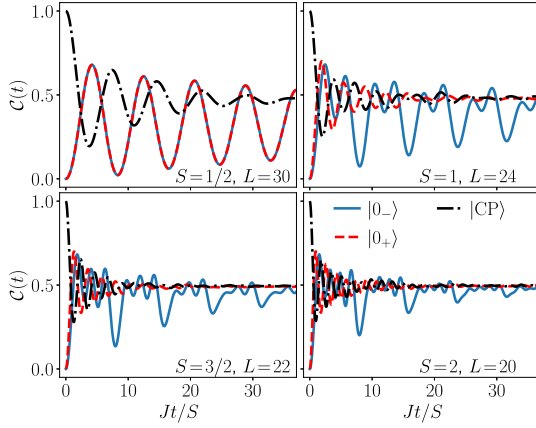
FIG. 3. Dynamics of the chiral condensate (18) in the wake of a quench with the QLM Hamiltonian (11) at $\mu = g = 0$ for initial states $|0_-\rangle$, $|0_+\rangle$, and $|CP\rangle$. Local observables show persistent oscillations up to all accessible times when the initial state is prepared in the extreme vacuum, a characteristic of scarred dynamics. In all other cases, the chiral condensate quickly thermalizes. We note again the exception for the case of $S = \frac{1}{2}$, where the physical vacuum is itself the extreme vacuum.

In Ref. [71], we have shown that zero-mass zero-g quenches in the QLM starting in $|0_-\rangle$ lead to revivals in the fidelity,

$$\mathcal{F}(t) = |\langle \psi_0 | \psi(t) \rangle|^2, \qquad (17)$$

where $|\psi_0\rangle$ is the initial state and $|\psi(t)\rangle = e^{-i\hat{H}t} |\psi_0\rangle$ with $\hat{H}$ being the quench Hamiltonian. These quenches also reveal an anomalously low and slowly growing entanglement entropy. We now introduce another useful quantity to probe the ergodicity of quench dynamics. The chiral condensate

$$\mathcal{C}(t) = \frac{1}{2} + \frac{1}{2L} \sum_{j=1}^{L} (-1)^j \langle \psi(t) | \hat{\sigma}_j^z | \psi(t) \rangle, \qquad (18)$$

and it is a measure of the spontaneous breaking of the chiral symmetry corresponding to fermions in the model. Quenching with the QLM Hamiltonian at $\mu = g = 0$ for different initial conditions, we plot the chiral-condensate dynamics in Fig. 3 for $S = \frac{1}{2}$ to 2. The results show strikingly nonthermal behavior for quenches starting in $|0_-\rangle$. Indeed, over the simulated timescales there are persistent oscillations in the signal and no equilibration, in agreement with experimental results for the spin-$\frac{1}{2}$ U(1) QLM [59,64]. On the other hand, systems prepared in $|0_+\rangle$ (for $S > \frac{1}{2}$) or $|CP\rangle$ show relatively fast thermalization, where oscillations are quickly suppressed in the dynamics, consistent with the ETH. For the extreme vacua, the leading frequency of the oscillations of $\mathcal{C}(t)$ is twice that of $\mathcal{F}(t)$. The reason behind this is that the dynamics after a quench from $|0_-\rangle$ consists of a series of state transfers to $|0'_-\rangle$ and back. So after one full revival period the state comes back close to $|0_-\rangle$, but at half of that period it is close to $|0'_-\rangle$. The fidelity revival is only high in the first case, but as both states are vacua, the chiral condensate value is close to zero at both times. Smaller oscillations at a faster frequency can also be seen; see Sec. IV for more details.
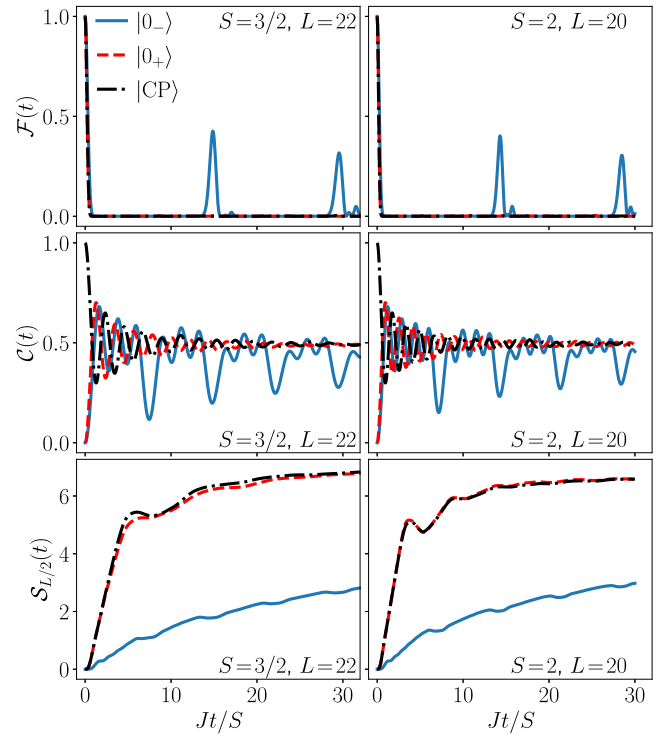

FIG. 4. Dynamics of the fidelity, chiral condensate, and bipartite entanglement entropy for the TSM with $S = \frac{3}{2}$ and $S = 2$ after a zero-mass quench. For all these quantities, the extreme vacuum $|0_-\rangle$ shows anomalous dynamics whereas $|0_+\rangle$ and $|CP\rangle$ are thermalizing, as expected.

For the TSM, we find qualitatively the same behavior as in the QLM. This is true for fidelity, entanglement entropy, and chiral condensate, as shown in Fig. 4. Just as in the case of the QLM, scarring dynamics occurs only when starting in $|0_-\rangle$ and the quench Hamiltonian is that of the TSM (15) at $\mu = g = 0$. This is evident in the prominence of fidelity revivals when starting in $|0_-\rangle$, while starting in $|0_+\rangle$ or $|CP\rangle$ leads to the fidelity exhibiting fast decay without revivals, which is typical of a thermalizing system. Quantitatively, we find better revivals in the case of the TSM than the QLM [71] when starting in $|0_-\rangle$. This is surprising because unlike a free-spin model $\hat{H} = \hat{s}^x$, the unconstrained version of the TSM, $\hat{H} = \hat{\tau}^x$, does not lead to perfect revivals for larger values of S. Indeed, the latter can be mapped to a single particle with uniform hopping on a one-dimensional chain with $2S + 1$ states, for which it has been proven that perfect state transfer or revivals are not possible beyond $S = 1$ when starting at one end of the chain [82].

For the TSM, we also find a different scaling of the revival period T_{TSM} with S compared to the QLM. Unlike the QLM where we observed numerically that $T_{\text{QLM}} \approx 5.13\pi S$ scales linearly with S [71], in the TSM the scaling is closer to $\sqrt{S(S+1)}$. In particular, we find that the revival period can be approximated as $T_{\text{TSM}} \approx 11.5\sqrt{S(S+1)}/J$, which is relatively accurate for small S. As in the case of the QLM, the revival frequency is set by the energy spacing of scarred states near the middle of the spectrum.
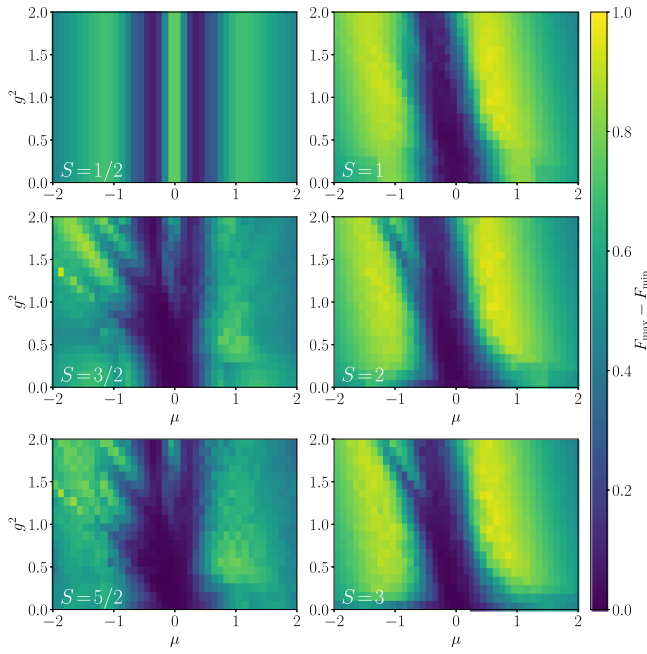
FIG. 5. Difference between the maximum and minimum amplitudes of the fidelity revival when quenching from the state $|0_+\rangle$ for $L = 16$ and various values of μ and g^2 in the spin-S QLM. The revival pattern is different for half-integer vs integer S, but in both cases we find regions in the phase diagram with clear revivals.

FIG. 6. Difference between the maximum and minimum amplitudes of the fidelity revival when quenching from the state $|CP\rangle$ for $L = 16$ and various values of μ and g^2 in the QLM. For half-integer spin, we find detuned scarring for all S, similar to the spin-$\frac{1}{2}$ PXP model [64].

Turning to local observables such as the chiral condensate, we find persistent oscillations in the latter over all investigated evolution times when the quench starts in $|0_-\rangle$, but not in $|0_+\rangle$ and $|CP\rangle$ where the oscillations are quickly damped, indicative of thermalization. Moreover, in the case of $|0_-\rangle$ initial state, we find more pronounced oscillations in the case of the TSM compared to the QLM [71].

Further confirming the existence of scarring for zero-mass zero-g quenches in the TSM and $|0_-\rangle$ initial state, we find an anomalously slow growth of entanglement entropy in the time-evolved state, in sharp contrast to the quench starting in $|0_+\rangle$ or $|CP\rangle$ where $\mathcal{S}_{L/2}(t)$ immediately shows fast growth, typical of ergodic dynamics. In agreement with our observations for the fidelity and chiral condensate, when starting in $|0_-\rangle$ and quenching with the TSM Hamiltonian (15) at $\mu = g = 0$, we find that the entanglement entropy is even lower than for the corresponding quench in the case of the QLM [71].

In summary, we have shown that the TSM exhibits scarred dynamics similar to that of the QLM, but with two major differences: (i) the scarred eigenstates of the quench Hamiltonian show qualitatively more nonthermal behavior in the overlap with the extreme vacuum and in the bipartite entanglement entropy (see Fig. 1), and (ii) scarring dynamics is quantitatively more prominent in the TSM compared to the QLM, as can be seen in stronger fidelity revivals, larger chiral condensate oscillations, and lower entanglement entropy in the former model at all investigated evolution times starting from the extreme vacuum. We further compare the prominence of scarring between the QLM and TSM in Secs. III and IV.
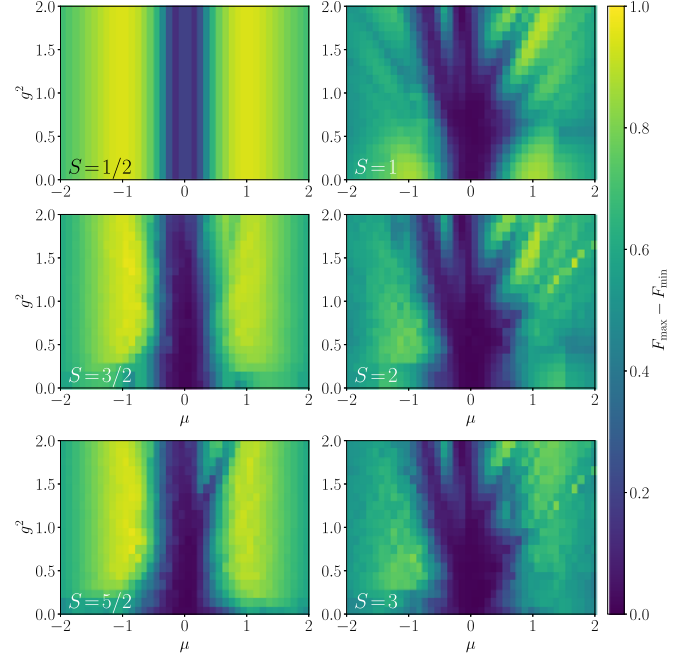
C. Detuned scarring: Quenches to finite values of μ and g^2

For $\mu = g = 0$, only the extreme vacua are scarred (see Appendix A). However, as in the case of the spin-$\frac{1}{2}$ PXP model, quenching to some specific values of μ and g can lead to nonthermal behavior when starting in the physical vacuum or the charge-proliferated state [64]. In this section we characterize this behavior for a wider range of these parameters in the QLM. We study the difference between the maximal and minimal fidelity revival amplitude after a quench for the states $|0_-\rangle$, $|0_+\rangle$, and $|CP\rangle$. A large difference indicates good revivals separated by intervals of low fidelity, as is typical when scarring is present. For the $|0_-\rangle$ state, we see revivals for finite values of μ and g^2, however, these revivals are due to Hilbert space fragmentation at the resonance point $\mu = g^2(2S - 1)/4$, $\mu, g^2 \gg J/\sqrt{S}$ (see Appendix B). For the $|0_+\rangle$ and $|CP\rangle$ states, the pattern is relatively similar but their behavior is switched for integer and half-integer S (Figs. 5 and 6). The best revivals occur for integer S in the case of $|0_+\rangle$ and for half-integer S in the case of $|CP\rangle$. This corresponds to the case where the state is not degenerate.

In Ref. [71], we show an example of a quench leading to detuned scarring in a system with $L = 20$ and $S = \frac{3}{2}$. Both states investigated, $|0_+\rangle$ and $|CP\rangle$, show similar behavior, with the presence of towers of states in the overlap plots and clear revivals in the fidelity with a very slow decay. It is important to note that there are revivals from these two states in a regime where all the terms in the Hamiltonian are of equal strength. These oscillations do not have a trivial explanation in terms of conservation of mass or electric energy. The nongenerality of this behavior is highlighted in Fig. 7, which shows quenches from random basis states. For all states shown except $|0_+\rangle$ and
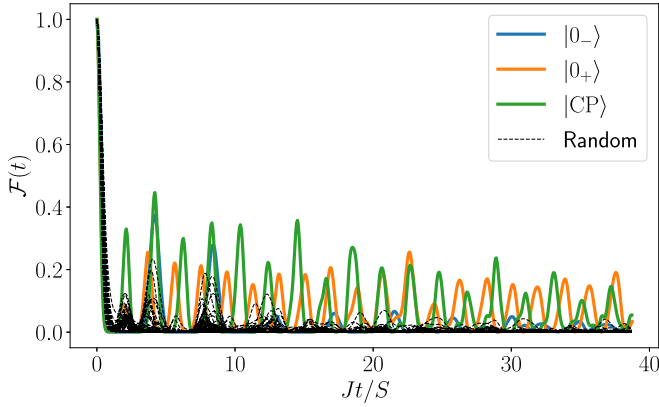
FIG. 7. Fidelity dynamics for quenches in the QLM starting in the $|0_-\rangle$, $|0_+\rangle$, and $|CP\rangle$ states as well as from random basis states for $L = 20$, $S = \frac{3}{2}$, $\mu = 0.486J$, and $g^2 = 0.6J$. While several states show some oscillations at short times, only $|0_+\rangle$ and $|CP\rangle$ show this behavior persisting at a longer timescale, indicative of detuned scarring.

$|CP\rangle$, revivals either decay rapidly or they are not present at all, as expected in a thermalizing system.

III. COMPARISON WITH THE SPIN-S PXP MODEL

In Sec. II, we have shown that both the QLM and TSM display scarring for zero-mass zero-g quenches starting in the extreme vacuum $|0_-\rangle$. This is the same state showing scarring in the PXP model at $S = \frac{1}{2}$ [77]. For $S > \frac{1}{2}$, the PXP model has been generalized as [58]

$$\hat{H}_{\text{PXP}} = \Omega \sum_j \hat{\mathcal{P}}_{j-1}^{-S} \hat{s}_j^x \hat{\mathcal{P}}_{j+1}^{-S}, \quad (19)$$

with $\hat{\mathcal{P}}_j^{-S}$ the local projector on the lowest weight spin state with eigenvalue $-S$. This model has been studied in Ref. [58] for $S > \frac{1}{2}$ and revivals have been found. Here, we show that the generalized PXP model (19) is fundamentally different from the QLM and TSM because of the form of their respective constraints, which results in different Hilbert space structures and, as a consequence, in different classical limits.

A. Hilbert space structure

In order to characterize the constraint in the TSM and QLM, it is informative to look at the asymptotic quantum dimension. This quantity tells us how fast the Hilbert space dimension $\mathcal{D}$ grows with the number of sites L, i.e., $\mathcal{D} = \alpha^L$, with α the quantum dimension. For an unconstrained spin-S model, we simply have $\alpha = 2S + 1$. However, for constrained systems we generally have $\alpha_S < 2S + 1$. For example, in the PXP model with $S = \frac{1}{2}$, it was shown that $\alpha = \phi < 2$, where ϕ is the golden ratio since the Hilbert space dimension scales according to the Fibonacci or Lucas numbers [51]. In Appendix C we show analytically that the quantum dimension for both the QLM and TSM is given by

$$\alpha_S = 2 \cos\left(\frac{\pi}{4S + 3}\right), \quad (20)$$

TABLE I. Quantum dimension for the various constrained spin models investigated in this work. For the QLM and TSM, the quantum dimension converges towards 2 for $S \to \infty$, while for the PXP and the unconstrained models it is unbounded.

S	1/2	1	3/2	2	5/2	3
Unconstrained	2	3	4	5	6	7
QLM/TSM	1.6180	1.8019	1.8794	1.9190	1.9419	1.9563
PXP	1.6180	2	2.3028	2.5616	2.7913	3

which converges to 2 as $S \to \infty$; see Table I for examples. This has a clear physical cause: if the value of the leftmost site is m, we can only glue to it a site with spin value $-m$ or $-m - 1$ without violating Gauss's law. For a finite S, we encounter a further limitation when $m = S$, as $-S - 1$ is not a possible spin eigenvalue. However, for infinite S this is not an issue and there are always two different ways of adding a new site. Hence, going from L to $L + 1$ doubles the number of states and the quantum dimension is 2.

For the generalized PXP model (19), it can be analytically shown that the quantum dimension is $\alpha_S = (1 + \sqrt{1 + 8S})/2$ (see Ref. [58] and Appendix C for details). In contrast to the TSM/QLM, the Hilbert space dimension of the spin-S PXP model becomes infinite as $S \to \infty$ and can be well approximated as $\sqrt{2S}$, which is close to the square root of the expected $2S + 1$ for an unconstrained spin-S paramagnet. Again, the physical interpretation is straightforward. In that limit, most of the Hilbert space is taken up by states of the form $|m_1, -S, m_3, -S, m_4, \ldots\rangle$ and $|-S, m_2, -S, m_4, -S, \ldots\rangle$, where the m_i can take any value between $-S$ and $+S$. The number of these states scales as $2(2S + 1)^{L/2} - 1$, giving a quantum dimension of $\sqrt{2S + 1}$. In the large-S limit, we recover $\alpha_S \approx \sqrt{2S}$, in agreement with the exact expression.

This difference highlights that the QLM and TSM are fundamentally different from the generalized PXP model, especially as S becomes large. This difference in the Hilbert space structure can be revealed further by looking at the adjacency graph of the Hamiltonian. In the spin-$\frac{1}{2}$ PXP model, the graph structure consists of two hypercubes of dimension $L/2$ joined at a single vertex (the state $|CP\rangle = |-\frac{1}{2}, -\frac{1}{2}, \ldots, -\frac{1}{2}\rangle$), with the rest of the Hilbert space acting as bridges between these two cubes (see Fig. 8). At the opposite corners of each cube, we find one of the two extreme vacua $|0_-\rangle$ (usually called the Néel states in the PXP model). A single hypercube possesses perfect revivals on its own as long as all the hopping strengths are identical, and two stitched hypercubes also have finite revivals in the thermodynamic limit [83,84]. As such, it has been proposed that the revivals in the spin-$\frac{1}{2}$ PXP model can be understood as due to its proximity to this toy model of two joined hypercubes [83]. The dynamics can then be thought of as state transfer from the Néel state to the shared vertex in the first hypercube, and then from it to the other Néel state and back. For the generalized PXP model in Eq. (19), as S is increased these two hypercubes turn into two hypergrids of order $2S + 1$ and dimension $L/2$, so equivalent to the graph of a free paramagnet with spin S and $L/2$ sites (see Fig. 8). The state shared between the
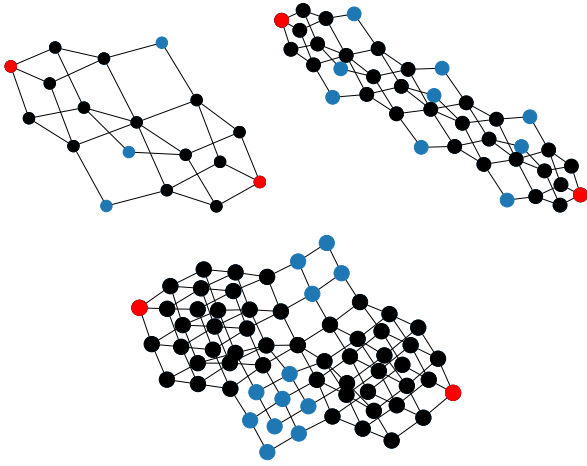
FIG. 8. Adjacency graph of the PXP model with $S = \frac{1}{2}$ (top left), of the QLM/TSM with $S = 1$ (top right), and of the PXP model with $S = 1$ (bottom), all for $L = 6$. The black vertices show the largest hypercubes and hypergrids in the graphs. The red vertices show the best reviving states.
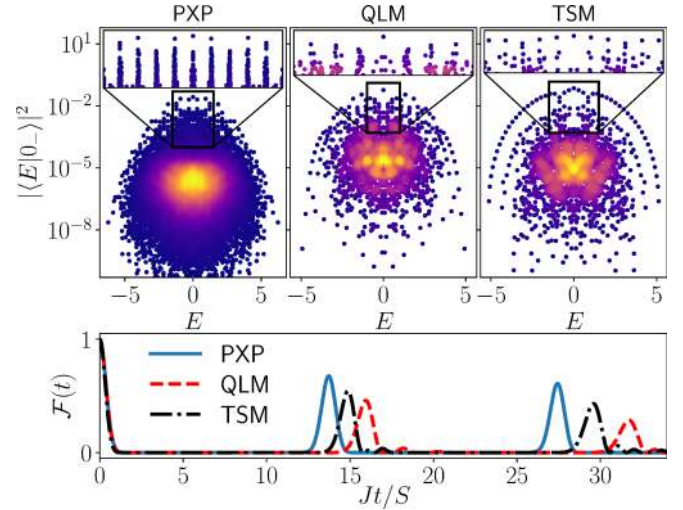

FIG. 9. Comparison of the PXP, QLM, and TSM for $L = 16$ and $S = \frac{3}{2}$. For the PXP model, we set $\Omega = 1/\sqrt{S(S+1)}$ to match the QLM. Even if all three models exhibit $2SL + 1 = 49$ towers of states, their characteristics differ greatly. These differences translate to the revivals from the $|0_-\rangle$ state. The color indicates the density of data points, with yellow color representing higher density.

two hypergrids is always $|-S, -S, \ldots, -S\rangle$, and the opposite corners in each hypergrid are the same as the extreme vacua: $|S, -S, \ldots, S, -S\rangle$ and $|-S, S, \ldots, -S, S\rangle$. These two states are also the ones displaying revivals in that model, and the picture of consecutive state transfer in each hypergrid still holds.

In contrast, for the spin-S QLM and TSM, as S is increased we still have hypercubes of dimension $L/2$, but their number increases. Indeed, instead of two hypercubes there are $4S$ of them in a line pattern, as shown in Fig. 8. Each hypercube shares states with two neighbors, except for the two hypercubes at the ends of the chain. The "unpaired" states at the corners of these cubes are the extreme vacua. The state located in the middle of the chain is always nondegenerate and corresponds to either the physical vacuum (for integer spin) or the physical charge-proliferated state (for half-integer spin). In any case, all the vacua, except the two extreme ones, and charge-proliferated states are always located at the intersection of two hypercubes. For the TSM and QLM models, the simple picture of dynamics being consecutive state transfer along the chain of hypercubes works as well. It also explains why we get revivals in the TSM despite the unconstrained version of the same model showing no revivals for higher S. Due to the constraint, the relevant dynamics happens in the hypercubes, which mimic the effective systems with spin $\frac{1}{2}$. In the special case $S = \frac{1}{2}$, the unconstrained TSM also has perfect revivals.

This difference in the graph structure further amplifies the dissimilarities between the PXP model on one hand, and the QLM and TSM on the other. It also implies that the physical interpretation of the relevant classical limit is different for PXP and for the QLM and TSM, as we will show below. Nevertheless, there are still some striking similarities between them. The main similarity is the same number of special towers of eigenstates, which is equal to $2SL + 1$. This number simply corresponds to the distance in the graph between the two extreme vacua plus one. In all models, these

special eigenstates can be well approximated by the forward scattering approximation proposed in Ref. [51]. As shown in Appendix D, the revivals can be further enhanced by adding a perturbation whose form is inspired by the forward scattering, as previously done in Refs. [85,86] for the PXP model.

However, even if the number of towers of states is the same in all three models, there are significant differences in their structure, as we illustrate in Fig. 9. Indeed, for the PXP model the towers are dense, but very narrow in energy and extending far above the bulk of the spectrum in terms of overlap with the initial state. For the QLM, this is not the case, as the spread in energy among the states in the same tower is much larger. This leads to a faster dephasing and decay of the fidelity revivals. Finally, the TSM shows a picture closer to the one of the PXP model with $S = \frac{1}{2}$: the towers of states are relatively sparse, with a single eigenstate at the top which is well separated from the rest.

B. Classical limit

The graph representation in Fig. 8 is helpful for constructing the classical limit of scarred dynamics. For the PXP model, it was shown that there is a classical periodic orbit corresponding to the trajectory of the extreme vacua [58]. The mapping to a classical dynamical system was obtained using the time-dependent variational principle (TDVP) [87]. The ansatz proposed in Ref. [58] simply corresponds to setting coherent spin states $|(\theta, \phi)\rangle = e^{i\phi S} e^{i\phi \hat{S}^z} e^{-i\theta \hat{S}^x} |-S\rangle$ on odd and even sites separately and projecting that wave function into the constrained Hilbert space. The ansatz incorporates the kinetic constraint and it was shown that it has a compact representation in terms of a matrix product state with bond dimension equal to 2, regardless of the magnitude of spin. The intuitive picture behind the ansatz is that each sublattice acts as a big spin, whose evolution is dependent on the value of

the spin corresponding to the other sublattice [88]. These spin coherent states naturally describe each hypergid on its own (which corresponds to having excitations on only one sublattice), while the constraint incorporates the coupling between them.

For the QLM and TSM, however, this two-angle description is not sufficient to capture the dynamics. Indeed, as hinted by the graph structure, we do not have two big spins SL coupled together, but instead there are $4S$ spins with magnitude $L/2$. Hence, in order to describe the evolution of this system, we conjecture that we would have to keep track of $8S$ angles, i.e., two per big spin, or alternatively $4S$ per sublattice. While this already makes the definition of a classical limit that could expand all the way to the Schwinger model basically impossible, the bond dimension needed will also be problematic. Indeed, unlike for the generalized PXP model, there is no simple way to encode the constraint into a fixed bond dimension MPO for any S. In Appendix E, we present an argument that for the TSM and QLM, the minimum bond dimension required to encode the constraint grows linearly with S. This shines light on the profound difference of the constraint between the PXP model and the QLM, and shows that obtaining a classical limit using a TDVP ansatz quickly becomes intractable as S increases.

Thus, developing a classical limit using TDVP for $S > 1$ for the QLM and TSM appears to be a nontrivial task due to the form of the constraint. However, we can still use a "mean-field-like" approximation that confines the dynamics to the span of the desired TDVP manifold. This was done for the PXP model with $S = \frac{1}{2}$ using the symmetric subspace approximation [88]. While in the TDVP ansatz each sublattice is characterized by an angle that sets the probability of having $m = +\frac{1}{2}$ on any site, in the quantum versions we simply create a basis where each state is a symmetric superposition of all states having a set number n_i of site $m = +\frac{1}{2}$ on each sublattice. Each state in the basis is then characterized by the pair (n_1, n_2), and we obtain a basis of the span of the TDVP manifold. It was additionally shown that the dynamics in that symmetric subspace $\mathcal{K}$ corresponds to "requantizing" the semiclassical TDVP dynamics [88].

Here, we expand this approximation to the PXP model with higher S by using coherent spin states, as was done in the corresponding TDVP ansatz of Ref. [58]. We form a basis of these constrained coherent states, where each basis state is characterized by two numbers. These are directly related to the θ angles in the TDVP ansatz (see Appendix F). We next obtain the subspace $\mathcal{K}_2$ spanned by these basis states and project the Hamiltonian into this subspace, comparing the evolution within the subspace with the one in the full Hilbert space. The subspace yields a very good description of the dynamics from the $|0_-\rangle$ state, as can be seen in Fig. 10. We emphasize that this is highly nontrivial as the projection into the subspace corresponds to a reduction of the effective dimension of the Hilbert space from 40 477 states (taking into account only the relevant translation and reflection sectors) down to 238 states. On the other hand, this completely fails to capture the dynamics in both the TSM and QLM, even though the initial Hilbert space dimension is much smaller with only 1866 (symmetry resolved) states. In order to get a decent approximation of the dynamics in these
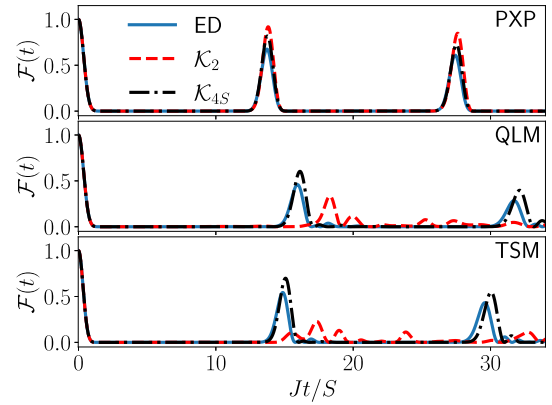

FIG. 10. Dynamics of the fidelity after a zero-mass zero-g quench from the $|0_-\rangle$ state in the PXP, QLM, and TSM with $L = 16$ and $S = \frac{3}{2}$. The solid line corresponds to exact diagonalization data, while the dashed and dashed-dotted lines correspond to the dynamics in the two different symmetric subspaces. The smaller subspace $\mathcal{K}_2$ already captures the behavior of the PXP model quite well but fails to do so for the QLM and TSM. Meanwhile, the larger subspace $\mathcal{K}_{4S}$ gives good results for all three models.

models, we have to expand our approximation to keep more information.

As mentioned previously, in the TDVP ansatz for these models we want to capture the dynamics of $4S$ effective spins $L/2$ corresponding to the hypercubes in the graph. In order to do this, we devise a larger subspace in which we keep track of the number of each spin eigenvalue $m = -S$ to $m = S$ for each sublattice (see Appendix F). We end up with a total of $4S$ numbers characterizing each basis state of our subspace. This is exactly half of the number of angles in the conjectured TDVP ansatz, as we do not need to incorporate the phase angles ϕ into our basis since they can evolve freely during the quantum evolution. The results of the dynamics projected into this new subspace $\mathcal{K}_{4S}$ can now be compared with the true dynamics in the full Hilbert space (see Fig. 10). We see that the behavior much more closely matches the actual fidelity for the TSM and QLM. This also gives a good result for the PXP model, however, this is expected as $\mathcal{K}_2 \subset \mathcal{K}_{4S}$.

This demonstrates that a low-dimensional subspace that captures the relevant dynamics from a zero-mass zero-g quench can be devised simply by studying the adjacency graph structure of the Hamiltonian. This structure could also theoretically be used to obtain a classical limit for these constrained models using the corresponding TDVP ansatz. These constructions then show that for the PXP model, the relevant classical limit is much simpler than for the QLM and TSM.

In summary, we have argued in this section that the spin-S PXP model is fundamentally different from its TSM and QLM counterparts. Nevertheless, we can still utilize tools developed for the PXP model in order to better understand the TSM and QLM, and to even enhance their scarring behavior. For further details, see Appendix D for results on the forward scattering approximation and enhanced scarring through algebra-correcting perturbations in the case of spin-1 QLM and TSM (recall that for $S = 1$, the QLM and TSM are identical).
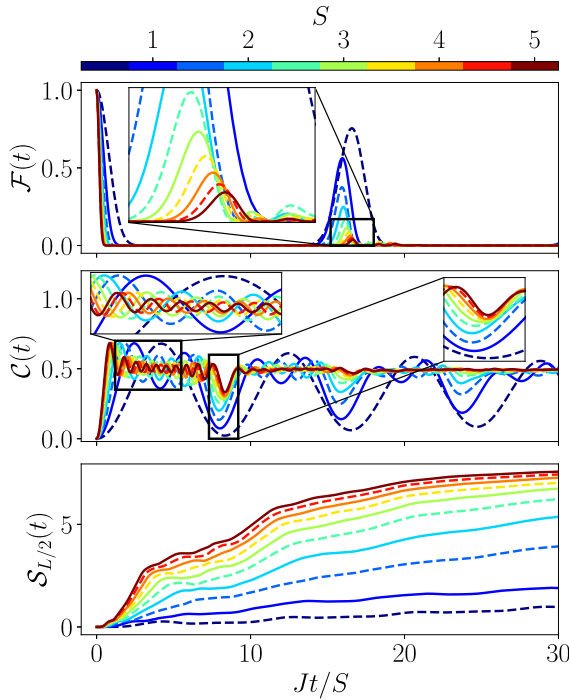
FIG. 11. Dynamical properties for zero-mass zero-g quenches from the extreme vacuum $|0_-\rangle$ for $L = 20$ and various values of S in the QLM. The solid lines show integer S, while the dashed lines denote half-integer S. No clear distinction can be made between these two cases, with both the fidelity revival amplitude and the difference of the chiral condensate from the equilibrium value decreasing monotonically with S.

FIG. 12. Dynamical properties for quenches from the extreme vacuum $|0_-\rangle$ for $L = 20$ and various values of S in the TSM, with $J_S = J/\sqrt{S(S+1)}$. The solid lines show integer S, while the dashed lines denote half-integer S. The results are qualitatively the same as in the QLM, however, all three quantities indicate much stronger scarring in the TSM.

IV. KOGUT–SUSSKIND LIMIT ($S \to \infty$)

In Sec. II B, we have shown that the extreme vacua exhibit persistent revivals in both the TSM and QLM for various values of S. Here we study the scaling of these revivals as S is varied. Figures 11 and 12 show how various quantities change with S when the system size is fixed to $L = 20$. In both models, the scarring signatures get weaker as S increases. The revivals in the fidelity and chiral condensate become less pronounced for larger S, while entropy growth becomes faster. This is not surprising since the fraction of states spanning the scarred subspace within the total Hilbert space decreases with S. Comparing these quantities between the two models also shows clearer scarring in the TSM.

These results also show an interesting behavior in the dynamics of the chiral condensate for both the TSM and QLM. In-between the main oscillations at twice the revival frequency, we also see oscillations with smaller amplitudes in the chiral condensate. These can be explained by considering the wave function propagation along the hypercubes forming the "backbone" of the graph (see Sec. III for details). We can thus visualize the dynamics as sequential state transfer through each of the hypercubes before finally reaching the opposite vertex of the graph. This is, of course, a very crude description as it ignores large parts of the Hilbert space. However, it helps us understand the intermediate states between the extreme vacua. As all states have a two-site periodicity, we will describe them by the value on the first two sites, i.e., $|M_1, M_2\rangle = |M_1, M_2, M_1, M_2, \dots, M_1, M_2\rangle$. Start-
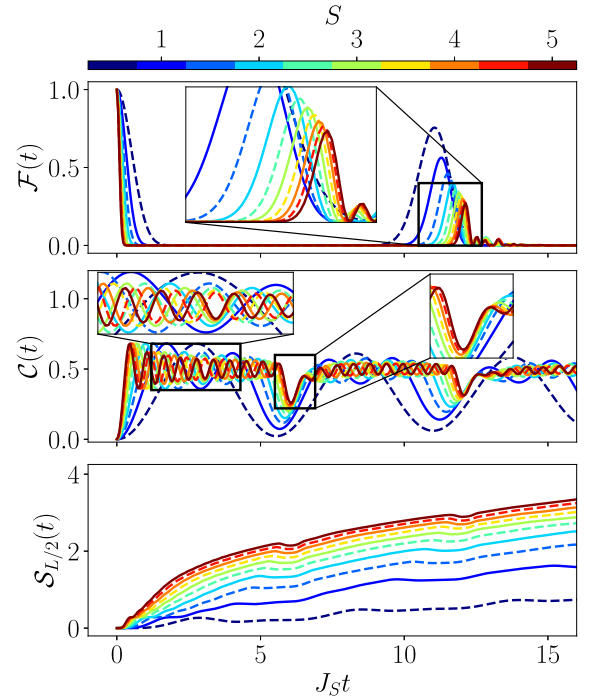
ing from $|0_-\rangle = |S, -S\rangle$, we have (approximate) state transfer to $|S-1, -S\rangle$, then to $|S-1, 1-S\rangle$, then $|S-2, 1-S\rangle$, and so on until we reach the other end of the chain with $|0'_-\rangle = |-S, S\rangle$. These intermediate states with periodicity two alternate between vacua and charge-proliferated states, leading to the oscillations in the chiral condensate. As the wave function is not perfectly peaked on these states but it is spread amongst states in the same "slice" of the graph (i.e., at the same distance from the two extreme vacua), we get smaller amplitude deviations of the chiral condensate. Nonetheless, this sequential state transfer picture allows us to predict the number of these lower-amplitude oscillations. As there are $4S - 1$ states between the extreme vacua, we expect to see the same number of local extrema in $\mathcal{C}(t)$. Out of these, $2S$ should be maxima and $2S - 1$ should be minima. This perfectly matches the dynamics of the chiral condensate and shows that this simple picture of propagation along the backbone of the graph is a good approximation of the dynamics from the extreme vacua.

While the scarring behavior getting weaker with S is expected, an important question is whether it disappears as $S \to \infty$ or if the two models will still display ergodicity breaking in that limit. The scaling with S is only meaningful if we can access sufficiently large system sizes L that are devoid of finite-size effects. Moreover, the scaling must be done on quantities that converge to a well-defined value in the limit $L \to \infty$, and we will use two such quantities: (i) the fidelity density, defined as $f_0 = \ln(\mathcal{F}_0)/L$ with $\mathcal{F}_0$ the fidelity amplitude at the first revival; (ii) the value of the chiral condensate $\mathcal{C}_0$ at its first revival (which happens after a half-period of
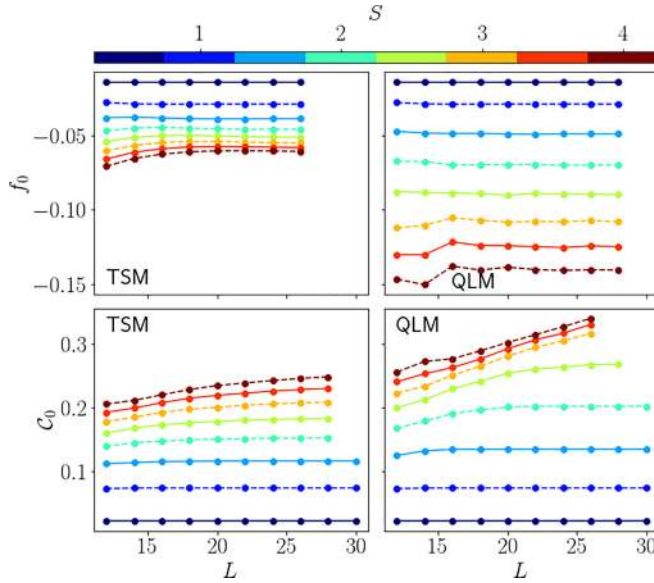
FIG. 13. Fidelity density $f_0 = \ln(\mathcal{F}_0)/L$ and chiral condensate $\mathcal{C}_0$ value at their first respective revival peak after a quench from the extreme vacuum for various values of S and L. The solid lines show integer S, while the dashed lines denote half-integer S. For the TSM, both quantities eventually converge with L, allowing us to make predictions about the behavior in infinite systems. For the QLM, the chiral condensate for large spins $S > \frac{5}{2}$ has clearly not reached convergence, indicating strong finite-size effects.
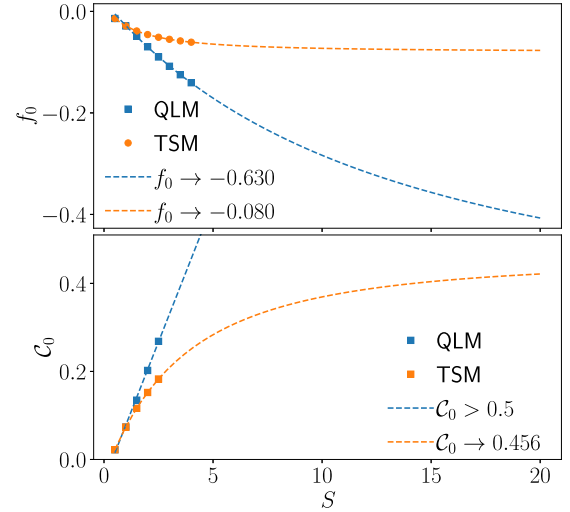

FIG. 14. Extrapolation of the fidelity density and chiral condensate value at their first respective revivals. The data are fitted with the function $a + b/(c + x)^\gamma$, with $\gamma = \frac{3}{2}$ for f_0 and $\gamma = 2$ for $\mathcal{C}$. Varying γ between 1 and 3 does not lead to a significant change for the infinite-S value. These results suggest that the TSM displays ergodicity breaking in the limit $S \rightarrow \infty$. On the other hand, for QLM the extrapolated fidelity density is close to the expected ergodic value $\ln 2$ in the $S \rightarrow \infty$ limit. However, the chiral condensate $\mathcal{C}_0$ shows no sign of saturation with S, indicating that the QLM data are affected by strong finite-size effects and precluding a reliable extrapolation to the Kogut-Susskind limit.

the fidelity revival). For a fully ergodic dynamics we expect fast thermalization to an infinite-temperature ensemble, which gives $\mathcal{C}_0 = 0.5$ independent of S. Similarly, during ergodic dynamics, the wave function should spread evenly across the entire Hilbert space, giving a fidelity of $1/\mathcal{D} = \alpha^{-L}$, with $\mathcal{D}$ the Hilbert space dimension and α the quantum dimension. Thus, for a fully ergodic system we expect the fidelity density to approach $f_0 = \ln(\alpha^{-L})/L = -\ln(\alpha)$, which converges to $f_0 = -\ln(2) \approx -0.6931$ in the limit $S \rightarrow \infty$, as derived in Sec. III.

Figure 13 shows the dependence of the fidelity density and chiral condensate on system size L, for different values of S in both the TSM and QLM. For the fidelity density, the convergence in L is quite fast for both models, allowing us to use the data for all spin values between $S = \frac{1}{2}$ to 4. However, somewhat surprisingly, for the observable $\mathcal{C}_0$ the convergence is seen to be much slower, especially in the QLM, and we can only perform thermodynamic-limit extrapolations for $S \leqslant \frac{5}{2}$.

For the TSM, both quantities are relatively well approximated by a power-law scaling of the form $a + b/(c + x)^\gamma$ with $1 < \gamma < 3$; see Fig. 14. While we are not aware of any predicted scaling that would fix γ, we note that the extrapolated value at $S \rightarrow \infty$ is fairly insensitive to γ. We find that the absolute value of the fidelity density is smaller than the thermal expectation by an order of magnitude as $S \rightarrow \infty$, indicating ergodicity breaking. While the chiral condensate also appears to extrapolate to a nonthermal value, this extrapolation is based on fewer data points and thus it likely suffers from a larger uncertainty. Nevertheless, the data for the TSM are consistent with ergodicy-breaking signatures persisting in the $S \rightarrow \infty$ limit.

The scaling behavior of the QLM is different from that of the TSM. Indeed, for the fidelity density the extrapolated value in the QLM is close to the ergodic value, within the error bars of the extrapolation. The available data for the chiral condensate $\mathcal{C}_0$ show a rapid increase with S towards the thermal value 0.5. Physically, we do not expect the value of the chiral condensate to rise above 0.5, but rather to saturate to it from below. Our data in Fig. 14 show no evidence of this saturation, implying that finite-size effects are strong and larger values of S are needed to perform a meaningful extrapolation. We note that we have observed a similar behavior in Ref. [71] where the dynamics of the electric flux was simulated directly in the thermodynamic limit using the infinite matrix product state (iMPS) method. The iMPS data show clear scarring signatures in the QLM model in the numerically tractable cases ($S \leqslant \frac{5}{2}$). However, similar to the above results, the iMPS data showed no convergence as a function of S within the range of spin values studied, precluding the extrapolation to $S \rightarrow \infty$ limit.

V. CONCLUSIONS AND OUTLOOK

In this work, we have investigated the spin-S QLM and TSM, two different constrained spin models based on the lattice Schwinger model. In both models, we have demonstrated clear signatures of quantum many-body scarring when quenching from the extreme vacua to zero mass and gauge coupling strength. We have also shown that both the physical vacua and the charge-proliferated states can exhibit detuned scarring for finite values of the mass and gauge coupling.

Both resonant and detuned scarring have been previously observed in the spin-$\frac{1}{2}$ PXP model [51,59,64], which is recovered from both the TSM and QLM for $S = \frac{1}{2}$. However, for any other value of S, these models are different from the generalized spin-S PXP model previously studied [58]. We explained this difference by investigating the structure of the adjacency graph of the corresponding Hamiltonians. Using this approach, we have also proposed a procedure to construct a classical limit for the QLM and TSM, which again differs from the one used for the PXP model. While for the TSM and QLM this classical limit is more complicated to implement, we have shown that its structure captures the resonant scarring phenomenology through a simpler quantum approximation.

Our simulations also show that for any $S \leqslant 4$, the TSM exhibits stronger scarring than the QLM in all the metrics used. These differences become more pronounced as S increases. Based on a finite-S scaling analysis, we expect that the TSM shows signs of weak ergodicity breaking for $S \to \infty$, while the scaling to the Kogut-Susskind limit cannot be reliably performed for the QLM with the existing computational resources. The different scaling behavior of the TSM and QLM also highlights one limitation of the graph-theoretical approach. As it does not directly take into account the strength of the matrix elements nor their structure outside of the dominant hypercubes, the graph method falls short of predicting different behaviors for the TSM and QLM as S increases. Understanding the source of these differences between the TSM and QLM models would be an interesting goal for future work, as it requires the understanding of the graph structures beyond the dominant subgraphs.

Another question raised by our work is the fate of quantum many-body scars in models corresponding to higher-dimensional versions of U(1) lattice gauge theories with dynamical matter. As the coordination number of the lattice increases, the number of configurations allowed by Gauss's law rapidly becomes larger. Thus, the constraint should get weaker and the graph structure associated with it should also change drastically. As a consequence, it is currently not known if these models also possess scarring behavior, or if the latter is only a feature present in low-dimensional cases. Given the massive current drive in implementations of lattice gauge theories on synthetic quantum matter setups [19,89–99], our work provides insights into how to potentially realize scarring in such experimental platforms.

In compliance with EPSRC policy framework on research data, this publication is theoretical work that does not require supporting research data.

APPENDIX A: QUENCHES FROM OTHER VACUA AND CP INITIAL STATES

In the main text, we have shown the results of zero-mass zero-g quenches from the extreme vacua, the physical vacua, and the charge-proliferated state for the TSM. Similar results for the QLM are available in Ref. [71]. For all values of S and L investigated, only the extreme vacua showed signatures of resonant scarring. However, as S is increased there are more and more vacua and charge-proliferated states corresponding to different values of the field. In the spin language, all the vacua have the structure $|M, -M\rangle$, and the charge-proliferated states $|M - 1, -M\rangle$. We can quantify these states by their proximity Δ_{0_-} to the extreme vacuum $|0_-\rangle = |S, -S\rangle$. The extreme vacuum then has $\Delta_{0_-} = 0$, the charge-proliferated state with maximum electric field $|S - 1, -S\rangle$ has $\Delta_{0_-} = 1$, the vacuum state $|S - 1, 1 - S\rangle$ has $\Delta_{0_-} = 2$ and so on. Figures 15 and 16 show that the extreme vacuum is the only state

FIG. 15. Dynamical properties for zero-mass zero-g quenches starting in various vacua (solid line) and charge-proliferated states (dashed lines) for $S = \frac{5}{2}$ and $L = 20$ in the QLM. Δ_{0_-} quantifies their proximity to the extreme vacuum $|0_-\rangle$, the only state showing clear revivals. The entanglement entropy growth also suggests that thermalization happens faster as Δ_{0_-} increases.
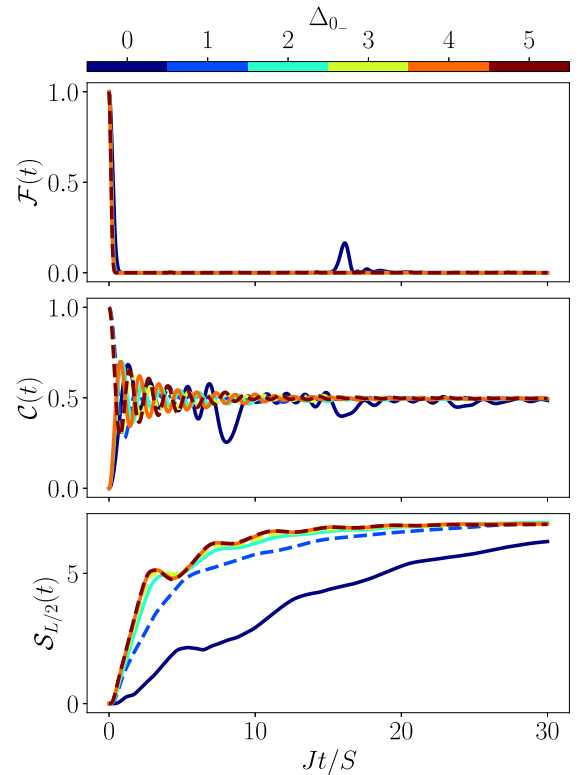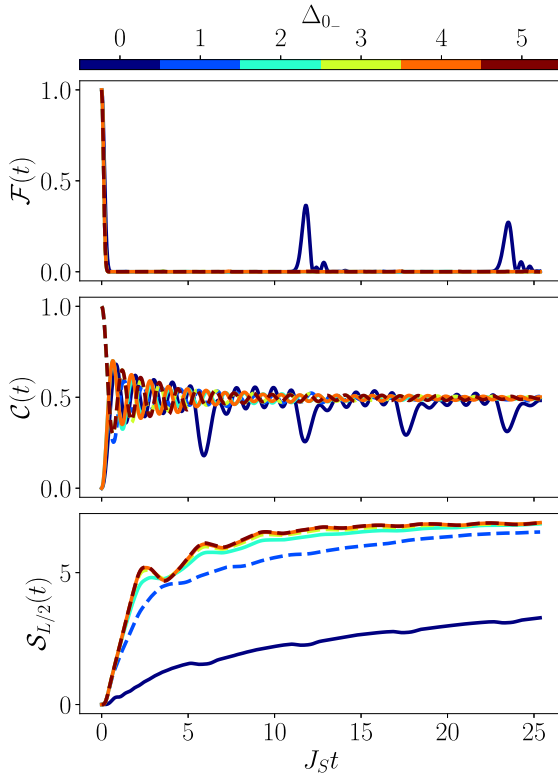
FIG. 16. Dynamical properties for zero-mass zero-g quenches starting in various various vacua (solid lines) and charge-proliferated states (dashed lines) for $S = \frac{5}{2}$ and $L = 20$ in the TSM, with $J_S = J/\sqrt{S(S+1)}$. Δ_{0_-} quantifies their proximity to the extreme vacuum $|0_-\rangle$, the only state showing clear revivals. The results are qualitatively very similar to the one in the QLM.

showing revivals in the wave function for a zero-mass zero-g quench in both the QLM and TSM. However, the growth of entanglement entropy seems to increase monotonically with Δ_{0_-}, hinting that states in the middle of the graph (far away form the extreme vacua) thermalize faster.

APPENDIX B: DETUNED QUENCHES FROM THE EXTREME VACUA

In this Appendix we investigate the fate of scarring when quenching from the extreme vacua to finite values of μ and g^2. As in the main text, to probe this we study the difference between the maximal and minimal fidelity revival after a quench. The results are presented in Fig. 17, where the most striking feature for each S is the main diagonal (red dashed) line showing close-to-perfect revivals. This line corresponds to $\mu = (2S - 1)g^2/4$. Indeed, when this condition is satisfied and we also have $\mu, g^2 \gg J/\sqrt{S}$, the Hilbert space fractures [100–102] and the $|0_-\rangle$ state and its translated counterpart both find themselves in a fragment of the Hilbert space that can be mapped to free spin-$\frac{1}{2}$ paramagnets with $L/2$ spins. We now demonstrate this by starting in $|0_-\rangle = |S, -S, S, -S, \ldots\rangle$. The total energy of that state is equal to $Lg^2S^2/2$. At first, the only move allowed in the constrained Hilbert space is taking any of the sites with spin eigenvalue S to $S - 1$. This also conserves the total energy. Indeed, this op-
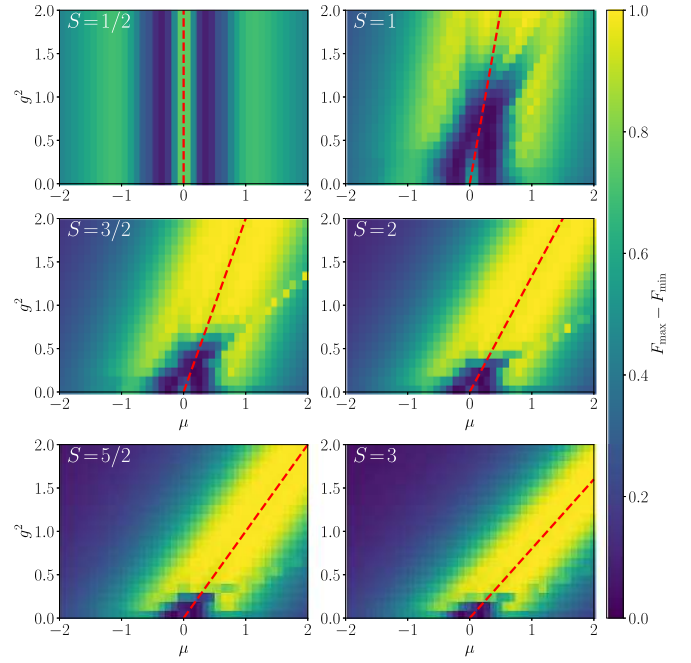
FIG. 17. Difference between the maximum and minimum amplitudes of the fidelity revival when quenching from the state $|0_-\rangle$ for $L = 16$ and various values of μ and g^2 in the QLM. The red dashed line in each plot shows the resonance condition $\mu = (2S - 1)g^2/4$ for which the Hilbert space fractures when $\mu, g^2 \gg J/\sqrt{2(S+1)}$.

eration creates two fermions that lead to an increase in energy of $2\mu = g^2(2S - 1)/2$, thus counteracting the decrease of $g^2[S^2 - (S - 1)^2]/2 = g^2(2S - 1)/2$ in electromagnetic energy. Hence, every other site can freely flip between S and $S - 1$. However, the next allowed step would be to take a site with spin eigenvalue $-S$ to $1 - S$. This leads to a large energy change as it both destroys fermions and reduces the electromagnetic energy. If this energy change is much larger than the hopping energy, which is roughly equal to $J/\sqrt{S}$ near the end of the chain, this move is greatly suppressed, hence these sites are frozen at $-S$. We thus have a system that is equivalent to a set of $L/2$ noninteracting two-level systems. The same is true when starting in the state $|-S, S, -S, S, \ldots\rangle$, but the odd and even sites are now flipped. It is important to distinguish these perfect revivals from scarring, as they emerge here as a sole consequence of Hilbert space fragmentation. Every product state located entirely within one of these two noninteracting disconnected subspaces will show perfect revivals with the same frequency.

APPENDIX C: QUANTUM DIMENSION

We now derive the quantum dimensions for the TSM/QLM and the generalized PXP model. By grouping states in equivalence classes depending on the value of their leftmost site, it is possible to get a transfer matrix that relates the class sizes for system sizes L and $L - 1$. The quantum dimension is then simply the dominant eigenvalue of this transfer matrix.

For the QLM (and equivalently, the TSM, as the constraint is the same for both), we simply need to keep track of the state of the leftmost site and the transfer matrix is of size $(2S + 1) \times (2S + 1)$. We can order the spin values by "compatibil-

ity," which means for integer spin $0, -1, 1, -2, 2, \ldots, -S, S$ and for half-integer $-\frac{1}{2}, \frac{1}{2}, -\frac{3}{2}, \frac{3}{2}, \ldots, -S, S$. The advantage of this ordering is that, due to Gauss's law, a value is only compatible with the one before or after it, except the first one which is also compatible with itself. This allows us to write the transfer matrix as

$$
\mathcal{T}_{\text{QLM}}(S) = \begin{pmatrix} 1 & 1 & 0 & 0 \\ 1 & 0 & \ddots & 0 \\ 0 & \ddots & 0 & 1 \\ 0 & 0 & 1 & 0 \end{pmatrix}, \quad \text{(C1)}
$$

which has the form of a tridiagonal matrix with unity entries on the superdiagonal and subdiagonal, and zeros everywhere else except at the (1,1) entry, which also carries a value of 1. The number of states in the case of PBC is given by

$$
\mathcal{D}_{\text{QLM}}(S, L) = \text{Tr}[(\mathcal{T}_{\text{QLM}}(S))^L] = \sum_{j=1}^{2S+1} \lambda_j^L \xrightarrow{L \to \infty} \lambda_{2S+1}^L, \quad \text{(C2)}
$$

where the λ_j are the eigenvalues of $\mathcal{T}_{\text{QLM}}(S)$ sorted by increasing modulus. For large L, the dominant eigenvalue is the only one contributing significantly and so its value sets the quantum dimension. Let $d = 2S + 1$, then the characteristic polynomial of the transfer matrix is

$$
P_{\text{QLM}}(S, \lambda) = \lambda^d + \sum_{i=1}^{d} (-1)^{\lceil i/2 \rceil} \lambda^{d-i} \binom{d - \lceil i/2 \rceil}{\lfloor i/2 \rfloor}, \quad \text{(C3)}
$$

where the $\binom{n}{k}$ are the binomial coefficients. For example, $P_{S=1/2} = \lambda^2 - \lambda \binom{1}{0} - \binom{1}{1} = \lambda^2 - \lambda - 1$ and $P_{S=1} = \lambda^3 - \lambda^2 \binom{2}{0} - \lambda \binom{2}{1} + \binom{1}{1} = \lambda^3 - \lambda^2 - 2\lambda^2 + 1$. The quantum dimension is the largest root of this polynomial, which is given by Eq. (20) in the main text, and which clearly becomes 2 at $S \to \infty$. Table I in the main text shows its values for selected values of S. Note that in Ref. [103], this quantum dimension was also calculated as

$$
\alpha_{S,L} = 2 \left[\sum_{j=1}^{2S+1} \cos^L \left(\frac{j\pi}{4S + 3} \right) \right]^{\frac{1}{L}} \quad \text{(C4)}
$$

for finite systems, which in the thermodynamic limit $L \to \infty$ converges to our result.

For the generalized PXP model [58], the procedure is even simpler. In that case, we can split the states into two equivalence classes: states with the leftmost site equal to $-S$ and other states. The resulting transfer matrix is

$$
\mathcal{T}_{\text{PXP}}(S) = \begin{pmatrix} 1 & 2S \\ 1 & 0 \end{pmatrix}. \quad \text{(C5)}
$$

The characteristic polynomial is easy to compute as $P_{\text{PXP}}(S, \lambda) = \lambda^2 - \lambda - 2S$, giving a dominant eigenvalue of $\lambda = (1 + \sqrt{1 + 8S})/2$, matching the result in Ref. [58].

APPENDIX D: DETAILED STUDY OF THE $S = 1$ CASE

The case of $S = 1$ in the TSM and QLM is the simplest example that is different from the PXP model (19). Here, we show that the other approaches developed to investigate the PXP model and enhance its revivals also work for the spin-1 U(1) QLM and TSM, which are identical to each other for $S = 1$.

For $S = 1$, the Hamiltonians in Eqs. (11) and (15) are equal and can be written with local constraints as

$$
\begin{aligned}
\hat{H} = \frac{J}{\sqrt{8}} \sum_{j=1}^{L} &\left[\hat{\mathcal{P}}_{j-1}^{-1} (\hat{s}_j^+ \hat{\mathcal{P}}_j^0) \hat{\mathcal{P}}_{j+1}^{-1} \right. \\
&+ \left. \hat{\mathcal{P}}_{j-1}^0 (\hat{\mathcal{P}}_j^0 \hat{s}_j^+) \hat{\mathcal{P}}_{j+1}^0 + \text{H.c.} \right] \\
&- 2\mu \sum_j \hat{s}_j^z + \frac{g^2}{2} \sum_j (\hat{s}_j^z)^2, \quad \text{(D1)}
\end{aligned}
$$

where $\hat{\mathcal{P}}^M$ is the projector on the state with spin eigenvalue M.

1. Forward scattering approximation

As in the case of $S = \frac{1}{2}$, for $S = 1$ we can use the forward scattering approximation (FSA) to approximate the scarred eigenstates [51]. First, we need to decompose the off-diagonal part of the Hamiltonian into raising and lowering operators $\hat{H}^+$ and $\hat{H}^-$, such that $\hat{H}^+$ takes us away from the initial reviving state $|0_-\rangle = |1, -1, 1, -1, \ldots, 1, -1\rangle$ while $\hat{H}^- = (\hat{H}^+)^\dagger$. It is straightforward to derive the exact form of these expressions as

$$
\begin{aligned}
\hat{H}^+ = \frac{1}{\sqrt{8}} \sum_{j=1}^{L/2} &\left[\hat{\mathcal{P}}_{2j-1}^0 (\hat{s}_{2j}^- \hat{\mathcal{P}}_{2j}^0) \hat{\mathcal{P}}_{2j+1}^0 \right. \\
&- \hat{\mathcal{P}}_{2j-1}^- (\hat{\mathcal{P}}_{2j}^0 \hat{s}_{2j}^-) \hat{\mathcal{P}}_{2j+1}^- \\
&+ \hat{\mathcal{P}}_{2j-2}^0 (\hat{\mathcal{P}}_{2j-1}^0 \hat{s}_{2j-1}^+) \hat{\mathcal{P}}_{2j}^0 \\
&- \left. \hat{\mathcal{P}}_{2j}^- (\hat{s}_{2j-1}^+ \hat{\mathcal{P}}_{2j-1}^0) \hat{\mathcal{P}}_{2j}^- \right]. \quad \text{(D2)}
\end{aligned}
$$

Using this raising operator and starting from the state $|F_0\rangle = |0_-\rangle = |1, -1, 1, -1, \ldots, 1, -1\rangle$, we can build the FSA states $|F_n\rangle = (1/\mathcal{N})(\hat{H}^+)^n |F_0\rangle$ for $n = 0$ to $2L$, with $\mathcal{N}$ denoting a normalization factor. It is useful to note that $|F_{2L}\rangle = |-1, 1, -1, 1 \ldots - 1, 1\rangle$ and $\hat{H}^+ |F_{2L}\rangle = 0$. Projecting the Hamiltonian to this set of $2L + 1$ states leads us to a tridiagonal matrix with off-diagonal elements $\beta_{n,n+1}$:

$$
\langle F_m | \hat{H} | F_n \rangle = \beta_{n,n+1} \delta_{m,n+1} + \beta_{n-1,n}^* \delta_{m,n-1}. \quad \text{(D3)}
$$

As for the spin-$\frac{1}{2}$ PXP model, the eigenstates in this low-dimensional subspace have energies very close to the ones of the actual scarred eigenstates [51]. This is demonstrated in Fig. 18. The main difference between the FSA states and the exact scarred eigenstates lies in their number. Indeed, in the FSA we obtain exactly $2SL + 1$ states, whereas in reality the model has $2SL + 1$ towers of states. Thus, the FSA only gives one scarred state per tower. As a result, the FSA eigenstates are very atypical, having a very low entanglement entropy. In the full model, this atypicality is in fact spread amongst many eigenstates in each tower, leading to individual states with larger entanglement entropy.

2. Algebra-correcting perturbation for $S = 1$

As for the PXP model with spins $\frac{1}{2}$ [85,86], the accuracy of the FSA implies that there is an approximate su(2) algebra structure in the scarred subspace. We can derive a perturbation to "correct" this algebraic structure by following the prescription in Ref. [104]. We consider $\hat{H}^+$ and $\hat{H}^-$ to be the raising
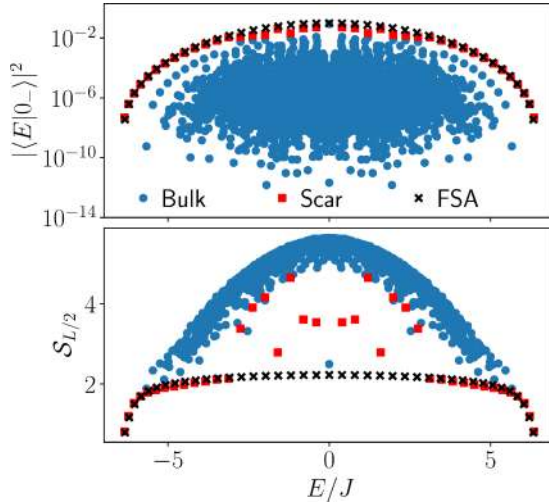
FIG. 18. Overlap of the $|0_-\rangle$ state with the eigenstates (top) and half-chain entanglement entropy (bottom) in the QLM/TSM with $S = 1$ and $L = 20$. The FSA results closely reproduce the exact diagonalization results, in particular for the overlaps with $|0_-\rangle$. In contrast, the entanglement entropy of scarred eigenstates in the middle of the spectrum is less accurately reproduced, due to the strong mixing of states within the towers.

and lowering operators of that algebra. We can derive the effective $\hat{H}^z$ operators as

$$\hat{H}^z = 2[\hat{H}^+, \hat{H}^-]$$

$$= \frac{1}{\sqrt{8}} \sum_{j=1}^{L/2} \left[\hat{\mathcal{P}}_{2j-1}^0 (\hat{\mathcal{P}}_{2j}^0 - \hat{\mathcal{P}}_{2j}^{-1}) \hat{\mathcal{P}}_{2j+1}^0 \right.$$

$$+ \hat{\mathcal{P}}_{2j-1}^{-1} (\hat{\mathcal{P}}_{2j}^1 - \hat{\mathcal{P}}_{2j}^0) \hat{\mathcal{P}}_{2j+1}^{-1}$$

$$- \hat{\mathcal{P}}_{2j-2}^0 (\hat{\mathcal{P}}_{2j-1}^0 - \hat{\mathcal{P}}_{2j-1}^{-1}) \hat{\mathcal{P}}_{2j}^0$$

$$\left. - \hat{\mathcal{P}}_{2j}^{-1} (\hat{\mathcal{P}}_{2j-1}^1 - \hat{\mathcal{P}}_{2j-1}^0) \hat{\mathcal{P}}_{2j}^{-1} \right]. \tag{D4}$$

From there, we compute the commutators

$$[\hat{H}^z, \hat{H}^+] = \hat{H}^+ + \hat{\delta}_1^+, \tag{D5a}$$

$$[\hat{H}^z, \hat{H}^-] = -\hat{H}^- + \hat{\delta}_1^-, \tag{D5b}$$

which obey the expected su(2) commutation rules, up to error terms denoted by $\hat{\delta}_1^\pm$. The latter are given by

$$\hat{\delta}_{(1)}^+ = -\frac{1}{4\sqrt{2}} \sum_{j=1}^{L/2} \left[2\hat{\mathcal{P}}_{2j-2}^0 (\hat{s}_{2j-1}^- \hat{\mathcal{P}}_{2j-1}^0) \hat{\mathcal{P}}_{2j}^0 \right.$$

$$+ 2\hat{\mathcal{P}}_{2j-1}^0 (\hat{\mathcal{P}}_{2j}^0 \hat{s}_{2j}^+) \hat{\mathcal{P}}_{2j+1}^0$$

$$+ \hat{\mathcal{P}}_{2j-1}^{-1} (\hat{s}_{2j}^+ \hat{\mathcal{P}}_{2j}^0) \hat{\mathcal{P}}_{2j+1}^{-1} \hat{\mathcal{P}}_{2j+2}^0$$

$$+ \hat{\mathcal{P}}_{2j-2}^0 \hat{\mathcal{P}}_{2j-1}^{-1} (\hat{s}_{2j}^+ \hat{\mathcal{P}}_{2j}^0) \hat{\mathcal{P}}_{2j+1}^{-1}$$

$$+ \hat{\mathcal{P}}_{2j-2}^{-1} (\hat{\mathcal{P}}_{2j-1}^0 \hat{s}_{2j-1}^-) \hat{\mathcal{P}}_{2j}^{-1} \hat{\mathcal{P}}_{2j+1}^0$$

$$\left. + \hat{\mathcal{P}}_{2j-3}^0 \hat{\mathcal{P}}_{2j-2}^{-1} (\hat{\mathcal{P}}_{2j-1}^0 \hat{s}_{2j-1}^-) \hat{\mathcal{P}}_{2j}^{-1} \right], \tag{D6}$$

and $\hat{\delta}_{(1)}^- = -[\hat{\delta}_{(1)}^+]^\dagger$. We can then partially cancel the unwanted error terms by introducing the following perturbation to the
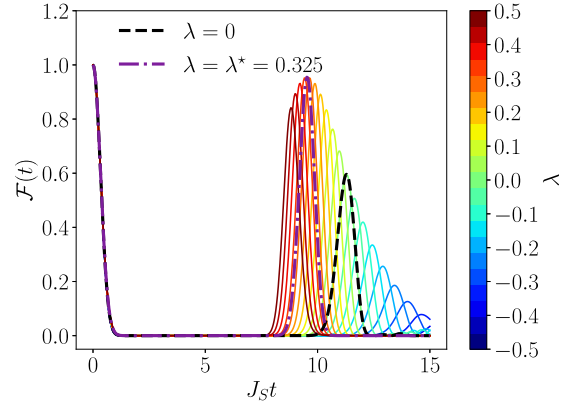
FIG. 19. Revivals in the QLM/TSM for $S = 1$ and $L = 18$ with different strengths of the perturbation $\delta\hat{H}_{(1)}$. For $\lambda = 0.325$, the revivals become close to perfect.

model:

$$\delta\hat{H}_{(1)} = \hat{\delta}_{(1)}^- - \hat{\delta}_{(1)}^+$$

$$= \frac{1}{4\sqrt{2}} \sum_{j+1}^{L} \left[2\hat{\mathcal{P}}_{j-1}^0 (\hat{\mathcal{P}}_j^0 \hat{s}_j^+) \hat{\mathcal{P}}_{j+1}^0 \right.$$

$$+ \hat{\mathcal{P}}_{j-1}^{-1} (\hat{s}_j^+ \hat{\mathcal{P}}_j^0) \hat{\mathcal{P}}_{j+1}^{-1} \hat{\mathcal{P}}_{j+2}^0$$

$$\left. + \hat{\mathcal{P}}_{j-2}^0 \hat{\mathcal{P}}_{j-1}^{-1} (\hat{s}_j^+ \hat{\mathcal{P}}_j^0) \hat{\mathcal{P}}_{j+1}^{-1} + \text{H.c.} \right]. \tag{D7}$$

We add this perturbation to the Hamiltonian $\hat{H} \to \hat{H} + \lambda \cdot \delta\hat{H}_{(1)}$, and look for the value λ that gives the best revivals for the extreme vacua. From Fig. 19 we see that we can get a substantial improvement of the revivals for $\lambda \approx 0.325$, with the revivals being close to perfect in that case. This procedure can be carried out in the same way for arbitrary spin length S. However, the number of local terms in $\hat{H}^+$ increases linearly with S and the derivation becomes increasingly tedious.

APPENDIX E: BOND DIMENSION OF THE CONSTRAINT FOR THE QLM AND TSM

We argue that to represent the constraint in the QLM and TSM models as a matrix-product operator (MPO), we need a bond dimension scaling as $2S + 1$. This is in stark contrast with the generalized PXP model where the bond dimension is equal to 2 for any S [58].

The first step is to write the global constraint $\mathcal{P}$ as a sum of products of local two-site constraints $\mathcal{P} = \prod_i \mathcal{P}_{i,i+1}$. Each local constraint can be expressed as

$$\mathcal{P}_{i,i+1} = \hat{P}_i^{-S} \hat{P}_{i+1}^S + \sum_{m=1-S}^{S} \left(\hat{P}_i^m \hat{P}_{i+1}^{-m} + \hat{P}_i^m \hat{P}_{i+1}^{-m-1} \right), \tag{E1}$$

where $\hat{P}_i^m = |m\rangle \langle m|$ is the projector on the spin eigenstate with magnetization m along the z direction. Already, this sum of $4S$ local terms contrasts with the PXP constraint which can be written as $\hat{P}_i^{-S} \hat{P}_{i+1}^{-S} + \hat{Q}_i \hat{P}_{i+1}^{-S} + \hat{P}_i^{-S} \hat{Q}_{i+1}$ for any S, with $\hat{Q} = \mathbb{1} - \hat{P}^{-S}$.

To find the minimal bond dimension, we need to represent the constraint as an MPO. A common approach is to write it as a state machine [105,106], where each transition must be

(a)

(b)

Integer S

Half-integer S
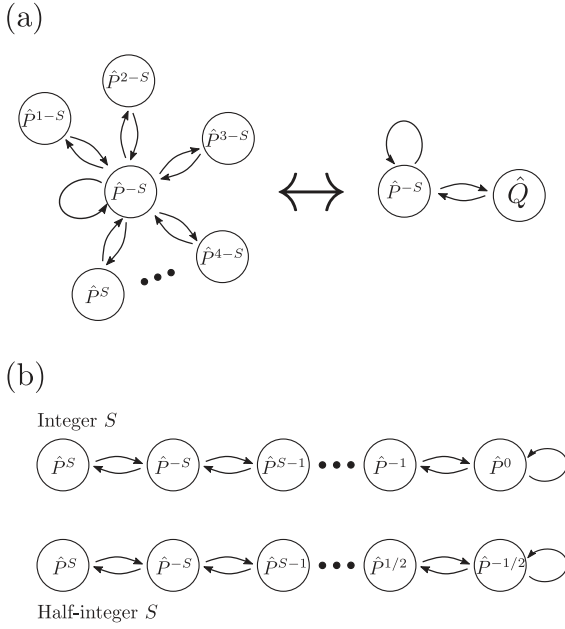
FIG. 20. State machine representing the local two-site constraint for (a) the generalized PXP model and (b) the QLM and TSM. For the PXP model, the state machine can be easily reduced to a total of two states by grouping together all states having the same rules. This is not the case for the QLM and TSM as all states have different rules.

between operators that can be placed next to each other. This is straightforward and the result is shown in Fig. 20. While both states can be written to have $2S + 1$ states, one can see that for the PXP model all states with $m \neq -S$ have exactly the same rules and so can be grouped together. For the QLM, all states have different rules and so there is no simple way to merge them. From the state machine one can then write the MPO as an operator-valued matrix where the element (i, j) is equal to $\hat{P}^{-S+i-1}$ if the transition $\hat{P}^{-S+i-1}$ to $\hat{P}^{-S+j-1}$ is allowed and 0 otherwise. The resulting MPO are then

$$\hat{W}_{\text{PXP}} = \begin{pmatrix} \hat{P}^{-S} & \hat{P}^{1-S} & \dots & \hat{P}^{S} \\ \hat{P}^{-S} & 0 & 0 & 0 \\ \vdots & 0 & 0 & 0 \\ \hat{P}^{-S} & 0 & 0 & 0 \end{pmatrix} \rightarrow \begin{pmatrix} \hat{P}^{-s} & \hat{Q} \\ \hat{P}^{-s} & 0 \end{pmatrix},$$

$$\hat{W}_{\text{QLM}} = \begin{pmatrix} \hat{P}^{0} & \hat{P}^{-1} & 0 & 0 \\ \hat{P}^{0} & 0 & \ddots & 0 \\ 0 & \ddots & 0 & \hat{P}^{S} \\ 0 & 0 & \hat{P}^{-s} & 0 \end{pmatrix}, \qquad \text{(E2)}$$

where we assumed integer spin for the QLM. For half-integer spin we obtain the same structure but with $\hat{P}^{-1/2}$ in the left-most column instead of $\hat{P}^{0}$. These matrices have exactly the same structure as the transfer matrices used in Appendix C. This is of course not a coincidence, as they encode the same constraint. However, in the present case they are operator-valued matrices.

It is important to note here that for the PXP model, even if we write it with all $\hat{P}$ operators explicitly, the MPO always has rank 2. For the QLM, the matrix has full rank $2S + 1$. While

it is still possible that the bond dimension could be reduced using a nontrivial global gauge transformation, the simple recipe used for PXP is not valid for that model and it is likely that the bond dimension cannot be reduced below $2S + 1$. This would make any analytical TDVP approach cumbersome for larger S in the case of the TSM/QLM.

APPENDIX F: SYMMETRIC SUBSPACE FOR HIGHER S

Here, we provide further details about the generalization of the symmetric subspace introduced in Ref. [88] to constrained models with higher spin. We develop two different subspaces $\mathcal{K}_2$ and $\mathcal{K}_{4S}$, where the subscript denotes the number of values characterizing each basis state in the subspace.

For $\mathcal{K}_2$, we first group all states based on the total number of excitations on each sublattice (encompassing all odd and even sites, respectively). By "excitations" we mean the number of times the spin raising operator was applied on top of the lowest spin states. For example, we can consider the case of $S = \frac{3}{2}$ and the state $|-\frac{1}{2}, -\frac{3}{2}, \frac{3}{2}, \frac{1}{2}\rangle$. On the first sublattice we need one application of $\hat{s}^{+}$ to go from $-\frac{3}{2}$ to $-\frac{1}{2}$ and three applications to go from $-\frac{3}{2}$ to $\frac{3}{2}$. Hence, there are $3 + 1 = 4$ excitations on it. On the second sublattice, there are $0 + 2 = 2$ excitations. This state will then belong to the equivalence class $(n_1 = 4, n_2 = 2)$. Each n_j takes values between 0 and SL, and so the number of classes scales as $O(S^2 L^2)$, which is much slower than the full Hilbert space.

We can then define the basis of $\mathcal{K}_2$ by creating one basis state per equivalence class. Following the TDVP ansatz in [58], we want our basis states to span a subspace formed by coherent spin states that do not violate the Hilbert space constraint. For the latter part, this means simply discarding any state that would violate the constraint. For the former, we have to make sure that our basis states can reproduce the spin coherent states defined on a single site as

$$|(\theta, \phi)\rangle = e^{i\phi(\hat{s}^z + S)} e^{-i\theta \hat{s}^x} |-S\rangle$$

$$= \sum_{k=0}^{2S} \sqrt{\binom{2S}{k}} e^{ik(\phi - \pi/2)}$$

$$\times \cos^{2S-k}\left(\frac{\theta}{2}\right) \sin^{k}\left(\frac{\theta}{2}\right) |k - S\rangle. \qquad \text{(F1)}$$

The main prefactor to look for here is the square root of the binomial coefficient. Indeed, if we now consider a state with spin coherent states on multiple sites we have to multiply all prefactors. So on a single sublattice, if we have a total of n excitations spread onto k sites, we will end up with a total prefactor of

$$e^{in(\phi - \pi/2)} \cos^{2kS-n}\left(\frac{\theta}{2}\right) \sin^{n}\left(\frac{\theta}{2}\right) \prod_{j=1}^{k} \sqrt{\binom{2S}{S - m_j}}, \qquad \text{(F2)}$$

where we could remove the sine, cosine, and exponential terms from the product because their final exponent only depends on the total number of excitations, which we know is equal to nS. Since these three prefactors are the same for all states in an equivalence class, they do not need to be incorporated into the basis. However, this is not the case for the binomial coefficient, as those vary from state to state.

Hence, the basis states of our subspace $\mathcal{K}_2$ take the form

$$|n_1, n_2\rangle = \frac{1}{\mathcal{N}} \sum_{|\phi\rangle \in (n_1, n_2)} \left(\prod_{j=1}^{L} \sqrt{\binom{2S}{S + m_j}} \right) |\phi\rangle, \quad (F3)$$

where the sum is over all basis states in the equivalence class (n_1, n_2), $\mathcal{N}$ is a normalization factor, and the m_j are the spin eigenvalues of the individual sites for the state $|\phi\rangle$. If there were no constraint, this would just be the set of *global* spin coherent states on each sublattice. However, as the equivalence classes only contain states that do not violate the constraint, they are nontrivial.

We now give some details on how to construct the basis of the larger subspace $\mathcal{K}_{4S}$. The goal of this subspace is to describe the state of the big spin formed by each of the $4S$ hypercubes in the QLM graph. Each of them corresponds to having one sublattice with all sites at a fixed spin eigenvalue m, and the other sublattice flipping freely between $-m$ and $-m - 1$. As a consequence, we have to keep track of the number of sites having the spin eigenvalue m on each sublattice for all m. As such, for each sublattice we have

$2S$ numbers characterizing each state, corresponding to the number of sites with spin eigenvalue m. Here we only deal with hypercubes, corresponding to sets of spins $\frac{1}{2}$, and we do not need to incorporate the prefactor as for the coherent states with higher spin in $\mathcal{K}_2$. So each basis state is simply a symmetric superposition of all states with the same population distribution (the same number of sites with spin eigenvalue m for each m) in both sublattices. For example, for $S = 1$ and $L = 4$ the state $|n_1^0 = 1, n_1^1 = 2, n_2^0 = 0, n_2^1 = 2\rangle$ would be defined as

$$|n_1^0 = 1, n_1^1 = 0, n_2^0 = 0, n_2^1 = 2\rangle = \frac{1}{\sqrt{2}}(|0, 1, -1, 1\rangle + |-1, 1, 0, 1\rangle). \quad (F4)$$

Note that $\mathcal{K}_{4S} = \mathcal{K}_2$ for $S = \frac{1}{2}$, and for higher S we have $\mathcal{K}_2 \subset \mathcal{K}_{4S}$. Indeed, as the population distribution in every basis state of $\mathcal{K}_{4S}$ is the same, all of the states in it would get the same prefactor in Eq. (F2). As such, every single basis state of $\mathcal{K}_2$ is in $\mathcal{K}_{4S}$, while the opposite is not true.

[1] W. S. Bakr, J. I. Gillen, A. Peng, S. Fölling, and M. Greiner, A quantum gas microscope for detecting single atoms in a Hubbard-regime optical lattice, Nature (London) **462**, 74 (2009).

[2] M. Greiner, O. Mandel, T. Esslinger, T. W. Hänsch, and I. Bloch, Quantum phase transition from a superfluid to a Mott insulator in a gas of ultracold atoms, Nature (London) **415**, 39 (2002).

[3] I. Bloch, J. Dalibard, and W. Zwerger, Many-body physics with ultracold gases, Rev. Mod. Phys. **80**, 885 (2008).

[4] M. C. Bañuls, R. Blatt, J. Catani, A. Celi, J. I. Cirac, M. Dalmonte, L. Fallani, K. Jansen, M. Lewenstein, S. Montangero, C. A. Muschik, B. Reznik, E. Rico, L. Tagliacozzo, K. Van Acoleyen, F. Verstraete, U.-J. Wiese, M. Wingate, J. Zakrzewski, and P. Zoller, Simulating lattice gauge theories within quantum technologies, Eur. Phys. J. D **74**, 165 (2020).

[5] Y. Alexeev, D. Bacon, K. R. Brown, R. Calderbank, L. D. Carr, F. T. Chong, B. DeMarco, D. Englund, E. Farhi, B. Fefferman, A. V. Gorshkov, A. Houck, J. Kim, S. Kimmel, M. Lange, S. Lloyd, M. D. Lukin, D. Maslov, P. Maunz, C. Monroe *et al.*, Quantum computer systems for scientific discovery, PRX Quantum **2**, 017001 (2021).

[6] N. Klco, A. Roggero, and M. J. Savage, Standard model physics and the digital quantum revolution: Thoughts about the interface, Rep. Prog. Phys. **85**, 064301 (2022).

[7] M. Aidelsburger, L. Barbiero, A. Bermudez, T. Chanda, A. Dauphin, D. González-Cuadra, P. R. Grzybowski, S. Hands, F. Jendrzejewski, J. Jünemann, G. Juzeliūnas, V. Kasper, A. Piga, S.-J. Ran, M. Rizzi, G. Sierra, L. Tagliacozzo, E. Tirrito, T. V. Zache, J. Zakrzewski *et al.*, Cold atoms meet lattice gauge theory, Philos. Trans. R. Soc. A **380**, 20210064 (2022).

[8] J. M. Deutsch, Quantum statistical mechanics in a closed system, Phys. Rev. A **43**, 2046 (1991).

[9] M. Srednicki, Chaos and quantum thermalization, Phys. Rev. E **50**, 888 (1994).

[10] M. Rigol, V. Dunjko, and M. Olshanii, Thermalization and its mechanism for generic isolated quantum systems, Nature (London) **452**, 854 (2008).

[11] J. Eisert, M. Friesdorf, and C. Gogolin, Quantum many-body systems out of equilibrium, Nat. Phys. **11**, 124 (2015).

[12] L. D'Alessio, Y. Kafri, A. Polkovnikov, and M. Rigol, From quantum chaos and eigenstate thermalization to statistical mechanics and thermodynamics, Adv. Phys. **65**, 239 (2016).

[13] J. M. Deutsch, Eigenstate thermalization hypothesis, Rep. Prog. Phys. **81**, 082001 (2018).

[14] A. M. Kaufman, M. E. Tai, A. Lukin, M. Rispoli, R. Schittko, P. M. Preiss, and M. Greiner, Quantum thermalization through entanglement in an isolated many-body system, Science **353**, 794 (2016).

[15] P. Jurcevic, H. Shen, P. Hauke, C. Maier, T. Brydges, C. Hempel, B. P. Lanyon, M. Heyl, R. Blatt, and C. F. Roos, Direct Observation of Dynamical Quantum Phase Transitions in an Interacting Many-Body System, Phys. Rev. Lett. **119**, 080501 (2017).

[16] B. Neyenhuis, J. Zhang, P. W. Hess, J. Smith, A. C. Lee, P. Richerme, Z.-X. Gong, A. V. Gorshkov, and C. Monroe, Observation of prethermalization in long-range interacting spin chains, Sci. Adv. **3**, e1700672 (2017).

[17] J. Zhang, G. Pagano, P. W. Hess, A. Kyprianidis, P. Becker, H. Kaplan, A. V. Gorshkov, Z.-X. Gong, and C. Monroe, Observation of a many-body dynamical phase transition with a 53-qubit quantum simulator, Nature (London) **551**, 601 (2017).

[18] H. B. Kaplan, L. Guo, W. L. Tan, A. De, F. Marquardt, G. Pagano, and C. Monroe, Many-Body Dephasing in a Trapped-Ion Quantum Simulator, Phys. Rev. Lett. **125**, 120605 (2020).

[19] Z.-Y. Zhou, G.-X. Su, J. C. Halimeh, R. Ott, H. Sun, P. Hauke, B. Yang, Z.-S. Yuan, J. Berges, and J.-W. Pan, Thermalization dynamics of a gauge theory on a quantum simulator, Science **377**, 311 (2022).

[20] D. M. Basko, I. L. Aleiner, and B. L. Altshuler, Metal–insulator transition in a weakly interacting many-electron system with localized single-particle states, Ann. Phys. **321**, 1126 (2006).

[21] R. Nandkishore and D. A. Huse, Many-body localization and thermalization in quantum statistical mechanics, Annu. Rev. Condens. Matter Phys. **6**, 15 (2015).

[22] D. A. Abanin, E. Altman, I. Bloch, and M. Serbyn, Colloquium: Many-body localization, thermalization, and entanglement, Rev. Mod. Phys. **91**, 021001 (2019).

[23] M. Schreiber, S. S. Hodgman, P. Bordia, H. P. Lüschen, M. H. Fischer, R. Vosk, E. Altman, U. Schneider, and I. Bloch, Observation of many-body localization of interacting fermions in a quasirandom optical lattice, Science **349**, 842 (2015).

[24] J. Smith, A. Lee, P. Richerme, B. Neyenhuis, P. W. Hess, P. Hauke, M. Heyl, D. A. Huse, and C. Monroe, Many-body localization in a quantum simulator with programmable random disorder, Nat. Phys. **12**, 907 (2016).

[25] S. S. Kondov, W. R. McGehee, W. Xu, and B. DeMarco, Disorder-Induced Localization in a Strongly Correlated Atomic Hubbard Gas, Phys. Rev. Lett. **114**, 083002 (2015).

[26] J.-y. Choi, S. Hild, J. Zeiher, P. Schauß, A. Rubio-Abadal, T. Yefsah, V. Khemani, D. A. Huse, I. Bloch, and C. Gross, Exploring the many-body localization transition in two dimensions, Science **352**, 1547 (2016).

[27] P. Roushan, C. Neill, J. Tangpanitanon, V. M. Bastidas, A. Megrant, R. Barends, Y. Chen, Z. Chen, B. Chiaro, A. Dunsworth, A. Fowler, B. Foxen, M. Giustina, E. Jeffrey, J. Kelly, E. Lucero, J. Mutus, M. Neeley, C. Quintana, D. Sank *et al.*, Spectroscopic signatures of localization with interacting photons in superconducting qubits, Science **358**, 1175 (2017).

[28] B. Chiaro, C. Neill, A. Bohrdt, M. Filippone, F. Arute, K. Arya, R. Babbush, D. Bacon, J. Bardin, R. Barends, S. Boixo, D. Buell, B. Burkett, Y. Chen, Z. Chen, R. Collins, A. Dunsworth, E. Farhi, A. Fowler, B. Foxen *et al.*, Direct measurement of nonlocal interactions in the many-body localized phase, Phys. Rev. Res. **4**, 013148 (2022).

[29] M. Rispoli, A. Lukin, R. Schittko, S. Kim, M. E. Tai, J. Léonard, and M. Greiner, Quantum critical behaviour at the many-body localization transition, Nature (London) **573**, 385 (2019).

[30] A. Lukin, M. Rispoli, R. Schittko, M. E. Tai, A. M. Kaufman, S. Choi, V. Khemani, J. Léonard, and M. Greiner, Probing entanglement in a many-body localized system, Science **364**, 256 (2019).

[31] B. Sutherland, *Beautiful Models: 70 Years of Exactly Solved Quantum Many-body Problems* (World Scientific, Singapore, 2004).

[32] M. Serbyn, Z. Papić, and D. A. Abanin, Local Conservation Laws and the Structure of the Many-Body Localized States, Phys. Rev. Lett. **111**, 127201 (2013).

[33] D. A. Huse, R. Nandkishore, and V. Oganesyan, Phenomenology of fully many-body-localized systems, Phys. Rev. B **90**, 174202 (2014).

[34] M. Schulz, C. A. Hooley, R. Moessner, and F. Pollmann, Stark Many-Body Localization, Phys. Rev. Lett. **122**, 040606 (2019).

[35] W. Morong, F. Liu, P. Becker, K. S. Collins, L. Feng, A. Kyprianidis, G. Pagano, T. You, A. V. Gorshkov, and C. Monroe, Observation of Stark many-body localization without disorder, Nature (London) **599**, 393 (2021).

[36] T. Gunawardana and B. Buča, Dynamical l-bits in Stark many-body localization, Phys. Rev. B **106**, L161111 (2022).

[37] M. Brenes, M. Dalmonte, M. Heyl, and A. Scardicchio, Many-Body Localization Dynamics from Gauge Invariance, Phys. Rev. Lett. **120**, 030601 (2018).

[38] A. Smith, J. Knolle, D. L. Kovrizhin, and R. Moessner, Disorder-Free Localization, Phys. Rev. Lett. **118**, 266601 (2017).

[39] A. Metavitsiadis, A. Pidatella, and W. Brenig, Thermal transport in a two-dimensional $\mathbb{Z}_2$ spin liquid, Phys. Rev. B **96**, 205121 (2017).

[40] A. Smith, J. Knolle, R. Moessner, and D. L. Kovrizhin, Absence of Ergodicity without Quenched Disorder: From Quantum Disentangled Liquids to Many-Body Localization, Phys. Rev. Lett. **119**, 176601 (2017).

[41] A. Russomanno, S. Notarnicola, F. M. Surace, R. Fazio, M. Dalmonte, and M. Heyl, Homogeneous Floquet time crystal protected by gauge invariance, Phys. Rev. Res. **2**, 012003(R) (2020).

[42] I. Papaefstathiou, A. Smith, and J. Knolle, Disorder-free localization in a simple U(1) lattice gauge theory, Phys. Rev. B **102**, 165132 (2020).

[43] P. Karpov, R. Verdel, Y.-P. Huang, M. Schmitt, and M. Heyl, Disorder-Free Localization in an Interacting 2D Lattice Gauge Theory, Phys. Rev. Lett. **126**, 130401 (2021).

[44] O. Hart, S. Gopalakrishnan, and C. Castelnovo, Logarithmic Entanglement Growth from Disorder-Free Localization in the Two-Leg Compass Ladder, Phys. Rev. Lett. **126**, 227202 (2021).

[45] G.-Y. Zhu and M. Heyl, Subdiffusive dynamics and critical quantum correlations in a disorder-free localized Kitaev honeycomb model out of equilibrium, Phys. Rev. Res. **3**, L032069 (2021).

[46] N. Chakraborty, M. Heyl, P. Karpov, and R. Moessner, Disorder-free localization transition in a two-dimensional lattice gauge theory, Phys. Rev. B **106**, L060308 (2022).

[47] M. Serbyn, D. A. Abanin, and Z. Papić, Quantum many-body scars and weak breaking of ergodicity, Nat. Phys. **17**, 675 (2021).

[48] S. Moudgalya, B. A. Bernevig, and N. Regnault, Quantum many-body scars and Hilbert space fragmentation: A review of exact results, Rep. Prog. Phys. **85**, 086501 (2022).

[49] S. Moudgalya, S. Rachel, B. A. Bernevig, and N. Regnault, Exact excited states of nonintegrable models, Phys. Rev. B **98**, 235155 (2018).

[50] S. Moudgalya, N. Regnault, and B. A. Bernevig, Entanglement of exact excited states of Affleck-Kennedy-Lieb-Tasaki models: Exact results, many-body scars, and violation of the strong eigenstate thermalization hypothesis, Phys. Rev. B **98**, 235156 (2018).

[51] C. J. Turner, A. A. Michailidis, D. A. Abanin, M. Serbyn, and Z. Papić, Weak ergodicity breaking from quantum many-body scars, Nat. Phys. **14**, 745 (2018).

[52] M. Schecter and T. Iadecola, Weak Ergodicity Breaking and Quantum Many-Body Scars in Spin-1 XY Magnets, Phys. Rev. Lett. **123**, 147201 (2019).

[53] D. K. Mark, C.-J. Lin, and O. I. Motrunich, Unified structure for exact towers of scar states in the Affleck-Kennedy-Lieb-Tasaki and other models, Phys. Rev. B **101**, 195131 (2020).

[54] H. Zhao, J. Vovrosh, F. Mintert, and J. Knolle, Quantum Many-Body Scars in Optical Lattices, Phys. Rev. Lett. **124**, 160604 (2020).

[55] H. Zhao, A. Smith, F. Mintert, and J. Knolle, Orthogonal Quantum Many-Body Scars, Phys. Rev. Lett. **127**, 150601 (2021).

[56] N. Shiraishi and T. Mori, Systematic Construction of Counterexamples to the Eigenstate Thermalization Hypothesis, Phys. Rev. Lett. **119**, 030601 (2017).

[57] C.-J. Lin and O. I. Motrunich, Exact Quantum Many-Body Scar States in the Rydberg-Blockaded Atom Chain, Phys. Rev. Lett. **122**, 173401 (2019).

[58] W. W. Ho, S. Choi, H. Pichler, and M. D. Lukin, Periodic Orbits, Entanglement, and Quantum Many-Body Scars in Constrained Models: Matrix Product State Approach, Phys. Rev. Lett. **122**, 040603 (2019).

[59] H. Bernien, S. Schwartz, A. Keesling, H. Levine, A. Omran, H. Pichler, S. Choi, A. S. Zibrov, M. Endres, M. Greiner, V. Vuletić, and M. D. Lukin, Probing many-body dynamics on a 51-atom quantum simulator, Nature (London) **551**, 579 (2017).

[60] D. Bluvstein, A. Omran, H. Levine, A. Keesling, G. Semeghini, S. Ebadi, T. T. Wang, A. A. Michailidis, N. Maskara, W. W. Ho, S. Choi, M. Serbyn, M. Greiner, V. Vuletić, and M. D. Lukin, Controlling quantum many-body dynamics in driven Rydberg atom arrays, Science **371**, 1355 (2021).

[61] W. Kao, K.-Y. Li, K.-Y. Lin, S. Gopalakrishnan, and B. L. Lev, Topological pumping of a 1D dipolar gas into strongly correlated prethermal states, Science **371**, 296 (2021).

[62] S. Scherg, T. Kohlert, P. Sala, F. Pollmann, B. Hebbe Madhusudhana, I. Bloch, and M. Aidelsburger, Observing non-ergodicity due to kinetic constraints in tilted Fermi-Hubbard chains, Nat. Commun. **12**, 4490 (2021).

[63] P. N. Jepsen, Y. K. E. Lee, H. Lin, I. Dimitrova, Y. Margalit, W. W. Ho, and W. Ketterle, Long-lived phantom helix states in Heisenberg quantum magnets, Nat. Phys. **18**, 899 (2022).

[64] G.-X. Su, H. Sun, A. Hudomal, J.-Y. Desaules, Z.-Y. Zhou, B. Yang, J. C. Halimeh, Z.-S. Yuan, Z. Papić, and J.-W. Pan, Observation of many-body scarring in a Bose-Hubbard quantum simulator, Phys. Rev. Res. **5**, 023010 (2023).

[65] S. Chandrasekharan and U.-J Wiese, Quantum link models: A discrete approach to gauge theories, Nucl. Phys. B **492**, 455 (1997).

[66] U.-J. Wiese, Ultracold quantum gases and lattice systems: Quantum simulation of lattice gauge theories, Ann. Phys. (Berlin) **525**, 777 (2013).

[67] D. Banerjee and A. Sen, Quantum Scars from Zero Modes in an Abelian Lattice Gauge Theory on Ladders, Phys. Rev. Lett. **126**, 220601 (2021).

[68] A. S. Aramthottil, U. Bhattacharya, D. González-Cuadra, M. Lewenstein, L. Barbiero, and J. Zakrzewski, Scar states in de-

[69] confined $\mathbb{Z}_2$ lattice gauge theories, Phys. Rev. B **106**, L041101 (2022).

[69] S. Biswas, D. Banerjee, and A. Sen, Scars from protected zero modes and beyond in U(1) quantum link and quantum dimer models, SciPost Phys. **12**, 148 (2022).

[70] J. C. Halimeh, L. Barbiero, P. Hauke, F. Grusdt, and A. Bohrdt, Robust quantum many-body scars in lattice gauge theories, arXiv:2203.08828.

[71] J.-Y. Desaules, D. Banerjee, A. Hudomal, Z. Papić, A. Sen, and J. C. Halimeh, Weak Ergodicity Breaking in the Schwinger Model, Phys. Rev. B **107**, L201105 (2023).

[72] F. M. Surace, P. P. Mazza, G. Giudici, A. Lerose, A. Gambassi, and M. Dalmonte, Lattice Gauge Theories and String Dynamics in Rydberg Atom Quantum Simulators, Phys. Rev. X **10**, 021041 (2020).

[73] V. Kasper, F. Hebenstreit, F. Jendrzejewski, M. K. Oberthaler, and J. Berges, Implementing quantum electrodynamics with ultracold atomic systems, New J. Phys. **19**, 023030 (2017).

[74] P. Fendley, K. Sengupta, and S. Sachdev, Competing density-wave orders in a one-dimensional hard-boson model, Phys. Rev. B **69**, 075106 (2004).

[75] I. Lesanovsky and H. Katsura, Interacting Fibonacci anyons in a Rydberg gas, Phys. Rev. A **86**, 041601(R) (2012).

[76] A. H. Al-Mohy and N. J. Higham, Computing the action of the matrix exponential, with an application to exponential integrators, SIAM J. Sci. Comput. **33**, 488 (2011).

[77] C. J. Turner, A. A. Michailidis, D. A. Abanin, M. Serbyn, and Z. Papić, Quantum scarred eigenstates in a Rydberg atom chain: Entanglement, breakdown of thermalization, and stability to perturbations, Phys. Rev. B **98**, 155134 (2018).

[78] K. Bull, I. Martin, and Z. Papić, Systematic Construction of Scarred Many-Body Dynamics in 1D Lattice Models, Phys. Rev. Lett. **123**, 030601 (2019).

[79] J.-Y. Desaules, A. Hudomal, C. J. Turner, and Z. Papić, Proposal for Realizing Quantum Scars in the Tilted 1D Fermi-Hubbard Model, Phys. Rev. Lett. **126**, 210601 (2021).

[80] P. Zhang, H. Dong, Y. Gao, L. Zhao, J. Hao, J.-Y. Desaules, Q. Guo, J. Chen, J. Deng, B. Liu, W. Ren, Y. Yao, X. Zhang, S. Xu, K. Wang, F. Jin, X. Zhu, B. Zhang, H. Li, C. Song *et al.*, Many-body Hilbert space scarring on a superconducting processor, Nat. Phys. **19**, 120 (2023).

[81] V. Karle, M. Serbyn, and A. A. Michailidis, Area-Law Entangled Eigenstates from Nullspaces of Local Hamiltonians, Phys. Rev. Lett. **127**, 060602 (2021).

[82] M. Christandl, N. Datta, A. Ekert, and A. J. Landahl, Perfect State Transfer in Quantum Spin Networks, Phys. Rev. Lett. **92**, 187902 (2004).

[83] J.-Y. Desaules, K. Bull, A. Daniel, and Z. Papić, Hypergrid subgraphs and the origin of scarred quantum walks in many-body Hilbert space, Phys. Rev. B **105**, 245137 (2022).

[84] B. Windt and H. Pichler, Squeezing Quantum Many-Body Scars, Phys. Rev. Lett. **128**, 090606 (2022).

[85] V. Khemani, C. R. Laumann, and A. Chandran, Signatures of integrability in the dynamics of Rydberg-blockaded chains, Phys. Rev. B **99**, 161101(R) (2019).

[86] S. Choi, C. J. Turner, H. Pichler, W. W. Ho, A. A. Michailidis, Z. Papić, M. Serbyn, M. D. Lukin, and D. A. Abanin, Emergent SU(2) Dynamics and Perfect Quantum Many-Body Scars, Phys. Rev. Lett. **122**, 220603 (2019).

[87] J. Haegeman, J. I. Cirac, T. J. Osborne, I. Pižorn, H. Verschelde, and F. Verstraete, Time-Dependent Variational Principle for Quantum Lattices, Phys. Rev. Lett. **107**, 070601 (2011).

[88] C. J. Turner, J.-Y. Desaules, K. Bull, and Z. Papić, Correspondence Principle for Many-Body Scars in Ultracold Rydberg Atoms, Phys. Rev. X **11**, 021021 (2021).

[89] E. A. Martinez, C. A. Muschik, P. Schindler, D. Nigg, A. Erhard, M. Heyl, P. Hauke, M. Dalmonte, T. Monz, P. Zoller, and R. Blatt, Real-time dynamics of lattice gauge theories with a few-qubit quantum computer, Nature (London) **534**, 516 (2016).

[90] C. Muschik, M. Heyl, E. Martinez, T. Monz, P. Schindler, B. Vogell, M. Dalmonte, P. Hauke, R. Blatt, and P. Zoller, U(1) Wilson lattice gauge theories in digital quantum simulators, New J. Phys. **19**, 103020 (2017).

[91] N. Klco, E. F. Dumitrescu, A. J. McCaskey, T. D. Morris, R. C. Pooser, M. Sanz, E. Solano, P. Lougovski, and M. J. Savage, Quantum-classical computation of Schwinger model dynamics using quantum computers, Phys. Rev. A **98**, 032331 (2018).

[92] A. Keesling, A. Omran, H. Levine, H. Bernien, H. Pichler, S. Choi, R. Samajdar, S. Schwartz, P. Silvi, S. Sachdev, P. Zoller, M. Endres, M. Greiner, V. Vuletić, and M. D. Lukin, Quantum Kibble–Zurek mechanism and critical dynamics on a programmable Rydberg simulator, Nature (London) **568**, 207 (2019).

[93] C. Kokail, C. Maier, R. van Bijnen, T. Brydges, M. K. Joshi, P. Jurcevic, C. A. Muschik, P. Silvi, R. Blatt, C. F. Roos, and P. Zoller, Self-verifying variational quantum simulation of lattice models, Nature (London) **569**, 355 (2019).

[94] F. Görg, K. Sandholzer, J. Minguzzi, R. Desbuquois, M. Messer, and T. Esslinger, Realization of density-dependent Peierls phases to engineer quantized gauge fields coupled to ultracold matter, Nat. Phys. **15**, 1161 (2019).

[95] C. Schweizer, F. Grusdt, M. Berngruber, L. Barbiero, E. Demler, N. Goldman, I. Bloch, and M. Aidelsburger, Floquet approach to ℤ2 lattice gauge theories with ultracold atoms in optical lattices, Nat. Phys. **15**, 1168 (2019).

[96] A. Mil, T. V. Zache, A. Hegde, A. Xia, R. P. Bhatt, M. K. Oberthaler, P. Hauke, J. Berges, and F. Jendrzejewski, A scalable realization of local U(1) gauge invariance in cold atomic mixtures, Science **367**, 1128 (2020).

[97] N. Klco, M. J. Savage, and J. R. Stryker, SU(2) non-Abelian gauge field theory in one dimension on digital quantum computers, Phys. Rev. D **101**, 074512 (2020).

[98] B. Yang, H. Sun, R. Ott, H.-Y. Wang, T. V. Zache, J. C. Halimeh, Z.-S. Yuan, P. Hauke, and J.-W. Pan, Observation of gauge invariance in a 71-site Bose–Hubbard quantum simulator, Nature (London) **587**, 392 (2020).

[99] J. Mildenberger, W. Mruczkiewicz, J. C. Halimeh, Z. Jiang, and P. Hauke, Probing confinement in a ℤ₂ lattice gauge theory on a quantum computer, arXiv:2203.08905.

[100] P. Sala, T. Rakovszky, R. Verresen, M. Knap, and F. Pollmann, Ergodicity Breaking Arising from Hilbert Space Fragmentation in Dipole-Conserving Hamiltonians, Phys. Rev. X **10**, 011047 (2020).

[101] V. Khemani, M. Hermele, and R. Nandkishore, Localization from Hilbert space shattering: From theory to physical realizations, Phys. Rev. B **101**, 174204 (2020).

[102] S. Moudgalya, A. Prem, R. Nandkishore, N. Regnault, and B. A. Bernevig, Thermalization and its absence within Krylov subspaces of a constrained Hamiltonian, in *Memorial Volume for Shoucheng Zhang* (World Scientific, Singapore, 2021) Chap. 7, pp. 147–209.

[103] T. V. Zache, M. V. Damme, J. C. Halimeh, P. Hauke, and D. Banerjee, Toward the continuum limit of a (1+1)D quantum link Schwinger model, Phys. Rev. D **106**, L091502 (2022).

[104] K. Bull, J.-Y. Desaules, and Z. Papić, Quantum scars as embeddings of weakly broken Lie algebra representations, Phys. Rev. B **101**, 165139 (2020).

[105] U. Schollwöck, The density-matrix renormalization group in the age of matrix product states, Ann. Phys. **326**, 96 (2011).

[106] G. M. Crosswhite and D. Bacon, Finite automata for caching in matrix product algorithms, Phys. Rev. A **78**, 012356 (2008).

Observation of many-body scarring in a Bose-Hubbard quantum simulator

Guo-Xian Su [1,2,3] Hui Sun,[1,2,3] Ana Hudomal [4,5] Jean-Yves Desaules [4] Zhao-Yu Zhou,[1,2,3] Bing Yang [6]
Jad C. Halimeh,[7] Zhen-Sheng Yuan [1,2,3,*] Zlatko Papić,[4,†] and Jian-Wei Pan[1,2,3,‡]

[1]*Hefei National Laboratory for Physical Sciences at Microscale and Department of Modern Physics,*
University of Science and Technology of China, Hefei, Anhui 230026, China
[2]*Physikalisches Institut, Ruprecht-Karls-Universität Heidelberg, Im Neuenheimer Feld 226, 69120 Heidelberg, Germany*
[3]*CAS Center for Excellence and Synergetic Innovation Center in Quantum Information and Quantum Physics,*
University of Science and Technology of China, Hefei, Anhui 230026, China
[4]*School of Physics and Astronomy, University of Leeds, Leeds LS2 9JT, United Kingdom*
[5]*Institute of Physics Belgrade, University of Belgrade, 11080 Belgrade, Serbia*
[6]*Department of Physics, Southern University of Science and Technology, Shenzhen 518055, China*
[7]*INO-CNR BEC Center and Department of Physics, University of Trento, Via Sommarive 14, I-38123 Trento, Italy*

The ongoing quest for understanding nonequilibrium dynamics of complex quantum systems underpins the foundation of statistical physics as well as the development of quantum technology. Quantum many-body scarring has recently opened a window into novel mechanisms for delaying the onset of thermalization by preparing the system in special initial states, such as the $\mathbb{Z}_2$ state in a Rydberg atom system. Here we realize many-body scarring in a Bose-Hubbard quantum simulator from previously unknown initial conditions such as the unit-filling state. We develop a quantum-interference protocol for measuring the entanglement entropy and demonstrate that scarring traps the many-body system in a low-entropy subspace. Our work makes the resource of scarring accessible to a broad class of ultracold-atom experiments, and it allows one to explore the relation of scarring to constrained dynamics in lattice gauge theories, Hilbert space fragmentation, and disorder-free localization.

DOI: [10.1103/PhysRevResearch.5.023010](https://doi.org/10.1103/PhysRevResearch.5.023010)

I. INTRODUCTION

Coherent manipulation of quantum many-body systems far from equilibrium is key to unlocking outstanding problems in quantum sciences including strongly coupled quantum field theories, exotic phases of matter, and development of enhanced metrology and computation schemes. These efforts, however, are frequently plagued by the presence of interactions in such systems, which lead to fast thermalization and information scrambling: the behavior known as quantum ergodicity [1–3]. A twist came with recent advances in synthetic quantum matter, which enabled detailed experimental study of thermalization dynamics in isolated quantum many-body systems, leading to the observation of ergodicity-violating phenomena in integrable [4] and many-body localized systems [5,6].

More recently, quantum many-body scarring has emerged as another remarkable ergodicity-breaking phenomenon,

*yuanzs@ustc.edu.cn
†Z.Papic@leeds.ac.uk
‡pan@ustc.edu.cn

where preparing the system in special initial states effectively traps it in a "cold" subspace that does not mix with the thermalizing bulk of the spectrum [7,8]. Such behavior hinders the scrambling of information encoded in the initial state and suppresses the spreading of quantum entanglement, allowing a many-body system to display persistent quantum revivals. Many-body scarring was first observed in the Rydberg atom experimental platform [9,10], and subsequent observations of weak ergodicity breaking phenomena have attracted much attention [11–13]. On the other hand, theoretical works have unearthed universal scarring mechanisms [14–17], pointing to the ubiquity of scarring phenomena in periodically driven systems [18–20] and in the presence of disorder [21,22]. Given that many-body scarring in Rydberg atom systems has previously been reported in a single initial state, the $\mathbb{Z}_2$-ordered state, many questions remain about the overall fragility of this phenomenon and its sensitivity to the initial condition. It is thus vital to extend the realm of scarring to a greater variety of experimental platforms and more accessible initial conditions, which would empower a fundamental understanding of nonergodic dynamics in various research areas ranging from lattice gauge theories to constrained glassy systems.

In this paper, we observe many-body scarring in a large-scale Bose-Hubbard quantum simulator, where we employ a tilted optical lattice to emulate the PXP model, a canonical model of many-body scarring [23–26]. We demonstrate that many-body scarring can result from a larger set of initial

states, including the unit-filling state at finite detuning, hitherto believed to undergo fast thermalization [9]. Furthermore, we demonstrate that periodic driving can be used to enhance scarring behavior. Taking advantage of spin-dependent optical superlattices, we measure the system's entanglement entropy by interfering identical copies in the double wells. We show the average entropy of single-site subsystems to be a good approximation of half-chain bipartite entropy, revealing a key property of scarring: the "trapping" of the quantum system in a low-entropy subspace, which prevents its relaxation into the exponentially large Hilbert space.

The remainder of this paper is organized as follows. In Sec. II we introduce our experimental setup and show how it can realize the PXP model. In Sec. III we benchmark our quantum simulation by observing many-body scarring from the previously known $\mathbb{Z}_2$ initial state. We also demonstrate the enhancement of scarring under periodic driving. In Sec. IV we present our measurements of entanglement entropy, providing deeper insight into the slow thermalization dynamics associated with scarred initial states. Finally, in Sec. V we extend the scarring phenomenon to a regime at moderate detuning for the unit-filling initial state. Our conclusions are presented in Sec. VI, while Appendixes A–D contain the derivation of the PXP mapping, further details on state preparation and measurement techniques, and a numerical study of other scarred initial conditions.

II. MAPPING THE PXP MODEL ONTO THE BOSE-HUBBARD MODEL

The PXP model [27,28] describes a kinetically constrained chain of spin-1/2 degrees of freedom. Each spin can exist in two possible states, $|\circ\rangle$ and $|\bullet\rangle$, corresponding to the ground state and excited state, respectively. An array of N such spins is governed by the Hamiltonian

$$\hat{H}_{\mathrm{PXP}} = \Omega \sum_{j=1}^{N} \hat{P}_{j-1}\hat{X}_j\hat{P}_{j+1}, \qquad (1)$$

where $\hat{X} = |\circ\rangle\langle\bullet| + |\bullet\rangle\langle\circ|$ is the Pauli x matrix, describing local spin precession with frequency Ω. The projectors onto the ground state, $\hat{P} = |\circ\rangle\langle\circ|$, constrain the dynamics by allowing a spin to flip only if both of its neighbors are in the ground state.

A remarkable property of the PXP model is that it is quantum chaotic and yet it exhibits persistent quantum revivals from a highly out-of-equilibrium $|\mathbb{Z}_2\rangle \equiv |\bullet\circ\bullet\circ\cdots\rangle$ initial state [23,29–31]. The presence of revivals from a special initial state in an overall chaotic system was understood to be a many-body analog of the phenomena associated with a single particle inside a stadium billiard, where nonergodicity arises as a "scar" imprinted by a particle's classical periodic orbit [16,32,33]. In many-body scarred systems, eigenstates were shown to form tower structures [23]. These towers are revealed by the anomalously high overlap of eigenstates with special initial states, and their equal energy spacing is responsible for quantum revivals. While previous experiments on Rydberg atoms [9,10] have primarily focused on the $|\mathbb{Z}_2\rangle$ initial state, we will demonstrate that the PXP model can effectively emerge in the Bose-Hubbard model, allowing us to

identify scarred revivals from a larger set of initial conditions, including the polarized state $|0\rangle \equiv |\circ\circ\circ\cdots\rangle$.

Our experiment begins with a ^{87}Rb Bose-Einstein condensate, which is compressed in the z direction and loaded into a single layer of a pancake-shaped trap. We then perform the superfluid-to-Mott-insulator phase transition with optical lattices in the x-y plane. In both x and y directions, we have a superlattice that is formed by superimposing the "short" lattice, with $a_s = 383.5$ nm spacing, and the "long" lattice, with $a_l = 767$ nm spacing [34,35], each of which can be individually controlled. We realize independent one-dimensional (1D) Bose-Hubbard systems in the y direction by ramping up the short-lattice depth in the x direction over $40E_r$, with $E_r = h^2/8ma_s^2$ being the short-lattice recoil energy, where h is the Planck constant and m is the ^{87}Rb atomic mass. The short lattice in the y direction makes an approximately $4°$ angle with gravity, which results in a static linear tilt per site of $\Delta_g = 816$ Hz; see Fig. 1(a). An external magnetic field gradient Δ_B may be further added to create a tunable linear tilting potential $\Delta = \Delta_g + \Delta_B$. The effective Hamiltonian describing our simulator is

$$\hat{H} = -J\sum_{i=1}^{L-1}(\hat{b}_i^\dagger\hat{b}_{i+1} + \hat{b}_{i+1}^\dagger\hat{b}_i) + \hat{U} + \hat{\Delta}, \qquad (2)$$

where J is the hopping amplitude, $\hat{b}$ and $\hat{b}^\dagger$ are the standard Bose annihilation and creation operators, the interaction energy is $\hat{U} = (U/2)\sum_{i=1}^{L}\hat{n}_i(\hat{n}_i - 1)$, and the tilt potential is $\hat{\Delta} = \Delta\sum_{i=1}^{L}i\hat{n}_i$. L denotes the number of sites in the chain with open boundary conditions, and we restrict ourselves to a total filling equal to 1, i.e., with the same number of bosons as lattice sites.

In order to realize the PXP model in the Bose-Hubbard quantum simulator, we tune the parameters to the resonant regime $U \approx \Delta \gg J$ [36,37], which has been studied extensively in the context of quantum Ising chains [38–40]. In this regime, three-boson occupancy of any site is strongly suppressed, and doublons can only be created by moving a particle to the left, e.g., $\cdots 11 \cdots \rightarrow \cdots 20 \cdots$, or destroyed by moving a particle to the right. The states of the PXP model are understood to live on the bonds of the Bose-Hubbard model. An excitation in the PXP model $\bullet_{j,j+1}$, living on the bond $(j, j+1)$, corresponds to the creation of a doublon 2_j0_{j+1} on site j in the Bose-Hubbard chain. We identify the unit-filling state $|111\cdots\rangle$ with the PXP polarized state, $|0\rangle$. Any other configuration of the PXP model can be mapped to a Fock state in the Bose-Hubbard model by starting from the unit filling, identifying the bonds that carry PXP excitations and replacing the corresponding sites in the Mott state with $11 \rightarrow 20$. Applying this rule across the chain allows us to map any basis state of the PXP model to a corresponding Fock state in the Bose-Hubbard model; for example, the $|\mathbb{Z}_2\rangle$ state maps to the Fock state $|\cdots 2020 \cdots\rangle$. Figure 1(b) illustrates the profound change in the connectivity of the Fock space near the resonance $U \approx \Delta \gg J$, with an emergent dynamical subspace isomorphic to the PXP model in the sector containing the $|\mathbb{Z}_2\rangle$ state. For a detailed derivation of the mapping, see Appendix A.
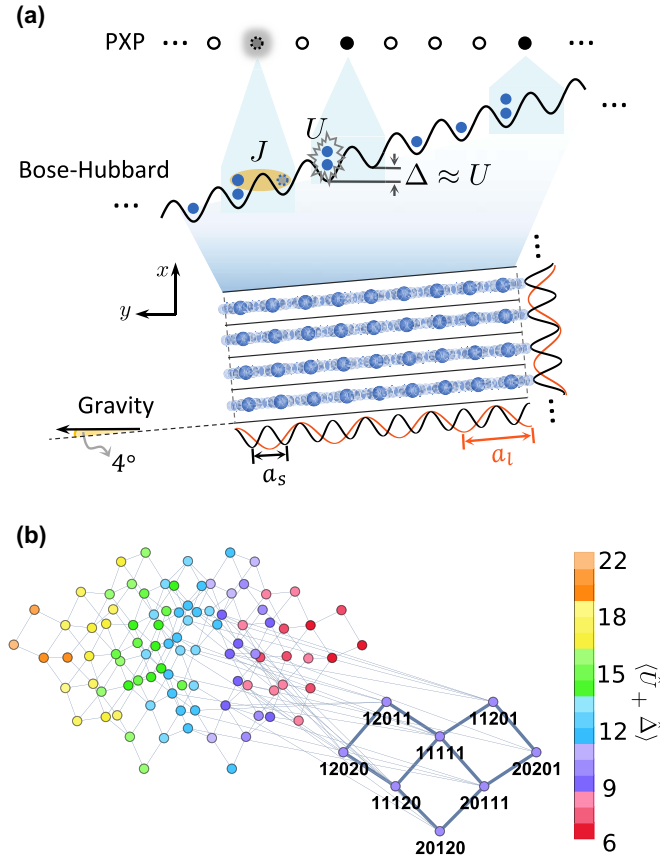
(a)

(b)

FIG. 1. Realizing the PXP model in a Bose-Hubbard quantum simulator. (a) A schematic of the optical lattice. Deep lattice potential in the x direction forms isolated chains in the y direction, where the linear tilting potential is applied. Spin-dependent superlattices consisting of two standing waves in each direction can be individually controlled for state preparation and measurement. At the resonance $U \approx \Delta \gg J$, the dominant hopping process is $11 \leftrightarrow 20$. The PXP excitations, ●, live on the bonds between the lattice sites. The doublon configuration 20 in the Bose-Hubbard model maps to an excitation in the PXP model, while all other configurations are mapped to an empty site, ○. For example, the given state $|\cdots \circ \bullet \circ \bullet \circ \circ \circ \bullet \cdots\rangle$ maps to the Fock state $|\cdots 120201120 \cdots\rangle$. (b) Emergence of the PXP subspace in the Bose-Hubbard model at the resonance $U \approx \Delta \gg J$. Dots represent Fock states of the tilted Bose-Hubbard model with five bosons on five sites (restricting ourselves to at most three bosons on any site). Lines denote the allowed hopping processes. The color scale shows the sum of interaction and tilt energies $\langle \hat{U} + \hat{\Delta} \rangle$ for each Fock state, and this value is conserved by resonant processes. The PXP dynamical subspace and its Fock states are explicitly labeled.

III. OBSERVATION OF $\mathbb{Z}_2$ QUANTUM MANY-BODY SCARS

To prepare the initial states, we first employ an entropy redistribution cooling method [34] with the superlattice in the y direction to prepare an $\bar{n} = 2$ Mott insulator in the left (odd) sites, while removing all atoms on the right (even) sites via site-dependent addressing [35]. This gives us the initial state $|\psi_0\rangle = |\mathbb{Z}_2\rangle = |2020 \cdots\rangle$ (see Appendix B). In the region of interest, we have prepared 50 copies of the initial

state $|\psi_0\rangle$ isolated by the short lattice along the x direction. Each copy extends over 50 short lattice sites along the y direction.

We quench the system out of equilibrium by abruptly dropping the y-lattice depth to $11.6 E_r$, which corresponds to switching J from 0 to 51(1) Hz. This is done while simultaneously adjusting the lattice depth in the x and z directions accordingly, such that the interaction strength matches the linear tilt with $U = \Delta = \Delta_g \approx 16J$. After evolution time t, we freeze the dynamics by ramping up the y-lattice depth rapidly and read out the atomic density on the left ($\langle \hat{n}_{\text{Left}} \rangle$) and right ($\langle \hat{n}_{\text{Right}} \rangle$) sites of the double wells formed by the y superlattice successively [35,41]. This provides access to the density imbalance, $\langle \hat{M}_z \rangle = (\langle \hat{n}_{\text{Left}} \rangle - \langle \hat{n}_{\text{Right}} \rangle)/(\langle \hat{n}_{\text{Left}} \rangle + \langle \hat{n}_{\text{Right}} \rangle)$, an observable corresponding to the staggered magnetization in the PXP model; see Fig. 2(a). Another observable is the density of excitations in the PXP model, which is measured by projecting out the even atomic number occupancy on each site, then reading out the average odd particle density $\langle \hat{P}_{\hat{n} \in \text{odd}} \rangle_{(1)}$ [41]. Due to highly suppressed multiboson occupancy, we have $\langle \hat{P}_{|\bullet} \rangle = \langle \hat{n}_{\text{doublon}} \rangle_{(1)} \approx (1 - \langle \hat{P}_{\hat{n} \in \text{odd}} \rangle_{(1)})/2$.

Away from the resonance, the dynamics is ergodic, and the staggered magnetization present in the initial $|\mathbb{Z}_2\rangle$ state quickly decays with time; see Fig. 2(b). In contrast, by tuning to the vicinity of the resonance, $\Delta = U$, we observe distinct signatures of scarring: The system approximately undergoes persistent oscillations between the $|\mathbb{Z}_2\rangle \equiv |\bullet \circ \bullet \circ \cdots\rangle$ configuration and its partner shifted by one site, $|\bar{\mathbb{Z}}_2\rangle \equiv |\circ \bullet \circ \bullet \cdots\rangle$, as can be seen in the staggered magnetization profile and the density of excitations in Fig. 2(b). The density of excitations does not distinguish between $|\mathbb{Z}_2\rangle$ and $|\bar{\mathbb{Z}}_2\rangle$ states; hence there is a trivial factor of 2 difference between the oscillation frequencies of $\langle \hat{P}_{|\bullet} \rangle$ and $\langle \hat{M}_z \rangle$.

The scarred oscillations in Fig. 2(b) are visibly damped with a decay time $\tau = 49.6 \pm 0.8$ ms. Nevertheless, as shown in Ref. [10], by periodically driving the system it is possible to "refocus" the spreading of the many-body wave function in the Hilbert space and thereby enhance the scarring effect, as we demonstrate numerically in Fig. 2(c) and experimentally in Fig. 2(d). Our driving protocol is based on modulating the laser intensity of the z lattice, which translates into periodic modulation of the interaction energy, $U(t) = \Delta + U_0 + U_m \cos(\omega t)$, while Δ is kept fixed. This results in a modulation of the density of doublons in the chain, acting as the analog of the chemical potential in the PXP model.

Numerical simulations of the PXP model with the driven chemical potential, shown in Fig. 2(c), demonstrate the dynamical stabilization of the Hilbert space trajectory. We visualize the trajectory by plotting the average sublattice occupations, $\langle \hat{n}_{\text{Left}} \rangle$ and $\langle \hat{n}_{\text{Right}} \rangle$, normalized to the interval [0,1]. The $|\mathbb{Z}_2\rangle$ and $|\bar{\mathbb{Z}}_2\rangle$ states are located at the coordinates (1,0) and (0,1), which are the lower right and upper left corners of this diagram, respectively. The polarized state $|0\rangle$ is at the origin (0,0).

In the undriven case [left panel of Fig. 2(c)], the trajectory at first oscillates between $|\mathbb{Z}_2\rangle$ and $|\bar{\mathbb{Z}}_2\rangle$ states, while passing through a region with a lower number of excitations. However, as the time passes, the trajectory drifts, exploring progressively larger parts of the Hilbert space. By contrast, when the driving is turned on [right panel of Fig. 2(c)], the
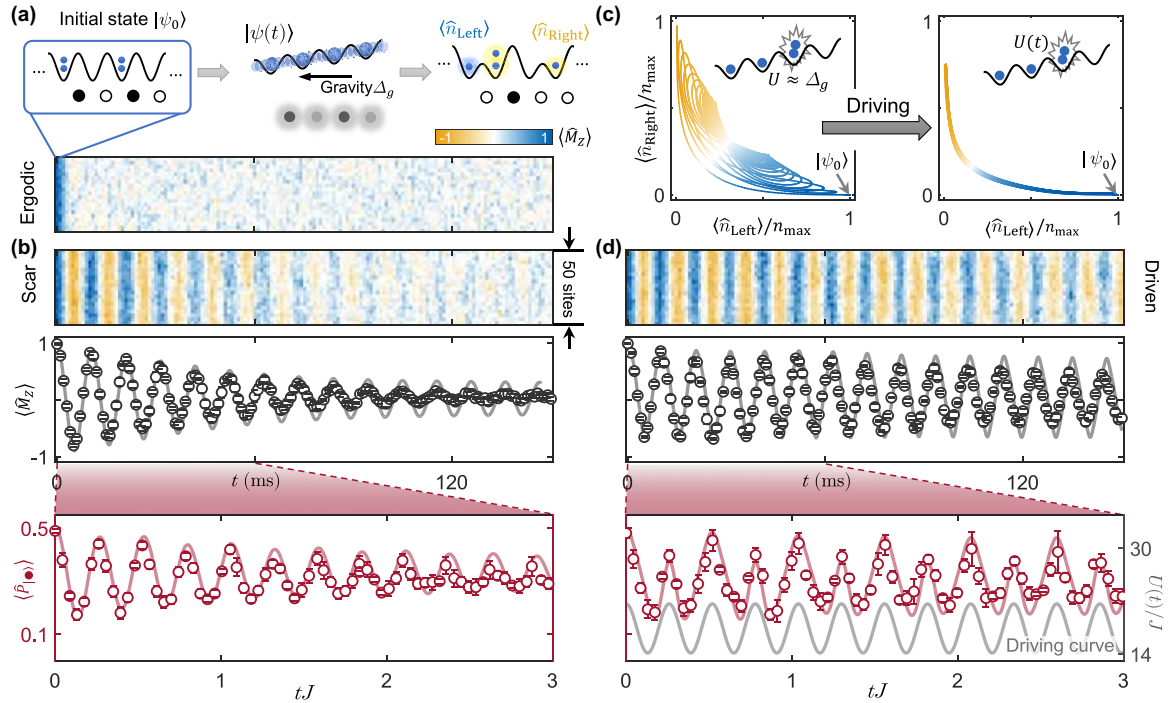
FIG. 2. Observation of $\mathbb{Z}_2$ quantum many-body scars in a Bose-Hubbard quantum simulator. (a) Starting from the state $|\psi_0\rangle = |\cdots 2020\cdots\rangle$—the analog of the $|\mathbb{Z}_2\rangle$ state in the PXP model—we utilize gravity to provide linear tilt $\Delta = \Delta_g$. We characterize quench dynamics by measuring density imbalance and the number of doublons, corresponding to staggered magnetization $\langle \hat{M}_z \rangle$ and density of excitations $\langle \hat{P}_{|\bullet\rangle} \rangle$ in the PXP model. In the detuned regime $\Delta - U \approx -2J$, the dynamics is ergodic, and the system has no memory of the initial state at late times. (b) Tuning to $U \approx \Delta$, we observe persistent oscillations in both $\langle \hat{M}_z \rangle$ and $\langle \hat{P}_{|\bullet\rangle} \rangle$. This memory of the initial state is a signature of weak ergodicity breaking due to quantum many-body scars. (c) and (d) Periodic modulation of the interaction $U(t) = \Delta + U_0 + U_m \cos(\omega t)$ with $U_0 = 1.85J$, $U_m = 3.71J$, and $\omega = 3.85J$ leads to an enhancement of scarring. (c) shows the numerically computed trajectory in the sublattice occupation plane for the PXP model with $N = 24$ sites, with and without driving. The sublattice occupancies $\langle \hat{n}_{\text{Left}} \rangle$ and $\langle \hat{n}_{\text{Right}} \rangle$ are normalized to the interval [0,1]. The driving is seen to strongly suppress the spreading of the trajectory. In (d), experimental measurements on the driven Bose-Hubbard model show robust scarred oscillations at all accessible times. In both the static and driven cases, experimental data for $\langle \hat{M}_z \rangle$ and $\langle \hat{P}_{|\bullet\rangle} \rangle$ are in excellent agreement with TEBD numerical simulations shown by gray and red solid curves. The gray curve in the lowest panel shows the modulation $U(t)$.

trajectory approximately repeats the first revival period of the undriven case, even at late times. Thus the driving stabilized the scarred revivals without significantly altering their period.

Experimental measurements on the driven Bose-Hubbard model in Fig. 2(d) find a strong enhancement of the amplitude of the oscillations in staggered magnetization with the decay time τ increasing to 208 ± 10 ms, while the period remains nearly the same as in the static case. Optimal driving parameters were determined numerically using a combination of simulated annealing and brute-force search; see Supplemental Material [42].

We note that the experimental measurement of $\langle \hat{M}_z \rangle$ damps slightly faster than the theory prediction, shown by a curve in Fig. 2(b), at late times ($t > 60$ ms). We attribute this to an inherent residual inhomogeneity across the lattice, which results in dephasing between different parts of the system, as well as possible decoherence induced by scattering of the lattice lasers. To avoid the effect of these undesired dephasing or decoherence effects, in the following we limit our investigation to times up to 60 ms.

IV. UNRAVELING THE DETAILS OF SCARRED DYNAMICS VIA QUANTUM INTERFERENCE

Entanglement entropy is key for characterizing scarring behavior. Entropy provides a window into the evolution of the system's wave function and the spreading of quantum entanglement. For a system trapped in a scarred subspace, thermalization is inhibited, and the system exhibits suppressed entropy growth and periodic fidelity revivals. Measuring these observables usually requires brute-force state tomography, but for our 50-site Bose-Hubbard system with a Hilbert space dimension exceeding 10^{28}, this approach is generally impossible.

However, the superlattice in the x direction allows us to probe entanglement entropy by interfering identical copies in the double wells, analogous to the 50 : 50 beam splitter (BS) interference employed in photonics experiments [43]; see Fig. 3(a). This is done by freezing the dynamics along the chains in the y direction after evolution time t; then we interfere copies of $|\psi(t)\rangle$ in the double wells formed by the x superlattice (see Appendix C). After the interference, a parity projection helps read out the average odd particle
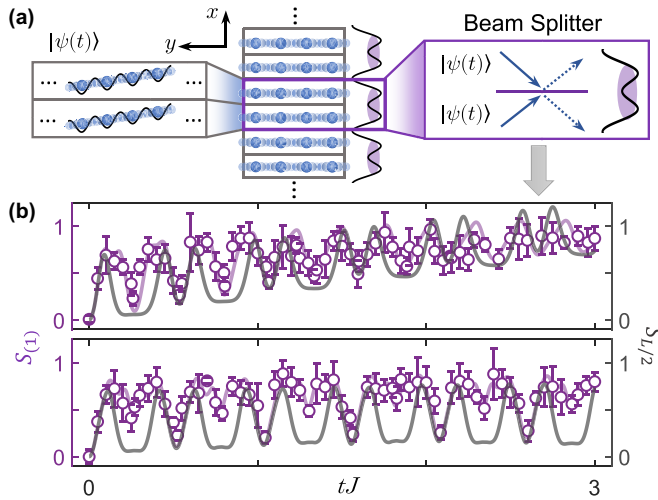
FIG. 3. Probing many-body scarred dynamics via quantum interference. (a) After evolution time t, we freeze the dynamics in the y direction, and then by interfering two identical copies in the double wells along the x direction, we obtain the second-order Rényi entropy. (b) The entropy for a single site, $S_{(1)}$, is seen to have robust oscillations with the same frequency as in Fig. 2(b), indicating a lack of thermalization. The slow growth of entropy in the absence of driving (upper panel) is strongly suppressed when we drive the system using the same parameters as in Fig. 2(d) (lower panel). In both cases, the single-site entropy is a good approximation to the half-chain entropy, $S_{L/2}$, evaluated numerically using TEBD (gray curve).

density $\langle \hat{P}_{\hat{n} \in \text{odd}}^{\text{BS}} \rangle_{(1)}$, which gives us access to the second-order Rényi entropy [44]. We measure the entropy of single-site subsystems $S_{(1)} = -\ln(\text{Tr}_{(1)}[\hat{\rho}(t)^2]) = -\ln(1 - 2\langle \hat{P}_{\hat{n} \in \text{odd}}^{\text{BS}} \rangle_{(1)})$, where $\hat{\rho}(t) = |\psi(t)\rangle \langle \psi(t)|$ is the density matrix. Entanglement entropy $S_{(1)}$, shown in Fig. 3(b), grows much more slowly than expected in a thermalizing system. The growth is accompanied by oscillations with the same frequency as $\langle \hat{P}_{\bullet} \rangle$ in Fig. 2(b), implying that the system returns to the neighborhood of product states $|\mathbb{Z}_2\rangle$ and $|\bar{\mathbb{Z}}_2\rangle$. Furthermore, the entropy growth becomes almost fully suppressed by periodic driving, indicating that the scarred subspace disconnects from the thermalizing bulk of the spectrum. Numerical time-evolving block decimation (TEBD) simulations confirm that this lack of thermalization at the single-site level provides a good approximation for the behavior of larger subsystems, as demonstrated by the half-chain bipartite entropy $S_{L/2}$ plotted in Fig. 3(b). This shows that scarring traps the system in a vanishingly small corner of an exponentially large Hilbert space.

V. EMERGENCE OF DETUNED SCARRING IN THE POLARIZED STATE

Up to this point, we have provided extensive benchmarks of our quantum simulator against the previously known case of $\mathbb{Z}_2$ quantum many-body scars [9]. In this section we demonstrate that our quantum simulator also hosts distinct scarring regimes for initial states other than $|\mathbb{Z}_2\rangle$, which are enabled by detuning and further stabilized by periodic drive. We highlight this finding by observation of scarring behavior in the polarized state $|0\rangle$, previously not associated with scars.

We first prepare the unit-filling state $|1111\cdots\rangle$ by transferring $|2, 0\rangle$ to $|1, 1\rangle$ states in the superlattice [34], which maps to the polarized state in the PXP model (see also Appendix B). In the absence of detuning or periodic drive, we observe fast relaxation: Both the density of excitations and single-site entropy rapidly relax, with no visible oscillations beyond the timescale $\sim 1/J$; see Fig. 4(a). Interestingly, when we bias the system by a static detuning, $U_0 = -2.38J$, we observe the emergence of oscillations in all three observables, accompanied by a slight decay; see Fig. 4(b). Finally, if we also periodically modulate the interaction with amplitude $U_m = 1.54J$ and frequency $\omega = 4.9J \times 2\pi$, we find a dramatic enhancement of scarring [Fig. 4(c)]. In particular, entropy now shows pronounced oscillations, signaling robust scar-induced coherence at all experimentally accessible times.

The intuitive picture behind our observations is summarized as follows. In the absence of detuning or periodic drive, the system initialized in the polarized state undergoes chaotic dynamics and rapidly explores the entire Hilbert space. By biasing the system via static detuning, thermalization can be suppressed over moderate timescales. Finally, by periodically driving the system it is possible to "refocus" the spreading of the many-body wave function in the Hilbert space and thereby enhance the scarring effect, similar to the findings of Ref. [10] for the $|\mathbb{Z}_2\rangle$ state. In the remainder of this section, we present our theoretical analysis of the experiment that supports this interpretation of the dynamics.

Figure 5 shows the results of exact diagonalizations of the PXP model in Eq. (1) in the presence of static detuning, $\hat{H}(\mu) = \hat{H}_{\text{PXP}} + \mu_0 \sum_i \hat{n}_i$, where $\hat{n}_i$ takes a value equal to 1 if site i contains an excitation and 0 otherwise. The static chemical potential μ_0 is proportional to the Bose-Hubbard detuning parameter U_0 in Fig. 4. Figure 5(a) plots the overlap of all energy eigenstates $|E\rangle$ of the pure PXP model ($\mu_0 = 0$) with the polarized state $|\psi_0\rangle = |0\rangle$. As expected, we do not see any hallmarks of scars, such as ergodicity-violating eigenstates with anomalously enhanced projection on $|0\rangle$. Moreover, the lowest-entropy eigenstates, denoted by squares in Fig. 5(b), are the known $\mathbb{Z}_2$ scarred eigenstates [31] which are hidden in the bulk of spectrum when the overlap is taken with the $|0\rangle$ state.

On the other hand, when we add the static chemical potential $\mu_0 = 1.68\Omega$, corresponding to the detuning value in Fig. 4, a band of scarred eigenstates with anomalously large overlap with $|0\rangle$ emerges; see Fig. 5(c). The band of scarred eigenstates, highlighted by star symbols in Fig. 5(c), spans the entire energy spectrum, but their support on $|0\rangle$ is biased towards the ground state due to the breaking of particle-hole symmetry by detuning. The detuned scarred states also have anomalously low entanglement entropy, as seen in Fig. 5(d).

A few comments are in order. We note that exact diagonalization confirms that the PXP model remains chaotic for the value of detuning used in Fig. 5(c), and this detuning is not large enough to trivially fragment the entire spectrum into disconnected sectors with the given numbers of excitations [42]. Moreover, we confirmed that the scarred eigenstates in Fig. 5(c) are distinct from the ones associated with the $|\mathbb{Z}_2\rangle$ state in Fig. 5(a). Thus it remains to be understood if these eigenstates can be described within the su(2)
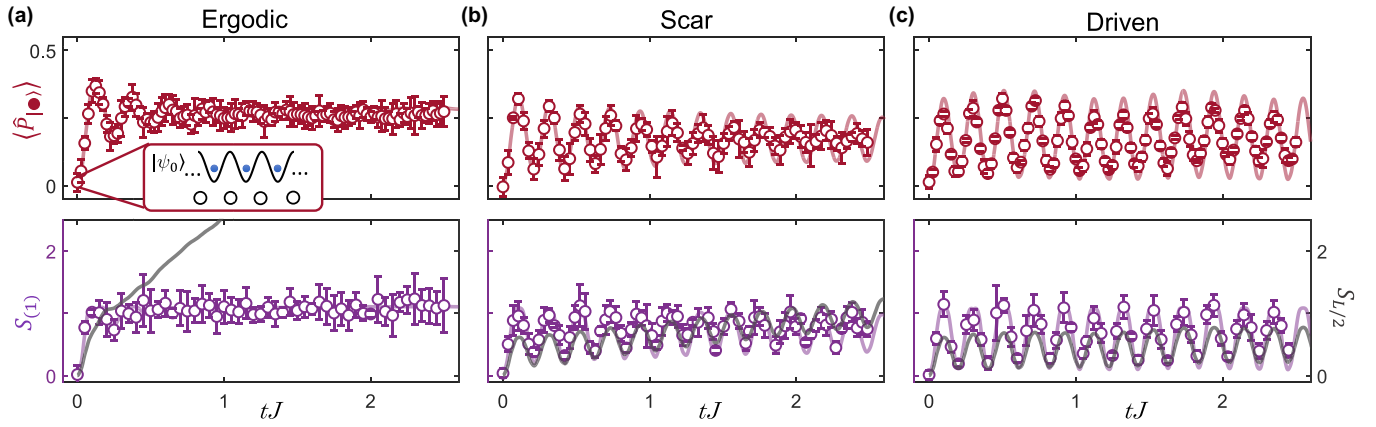
FIG. 4. Emergence of many-body scarring in the polarized state. (a) Fast thermalization from the unit-filling state in the Bose-Hubbard chain at $U = \Delta$ resonance. (b) Emergence of scarred dynamics in the presence of static detuning. (c) Dynamical stabilization of scarred dynamics in the presence of both detuning and periodic driving. The top and bottom rows show the experimental measurements of the density of excitations and second Rényi entropy, respectively. The ergodic case shows fast growth of the half-chain entropy compared with the single-site entropy, while for the scarred dynamics, the single-site entropy approximates well the half-chain entropy, with or without periodic driving. The static detuning is $U_0 = -2.38J$, and the modulation parameters are $U_m = 1.54J$ and $\omega = 4.9J \times 2\pi$. The curves are the results of TEBD simulations.

spectrum-generating algebra framework developed for the $|\mathbb{Z}_2\rangle$ state in Ref. [45].

Nevertheless, similar to the $|\mathbb{Z}_2\rangle$ case, the scarring from the $|0\rangle$ state can be further enhanced by periodic modulation of the PXP chemical potential, $\mu(t) = \mu_0 + \mu_m \cos(\omega t)$. By evaluating the corresponding Floquet operator, we find that a single Floquet mode develops a very large overlap with the $|0\rangle$ state [42]. The existence of a single Floquet mode, whose mixing with other modes is strongly suppressed, gives rise to robust oscillations in the dynamics well beyond the experimentally accessible timescales.

To probe the ergodicity of the dynamics from the polarized state, we compare the difference between the predictions of the diagonal and canonical ensembles for an observable such as the average number of excitations; see Fig. 6(a). These two ensembles are expected to give the same result if the strong eigenstate thermalization hypothesis (ETH) holds [46] and all eigenstates at a similar energy density yield the same expectation value for local observables. Figure 6(a) shows that the discrepancy between the two ensembles is the strongest around $\mu_0 \approx 1.68\Omega$, where we observe strong scarring. For μ_0/Ω close to 0, the polarized state
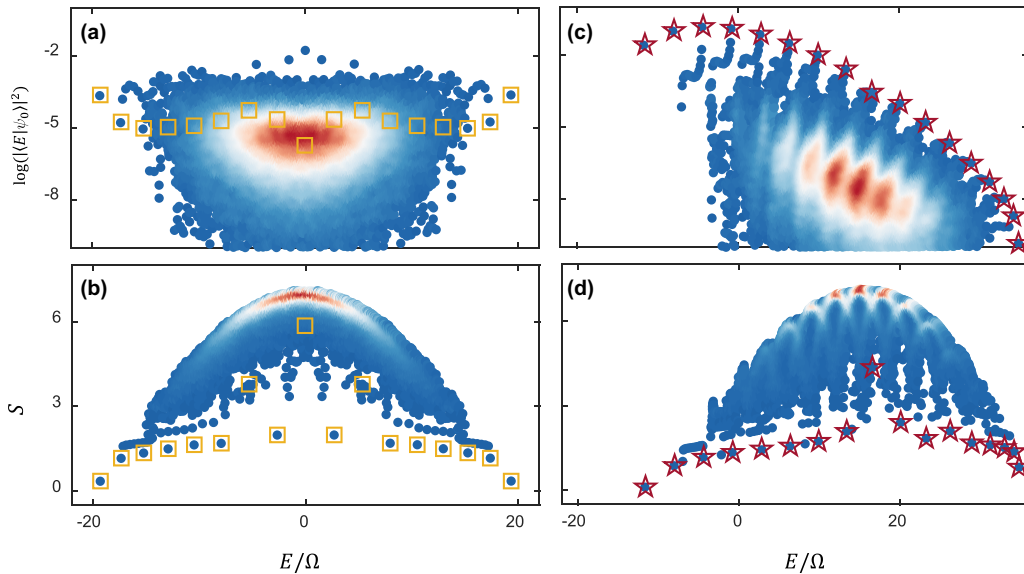
FIG. 5. Eigenstate properties of the detuned PXP model. (a) Overlaps of all eigenstates of the PXP model with the polarized state $|\psi_0\rangle = |0\rangle$. (b) Bipartite entanglement entropy of the eigenstates in (a). The squares mark the previously known $\mathbb{Z}_2$ scarred eigenstates. (c) and (d) Same as (a) and (b) but for the PXP model with the static chemical potential $\mu_0 = 1.68\Omega$, approximately corresponding to the experimental value of detuning in Fig. 4. The stars denote the detuned scar eigenstates, which have high overlap with the $|0\rangle$ state as well as low entropy. All data are obtained by exact diagonalization of the PXP model on a ring with $N = 32$ sites in the zero-momentum and inversion-symmetric sector.
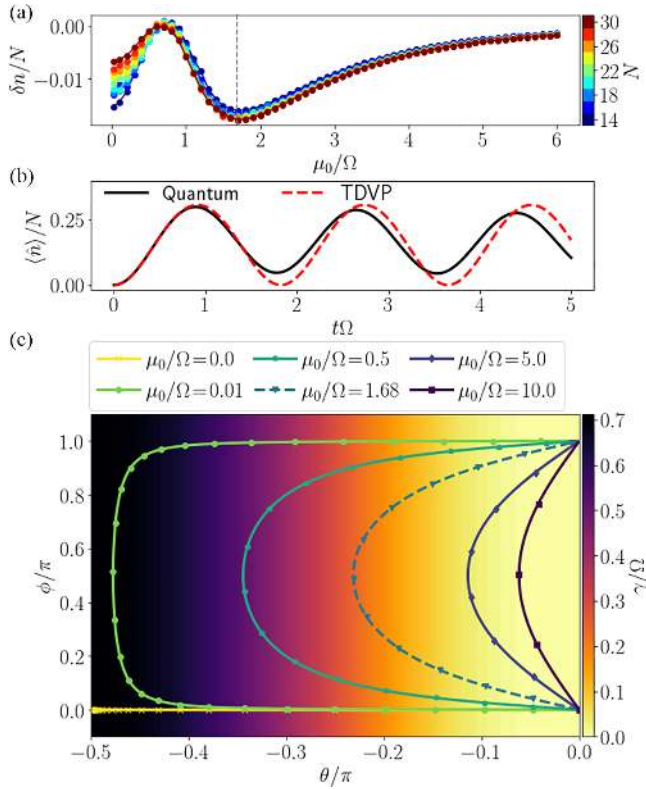
FIG. 6. Nonergodic dynamics from the polarized state in the detuned PXP model. (a) Difference between the expectation values of the diagonal and canonical ensembles for the average number of excitations. The discrepancy is maximized around $\mu_0/\Omega \approx 1.68$. (b) The average number of excitations at $\mu_0/\Omega = 1.68$ following the quench from the $|0\rangle$ state shows good agreement between the exact quantum dynamics and TDVP approximation. The exact dynamics is for system size $N = 32$ spins. (c) Trajectory in the TDVP manifold for different values of μ_0/Ω. The color scale denotes quantum leakage γ, defined in the text, which bounds the accuracy of the TDVP approximation. The markers are spaced in time by $\Delta t = 0.15/\Omega$. For the optimal value $\mu_0 = 1.68\Omega$, identified in (a) and also used in experiment, the trajectory avoids the high-leakage region and approximates well the quantum dynamics, while it is not limited to a small corner of the many-body Hilbert space.

thermalizes quickly towards the thermal value expected for a state whose expectation value of the energy is near the middle of the many-body spectrum. For very large μ_0/Ω, we enter a trivial regime where the polarized state is close to the ground state and only a few eigenstates at low energies are relevant for the dynamics. Hence, in this regime, quenching from the polarized state is similar to quenching from a thermal state at a very low temperature, and the agreement between the two ensembles is again very good. However, in this regime, only a very small part of the many-body Hilbert space is explored by the dynamics. This is not the case in the scarred regime that we investigate experimentally, and this can be demonstrated by studying the relevant classical limit, as shown next.

In the single-particle case, scarred quantum dynamics originates from an unstable periodic orbit in the classical limit $\hbar \to 0$ [47]. In a many-body system, one approach to establishing a quantum-classical correspondence is to project the Schrödinger dynamics into a variational manifold, e.g.,

spanned by matrix product states [48], a method known as the "time-dependent variational principle" (TDVP). It was shown that the scarred dynamics of the $|\mathbb{Z}_2\rangle$ state in the PXP model is well captured by the TDVP approach, allowing one to identify a classical orbit [16]. In Figs. 6(b) and 6(c) we utilize the TDVP approach to gain a semiclassical understanding of the detuned scarred dynamics from the $|0\rangle$ state. We parametrize the TDVP manifold using translation-invariant, spin-coherent states compatible with the Rydberg blockade constraint [49]. The states are defined by the Bloch sphere angles θ and ϕ, where $\sin(\theta)$ is proportional to the density of excitations, while ϕ describes the phase. In the thermodynamic limit, we can obtain classical equations of motion for θ and ϕ (see Ref. [50] for a detailed derivation). Figure 6(b) demonstrates that this classical dynamical system provides an excellent approximation of the quantum trajectory for sufficiently large values of μ_0, including $\mu_0 = 1.68\Omega$.

To quantify the accuracy of the TDVP approach in capturing the quantum dynamics, we use "quantum leakage": the instantaneous norm of a component of the state vector that lies outside the TDVP manifold, $\gamma^2 \equiv (1/N)|| |\dot\psi\rangle - i\hat{H}|\psi\rangle ||^2$ [16]. For the initial state $|0\rangle$, the leakage has a simple analytic expression $\gamma^2 = \Omega^2 \sin^6\theta/(1 + \sin^2\theta)$ [50]. The leakage is higher as θ is increased, corresponding to a larger density of excitations. In this regime, i.e., for small values of μ_0/Ω, the PXP constraint has a strong effect, and the spin-coherent state ansatz does not faithfully capture the dynamics. On the other hand, for large values of μ_0/Ω, the leakage is low, but θ is confined to values near zero; thus the trajectory does not explore much of the Hilbert space. This corresponds to the trivial case where the dynamics is confined to very low densities of excitations, rendering the constraint unimportant. Finally, in the intermediate regime of μ_0/Ω where we observe the scarring, the TDVP dynamics is able to "avoid" the high-leakage area, as seen in Fig. 6(c), while at the same time θ is not pinned to zero and the dynamics is not confined to one corner of the Hilbert space.

VI. DISCUSSION AND OUTLOOK

We performed a quantum simulation of the paradigmatic PXP model of many-body scarring using a tilted Bose-Hubbard optical lattice. We demonstrated the existence of persistent quantum revivals from the $|\mathbb{Z}_2\rangle$ initial state and their dynamical stabilization, opening up a route for the investigation of scarring beyond Rydberg atom arrays. By harnessing the effect of detuning, we observed a scarring regime associated with the polarized initial state. As the latter state is spatially homogeneous, its preparation does not require a superlattice, which makes further investigations of scarring phenomena accessible to a large class of ultracold-atom experiments.

Moreover, we have demonstrated that periodic driving can lead to a striking decoupling of the scarred subspace from the rest of the thermalizing bulk of the spectrum, as revealed by the arrested growth of entanglement entropy. The mechanism of this enhancement is a subject of ongoing investigations. On the one hand, Ref. [51] used a kicked toy model to argue that the scarring enhancement originates from a discrete time crystalline order. On the other hand, Ref. [52] studied the cosine

drive employed in experiment, finding two distinct regimes with long-lived scarred revivals. In the regime corresponding to the parameter values in Fig. 2 above, the driving parameters need to be fine-tuned to match the intrinsic revival frequency of the undriven scarred system. Moreover, the stabilization was no longer possible when the system was perturbed by terms which destroy scarring in the undriven case. This suggests that driving indeed acts as an enhancement mechanism, preventing dynamics from "leaking" into the thermalizing bulk.

Our demonstration of scarring in the $|0\rangle$ state highlights the importance of energy density. While the $|\mathbb{Z}_2\rangle$ has predominant support on the eigenstates in the middle of the spectrum, i.e., it constitutes an "infinite temperature" ensemble, the support of the $|0\rangle$ state is biased towards one end of the spectrum as a result of particle-hole symmetry breaking via the detuning potential. This suggests that, depending on the effective temperature, one can realize scarring from a much larger class of initial states with a suitable choice of detuning and periodic driving protocols. We illustrate this in Appendix D by simulating the quench of the chemical potential in the PXP model (see also Ref. [50]).

The versatility of optical lattice platforms allows one to directly probe the link between many-body scarring and other forms of ergodicity-breaking phenomena, such as Hilbert space fragmentation and disorder-free localization, as the latter can be conveniently studied in our setup by varying the tilt. In this context, we note that Ref. [12] has recently used the tilt potential to demonstrate Hilbert space fragmentation in the Fermi-Hubbard optical lattice. By contrast, in this paper we explored ergodicity breaking due to many-body scars occurring within a *single* fragment of the Hilbert space. While many-body scarring can be induced in the Fermi-Hubbard model by tuning to a similar resonance condition [53], the underlying mechanism is an approximate dimerization of the chain, which is conceptually different from the PXP-type scarring considered here.

In future work, it would be interesting to explore realizations of new scarring models by tuning to other resonance conditions and other types of lattices, including ladders and two-dimensional arrays. Indeed, it is known that the U(1) quantum link model (QLM) [54,55] can be exactly mapped to the PXP model [56]. As such, recent large-scale experiments realizing the U(1) QLM [57,58] can in principle also probe our results. A proposal has recently been introduced to extend these setups to $(2 + 1)$D [59], where a mapping between the U(1) QLM and PXP model does not hold, which would allow one to probe how the scarring regimes discovered in this paper would behave in higher spatial dimensions. Finally, the observation of long-lived quantum coherence due to scarring and its controllable enhancement via periodic modulation lays the foundation for applications such as quantum memories and quantum sensing [60,61].

APPENDIX A: MAPPING THE TILTED 1D BOSE-HUBBARD ONTO THE PXP MODEL AT $\Delta \approx U$ RESONANCE

The Hamiltonian describing our 1D Bose-Hubbard model is given in Eq. (2) of the main text, with J denoting the hopping amplitude, $\hat{H}_U$ denoting the corresponding interaction term, and $\hat{H}_\Delta$ denoting the tilt potential. We denote by L the number of lattice sites and assume open boundary conditions (OBCs). Unless specified otherwise, we fix the filling factor to $\nu = 1$, i.e., the number of bosons is equal to the number of sites in the chain.

In the $U, \Delta \gg J$ limit, the energy spectrum of the Hamiltonian in Eq. (2) splits into bands with approximately constant expectation value of the diagonal terms, $\langle \hat{H}_U + \hat{H}_\Delta \rangle \approx$ const, and the Hilbert space becomes fragmented. At the $U \approx \Delta \gg J$ resonance, the only process which conserves $\langle \hat{H}_U + \hat{H}_\Delta \rangle$ is $11 \leftrightarrow 20$, i.e., doublons can only be created by moving a particle to the left and destroyed by moving a particle to the right. In the connected component of the Fock state $|111 \cdots 111\rangle$, the system in the resonant regime is described by an effective Hamiltonian

$$\hat{H}_{\text{eff}} = -J \sum_{i=1}^{L-1} (\hat{b}_i^\dagger \hat{b}_{i+1} \hat{n}_i (2 - \hat{n}_i) \hat{n}_{i+1} (2 - \hat{n}_{i+1}) + \text{H.c.}), \quad \text{(A1)}$$

which results from the first-order Schrieffer-Wolff transformation applied to Eq. (2) [62]. In the Supplemental Material [42] we discuss the effect of higher-order terms in the Schrieffer-Wolff transformation.

In the remainder of this Appendix, we show that the Hamiltonian (A1) is equivalent to the PXP Hamiltonian [27,28] (see also Ref. [36] for the original derivation of the mapping and a recent review [37]). The connected component of the Hilbert space contains only certain types of two-site configurations (20, 11, 12, 02, 01), while all other two-site configurations are forbidden (22, 21, 10, 00). If we consider the configuration 20 to be an excitation, all allowed configurations can be mapped to those of the PXP model as follows:

$$
\begin{aligned}
\cdots 20 \cdots &\leftrightarrow \circ \bullet \circ, \\
\cdots 11 \cdots &\leftrightarrow \circ \circ \circ, \\
\cdots 12 \cdots &\leftrightarrow \circ \circ \bullet, \quad \text{(A2)} \\
\cdots 02 \cdots &\leftrightarrow \bullet \circ \bullet, \\
\cdots 01 \cdots &\leftrightarrow \bullet \circ \circ.
\end{aligned}
$$

Note that excitations live on the bonds between sites and this mapping also includes links to the two surrounding sites. For example, the configuration $\cdots 2020 \cdots$ maps to $\circ \bullet \circ \bullet \circ$ and not to $\circ \bullet \circ \circ \bullet \circ$. On the other hand, the configuration 2020 with OBCs on both sides maps to $\bullet \circ \bullet$, as there are no bonds across the boundaries.

The effective Hamiltonian (A1) can be rewritten as

$$\hat{H}_{\text{eff}} = -J \sum_{i=1}^{L-1} \left(\underbrace{\hat{b}_i^\dagger \hat{b}_{i+1} \delta_{\hat{n}_i, 1} \delta_{\hat{n}_{i+1}, 1}}_{\sqrt{2} \hat{P}_{j-1} \hat{\sigma}_j^+ \hat{P}_{j+1}} + \underbrace{\hat{b}_{i+1}^\dagger \hat{b}_i \delta_{\hat{n}_i, 2} \delta_{\hat{n}_{i+1}, 0}}_{\sqrt{2} \hat{P}_{j-1} \hat{\sigma}_j^- \hat{P}_{j+1}} \right). \quad \text{(A3)}$$

In this equation, the index i labels the sites, while j labels the bonds between sites. The Kronecker delta functions have been expressed in terms of projectors, $\hat{P}_j = |\circ_j\rangle\langle\circ_j|$, and the bosonic hopping terms correspond to the spin raising and lowering operators, $\hat{\sigma}_j^\pm$, on the bond j. We can use delta functions because there are no configurations with more than two particles per site in this connected component and the only possible values of $\hat{n}_i(2 - \hat{n}_i)$ are 0 and 1. Moving a particle to the neighboring site on the left corresponds to creating an excitation, and moving to the right corresponds to annihilating, while delta functions act as constraints.

Finally, the effective Hamiltonian is equivalent to the PXP Hamiltonian

$$\hat{H}_{\text{PXP}} = \Omega \sum_{j=1}^{N} (\hat{P}_{j-1} \hat{\sigma}_j^+ \hat{P}_{j+1} + \hat{P}_{j-1} \hat{\sigma}_j^- \hat{P}_{j+1})$$

$$= \Omega \sum_{j=1}^{N} \hat{P}_{j-1} \hat{X}_j \hat{P}_{j+1}, \quad \text{(A4)}$$

when we set $\Omega = -\sqrt{2} J$ and $N = L - 1$, with $\hat{X}_j \equiv |\circ_j\rangle\langle\bullet_j| + |\bullet_j\rangle\langle\circ_j|$ denoting the usual Pauli x matrix. In the case of OBCs, the two boundary terms become $\hat{X}_1 \hat{P}_2$ and $\hat{P}_{N-1} \hat{X}_N$. Note that the effective bosonic model in Eq. (A3) for a system size L is equivalent to the PXP model for size $N = L - 1$ since the number of bonds is the number of sites minus 1.

In the PXP model, the initial states which lead to pronounced quantum revivals are the two states with the maximal number of excitations: the Néel states, $|\bullet\circ\bullet\circ\cdots\bullet\circ\rangle$ and $|\circ\bullet\circ\bullet\cdots\circ\bullet\rangle$ [23,31]. The equivalent states in the tilted Bose-Hubbard model are $|2020\cdots 201\rangle$ and $|12020\cdots 20\rangle$, for odd system sizes, and $|2020\cdots 20\rangle$ and $|120\cdots 201\rangle$ for even sizes. In our experimental setup, it is not possible to exactly prepare the $|2020\cdots 201\rangle$ state due to the inability to independently control single sites. Instead, our experiment realizes the $|2020\cdots 20\rangle$ state, which corresponds to the Néel state $|\bullet\circ\bullet\circ\cdots\bullet\circ\bullet\rangle$ in the PXP model with an odd number of sites and OBCs.

Figure 7 numerically demonstrates the mapping between the tilted Bose-Hubbard model in Eq. (2) and the PXP model in Eq. (1) in a lattice size $L = 9$. The figure shows the overlap of eigenstates with the Néel state as a function of energy, for the choice of parameters $U = \Delta = 12$ and $J = 1$. The energy spectrum is split into bands with approximately constant expectation value of the sum of interaction and tilt
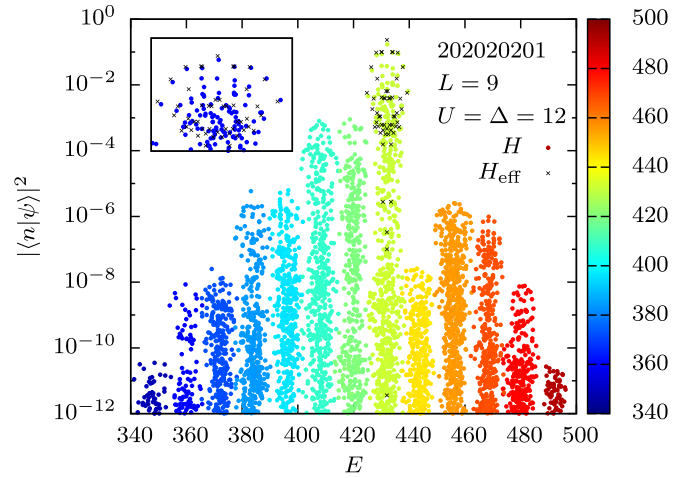

FIG. 7. Numerical demonstration of the mapping between the PXP and tilted Bose-Hubbard models. The overlap of the state $|202020201\rangle$ with the eigenstates of the tilted Bose-Hubbard model in Eq. (2) for $J = 1$ and $U = \Delta = 12$ (in units of $\hbar = 1$) is shown. The color indicates the expectation value of the diagonal part of the Hamiltonian, $\langle\hat{H}_U + \hat{H}_\Delta\rangle$, for each eigenstate. The black crosses correspond to the effective model in Eq. (A3), shifted by the energy $E = \langle 202020201|\hat{H}|202020201\rangle = 432$. The inset shows the top part of the band with the highest overlap, where a band of scarred eigenstates analogous to that in the PXP model can be seen.

terms $\langle\hat{H}_U + \hat{H}_\Delta\rangle$, as indicated by different colors. The inset shows the top part of the highest-overlap band, around the energy $E = \langle 202020201|\hat{H}|202020201\rangle = 432$. This band is described by the effective Hamiltonian (A1), which preserves the expectation value $\langle\hat{H}_U + \hat{H}_\Delta\rangle$ and is equivalent to the PXP Hamiltonian. A band of scarred eigenstates is magnified in the inset, and indeed resembles similar plots for the PXP model [31]. As the two Néel states have the maximal number of doublons at filling factor $\nu = 1$, this type of dynamics also leads to oscillations in doublon number, which was experimentally measured in Fig. 2.

APPENDIX B: STATE PREPARATION AND DETECTION

Our experiment starts out with a two-dimensional Bose-Einstein condensate of ^{87}Rb atoms prepared in the hyperfine state $|\downarrow\rangle = 5S_{1/2} |F = 1, m_F = -1\rangle$. By applying a microwave pulse, atoms can be adiabatically transferred to the state $|\uparrow\rangle = 5S_{1/2} |F = 2, m_F = -2\rangle$, which is resonant with the imaging laser and thus can be detected. The atoms are initially confined to a single layer of a pancake-shaped trap with 3 μm period. In both x and y directions, we have an optical superlattice that can be controlled separately. Each superlattice potential is generated by superimposing two standing waves with laser frequency $\lambda_s = 767$ nm and $\lambda_l = 1534$ nm, which can be described by

$$V(x) = V_s^x \cos^2(kx) - V_l^x \cos^2(kx/2 + \theta_x),$$
$$V(y) = V_s^y \cos^2(ky) - V_l^y \cos^2(ky/2 + \theta_y), \quad \text{(B1)}$$
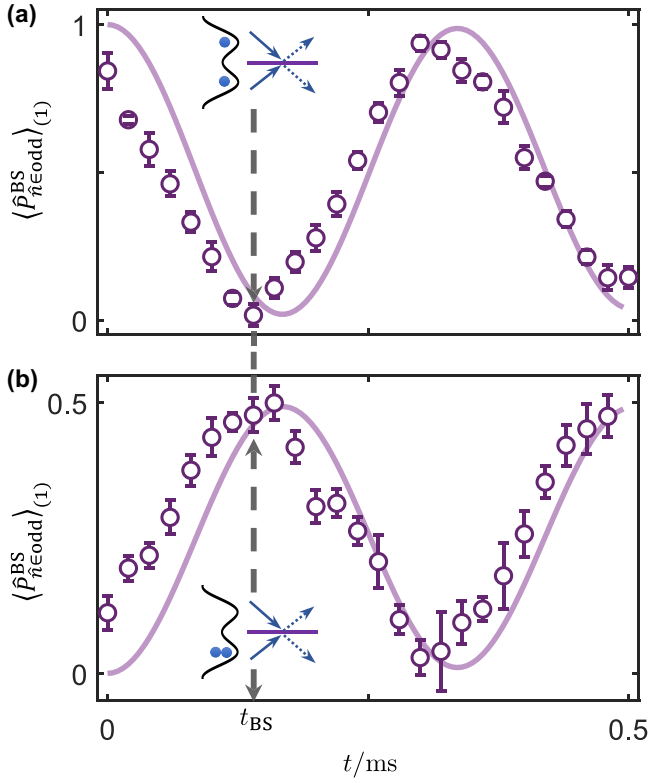
FIG. 8. Quantum interference. (a) Interfering $|1, 1\rangle$ product states in the double wells. (b) Interfering $|2, 0\rangle$ product states in the double wells. Solid curves are TEBD simulations. Experimental data are shifted forward at earliest times due to the 50 μs ramping time of the lattice potential.

where $V_{s(l)}^{x(y)}$ is the depth of the short (long) lattice in the x (y) direction, $k = 2\pi/\lambda_s$ is the short-lattice wave number, and $\theta_{x(y)}$ is the relative phase between the short and long lattices in the x (y) direction.

We first perform a cooling technique by loading the atoms into a staggered superlattice in the y direction at $\theta_y = \pi/4$, meanwhile ramping up only the short lattice in the x direction. We tune the y-superlattice potential to create a Mott insulator with $\bar{n} = 2$ filling in odd sites, while even sites form a $\bar{n} = 1.5$ superfluid, serving as a reservoir for carrying away the thermal entropy [34].

Atoms at even sites are removed by performing site-selective addressing. This is done by first setting $\theta_y = 0$ to form double wells and then tuning the polarization of the short-lattice laser along the y direction to create an energy splitting between even and odd sites for the $|\downarrow\rangle$-to-$|\uparrow\rangle$ transition. We transfer the atoms at even sites to $|\uparrow\rangle$ and remove them with the imaging laser [35]. In this way we have prepared the initial $|\mathbb{Z}_2\rangle$ state $|2020\cdots\rangle$. The same site-selective addressing procedure is also utilized to read out atomic density on even and odd sites separately in experiment. Inside each isolated double-well unit, we can perform state engineering that transfers the state $|2, 0\rangle$ to $|1, 1\rangle$ [34]. This results in the unit-filling state $|1111\cdots\rangle$ which corresponds to the polarized state $|0\rangle$ in the PXP model.

APPENDIX C: QUANTUM INTERFERENCE IN THE DOUBLE WELLS

The beam splitter (BS) interference is realized in the balanced double wells formed by the superlattices in the x direction, expressed in Eq. (B1) by setting $\theta_x = 0$. In the noninteracting limit, indistinguishable bosonic particles coming into the interference at $t = 0$ interfere according to the bosonic bunching. Therefore having equal numbers of atoms coming into the two ports at $t = 0$ results in $\langle \hat{P}_{\hat{n} \in \mathrm{odd}}^{\mathrm{BS}} \rangle = 0$ at t_{BS}, while having different numbers of atoms interfering results in $\langle \hat{P}_{\hat{n} \in \mathrm{odd}}^{\mathrm{BS}} \rangle = 0.5$. Each copy of atoms coming into the interference is prepared individually, and hence there is no global phase between them, resulting in the equivalence between the two output ports [44].

To implement the quantum-interference protocol, we quench the x-lattice potentials to $V_s^x = 6E_r$ and $V_l^x = 5E_r$, resulting in the intra-double-well tunneling at $J \approx 740$ Hz and inter-double-well tunneling $J' \approx 35$ Hz. Simultaneously, we lower the lattice depth in the x direction to $25E_r$ and trapping frequency in the z direction to 1.4 kHz, achieving an interaction of $U \approx 360$ Hz. Two examples are shown here in Fig. 8, where we interfere product states $|1, 1\rangle$ [Fig. 8(a)] or $|2, 0\rangle$ [Fig. 8(b)] in the double wells and read out the average odd particle density. At $t_{\mathrm{BS}} = 0.14$ ms we identify the beam splitter operation, where $|1, 1\rangle$ gives $\langle \hat{P}_{\hat{n} \in \mathrm{odd}}^{\mathrm{BS}} \rangle_{(1)} = 0.01(3)$, while $|2, 0\rangle$ gives $\langle \hat{P}_{\hat{n} \in \mathrm{odd}}^{\mathrm{BS}} \rangle_{(1)} = 0.48(3)$. We simulate the interference dynamics with a 20-site chain consisting of ten double-well units. We find good agreement at later times,
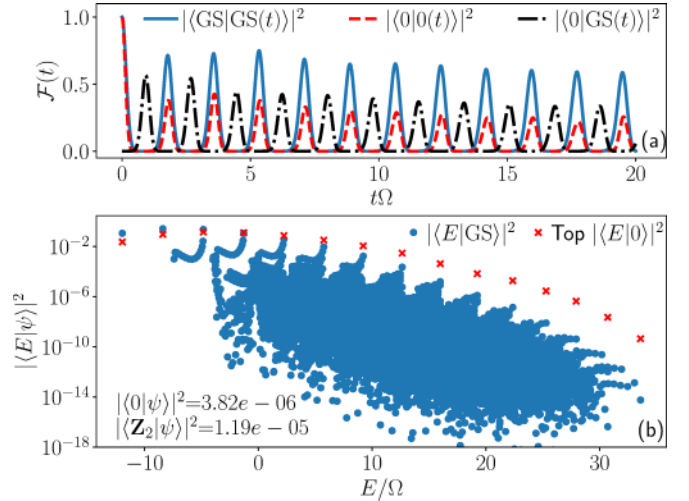
FIG. 9. Emergence of many-body scarring by quenching the chemical potential in the PXP model from $\mu_i = -0.76\Omega$ to $\mu_f = 1.6\Omega$. (a) The dynamics of quantum fidelity (blue solid curve) is similar to that of the polarized state for the same value of μ_f (red dashed curve). The overlap between the time-evolved state and $|0\rangle$ (black dash-dotted curve) shows that a significant state transfer occurs between them. (b) The overlap of the prequench ground state with the eigenstates of $\hat{H}(\mu_f)$ displays characteristic scar tower structures. Red crosses denote the highest overlaps with the $|0\rangle$ state in each scarred tower. The overlap of the prequench ground state with $|0\rangle$ and $|\mathbb{Z}_2\rangle$ states is given in the inset. All data are for $N = 32$ spins in the zero-momentum, inversion-symmetric sector of the Hilbert space.

while the earlier times are affected by the finite time in the lowering and raising of lattice potentials, which takes 50 μs. The finite interaction strength and inter-double-well tunneling together result in about 1% error in the beam splitter operation in the simulation, but this is beyond the precision of our absorption imaging.

APPENDIX D: OTHER SCARRED STATES

In addition to the $|\mathbb{Z}_2\rangle$ and $|0\rangle$ states, we find other reviving states in the PXP model with static detuning, $\hat{H}(\mu)$, introduced in Sec. V. These initial states are the ground states of $\hat{H}(\mu_i)$, and they exhibit revivals when the detuning is quenched to a different value, $\hat{H}(\mu_i) \to \hat{H}(\mu_f)$. This setup generalizes the quench protocols studied in the main text. For example, setting $\mu_i \to -\infty$, the prequench ground state is simply the $|\mathbb{Z}_2\rangle$ state, and then quenching to $\mu_f = 0$ (pure PXP model) gives rise to scarred many-body revivals. Conversely, if we set $\mu_i \to \infty$, the ground state is $|0\rangle$, and quenching to $\mu_f = 1.68\Omega$ also leads to scarring, as this value corresponds to the Bose-Hubbard detuning value in Fig. 4.

We numerically identify similar scarring phenomenology in a larger set of initial conditions by varying the parameters μ_i and μ_f. In Fig. 9 we present an illustrative example for $\mu_i = -0.76\Omega$ and $\mu_f = 1.6\Omega$. Unlike the $|\mathbb{Z}_2\rangle$ and $|0\rangle$ states, the ground state of $\hat{H}(\mu_i)$, for general values of $|\mu_i| < 2$, is not a product state. Nevertheless, such ground states have low entanglement entropy and can be prepared experimentally, while at the same time they are nearly orthogonal to the $|\mathbb{Z}_2\rangle$ and $|0\rangle$ states (the overlap with the latter is on the order 10^{-5}). We emphasize that this does not require fine-tuning: We find large regions of μ_i and μ_f leading to scarring.

The dynamics in Fig. 9 is similar to that of the polarized state evolved with $\hat{H}(\mu = 1.68\Omega)$. During the evolution, the state periodically transfers to the polarized state and then returns to itself. The frequency of revivals is approximately the same as that for the polarized state evolved with the same static detuning μ_f, but the revivals are more prominent. The overlap of the $\hat{H}(\mu_i)$ ground state with all the eigenstates of $\hat{H}(\mu_f)$ is shown in Fig. 9(b). These overlaps exhibit a similar pattern to the overlap of eigenstates with the polarized states (red crosses). Furthermore, the atypical eigenstates appear to be the same in the two cases, up to a difference in phase. This is similar to what we find for the $|\mathbb{Z}_2\rangle$ and $|\bar{\mathbb{Z}}_2\rangle$ states at $\mu_f = 0$: Both states have the same magnitude of overlap with each eigenstate, while the phases are different.

[1] J. M. Deutsch, Quantum statistical mechanics in a closed system, Phys. Rev. A **43**, 2046 (1991).

[2] M. Srednicki, Chaos and quantum thermalization, Phys. Rev. E **50**, 888 (1994).

[3] M. Rigol, V. Dunjko, and M. Olshanii, Thermalization and its mechanism for generic isolated quantum systems, Nature (London) **452**, 854 (2008).

[4] T. Kinoshita, T. Wenger, and D. S. Weiss, A quantum Newton's cradle, Nature (London) **440**, 900 (2006).

[5] R. Nandkishore and D. A. Huse, Many-body localization and thermalization in quantum statistical mechanics, Annu. Rev. Condens. Matter Phys. **6**, 15 (2015).

[6] D. A. Abanin, E. Altman, I. Bloch, and M. Serbyn, Colloquium: Many-body localization, thermalization, and entanglement, Rev. Mod. Phys. **91**, 021001 (2019).

[7] M. Serbyn, D. A. Abanin, and Z. Papić, Quantum many-body scars and weak breaking of ergodicity, Nat. Phys. **17**, 675 (2021).

[8] S. Moudgalya, B. A. Bernevig, and N. Regnault, Quantum many-body scars and Hilbert space fragmentation: A review of exact results, Rep. Prog. Phys. **85**, 086501 (2022).

[9] H. Bernien, S. Schwartz, A. Keesling, H. Levine, A. Omran, H. Pichler, S. Choi, A. S. Zibrov, M. Endres, M. Greiner, V. Vuletić, and M. D. Lukin, Probing many-body dynamics on a 51-atom quantum simulator, Nature (London) **551**, 579 (2017).

[10] D. Bluvstein, A. Omran, H. Levine, A. Keesling, G. Semeghini, S. Ebadi, T. T. Wang, A. A. Michailidis, N. Maskara, W. W. Ho, S. Choi, M. Serbyn, M. Greiner, V. Vuletić, and M. D. Lukin, Controlling quantum many-body dynamics in driven Rydberg atom arrays, Science **371**, 1355 (2021).

[11] W. Kao, K.-Y. Li, K.-Y. Lin, S. Gopalakrishnan, and B. L. Lev, Topological pumping of a 1D dipolar gas into strongly correlated prethermal states, Science **371**, 296 (2021).

[12] S. Scherg, T. Kohlert, P. Sala, F. Pollmann, B. Hebbe Madhusudhana, I. Bloch, and M. Aidelsburger, Observing nonergodicity due to kinetic constraints in tilted Fermi-Hubbard chains, Nat. Commun. **12**, 4490 (2021).

[13] P. N. Jepsen, Y. K. Lee, H. Lin, I. Dimitrova, Y. Margalit, W. W. Ho, and W. Ketterle, Catching Bethe phantoms and quantum many-body scars: Long-lived spin-helix states in Heisenberg magnets, Nat. Phys. **18**, 899 (2022).

[14] S. Moudgalya, N. Regnault, and B. A. Bernevig, Entanglement of exact excited states of Affleck-Kennedy-Lieb-Tasaki models: Exact results, many-body scars, and violation of the strong eigenstate thermalization hypothesis, Phys. Rev. B **98**, 235156 (2018).

[15] N. Shiraishi and T. Mori, Systematic Construction of Counterexamples to the Eigenstate Thermalization Hypothesis, Phys. Rev. Lett. **119**, 030601 (2017).

[16] W. W. Ho, S. Choi, H. Pichler, and M. D. Lukin, Periodic Orbits, Entanglement, and Quantum Many-Body Scars in Constrained Models: Matrix Product State Approach, Phys. Rev. Lett. **122**, 040603 (2019).

[17] D. K. Mark, C.-J. Lin, and O. I. Motrunich, Unified structure for exact towers of scar states in the Affleck-Kennedy-Lieb-Tasaki and other models, Phys. Rev. B **101**, 195131 (2020).

[18] S. Sugiura, T. Kuwahara, and K. Saito, Many-body scar state intrinsic to periodically driven system, Phys. Rev. Res. **3**, L012010 (2021).

[19] K. Mizuta, K. Takasan, and N. Kawakami, Exact Floquet quantum many-body scars under Rydberg blockade, Phys. Rev. Res. **2**, 033284 (2020).

[20] B. Mukherjee, S. Nandy, A. Sen, D. Sen, and K. Sengupta, Collapse and revival of quantum many-body scars via Floquet engineering, Phys. Rev. B **101**, 245107 (2020).

[21] I. Mondragon-Shem, M. G. Vavilov, and I. Martin, Fate of quantum many-body scars in the presence of disorder, PRX Quantum **2**, 030349 (2021).

[22] N. Shibata, N. Yoshioka, and H. Katsura, Onsager's Scars in Disordered Spin Chains, Phys. Rev. Lett. **124**, 180604 (2020).

[23] C. J. Turner, A. A. Michailidis, D. A. Abanin, M. Serbyn, and Z. Papić, Weak ergodicity breaking from quantum many-body scars, Nat. Phys. **14**, 745 (2018).

[24] C.-J. Lin and O. I. Motrunich, Exact Quantum Many-Body Scar States in the Rydberg-Blockaded Atom Chain, Phys. Rev. Lett. **122**, 173401 (2019).

[25] T. Iadecola, M. Schecter, and S. Xu, Quantum many-body scars from magnon condensation, Phys. Rev. B **100**, 184312 (2019).

[26] V. Khemani, C. R. Laumann, and A. Chandran, Signatures of integrability in the dynamics of Rydberg-blockaded chains, Phys. Rev. B **99**, 161101(R) (2019).

[27] P. Fendley, K. Sengupta, and S. Sachdev, Competing density-wave orders in a one-dimensional hard-boson model, Phys. Rev. B **69**, 075106 (2004).

[28] I. Lesanovsky and H. Katsura, Interacting Fibonacci anyons in a Rydberg gas, Phys. Rev. A **86**, 041601(R) (2012).

[29] B. Sun and F. Robicheaux, Numerical study of two-body correlation in a 1D lattice with perfect blockade, New J. Phys. **10**, 045032 (2008).

[30] B. Olmos, M. Müller, and I. Lesanovsky, Thermalization of a strongly interacting 1D Rydberg lattice gas, New J. Phys. **12**, 013024 (2010).

[31] C. J. Turner, A. A. Michailidis, D. A. Abanin, M. Serbyn, and Z. Papić, Quantum scarred eigenstates in a Rydberg atom chain: Entanglement, breakdown of thermalization, and stability to perturbations, Phys. Rev. B **98**, 155134 (2018).

[32] E. J. Heller, Bound-State Eigenfunctions of Classically Chaotic Hamiltonian Systems: Scars of Periodic Orbits, Phys. Rev. Lett. **53**, 1515 (1984).

[33] C. J. Turner, J.-Y. Desaules, K. Bull, and Z. Papić, Correspondence Principle for Many-Body Scars in Ultracold Rydberg Atoms, Phys. Rev. X **11**, 021021 (2021).

[34] B. Yang, H. Sun, C.-J. Huang, H.-Y. Wang, Y. Deng, H.-N. Dai, Z.-S. Yuan, and J.-W. Pan, Cooling and entangling ultracold atoms in optical lattices, Science **369**, 550 (2020).

[35] B. Yang, H.-N. Dai, H. Sun, A. Reingruber, Z.-S. Yuan, and J.-W. Pan, Spin-dependent optical superlattice, Phys. Rev. A **96**, 011602(R) (2017).

[36] S. Sachdev, K. Sengupta, and S. M. Girvin, Mott insulators in strong electric fields, Phys. Rev. B **66**, 075128 (2002).

[37] K. Sengupta, Phases and dynamics of ultracold bosons in a tilted optical lattice, in *Entanglement in Spin Chains: From Theory to Quantum Technology Applications*, edited by A. Bayat, S. Bose, and H. Johannesson (Springer, New York, 2022), pp. 425–458.

[38] F. Meinert, M. J. Mark, E. Kirilov, K. Lauber, P. Weinmann, A. J. Daley, and H.-C. Nägerl, Quantum Quench in an Atomic One-Dimensional Ising Chain, Phys. Rev. Lett. **111**, 053003 (2013).

[39] F. Meinert, M. J. Mark, E. Kirilov, K. Lauber, P. Weinmann, M. Gröbner, A. J. Daley, and H.-C. Nägerl, Observation of many-body dynamics in long-range tunneling after a quantum quench, Science **344**, 1259 (2014).

[40] J. Simon, W. S. Bakr, R. Ma, M. E. Tai, P. M. Preiss, and M. Greiner, Quantum simulation of antiferromagnetic spin chains in an optical lattice, Nature (London) **472**, 307 (2011).

[41] B. Yang, H. Sun, R. Ott, H.-Y. Wang, T. V. Zache, J. C. Halimeh, Z.-S. Yuan, P. Hauke, and J.-W. Pan, Observation of gauge invariance in a 71-site Bose–Hubbard quantum simulator, Nature (London) **587**, 392 (2020).

[42] See Supplemental Material at http://link.aps.org/supplemental/10.1103/PhysRevResearch.5.023010 for additional results and background calculations supporting the results in this paper, which contains Refs. [1,2,9,10,23,26,31,51,52,56,62–68].

[43] A. M. Kaufman, M. C. Tichy, F. Mintert, A. M. Rey, and C. A. Regal, *Advances in Atomic, Molecular and Optical Physics*, 1st ed. (Elsevier, New York, 2018), Vol. 6w7, pp. 377–427.

[44] R. Islam, R. Ma, P. M. Preiss, M. Eric Tai, A. Lukin, M. Rispoli, and M. Greiner, Measuring entanglement entropy in a quantum many-body system, Nature (London) **528**, 77 (2015).

[45] S. Choi, C. J. Turner, H. Pichler, W. W. Ho, A. A. Michailidis, Z. Papić, M. Serbyn, M. D. Lukin, and D. A. Abanin, Emergent SU(2) Dynamics and Perfect Quantum Many-Body Scars, Phys. Rev. Lett. **122**, 220603 (2019).

[46] L. D'Alessio, Y. Kafri, A. Polkovnikov, and M. Rigol, From quantum chaos and eigenstate thermalization to statistical mechanics and thermodynamics, Adv. Phys. **65**, 239 (2016).

[47] E. J. Heller, Wavepacket dynamics and quantum chaology, in *Chaos and Quantum Physics*, (North-Holland, Amsterdam, 1991), Vol. 52, pp. 547–663.

[48] J. Haegeman, J. I. Cirac, T. J. Osborne, I. Pižorn, H. Verschelde, and F. Verstraete, Time-Dependent Variational Principle for Quantum Lattices, Phys. Rev. Lett. **107**, 070601 (2011).

[49] A. A. Michailidis, C. J. Turner, Z. Papić, D. A. Abanin, and M. Serbyn, Slow Quantum Thermalization and Many-Body Revivals from Mixed Phase Space, Phys. Rev. X **10**, 011055 (2020).

[50] A. Daniel, A. Hallam, J.-Y. Desaules, A. Hudomal, G.-X. Su, J. C. Halimeh, and Z. Papić, Bridging quantum criticality via many-body scarring, arXiv:2301.03631.

[51] N. Maskara, A. A. Michailidis, W. W. Ho, D. Bluvstein, S. Choi, M. D. Lukin, and M. Serbyn, Discrete Time-Crystalline Order Enabled by Quantum Many-Body Scars: Entanglement Steering via Periodic Driving, Phys. Rev. Lett. **127**, 090602 (2021).

[52] A. Hudomal, J.-Y. Desaules, B. Mukherjee, G.-X. Su, J. C. Halimeh, and Z. Papić, Driving quantum many-body scars in the PXP model, Phys. Rev. B **106**, 104302 (2022).

[53] J.-Y. Desaules, A. Hudomal, C. J. Turner, and Z. Papić, Proposal for Realizing Quantum Scars in the Tilted 1D Fermi-Hubbard Model, Phys. Rev. Lett. **126**, 210601 (2021).

[54] S Chandrasekharan and U.-J Wiese, Quantum link models: A discrete approach to gauge theories, Nucl. Phys. B **492**, 455 (1997).

[55] U.-J. Wiese, Ultracold quantum gases and lattice systems: Quantum simulation of lattice gauge theories, Ann. Phys. (Berlin) **525**, 777 (2013).

[56] F. M. Surace, P. P. Mazza, G. Giudici, A. Lerose, A. Gambassi, and M. Dalmonte, Lattice Gauge Theories and String Dynamics in Rydberg Atom Quantum Simulators, Phys. Rev. X **10**, 021041 (2020).

[57] Z.-C. Yang, F. Liu, A. V. Gorshkov, and T. Iadecola, Hilbert-Space Fragmentation from Strict Confinement, Phys. Rev. Lett. **124**, 207602 (2020).

[58] Z.-Y. Zhou, G.-X. Su, J. C. Halimeh, R. Ott, H. Sun, P. Hauke, B. Yang, Z.-S. Yuan, J. Berges, and J.-W. Pan, Thermalization dynamics of a gauge theory on a quantum simulator, Science **377**, 311 (2022).

[59] J. Osborne, I. P. McCulloch, B. Yang, P. Hauke, and J. C. Halimeh, Large-scale $2+1$D U(1) gauge theory with dynamical matter in a cold-atom quantum simulator, arXiv:2211.01380.

[60] S. Dooley, Robust quantum sensing in strongly interacting systems with many-body scars, PRX Quantum **2**, 020330 (2021).

[61] J.-Y. Desaules, F. Pietracaprina, Z. Papić, J. Goold, and S. Pappalardi, Extensive Multipartite Entanglement from su(2) Quantum Many-Body Scars, Phys. Rev. Lett. **129**, 020601 (2022).

[62] S. Bravyi, D. P. DiVincenzo, and D. Loss, Schrieffer–Wolff transformation for quantum many-body systems, Ann. Phys. (Amsterdam) **326**, 2793 (2011).

[63] J. C. Halimeh, R. Ott, I. P. McCulloch, B. Yang, and P. Hauke, Robustness of gauge-invariant dynamics against defects in ultracold-atom gauge theories, Phys. Rev. Res. **2**, 033361 (2020).

[64] B. Mukherjee, A. Sen, D. Sen, and K. Sengupta, Dynamics of the vacuum state in a periodically driven Rydberg chain, Phys. Rev. B **102**, 075123 (2020).

[65] Z. Yao, L. Pan, S. Liu, and H. Zhai, Quantum many-body scars and quantum criticality, Phys. Rev. B **105**, 125123 (2022).

[66] V. Oganesyan and D. A. Huse, Localization of interacting fermions at high temperature, Phys. Rev. B **75**, 155111 (2007).

[67] G. Vidal, Efficient Classical Simulation of Slightly Entangled Quantum Computations, Phys. Rev. Lett. **91**, 147902 (2003).

[68] J. Hauschild and F. Pollmann, Efficient numerical simulations with Tensor Networks: Tensor Network Python (TeNPy), SciPost Phys. Lect. Notes, 5 (2018), code available from https://github.com/tenpy/tenpy.

Driving quantum many-body scars in the PXP model

Ana Hudomal [●],[1,2] Jean-Yves Desaules [●],[1] Bhaskar Mukherjee,[3] Guo-Xian Su,[4,5,6] Jad C. Halimeh [●],[7,8] and Zlatko Papić [●][1]

[1]*School of Physics and Astronomy, University of Leeds, Leeds LS2 9JT, United Kingdom*
[2]*Institute of Physics Belgrade, University of Belgrade, 11080 Belgrade, Serbia*
[3]*Department of Physics, University College London, Gower Street, London WC1E 6BT, United Kingdom*
[4]*Hefei National Laboratory for Physical Sciences at Microscale and Department of Modern Physics,*
University of Science and Technology of China, Hefei, Anhui 230026, China
[5]*Physikalisches Institut, Ruprecht-Karls-Universität Heidelberg, Im Neuenheimer Feld 226, 69120 Heidelberg, Germany*
[6]*CAS Center for Excellence and Synergetic Innovation Center in Quantum Information and Quantum Physics,*
University of Science and Technology of China, Hefei, Anhui 230026, China
[7]*Department of Physics and Arnold Sommerfeld Center for Theoretical Physics (ASC),*
Ludwig-Maximilians-Universität München, Theresienstraße 37, D-80333 München, Germany
[8]*Munich Center for Quantum Science and Technology (MCQST), Schellingstraße 4, D-80799 München, Germany*

Periodic driving has been established as a powerful technique for engineering novel phases of matter and intrinsically out-of-equilibrium phenomena such as time crystals. Recent paper by Bluvstein *et al.* [Science **371**, 1355 (2021)] has demonstrated that periodic driving can also lead to a significant enhancement of quantum many-body scarring, whereby certain nonintegrable systems can display persistent quantum revivals from special initial states. Nevertheless, the mechanisms behind driving-induced scar enhancement remain poorly understood. Here we report a detailed study of the effect of periodic driving on the PXP model describing Rydberg atoms in the presence of a strong Rydberg blockade—the canonical static model of quantum many-body scarring. We show that periodic modulation of the chemical potential gives rise to a rich phase diagram, with at least two distinct types of scarring regimes that we distinguish by examining their Floquet spectra. We formulate a toy model, based on a sequence of square pulses, that accurately captures the details of the scarred dynamics and allows for analytical treatment in the large-amplitude and high-frequency driving regimes. Finally, we point out that driving with a spatially inhomogeneous chemical potential allows to stabilize quantum revivals from arbitrary initial states in the PXP model, via a mechanism similar to prethermalization.

I. INTRODUCTION

Quantum many-body scarring (QMBS) [1] has recently been added to the growing list of ergodicity-breaking phenomena, previously actively studied in integrable models [2] and many-body localization [3,4]. In conventional ergodic systems, even in the absence of a coupling to a thermal bath, the interactions between constituent degrees of freedom lead to fast thermalization [5–7]. A distinguishing feature of QMBS systems is that ergodicity is broken by a relatively small subset of the system's energy eigenstates, which coexist with the thermalizing bulk of the spectrum [1,8]. Experimentally, QMBS can be detected by preparing the system in special initial states that have predominant support on the ergodicity-breaking eigenstates. Such initial states are found to display persistent quantum revivals, in contrast to other "generic" initial states whose dynamics is featureless [9,10]. The investigations of such "weak" ergodicity breaking phenomena continue to attract much attention, both in terms of new experimental realizations [11–13] as well as universal mechanisms [14–19] for violating the eigenstate thermalization hypothesis (ETH) [5,6]. Theoretical studies continue to

identify large classes of models that exhibit various aspects of QMBS phenomena. Some notable examples include various nonintegrable lattice models [20–27], models of correlated fermions and bosons [28–36], frustrated magnets [37,38], topological phases of matter [39,40], lattice gauge theories [41–45], and periodically-driven systems [46–52].

Recent experiments [10] on QMBS utilising Rydberg atom arrays in various geometries, both one-dimensional and two-dimensional, have shown that periodic driving can stabilize the revivals that occur in the static system [53–55]. Similar effect was also observed in experiments on a Bose-Hubbard quantum simulator [36], where QMBS phenomenon was identified in a larger class of initial states. In both cases, the optimal driving frequency was empirically found to be related to the frequency of revivals in the static model. Although the driving protocol is relatively simple, the mechanism behind it remains to be understood. Previous work in Ref. [56] provided an important insight that the experimental driving protocol can be approximated by a simpler two-step (kicked) driving scheme. Such a toy model is easier to treat analytically and it captures some of the observed phenomenology. However, its relation to the experimental driving protocol is not

transparent, in particular there is no direct mapping between the parameters of the two protocols (except for the driving frequency, which is equal in the two cases).

Moreover, further questions naturally arise. For example, the only two initial states whose revivals were stabilized by periodic driving (the Néel and polarized states) are precisely the ones that exhibit QMBS in the static version of the same model (the polarized state becomes scarred in the presence of static detuning [36]). This suggests that there are fundamental limitations to the driving, which only "works" for such special states. If the enhancement mechanism is indeed related to QMBS, it would imply that it should be possible to improve the revivals in a variety of other QMBS models that have been studied theoretically. Another question is how to predict the optimal driving parameters without performing a computationally-costly brute force search. To this end, Ref. [10] has identified a window of driving frequencies centered around twice the frequency of revivals in the static model. A subharmonic response to driving was observed in this frequency regime, suggesting a relation to the discrete time crystal, which also warrants further investigation.

In this paper we numerically and analytically study the effects of driving on the PXP model describing Rydberg atoms in the regime of strong Rydberg blockade. In Sec. II we introduce the model and investigate in detail the spatially-uniform cosine driving scheme that was used in recent experiments. We identify two regimes with distinct properties (dubbed Type-1 and Type-2). In Sec. III we focus on the optimally driven Néel and polarized state. In Sec. IV we introduce a toy model based on the square pulse driving protocol. We show that this protocol better approximates the cosine-drive dynamics than the previously studied kicked drive [56]. The square-pulse protocol is amenable to analytical treatment in certain limits, as we demonstrate for the high-amplitude and high-frequency drive regimes. Finally, in Sec. V we discuss the implications of our results on the relation between QMBS and the enhancement by periodic driving, suggesting that QMBS is a necessary ingredient in the Type-1 (typically low-amplitude) regime, while Type-2 driving (typically high-amplitude) can be also applied to nonscarred models. We summarize our findings and identify some future directions in Sec. VI. Appendices A–D provide additional information on system size scaling, a modified (spatially inhomogeneous) cosine driving protocol that can generate revivals from *any* initial product state, high-frequency expansion for the Floquet Hamiltonian, and an alternative way to visualize the trajectory of a state in Hilbert space.

II. PXP MODEL AND COSINE DRIVE

The PXP model [57,58] describes a kinetically constrained chain of spin-1/2 degrees of freedom. The chain serves as a model for the system of Rydberg atoms, each of which can exist in two possible states, $|\circ\rangle$ and $|\bullet\rangle$, corresponding to the ground state and the excited state, respectively. An array of N such atoms is governed by the Hamiltonian

$$H_{\mathrm{PXP}} = \Omega \sum_{j=1}^{N} P_{j-1} X_j P_{j+1}, \qquad (1)$$

where $X_j = |\circ_j\rangle\langle\bullet_j| + |\bullet_j\rangle\langle\circ_j|$ is the Pauli x matrix on site j, describing local Rabi precession with frequency Ω. The projectors onto the ground state, $P_j = |\circ_j\rangle\langle\circ_j|$, constrain the dynamics by allowing an atom to flip its state only if both of its neighbors are in the ground state. Unless specified otherwise, we use periodic boundary conditions (PBC) and set the PXP term strength to $\Omega = 1$.

Before introducing the driving scheme, we briefly review some pertinent properties of the static PXP model. The PXP model is quantum chaotic [53]. However, it was found that preparing the system in the Néel or $|\mathbb{Z}_2\rangle \equiv |\bullet \circ \bullet \circ ... \bullet \circ\rangle$ state, which has an excitation on every other site, leads to persistent quantum revivals [54,59,60]. Analogously, the translated Néel state, $|\mathbb{Z}_2'\rangle \equiv |\circ \bullet \circ \bullet ... \circ \bullet\rangle$, also displays revivals. In a conventional thermalizing system, the revivals are not expected as the $|\mathbb{Z}_2\rangle$ initial state has predominant support on the energy eigenstates in the middle of the many-body spectrum, thus it corresponds to "infinite" temperature. The presence of revivals in a special initial state in an overall chaotic system was understood to be a many-body analog of the phenomena associated with a single particle inside a stadium billiard, where nonergodicity arises as a "scar" imprinted by a particle's classical periodic orbit [55,61,62]. In QMBS systems, the eigenstates were shown to form tower structures [53], resulting from the anomalously high overlap of eigenstates with the $|\mathbb{Z}_2\rangle$ initial state, and the equal energy spacing between the towers leads to quantum revivals. We mention that the scarring in the PXP model was also shown to persist in higher dimensions [10,63,64] and in the presence of certain perturbations [54,65,66], including disorder [67].

The revivals in the PXP model are not perfect, in particular the wave function fidelity,

$$F(t) \equiv |\langle\psi(t)|\psi_0\rangle|^2, \qquad (2)$$

with the initial state chosen to be $|\psi_0\rangle = |\mathbb{Z}_2\rangle$, visibly decays over moderate times [54]. Reference [10] showed that the decay timescale can be significantly extended by introducing a cosine modulation $\Delta(t)$ of the chemical potential,

$$H(t) = H_{\mathrm{PXP}} - \Delta(t) \sum_i n_i, \quad \Delta(t) = \Delta_0 + \Delta_m \cos(\omega t), (3)$$

where $n_i = |\bullet_i\rangle\langle\bullet_i|$ is the density of excitations on site i, Δ_0 is the static detuning, Δ_m modulation amplitude and ω the driving frequency.

The periodic modulation of the chemical potential in Eq. (3) was shown to stabilize and enhance the revivals in the quantum fidelity, both in numerical simulations and in experiments on quantum simulators [36]. The enhancement was achieved for two different initial states, the previously mentioned $|\mathbb{Z}_2\rangle$ state, as well as the polarized state, which has no excitations, $|0\rangle \equiv |\circ\circ\circ...\circ\circ\rangle$. The optimal driving frequency for the Néel state was found to be close to twice the frequency of revivals in the pure PXP model [$\Delta(t) = 0$]; for the polarized state, the optimal frequency was instead close to the frequency of revivals in the detuned PXP model [$\Delta(t) = \Delta_0$]. The optimal values of Δ_0 and Δ_m were found empirically and have different values for these two states.

In order to determine more precisely the optimal driving parameters, we scan the parameter space $(\Delta_0, \Delta_m, \omega)$ for the

highest average fidelity between the times $t = 0$ and $t = \tau$,

$$\langle F \rangle_t = \frac{1}{\tau} \int_0^\tau F(t) dt, \qquad (4)$$

where we set $\tau = 100$. In Figs. 1(a) and 1(b) we plot the average fidelity as a function of Δ_0 and Δ_m at the fixed frequency ω, for the Néel and polarized initial state. In this figure we restrict to the case $\Delta_m \geqslant 0$ since $\langle F \rangle_t (\Delta_0, \Delta_m, \omega) = \langle F \rangle_t (-\Delta_0, -\Delta_m, \omega)$. This symmetry comes from the fact that the dynamics of the system is exactly equal for $\pm \Delta(t)$. Changing the sign of $\Delta(t)$ only changes the sign of the quasienergy spectrum and multiplies the corresponding Floquet modes by the operator $\prod_j Z_j$ (with Z_j being the Pauli z matrix on site j), which commutes with the driving term and anticommutes with the PXP term. The frequency is fixed to a value close to the revival frequency of the static model, i.e., we choose $\omega = 2.72$ in (a) and $\omega = 3.71$ in (b). These two figures have many similarities, such as parallel diagonal lines consisting of "butterfly-shaped" peaks. However, a closer look reveals an important difference. The Néel state plot contains several additional peaks, which are very narrow and typically located between the bright diagonal lines. For example, one of these peaks is approximately around the point $(\Delta_0, \Delta_m) = (1.15, 2.67)$ and corresponds to an interesting optimal parameter regime for the Néel state, which will be studied below. We will call these narrow peaks "Type-1" peaks.

The other bright regions present in both Figs. 1(a) and 1(b) will be dubbed "Type-2 peaks" (excluding $|\Delta_0| \gg 1$ and $\Delta_m \lesssim |\Delta_0|$). These parameter regions are broader, i.e., the parameters do not have to be finely tuned, and they typically occur at higher driving amplitudes than Type-1 peaks. Like Type-1, their position depends on the driving frequency, but the mechanism of revival stabilization is different. We will discuss Type-2 peaks below in relation to the polarized initial state.

It is important to note that the Néel and polarized state are two special cases. The cross sections in Figs. 1(a) and 1(b) look very different for other initial product states, with low and very narrow peaks of the cost function instead of Type-2 peaks, while the Type-1 peaks are completely absent. One such example is shown in Fig. 16(a) in Appendix B.

Finally, Fig. 1(c) shows three illustrative cross sections taken at different frequencies, $\omega \in \{1, 2, 3\}$. The initial state is the Néel state and the color scale corresponds to the value of the average fidelity cost function. We see that this cost function has many peaks (bright regions), which move and deform as ω is varied. The position of the fidelity peaks in (Δ_0, Δ_m) space depends approximately linearly on the driving frequency. In all three cases, there are two large bright regions in the $|\Delta_0| \gg 1$ and $\Delta_m \lesssim |\Delta_0|$ regime. When the static detuning Δ_0 is large, the energy spectrum splits into disconnected bands. This means that the wave function cannot spread through the entire Hilbert space and the fidelity remains relatively high during the evolution, never dropping down to zero. These trivial regimes do not correspond to typical QMBS behavior, hence we exclude those where the *minimal* fidelity from $t = 0$ to $t = 100$ is nonzero. The optimal parameter regimes that will be discussed in detail below are summarized in Table I.
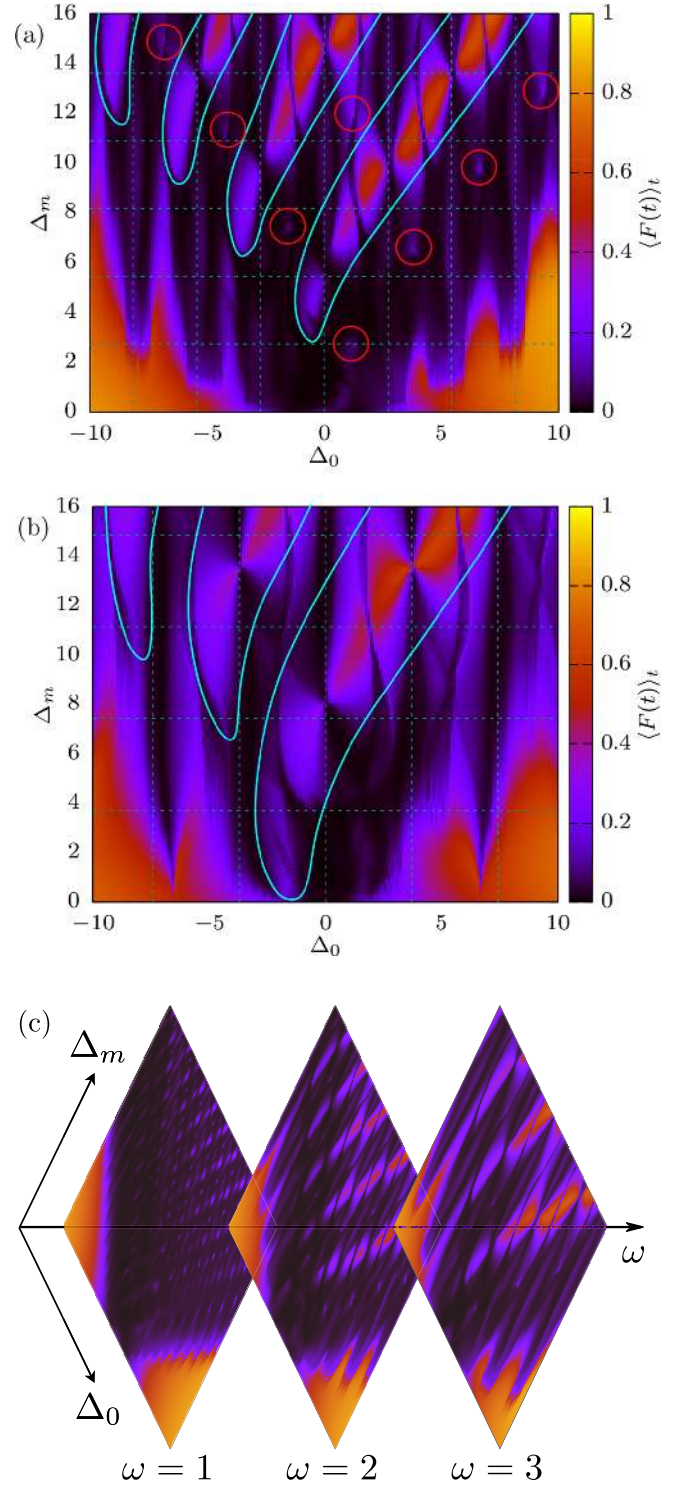
FIG. 1. Average revival fidelity $\langle F(t) \rangle_t$ over time interval $[0, 100]$ for the PXP model with $\Omega = 1$ and cosine drive at system size $N = 20$. The Type-1 peaks are encircled in red, while the regions containing Type-2 peaks are denoted by cyan lines. (a) Néel initial state at fixed frequency $\omega = 2.72$. (b) Polarized initial state at fixed frequency $\omega = 3.71$. (c) Néel initial state for three different frequencies, $\omega \in \{1, 2, 3\}$, $\Delta_0 \in [-10, 10]$, $\Delta_m \in [0, 16]$.

Next we determine the optimal window of driving frequencies. In order to do this, we choose one of the narrow peaks of the cost function in Fig. 1 and follow it as we

TABLE I. Optimal driving parameters (cosine drive).

Initial state	Δ_0	Δ_m	ω	Floquet spectrum
Néel	1.15	2.67	2.72	two arcs
Polarized	1.68	-0.5	3.71	one arc
Polarized	0.64	7.55	2.90	multiple arcs

vary the frequency ω. The driving parameters Δ_0 and Δ_m are reoptimized for each frequency. When we leave the optimal frequency window, the peak disappears, but other peaks may become more prominent, as summarized in Fig. 2. We note that even though the original peak is no longer clearly visible, there is still a local maximum of the cost function and we are able to track it outside of the optimal frequency window. In order to characterize the quality of revivals, in Fig. 2 we used the following cost function:

$$\mathcal{C}_l = \frac{1}{M} \sum_{n=1}^{M} [F(lnT) - F(l(n-1/2)T)], \qquad (5)$$

where T is the driving period and M denotes the number of revivals averaged over. The integer l defines the order of the response, e.g., $l = 1$ for the harmonic and $l = 2$ for the subharmonic responses we will study below. In both cases we average over $lM = 40$ driving periods. The value of $\mathcal{C}_l$ corresponds to the difference between average maximum fidelity and average minimum fidelity over the first M revivals, with the value of 1 corresponding to perfect revivals. In Fig. 2 we use $\mathcal{C}_l$ instead of the previously introduced average fidelity because it gives better results when comparing different frequencies. Namely, as the driving frequency is increased, the revivals become more dense and the width of an individual
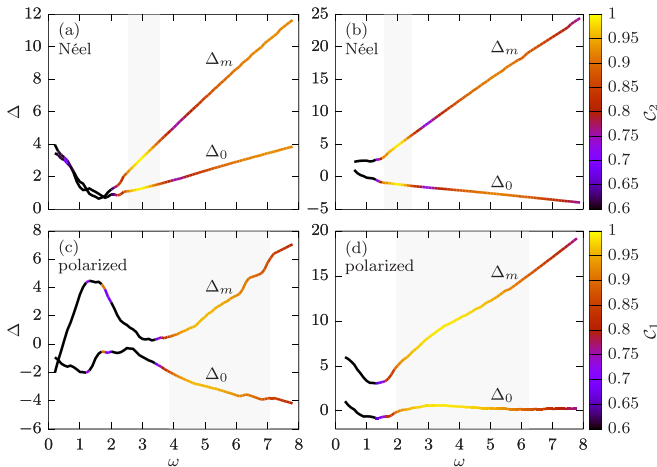

FIG. 2. Optimal values of Δ_0 and Δ_m depending on the driving frequency ω. The color represents the value of $\mathcal{C}_k$ in Eq. (5), with $k = 2$ for the top panels (subharmonic response) and $k = 1$ for the bottom panels (harmonic response). The shadowed regions mark the optimal frequency windows ($\mathcal{C}_k$ higher than 90% of its maximal value). Top row: Néel state. (a) "Main" Type-1 peak (maximum around $\omega = 2.72$). (b) Another Type-1 peak (maximum around $\omega = 2$). Bottom row: Polarized state, Type-2 peaks. (c) Low amplitude. (d) High amplitude.

revival increases in comparison with the revival period, which then results in increased average fidelity. Therefore, decaying revivals at higher frequencies can lead to higher average fidelity than stabilized and constantly high revivals at lower frequencies. The new cost function does not suffer from this problem and can accurately estimate the quality of revivals independently of the frequency. However, we still use the first cost function for fixed frequency scans, such as those in Fig. 1, since the average fidelity can capture all types of revivals (e.g., harmonic, subharmonic, or even incommensurate with the driving frequency), without the need to specify their expected frequency.

In Fig. 2(a) we plot the data for the peak that passes through a set of Néel state optimal parameters ($\Delta_0 = 1.15$, $\Delta_m = 2.67$, $\omega = 2.72$). We look at $M = 20$ revivals in evaluating the cost function $\mathcal{C}_2$ in Eq. (5). The dependence of Δ_0 and Δ_m on ω is seen to be approximately linear. In Fig. 2(a) we see that there is indeed a window of optimal frequencies, approximately $2.5 < \omega < 3.5$, where we can obtain a good subharmonic response to periodic driving. This window is centered at a frequency slightly higher than twice the bare revival frequency of the Néel state in the pure PXP model ($\omega_0 \approx 2.66$). In Appendix A, we study the system size scaling of this optimal driving frequency, see Fig. 13. For $N \geqslant 10$, the optimal frequency window for the Néel state barely changes with increasing system size. Note that there is a minimal frequency in Fig. 2(a) bellow which it is impossible to obtain revivals. On the other hand, it is possible to enhance the revivals in the high-frequency regime, but the lifetime of these revivals is finite and decreases with increasing frequency.

We can repeat the same procedure for other Type-1 peaks, see Fig. 2(b) for one example. In this case we start from the optimal parameters that correspond to the "one-loop" trajectory, which will be studied in more detail in Sec. V B ($\Delta_0 = -1.17$, $\Delta_m = 4.81$, $\omega = 2.00$). The dependence of optimal Δ_0 and Δ_m on ω is again linear, but the optimal frequency window is now more narrow and centered around $\omega = 2$, which significantly deviates from $\omega_0 \approx 2.66$. The results for other Type-1 peaks are found to be similar (data not shown).

Finally, this procedure can also be adapted to the harmonic response, e.g. for the polarized and other initial states with the cost function $\mathcal{C}_1$. The results for the polarized state and $M = 40$ in the low- and high-amplitude regime (parameters from Table I) are shown in Figs. 2(c) and 2(d), respectively. In both regimes, the optimal frequency window is much wider than for the Néel state.

III. NÉEL AND POLARIZED STATE REVIVALS

In this section we investigate in more detail the optimally driven Néel and polarized initial states.

A. Néel state

Using the procedure described in Sec. II—scanning the parameter space for the highest average fidelity—we found the following optimal parameters for the Néel state: $\Delta_0 = 1.15$, $\Delta_m = 2.67$, $\omega = 2.72$. This is the lowest-amplitude Type-1 peak in Fig. 1(a). In addition to brute force scanning, we also employed the simulated annealing optimization algorithm,
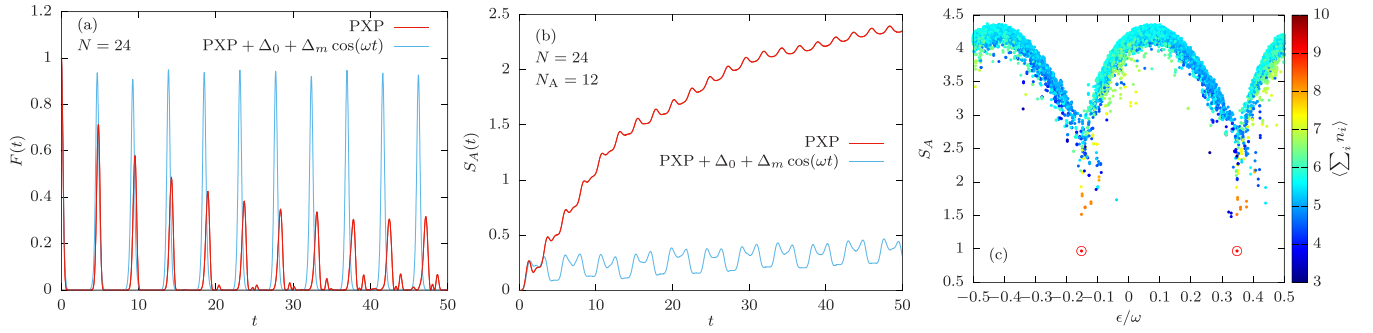
FIG. 3. Driven Néel state ($\Delta_0 = 1.15$, $\Delta_m = 2.67$, $\omega = 2.72$). (a) Quantum fidelity $F(t)$ for system size $N = 24$. (b) Entanglement entropy S_A for a subsystem with $N_A = 12$ sites. (c) Entanglement entropy of the Floquet modes for system size $N = 20$. Color scale shows the average number of excitations $\langle \sum_i n_i \rangle$ in each Floquet mode.

which produced similar optimal values. We note that our driving parameters slightly differ from those considered in Ref. [10], $\Delta_0 = 1.00$ and $\Delta_m = 2.00$, which were obtained at the fixed frequency $\omega = 2.66$.

Figure 3(a) shows the evolution of quantum fidelity for the optimal parameters quoted above. In contrast to the undriven case, the revivals are clearly enhanced and remain stable over long times. Note that the revival frequency is half the driving frequency. This is an example of period doubling (subharmonic response), which was related to a discrete time crystal in Ref. [10]. The growth of the bipartite von Neumann entanglement entropy S_A is strongly suppressed by driving, as shown in Fig. 3(b). To evaluate S_A, we partition the chain into two equal halves and evaluate the reduced density matrix for one of the subsystems, $\rho_A(t) = \mathrm{tr}_B |\psi(t)\rangle \langle \psi(t)|$, by tracing out the other (B) subsystem. This yields $S_A = -\mathrm{tr}\, \rho_A \ln \rho_A$.

Furthermore, we numerically construct the one period evolution operator of the optimally driven system and diagonalize it in order to obtain the corresponding Floquet modes. The bipartite entanglement entropy versus the quasienergy of all the Floquet modes is plotted in Fig. 3(c). The color represents the expectation value of the number of excitations $\langle \sum_i n_i \rangle$ for each mode. This entropy plot has an interesting "two arc" structure. The origin of these two arcs will be explained in Sec. III C below. The two lowest-entropy modes (marked by the red circles) also have the highest overlap with the Néel state. These two modes are said to be π paired, since they are separated by $\Delta \epsilon \approx \omega / 2 = \pi / T$ in quasienergy. Such two π-paired Floquet modes were also observed in Ref. [56], where the cosine drive was approximated by a delta function pulsed drive, as well as in other systems, which exhibit time-crystalline behavior but no scarring [68]. We find that the two modes are approximately $(|\mathbb{Z}_2\rangle + |\mathbb{Z}_2'\rangle)/\sqrt{2}$ and $(|\mathbb{Z}_2\rangle - |\mathbb{Z}_2'\rangle)/\sqrt{2}$, which explains the observed period doubling [36]. However, the subharmonic response becomes harmonic if we work in the momentum $k = 0$ sector and choose a translation invariant initial state $(|\mathbb{Z}_2\rangle + |\mathbb{Z}_2'\rangle)/\sqrt{2}$. In that case, there will still be two arcs in the entropy plot, but only one high-overlap Floquet mode.

In addition to $(\Delta_0, \Delta_m) = (1.15, 2.67)$ parameters, there are several other Type-1 peaks in the cost-function scan at fixed frequency $\omega = 2.72$ that we have seen in Fig. 1(a). The entanglement entropy plots of their Floquet modes also

display the distinct "two arcs" structure. These other Type-1 peaks also lead to enhanced revivals, although with a finite lifetime at this particular driving frequency. However, some of those peaks are higher at other frequencies and can lead to completely stabilized revivals, see for example Fig. 2(b) and the discussion in Sec. V B. The number, position, and height of Type-1 peaks depends on the driving frequency, while the driving amplitude of peaks that result in stable revivals is typically lower than that of Type-2 peaks.

B. Polarized state

For the polarized initial state, particularly in the low-amplitude driving regime, the optimal frequency value is found to be more sensitive to the cost function ($\langle F \rangle_t$ or $\mathcal{C}_1$) used for the optimization. In particular, the $\mathcal{C}_1$ cost function results in a larger value of the driving amplitude, see Fig. 2(c). Below we will use a set of parameters close to the low-amplitude edge of the optimal frequency window. These parameters were also used to drive the polarized state in a recent experiment on the Bose-Hubbard quantum simulator of the PXP model [36].

Although the fully polarized state $|0\rangle$ shows no QMBS behavior and quickly thermalizes in the pure PXP model, it was shown that this can be changed by applying a static detuning term and then further enhanced by periodic driving [36]. Figure 4(a) shows the evolution of quantum fidelity for the polarized state in the pure PXP model (black), with static detuning (red), and with periodic driving (blue). Similar to the Néel state, the growth of entanglement entropy is strongly suppressed by the static detuning and even more so with periodic driving, see Fig. 4(b). The entanglement entropies and the numbers of excitations for all Floquet modes of the optimally driven system ($\Delta_0 = 1.68$, $\Delta_m = -0.50$, $\omega = 3.71$) can be observed in Fig. 4(c). This driving frequency approximately matches that of revivals in a static system with detuning $\Delta_0 = 1.68$ [red line in Fig. 4(a)], where QMBS for the polarized state has been previously observed [36]. However, unlike the Néel state, there is now only one arc and a single Floquet mode that has high overlap with the polarized state ($\approx 64\%$, encircled in red).

Apart from this set of driving parameters, which were studied in Ref. [36], there are also other sets of driving parameters that lead to robust revivals from the polarized state. One such
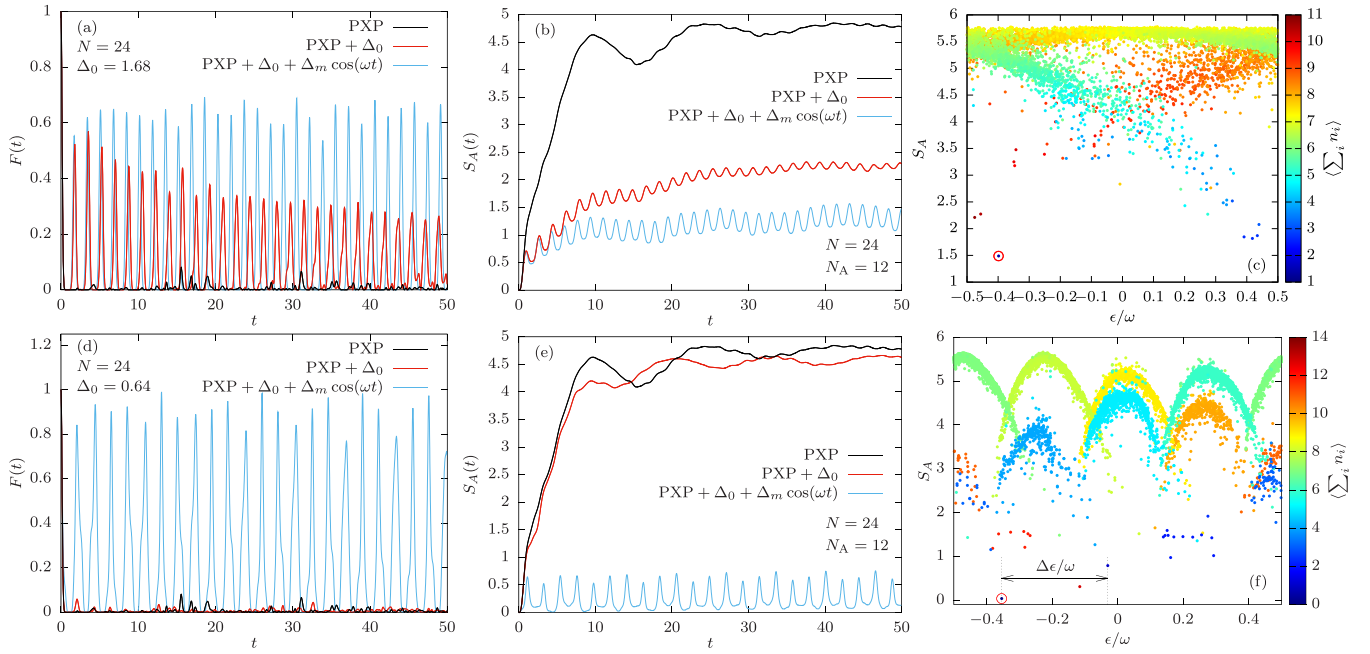
FIG. 4. Driven polarized state. Top row: "low-amplitude" driving regime ($\Delta_0 = 1.68$, $\Delta_m = -0.50$, $\omega = 3.71$). (a) Quantum fidelity, system size $N = 24$. (b) Entanglement entropy for the subsystem size $N_A = 12$. (c) Entanglement entropy of Floquet modes, $N = 26$ in zero momentum sector. Color scale shows the average number of excitations $\langle \sum_i n_i \rangle$ in each Floquet mode. Bottom row: Same as the top row, but for "high-amplitude" driving regime ($\Delta_0 = 0.64$, $\Delta_m = 7.55$, $\omega = 2.90$).

example is shown in Figs. 4(d)–4(f) ($\Delta_0 = 0.64$, $\Delta_m = 7.55$, $\omega = 2.90$). Upon first glance, this situation is completely different from Figs. 4(a)–4(c). In the latter case, the revivals essentially stem from static detuning, which creates scarring, and the driving further stabilizes them. By contrast, in the former case, the revivals are generated by periodic driving. The optimal driving frequency was found using simulated annealing and it does not appear to correspond to any special frequency in the static system. Moreover, the Floquet mode entanglement entropy plot also has a different structure, as can be observed in Fig. 4(e). There are now multiple arcs ($N/2 + 1$ of them), each with a well-defined excitation number. This suggests that the Floquet Hamiltonian is fragmented in this parameter regime (see further discussion in Sec. III C below). There is a single Floquet mode that has near-unity overlap (>90%) with the polarized state, which accounts for the revivals. The mode belongs to its own one-dimensional excitation number sector, since the polarized state is the only state that contains no excitations. The mode is furthermore separated from the neighboring $\langle \sum_i n_i \rangle = 1$ sector by a gap $\Delta\epsilon$, which practically does not depend on the system size— see Fig. 12 in Appendix A.

Based on these insights, in Appendix B we present a modified, spatially inhomogeneous cosine driving scheme, which can enhance the revivals from any initial product state, including generic states that do not display QMBS. The main idea is to change the driving protocol in such a way that the desired initial state becomes the ground state of the new time-dependent term. Driving with optimal parameters then results in similar phenomenology to the polarized state in the high-amplitude regime [Fig. 4(d)–4(f)], including the fragmentation of the Floquet Hamiltonian into sectors with different quantum numbers.

We note that both of the driving regimes presented in Fig. 4 belong to what we referred to as Type-2 peaks. In these cases, the optimal parameters do not require particular fine tuning, i.e., there is a fairly broad range of parameter values for which the driving stabilizes QMBS revivals, unlike the Type-1 peaks where such regions are more narrow and finding optimal parameters requires more careful optimization. It was not possible to produce a subharmonic response for the polarized state, which is expected since it does not have a translated partner state, such as $\mathbb{Z}_2$ and $\mathbb{Z}'_2$. Since the two Néel states also belong to their own excitation number sector in Fig. 4(f), it is also possible to use the $\Delta_0 = 0.64$, $\Delta_m = 7.55$, $\omega = 2.90$ parameters to stabilize the revivals from these states, as will be explained in Sec. V.

C. Origin of "multiple arcs" structure

In order to explain the structure of entanglement entropy plots in Figs. 3 and 4, we treat the PXP term in Eq. (3) as a perturbation. First we consider the $\Omega = 0$ case when the Hamiltonian is diagonal but still time periodic. The Floquet modes are then product states and their quasienergies depend only on the value of static detuning Δ_0 and their number of excitations $\langle \sum_i n_i \rangle$, while the quasienergy spectrum has periodicity ω,

$$\epsilon = \left\langle \sum_i n_i \right\rangle \Delta_0 \quad \text{mod } \omega. \qquad (6)$$

As the number of excitations increases, the Floquet modes are winding around the spectrum. Different ratios of Δ_0/ω will result in different structures. When the PXP term is turned on, these states start to hybridize. However, only those states that are close in excitation number can hybridize, since the PXP

term can only change this number by ± 1. They also need to be close in quasienergy, but what is "close enough" depends on the magnitude of the PXP term in the Floquet Hamiltonian. Since the cosine drive is difficult to treat analytically, especially for the Néel state optimal parameters, which are in the nonperturbative regime, in the following Sec. IV we introduce a more tractable square pulse approximation of the cosine driving protocol.

In the parameter regime optimal for the Néel state (Type-1), the $\Omega = 0$ Floquet modes form two diagonal lines (even and odd excitation numbers). Only the states belonging to the same diagonal will mix when $\Omega > 0$, which will result in two separate structures at $\Omega = 1$. This is the origin of the two arcs in Fig. 3(c). Note that the Floquet modes in the two arcs no longer consist of the states with only even or only odd number of excitations. No symmetry that distinguishes between the two arcs could be identified.

The situation is different for the polarized state high-amplitude optimal parameters (Type-2). At $\Omega = 0$, the Floquet modes that are close in quasienergy are far apart in excitation number, and the magnitude of the PXP term in the Floquet Hamiltonian is small for these parameters, so there is no mixing between the sectors even when $\Omega = 1$. This results in $N/2 + 1$ separate sectors as shown in Fig. 4(f), each containing only the modes with a certain number of excitations. The low-amplitude regime from Fig. 4(c) is a special case where the smaller arcs merge into one large arc, while the Floquet modes are still arranged according to their numbers of excitations and the $\langle \sum_i n_i \rangle = 0$ sector is sufficiently separated from the rest.

IV. SQUARE PULSE DRIVE

The cosine drive in Eq. (3) is difficult to treat analytically. Therefore, it is desirable to find a simpler model that accurately captures the dynamics, at least at the qualitative level. Previous papers [10,56] have considered the following delta function pulse driving model:

$$\Delta(t) = \theta \sum_{n \in \mathbb{Z}} \delta(t - nT), \tag{7}$$

where $T = 2\pi/\omega$ is the driving period and θ is a parameter of the drive. This driving protocol results in perfect revivals from any initial state when $\theta = \pi$ due to a special symmetry property of the Floquet operator in that case [56]. However, the Néel state is seen to be special when θ is varied away from π: while the revival from other initial states sharply decays, the Néel revival stays robust over a finite range of θ in the vicinity of π. Although this model has been well understood, its relation to the cosine driving scheme is not completely transparent.

We will now show that a simple square pulse model is a better approximation for the cosine drive. The square pulse protocol is defined by

$$\Delta(t) = \Delta_0 + \Delta_m(t),$$

$$\Delta_m(t) = \begin{cases} \Delta_m, & 0 \leqslant t \leqslant T/4 \\ -\Delta_m, & T/4 < t \leqslant 3T/4 \\ \Delta_m, & 3T/4 < t \leqslant T, \end{cases} \tag{8}$$
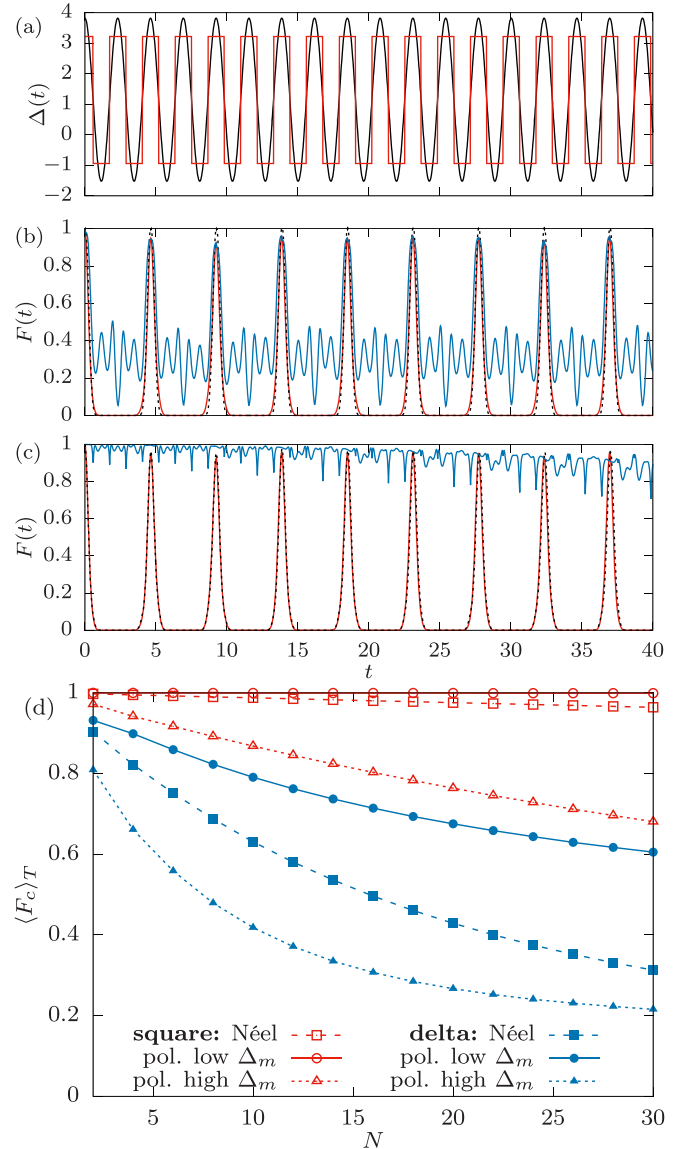
FIG. 5. (a) Cosine drive (black) vs square pulse drive (red). (b) Red: Cosine drive fidelity, $F(t) = |\langle \psi(0)|\psi(t)\rangle|^2$. Black (dashed): Delta function pulse fidelity, $F'(t) = |\langle \psi(0)|\psi'(t)\rangle|^2$. Blue: Comoving fidelity $F_c(t) = |\langle \psi(t)|\psi'(t)\rangle|^2$. Néel state, $L = 20$, optimal driving parameters. (c) Same for square pulse instead of delta function pulse. (d) System size scaling of comoving fidelity averaged over the first driving period for the square (red) and delta function pulse (blue). Optimal driving parameters: Néel state (squares), polarized state low-amplitude (circles), polarized state high-amplitude (triangles).

as illustrated in Fig. 5(a). We note that similar driving schemes were previously considered in Refs. [50,51], however, our square pulse model differs from those by a quarter of driving period time shift, which results in very different Floquet dynamics.

A comparison of the delta pulse in Eq. (7) and the square pulse in Eq. (8) is shown in Figs. 5(b) and 5(c), where we plot the quantum fidelity $F(t)$ for the exact evolution under cosine drive, as well as the fidelity for the system driven by the delta or square pulse. Moreover, we directly evaluate and plot the

comoving fidelity, $F_c(t) = |\langle \psi(t)|\psi'(t)\rangle|^2$, which represents the overlap between the wave function evolved using the cosine driving protocol, $|\psi(t)\rangle$, and the one evolved using the approximate protocol, $|\psi'(t)\rangle$ (delta or square pulse). Here, the initial state is the Néel state and the driving parameters are set to their optimal values ($\Delta_0 = 1.14$, $\Delta_m = 2.08$, $\omega = 2.72$ for the square pulse). We note that the optimal driving frequency and static detuning are approximately the same for both the cosine and square pulse drive, but the driving amplitude has to be reoptimized and is approximately 20% lower in the latter case. For the delta function pulse, we use $\theta = \pi$ and the same frequency as the cosine drive.

The comoving fidelity is seen to be much higher for the square pulse drive, compare Figs. 5(b) and 5(c). This signals that the square pulse driving protocol is a much better approximation for the cosine drive than the delta function pulse. In particular, while the delta pulse is highly accurate near the revival points, the square pulse remains accurate throughout the evolution, including away from the revival points. This difference becomes more pronounced in larger system sizes, as can be observed in Fig. 5(d), where we plot the scaling of the co-moving fidelity, averaged over the first driving period with the system size N. In general, the agreement between the cosine drive and square pulse is better when the driving frequency is high and amplitude low. For example, the agreement is particularly good for the polarized state in the low-amplitude regime, where the comoving fidelity is almost equal to 1 over many driving periods. In addition to accurately capturing the dynamics of the cosine drive, the square pulse drive also reproduces the two special Floquet modes and a "two arc" entanglement entropy spectrum resembling the one in Fig. 3(c). Finally, knowing the optimal driving parameters for the square pulse allows us to estimate the parameters for the cosine drive by simply using the same driving frequency and static detuning while increasing the amplitude by 25%.

The optimal driving parameters identified for the Néel state ($\Delta_0 = 1.15$, $\Delta_m = 2.67$, $\omega = 2.72$) and for the polarized state ($\Delta_0 = 1.68$, $\Delta_m = -0.50$, $\omega = 3.71$) are all of the same order of magnitude as $\Omega = 1$, the characteristic energy scale of the static Hamiltonian. Thus, the stabilization of revivals in these cases due to periodic driving appears to be a nonperturbative effect. Nevertheless, for the square pulse protocol, we can obtain useful analytical insights into the mechanism of the revival stabilization in two extreme limits: the limit of high amplitudes and the limit of high driving frequency. In the remainder of this section, we discuss separately these two cases.

A. High-amplitude regime

When the driving amplitude Δ_m is high, the square pulse allows us to describe the dynamics perturbatively. At first order in the small parameter $\lambda_\pm \equiv \Omega/(\Delta_m \pm \Delta_0) \ll 1$, it straightforward to obtain the Floquet Hamiltonian using the Pauli algebra. We start from the Hamiltonian

$$H(t) = -\frac{\Delta(t)}{2} \sum_j (I_j + Z_j) - \Omega \sum_j \tilde{X}_j, \qquad (9)$$

where $\tilde{X}_j \equiv P_{j-1} X_j P_{j+1}$ denotes the Pauli x matrix dressed by projectors, and $\Delta(t)$ is given by the square pulse in Eq. (8). We ignore the energy shift $-\Delta(t)/2$ and assume $\Delta_m \pm \Delta_0 \gg \Omega > 0$.

The evolution operator from $t = 0$ to $t = T/4$ and from $t = 3T/4$ to T is denoted U_+ and from $t = T/4$ to $t = 3T/4$ by U_-. At first order $\lambda_\pm \ll 1$, we can factorize these evolution operators

$$U_+ \approx \prod_j e^{i(\lambda_+ \tilde{X}_j + Z_j)\frac{T}{4}}, \qquad (10)$$

$$U_- \approx \prod_j e^{i(\lambda_- \tilde{X}_j + Z_j)\frac{T}{2}}, \qquad (11)$$

since the commutator between $\lambda \tilde{X}_j + Z_j$ and $\lambda \tilde{X}_{j'} + Z_{j'}$ on different sites j and j' is second order in λ. We can then expand the exponentials using the properties of Pauli operators ($Z^2 = I$ as well as $\tilde{X}^2 = I$) in terms of sine and cosine functions, and evaluate the total evolution operator for one period $U = U_+ U_- U_+$. At first order in λ, the final expression can be easily converted back into exponential form, from which the first-order Floquet Hamiltonian can be directly read off. While the algebra is tedious, the calculation is straightforward and results in the following first-order Floquet Hamiltonian:

$$H_F^{(1)} = -\frac{\Delta_0}{2} \sum_i g_{T,\Delta_0,\Delta_m} P_{i-1} X_i P_{i+1} + Z_i,$$

$$g_{T,\Delta_0,\Delta_m} = \frac{2\Omega}{\Delta_m^2 - \Delta_0^2} \left\{ \left[1 + 2\frac{\sin\frac{(\Delta_m - \Delta_0)T}{4}}{\sin\frac{\Delta_0 T}{2}} \right] \Delta_m - \Delta_0 \right\}. \tag{12}$$

The first-order Floquet Hamiltonian contains a PXP term whose magnitude is controlled by the prefactor g, which depends on the values of driving parameters Δ_0, Δ_m and the drive period $T = 2\pi/\omega$.

The g prefactor explains several features of the fidelity phase diagram, as can be seen in Fig. 6. When g is small, the Floquet Hamiltonian is almost diagonal and the Floquet modes are close to product states, which have well-defined numbers of excitations. As long as g is small enough [bright regions in Fig. 6(a)], there is no mixing between different excitation-number sectors. This leads to fragmentation and the polarized state ends up in its own one-dimensional sector, while the two Néel states belong to another two-dimensional sector. These states are therefore close to a Floquet mode and keep reviving in the driven system, which leads to high average fidelity [bright regions in Fig. 6(b)]. This explains the origin of Type-2 peaks.

Conversely, when g is large (for example around the diagonals $\Delta_0 = \pm \Delta_m$) the sectors are mixed and the Floquet modes have large variance of the excitation number, meaning that they are superpositions of many product states with different excitation numbers. We do not expect revivals in these regions and Fig. 6(b) confirms that this is mostly the case. However, the optimal driving parameters for the Néel state (Type-1 peaks) are actually in the dark region along the diagonal.

Some features of the phase diagram in Fig. 6(b) cannot be explained only by Eq. (12). Irrespective of the value of g, there are dark lines (no revivals) around $\Delta_0 = n\omega/2$, where
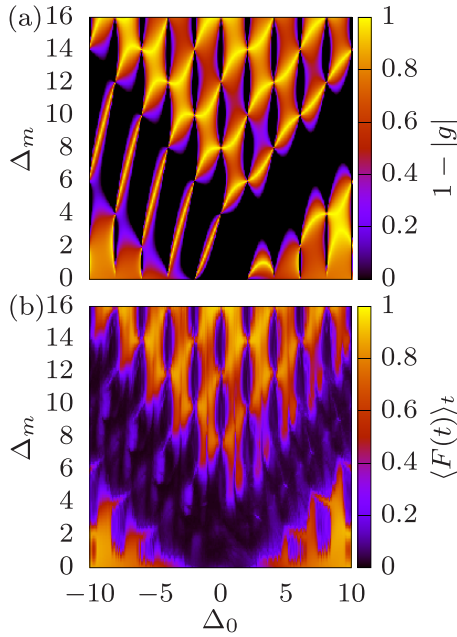
FIG. 6. Analytical versus numerical results. Néel state, $\omega = 2$. (a) $1 - |g_{T,\Delta_0,\Delta_m}|$. Note that some values are outside of $[0,1]$ interval. (b) Average fidelity $\langle F(t) \rangle_t$.

n is an integer (this is more visible for the cosine drive in Fig. 1). The explanation is related to the quasienergies of the Floquet modes when the PXP term is turned off ($\Omega = 0$), see the discussion in Sec. III C. In this case, the Hamiltonian is diagonal and the Floquet modes are product states. Their quasienergies depend only on the value of static detuning Δ_0 and the Floquet spectrum has periodicity ω, see Eq. (6). When $\Delta_0 = n\omega$, all $\Omega = 0$ modes have the same quasienergy $\epsilon = 0$. For $\Omega = 1$, any finite value of g will lead to mixing between all sectors. Consequently, no single mode will be close to a product state and there will be no revivals. This underlines the importance of nonzero static detuning. The situation is similar when $\Delta_0 = (2n+1)\omega/2$, but in this case the $\Omega = 0$ Floquet modes split into two groups with same quasienergies (even and odd numbers of excitations). Finite g then causes mixing within these two groups, leading to the appearance of two arcs in the entanglement entropy plots [similar to Fig. 3(c)].

In conclusion, the square pulse drive provides analytical understanding of a large part of phase diagram corresponding to high driving amplitudes. However, we note that the agreement between the square pulse and cosine drive is not as good in the high-amplitude regime for the polarized state with parameters $\Delta_0 = 0.64$, $\Delta_m = 7.55$, $\omega = 2.90$, recall Fig. 5(d). Nevertheless, the square pulse still accurately captures the revivals and the comoving fidelity is higher than for the delta function pulse protocol.

B. High-frequency regime

Although the optimal set of parameters for the Néel state is deeply in the nonperturbative regime with $\Omega = 1$, $\Delta_0 = 1.15$, $\Delta_m = 2.67$ and $\omega = 2.72$ of the same order of magnitude, in Fig. 2 we have seen that it is also possible to somewhat stabilize the revivals by driving with relatively high frequencies. If
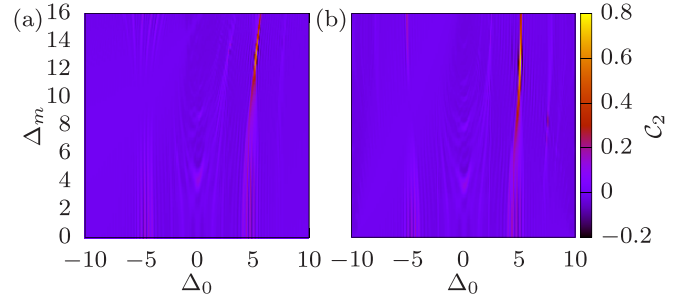

FIG. 7. Quality of the subharmonic response, $\mathcal{C}_2$ in Eq. (5), for the Néel initial state and $\omega = 10$. (a) Third-order Floquet Hamiltonian in the high-frequency regime $H_{F,\omega}^{(3)}$. (b) Time-dependent Hamiltonian $H(t)$ with the square pulse driving scheme.

we follow the same peak by reoptimizing the static detuning and amplitude while increasing the frequency, as in Fig. 2(a), the resulting driving parameters still result in a subharmonic response and its Floquet modes are split into two arcs. This suggests that we can obtain useful insights into the revival stabilization mechanism by studying the dynamics using the high-frequency expansion.

In Appendix C we derive the following third-order Floquet Hamiltonian for the square pulse driving protocol in the limit of high driving frequency:

$$H_{F,\omega}^{(3)} = \Omega \left[1 + \frac{\Delta_m T^2 (3\Delta_0 - \Delta_m)}{96} \right] \sum_i P_{i-1} X_i P_{i+1}$$
$$- \Delta_0 \sum_i n_i + \frac{\Omega^2 \Delta_m T^2}{16} \sum_i P_{i-1} Z_i P_{i+1}$$
$$+ \frac{\Omega^2 \Delta_m T^2}{16} \sum_i P_{i-1} (\sigma_i^+ \sigma_{i+1}^- + \sigma_i^- \sigma_{i+1}^+) P_{i+2}.$$

$$(13)$$

In addition to the renormalized PXP term and time-averaged detuning Δ_0, this Hamiltonian also contains a diagonal PZP term and constrained nearest-neighbor hopping terms. Note that the Floquet Hamiltonian only describes stroboscopic evolution at times $t = nT$, where n is an integer. We have numerically confirmed that the first three orders are enough to correctly reproduce the dynamics of the first few revivals at $\omega = 10$. Further increase in frequency makes the agreement even better.

In Fig. 7 we plot the subharmonic cost function, Eq. (5), for the Néel state at $\omega = 10$, and compare the evolution using $H_{F,\omega}^{(3)}$ and the actual square pulse driving protocol. The high-frequency Floquet Hamiltonian correctly reproduces most features of this phase diagram and approximately locates the narrow Type-1 optimal parameter regime (around $\Delta_0 \approx 5$, $\Delta_m \approx 13$). At the optimal parameters, the dominant term in $H_{F,\omega}^{(3)}$ is the static detuning, while PZP and hopping are relatively small. The energy spectrum thus resembles that of a strongly detuned PXP model, with several disconnected energy bands defined by their numbers of excitations and the gaps between them approximately equal to Δ_0. If we want to obtain a subharmonic response, this gap should be half the driving frequency, so we expect the optimal detuning to be

around $\Delta_0 = \omega/2$, which is indeed the case here. The best revivals will be obtained when the energy bands are very narrow, which will make the eigenstates that have the highest overlap with the Néel state almost exactly equidistant. The widths of individual bands are controlled by the other three terms. Assuming that PXP, PZP and $P\sigma^{\pm}\sigma^{\mp}P$ are approximately of the same order of magnitude and minimizing the sum of their coefficients, $T^2(3\Delta_0\Delta_m - \Delta_m^2 + 12\Delta_m)/96$, at $\Omega = 1$ and fixed T and Δ_0, results in the optimal driving amplitude

$$\Delta_m = 3\Delta_0/2 + 6, \tag{14}$$

which gives ≈ 13.5—close to the numerically obtained optimal value.

We can reproduce Fig. 2(a) for the square pulse drive (not shown) and compare the dependence of optimal Δ_0 and Δ_m on the driving frequency with our analytical predictions from the previous paragraph. The optimal static detuning indeed closely follows the relation $\Delta_0(\omega) = \omega/2$, even at relatively low frequencies ($\omega \gtrsim 5$). As expected since the high-frequency expansion is no longer valid in that regime, there are some deviations from this rule at lower frequencies, for example $\Delta_0 \approx 0.42\omega$ at $\omega = 2.72$. Regarding the relation for the optimal driving amplitude $\Delta_m(\omega) = 3\omega/4 + 6$ in Eq. (14), the numerical results start to approach this line at higher frequencies, $\omega > 10$. Since we have already established that the optimal values of static detuning are approximately equal for the cosine drive and square pulse, while the driving amplitude is around 20% lower for the square pulse, we can use these analytical results to estimate the Type-1 optimal driving parameters for the cosine driving protocol.

V. RELATION TO QUANTUM MANY-BODY SCARS

Finally, we come to the important set of questions concerning the relation between QMBS and the enhancement of fidelity revivals by periodic driving. We focus on two questions in particular: (i) Is it still possible to stabilize the revivals from some initial state if the PXP part of the Hamiltonian in Eq. (3) is replaced by some other, fully ergodic Hamiltonian? (ii) How do we prove that the optimally-driven system is "scarred"? The second question, in particular, is nontrivial as many probes of QMBS in static systems do not directly translate to the driven case. For example, QMBS are typically diagnosed as a band of atypical eigenstates at equidistant energies. Since the driven model is time dependent, the Floquet modes assume the role of the eigenstates. However, in all the cases studied here, there is no band of special Floquet modes in the quasienergy spectrum of the Floquet Hamiltonian. Instead, there is only one or in some cases two special modes, which have unusually low entanglement entropy and very high overlap with the initial state. Also, it could be said that these modes are typically located at the edges of the quasienergy spectrum rather than the middle of it, see Fig. 3(c). However, one must keep in mind it is hard to rigorously define the "edge" when the quasienergy spectrum is periodic. In light of this difference between driven and static systems, it is pertinent to ask if the dynamics in the driven case is still "scarred" in the sense that it represents merely an enhancement of the effect already present in the static case. In this section we address these questions.

A. The effect of perturbation

QMBS can be destroyed by applying suitable perturbations to the PXP model [54]. The destruction of QMBS was found to coincide with the overall level statistics of the model converging faster to the Wigner-Dyson distribution, signaling faster thermalization. Here we study the PXPXP perturbation and apply the usual spatially homogeneous cosine driving protocol, Eq. (3), to the perturbed PXP Hamiltonian,

$$H'_{\text{PXP}}(W) = H_{\text{PXP}} + W \sum_i P_{i-1} X_i P_{i+1} X_{i+2} P_{i+3}, \tag{15}$$

$$H'(t) = H'_{\text{PXP}}(W) - \Delta(t) \sum_i n_i. \tag{16}$$

The PXPXP perturbation is off-diagonal, thus it changes the connectivity of the Hilbert space.

In Fig. 8 we scan the (Δ_0, Δ_m) parameter space for three different perturbation strengths, while the driving frequency is fixed at $\omega = 2$. Similar to Fig. 1, the color corresponds to the average fidelity $\langle F(t) \rangle_t$ between $t = 0$ to $t = 100$, such that the bright regions correspond to parameter regimes where we expect robust revivals. The perturbation destroys some of the optimal parameter regimes, mostly those close to the diagonals $\Delta_0 = \pm\Delta_m$. For example, the main Type-1 optimal regime for the Néel state belongs to this region, as shown in Fig. 1(a) for $\omega = 2.72$. The higher-amplitude optimal parameter regions (Type-2) are affected by the perturbation and their position, shape and size all depend on the perturbation strength. However, these bright regions are still present even when the perturbation is fairly strong ($W = 0.5$). Those regions are related to Hilbert space fragmentation, see Fig. 4. This allows us to conclude that the Floquet Hamiltonian fragmentation mechanism is not specific to the PXP model, which is in line with the discussion from Sec. III C. However, a possibility remains that the original, weakly nonergodic PXP model is in some way important for the revival enhancement in the low-amplitude driving regime for the Néel state (Fig. 3).

Similar behavior was also observed with different types of perturbations, such as next-nearest-neighbor interaction $W_1 \sum_i n_i n_{i+2}$, or constrained nearest-neighbor hopping $W_2 \sum_i P_{i-1}(\sigma_i^+ \sigma_{i+1}^- + \sigma_i^- \sigma_{i+1}^+) P_{i+2}$. It is, however, interesting to note that, while destroying scars for the $\mathbb{Z}_2$ state, the next-nearest-neighbor interaction can actually create scars for the polarized state, which is reminiscent of the effects of static detuning [36]. The stabilization of revivals from the polarized state using periodic driving works even better (quantified by higher $\mathcal{C}_1$) in a certain range of nonzero values of W_1 that coincides with the existence of quantum many-body scars for this state in the static system.

B. Trajectory in the Hilbert space

Another way to relate the reviving dynamics in the driven system with QMBS in the static case is to examine the Hilbert space trajectory of the Néel state, with and without driving. We can visualize this trajectory by plotting the expectation values of the (normalized) numbers of excitations on the even and odd sublattice, $\langle n_A \rangle$ and $\langle n_B \rangle$ respectively, see Fig. 9. The two Néel states only have excitations on one of the sublattices, so they correspond to the bottom right (1,0) and top left (0,1) corner, while the polarized state with no excitations is in the
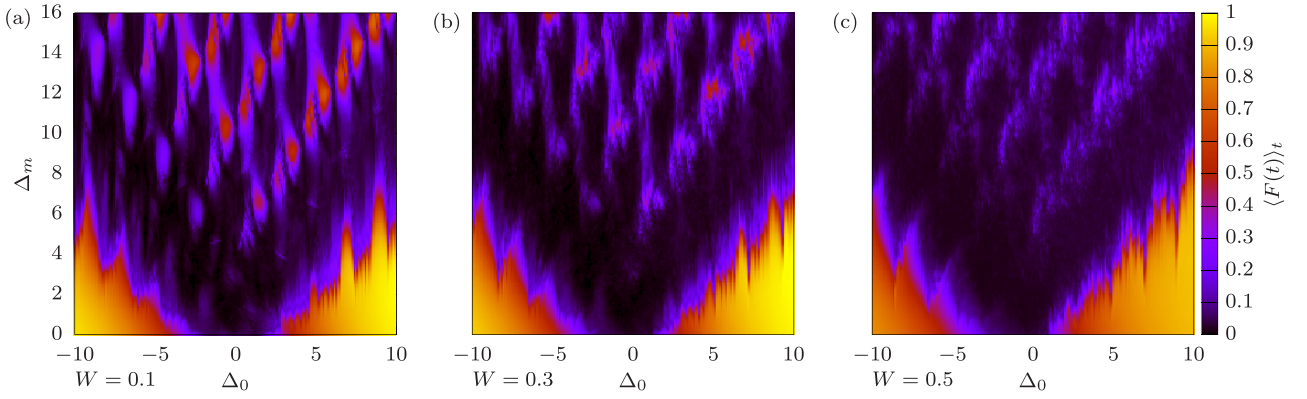
FIG. 8. PXP model perturbed by PXPXP perturbation from Eq. (15). The color scale shows the average fidelity $\langle F(t) \rangle_t$ in a time window [0,100] for the initial Néel state. The driving frequency is fixed to $\omega = 2$. (a) $W = 0.1$. (b) $W = 0.3$. (c) $W = 0.5$.

bottom left corner (0,0). All other states on the main diagonal or above it are forbidden due to the PXP blockade constraint.

Up to this point, for the Néel state we have mostly used the driving frequency $\omega = 2.72$, which is approximately twice the frequency of revivals in the static PXP model ($\omega \approx 2.66$). Similarly, the optimal driving frequency for the polarized state in the low-amplitude regime is close to the frequency of revivals in the detuned PXP model. However, we were also able to stabilize the revivals at driving frequencies that are not particularly close to the original revival frequency. Upon first glance, this fact does not seem to support the claim that the driven system hosts QMBS, however we will show bellow that driving with frequencies close to $\omega = 2.72$ leads to Hilbert space trajectories with some special properties.
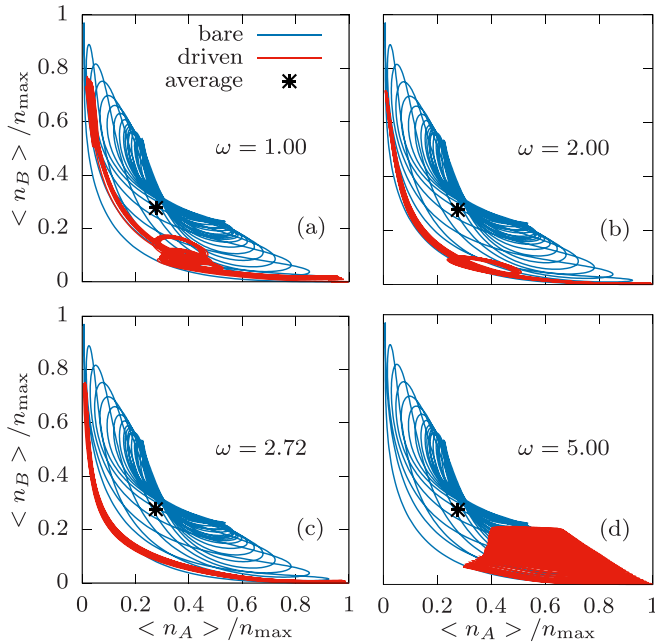

FIG. 9. Trajectory in the Hilbert space. Néel state without (blue) and with optimal driving (red). $N = 24$. The maximal number of excitations per sublattice is $n_{\max} = N/2$. (a) $\omega = 1.00$, $\Delta_0 = -0.65$, $\Delta_m = 8.31$. (b) $\omega = 2.00$, $\Delta_0 = -1.17$, $\Delta_m = 4.81$. (c) $\omega = 2.72$, $\Delta_0 = 1.15$, $\Delta_m = 2.67$. (d) $\omega = 5.00$, $\Delta_0 = 2.34$, $\Delta_m = 6.85$.

It is possible to obtain high and long-lived revivals from the Néel state at frequencies significantly below $\omega = 2.72$. Two examples of such trajectories are shown by the red lines in Figs. 9(a) and 9(b), for driving frequencies $\omega = 1$ and $\omega = 2$ respectively, while the trajectory in the static model is plotted in blue. For comparison, the trajectory for $\omega = 2.72$ is shown in Fig. 9(c). In this special case, the trajectory precisely repeats the approximate first revival period of the undriven case. It could therefore be said that driving with optimal parameters stabilizes the scarred dynamics of the pure PXP model. This suggests that the true optimal driving frequency is indeed related to quantum many-body scars in the static model. The most significant difference between this trajectory and the previous two is that the low-frequency trajectories contain loops. The number of loops grows as the driving frequency decreases. Although the trajectory can still be made to oscillate between the two Néel states at lower frequencies, the intermediate dynamics differs from that in the static PXP model.

However, the revivals cannot be stabilized for any arbitrarily chosen driving frequency. When the frequency is too high, for example $\omega = 5$ in Fig. 9(d), the revivals decay and the trajectory explores only one corner of the Hilbert space, staying in the vicinity of the initial state. This could be better understood using the square pulse approximation of the driving protocol from Sec. IV. Close to integer multiples of the driving period, the drive is in the high-detuning regime ($\Delta_0 + \Delta_m$) where the spectrum is split into bands and the Néel state is approximately one of the eigenstates. Frequent returning to this regime therefore prevents the wave function from moving away from the Néel state. The intermediate low-detuning regime ($\Delta_0 - \Delta_m$) needs to be long enough in order for the trajectory to reach the other side of the Hilbert space, and its detuning low enough so that the system is closer to the pure PXP model. In other words, the frequency needs to be low enough for the driven system to oscillate between the two Néel states.

Two remarks are in order. First, driving with high-amplitude optimal parameters for the polarized state can also produce high revivals from the Néel state. This is not surprising since in this case there are two Floquet modes with high overlap with the Néel states [see Fig. 4(f)], but the wave function is in that case "stuck" in one corner of the Hilbert space. The trajectory is similar to Fig. 9(d), albeit more
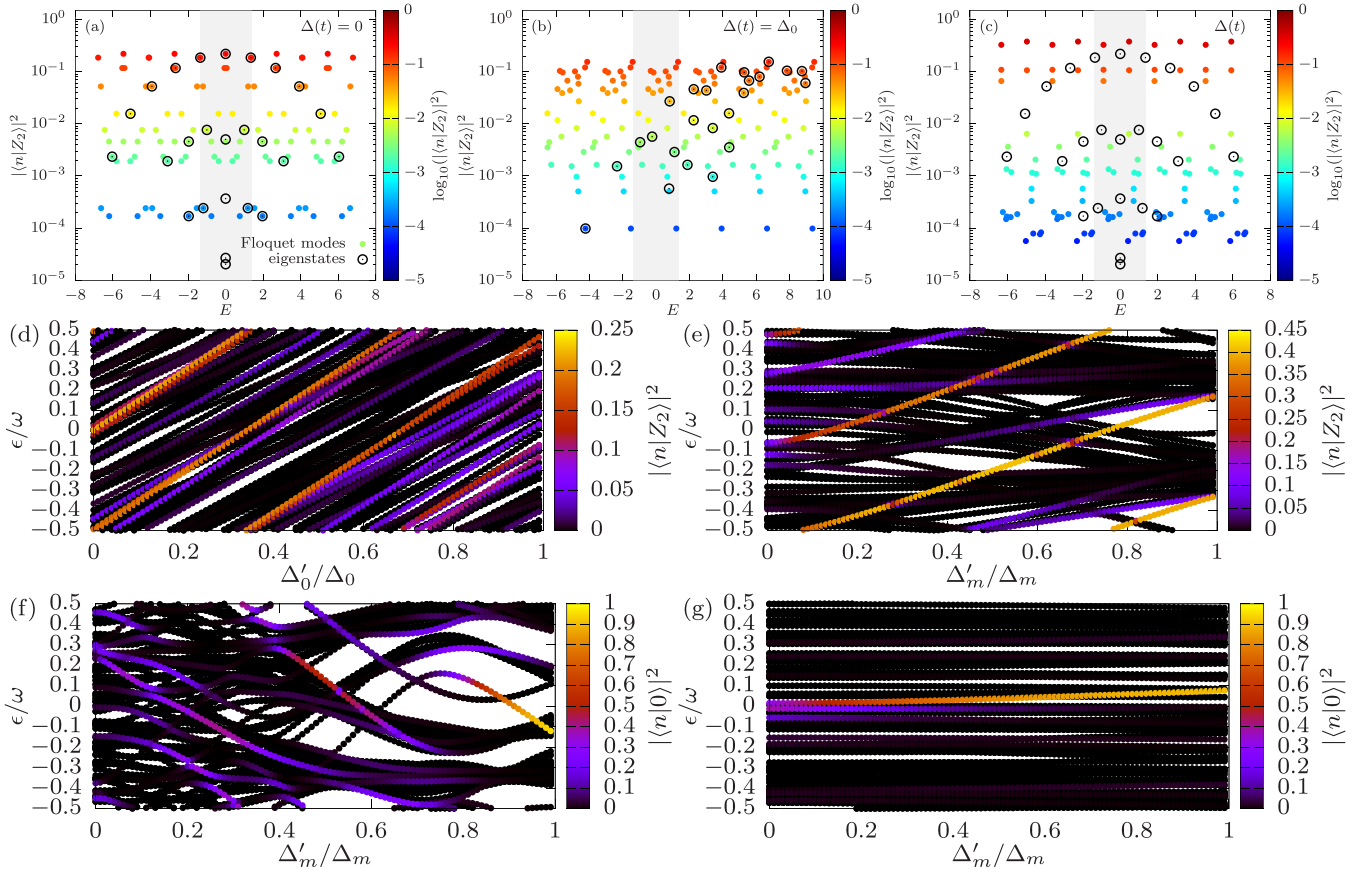
FIG. 10. Overlap of the Floquet modes with the initial state, $N = 10$. (a) Bare PXP model (Néel, $\omega = 2.72$). Floquet modes (color) versus eigenstates (black circles). The shaded area marks the $[-\omega/2, \omega/2]$ interval of the Floquet spectrum. (b) Same, but with static detuning $\Delta_0 = 1.15$. (c) Same, but optimally driven ($\Delta_0 = 1.15$, $\Delta_m = 2.67$). The eigenstates of the bare PXP model are shown for comparison. (d) Interpolation between bare and detuned (Néel). (e) Interpolation between detuned and optimally driven (Néel). (f) Interpolation between detuned and optimally driven (polarized, high amplitude, $\Delta_0 = 0.64$, $\Delta_m = 7.55$, $\omega = 2.90$). (g) Interpolation between detuned and optimally driven (polarized, low amplitude, $\Delta_0 = 1.68$, $\Delta_m = -0.50$, $\omega = 3.71$).

narrow. Second, representing the Hilbert space trajectory in the $\langle n_A \rangle$-$\langle n_B \rangle$ plane is not suitable for the polarized state, since both that state and the full (uniformly driven) Hamiltonian are symmetric with respect to the two sublattices, thus $\langle n_A \rangle = \langle n_B \rangle$ at all times, i.e., the trajectory starting from the polarized state always stays on the diagonal. In Appendix D we discuss an alternative way to plot the trajectory for the polarized state.

C. From scarred eigenstates to Floquet modes

Finally, we would like to explore the connection between scarred eigenstates in the static PXP model and the two π-paired Floquet modes that have high overlap with the Néel state. To this end, we interpolate between the static $[\Delta(t) = 0]$ and optimally driven system $[\Delta(t) = \Delta_0 + \Delta_m \cos(\omega t)]$ by first increasing the static detuning from 0 to Δ_0 while keeping $\Delta_m = 0$, and then increasing the driving amplitude to its optimal value. The driving frequency is kept constant throughout this process ($\omega = 2.72$). The Floquet modes can be formally computed even in the $\Delta_m \to 0$ limit. In this case the Floquet modes should be exactly equal to the eigenstates of the static system. However, the Floquet quasienergy spectrum is periodic with periodicity ω, and we therefore need to "unfold" it in order to match the Floquet modes with their corresponding

eigenstates. This situation is shown in Fig. 10(a) where we plot the overlap of the PXP eigenstates and Floquet modes with the Néel state. For clarity, we use a small system size $N = 10$. The shaded region marks the original $[-\omega/2, \omega/2]$ interval of the Floquet spectrum, which is translated by ω several times so that the full energy spectrum is covered.

Next, the Floquet modes are computed for various values of static detuning Δ_0' and their quasienergies and overlap with the Néel state are plotted in Fig. 10(d). The highest overlap states of the bare PXP model are continuously deformed into the highest-overlap states of the detuned model at $\Delta_0 = 1.15$, which are also shown in Fig. 10(b). Similarly, these two states are then transformed into the two special Floquet modes by increasing the driving amplitude Δ_m' from 0 to $\Delta_m = 2.67$, see Fig. 10(e). To summarize, it is possible to establish a connection between the scarred eigenstates of the static PXP model [for example, $\epsilon = 0$ and $\epsilon \approx \omega/2$ at $\Delta_0'/\Delta_0 = 0$ in Fig. 10(d)] and the π-paired modes that are responsible for near-perfect revivals in the optimally driven model [two highest-overlap modes at $\Delta_m'/\Delta_m = 1$ in Fig. 10(e)]. Driving leads to scarred Floquet modes, which are more separated from the bulk than in the original bare PXP model, see Fig. 10(c). The π pairing was already present in the static model and was never broken during the interpolation procedure.

The interpolation between the detuned and optimally driven system was repeated for the polarized state and the results are shown in Figs. 10(f) and 10(g). Unlike for the Néel state, it is not possible to continuously deform the eigenstate of the static detuned model into the the high-overlap Floquet mode of the driven system in the high-amplitude regime, see Fig. 10(f). However, as shown in Fig. 10(g), the low-amplitude driving regime is different. In that case, one of the scarred eigenstates indeed transforms into the highest-overlap Floquet mode.

VI. CONCLUSIONS

In this paper we studied the periodically driven PXP model in order to gain a better understanding of how driving can enhance the revivals that are present in the static model due to QMBS. We introduced a square pulse approximation for the cosine driving protocol that was used in earlier experiments, and demonstrated that this approximation much more accurately reproduces the dynamics of the cosine drive than the previously studied delta function pulse drive, while still being amenable to analytical treatment. This allowed us to analytically predict the optimal driving parameters in the high-amplitude and high-frequency regimes. We were also able to modify the cosine driving protocol in such a way that any initial product state can be made to revive until late times.

We identified two distinct classes of optimal parameter regimes, which were dubbed Type-1 and Type-2. The second class is related to the splitting of the Floquet Hamiltonian into disconnected sectors, where a single Floquet mode belongs to a one-dimensional sector and has high overlap with one of the product states. The sectors consist only of Floquet modes with a certain number of excitations, thus the drive, being the largest energy scale, produces an emergent U(1) symmetry, similar to prethermalization scenario [69]. Type-2 mechanism of revival creation and stabilization is well understood, relatively trivial, and likely not connected with QMBS. The optimal driving parameter regimes were found for completely arbitrary initial product states, and were shown to be insensitive to perturbations that destroy quantum many-body scars in the original PXP model.

The other class of optimal driving parameters (Type-1) is more interesting, but also more challenging to study analytically due to it being in the nonperturbative regime. This revival enhancement mechanism was so far only observed for the Néel state and is destroyed by perturbations that also destroy QMBS. Visualising the trajectory of the evolved state in the Hilbert space and comparing the static and driven cases reveals that optimal driving stabilizes this trajectory—the system is made to precisely repeat the dynamics of the first revival period of the undriven model. When the system is initialized in one of the two Néel states, the response to driving is subharmonic, meaning that the revival frequency is half the driving frequency [56]. However, the subharmonic response becomes harmonic when the initial state is a translation-invariant superposition of the two Néel states. The origin of the subharmonic response is related to the presence of two π-paired Floquet modes in the quasienergy spectrum of the optimally driven system. These two atypical modes have very high overlap with the Néel states and can be thought of as

equivalents of scarred eigenstates in a periodically driven system.

An interesting direction for future work is the extension of driving protocols to other models that host inexact QMBS states and revival dynamics. This would involve finding a suitable driving term whose ground state is the scarred initial state. While Type-2 parameters (high-amplitude regime) are expected to trivially work even in the absence of scars, a more interesting question is whether Type-1 phenomenology exists beyond the PXP model.

APPENDIX A: SYSTEM SIZE SCALING

In this Appendix we examine the system size scaling of several important quantities. We fix the driving frequency and scan the (Δ_0, Δ_m) parameter space in the vicinity of two Type-1 peaks, $(\Delta_0, \Delta_m, \omega) = (-1.17, 4.81, 2.00)$ and $(\Delta_0, \Delta_m, \omega) = (1.15, 2.67, 2.72)$, for different system sizes N. The results are presented in Figs. 11(a)–11(d), showing that the optimal driving parameters are relatively stable for $N \geqslant 10$. Additionally, we plot the maximal average fidelity $\langle F \rangle_t$ as a function of system size in Figs. 11(e) and 11(f). Based on these results, we predict that the same parameters will still be optimal and produce revivals of finite height in relatively large systems. Such system sizes are out of reach of numerical simulations based on exact diagonalization, but could be realized experimentally. For example, a recent experiment has realized the PXP model with approximately 50 sites using a Bose-Hubbard quantum simulator [36].

In Fig. 4(f) we showed the quasienergy spectrum of the Floquet modes that correspond to the optimally driven polarized state in the high-amplitude regime. This spectrum is split into separate bands according to the number of excitations, with a single Floquet mode approximately equal to the polarized state belonging to a one-dimensional sector (0 excitations) and separated from the neighboring sector (1 excitation) by a gap $\Delta\epsilon$. In Fig. 12 we show that this gap is almost independent of system size. The inset zooms in on the data points in order to show that weak exponential decay
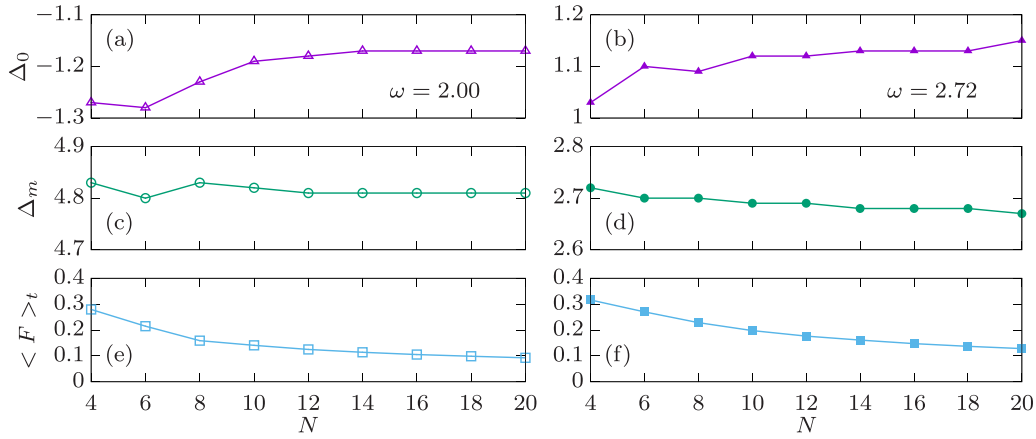
FIG. 11. System size scaling of the optimal driving parameters and the average fidelity for the Néel state. Left: $\omega = 2.00$ (one-loop trajectory). Right: $\omega = 2.72$ (ideal trajectory). [(a),(b)] Static detuning Δ_0. [(c),(d)] Driving amplitude Δ_m. [(e),(f)] Average fidelity from $t = 0$ to $t = 100$, $\langle F \rangle_t$.

is nevertheless present. If this trend continues, we estimate a finite gap even at sizes $N \approx 300$, implying that it would still be possible to create fidelity revivals in such large systems by applying the same driving parameters found in smaller systems.

We also investigated the dependence of the optimal frequency on system size. We use the same procedure as in Fig. 2 and plot the cost function $\mathcal{C}_2$ as a function of driving frequency in Fig. 13. The optimal frequency window is quite stable for $N \geqslant 10$, although it becomes slightly narrower as the system size increases.

APPENDIX B: SPATIALLY INHOMOGENEOUS DRIVE

Based on previous results, we now introduce a generalized driving protocol, which can stabilize revivals from *any* product state. A key observation is that the two initial states whose revivals can be stabilized by driving (Néel and polarized)

are the ground and the highest-excited state of the spatially homogeneous driving term in Eq. (3), since these two states have the highest and lowest possible number of excitations allowed by the blockade. In order to achieve a similar scenario for other states, the driving term should be chosen as spatially dependent,

$$H(t) = H_{\text{PXP}} + \Delta(t) \sum_i (-1)^{n_{0i}} n_i, \tag{B1}$$

where $n_{0i} = \langle \psi(0) | n_i | \psi(0) \rangle$ is determined by the initial state. In this protocol, each site is driven by $\pm \Delta(t)$, where the sign depends on whether the site initially contains an excitation or not, see Fig. 14 for an illustration. In this way, the initial state becomes the (nondegenerate) ground state of the driving term.

Using the inhomogeneous driving protocol, we were able to generate very high and long-lived revivals for any initial state, even randomly chosen ones with no symmetries. The driving parameters Δ_0, Δ_m, and ω need to be separately optimized for each initial state. To this end, we use the simulated
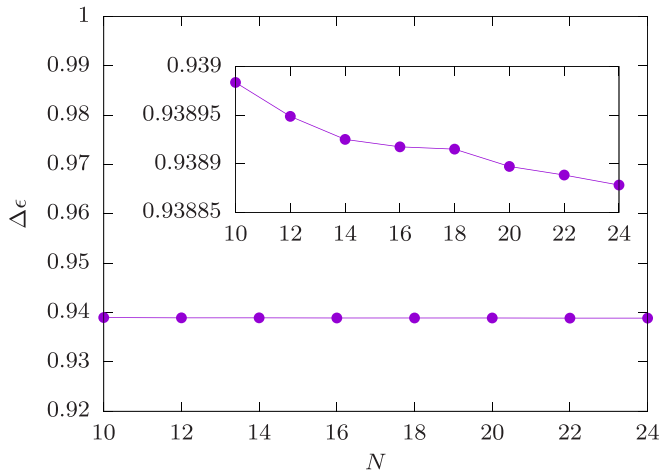
FIG. 12. System size scaling of the quasienergy gap between the two lowest entropy Floquet modes. Optimal parameters for the polarized state ($\Delta_0 = 0.64$, $\Delta_m = 7.55$, $\omega = 2.90$). The inset shows the same data with a different y-axis range.

FIG. 13. Cost function $\mathcal{C}_2$ in Eq. (5) with $M = 20$ as a function of frequency for different system sizes. "Main" Type-1 peak, which passes through the point $(\Delta_0, \Delta_m, \omega) = (1.15, 2.67, 2.72)$.

FIG. 14. Modified driving protocol for an arbitrary product state. The protocol is now site dependent, i.e., each site is driven by a term $(-1)^{n_{0i}}\Delta(t)$ whose sign depends on whether or not the site initially hosts an excitation.

annealing optimization algorithm, which limits the system sizes we can reach. However, when the initial state is sufficiently symmetric, for example $\mathbb{Z}_2$, $\mathbb{Z}_3$, $\mathbb{Z}_4$ and combinations of such states, it is sufficient to find the optimized parameters in a smaller system and the same driving parameters can be applied to the same state in larger systems, as was the case for $\mathbb{Z}_2$ with uniform driving.

Some optimal parameter values obtained by simulated annealing are listed in Table II. It is interesting to note that these values are similar in most cases, with $|\Delta_0| < 1$, $\Delta_m \gg 1$ and $\omega \approx 2$. From these values, we see that the phenomenology is similar to the polarized state in the high-amplitude driving regime [cf. Figs. 4(d)–4(f)]: the quasienergy spectrum is split into sectors with different values of $\langle \sum_i (-1)^{n_{0i}} n_i \rangle$ and there is a single Floquet mode that has very high overlap with the initial state. Ultimately, the mechanism of scar enhancement in this case is very special case of prethermalization [69]: Δ_m assumes the role of the large energy scale, which gives rise to an approximate U(1) symmetry. The initial state belongs to a one-dimensional sector and its mixing with other states is suppressed over long times, in accordance with general results in Ref. [69].

To illustrate the spatially inhomogeneous drive in Eq. (B1), we consider a completely random state $|\bullet\circ\bullet\circ\circ\circ\circ\circ\bullet\circ\circ\bullet\circ\circ\circ\circ\rangle$. This state has no special properties and quickly thermalizes in the pure PXP model, but driving with optimal parameters results in stable revivals, see Fig. 15(a). It might be hard to see due to a large number of different sectors and relatively small system size, but the quasienergy spectrum is also fragm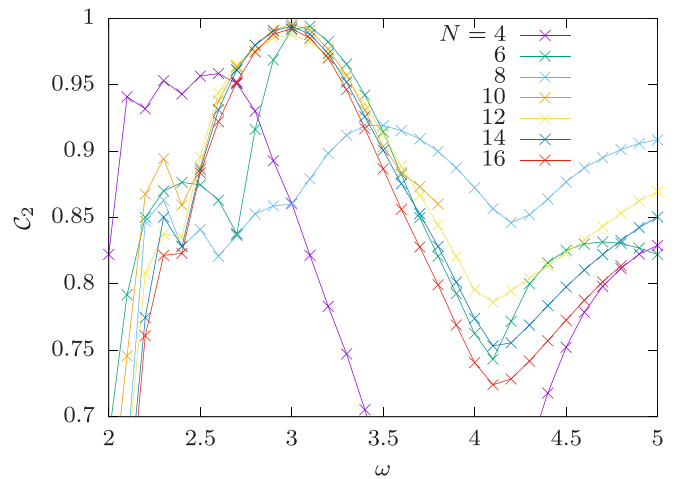ented in this case. As can be observed in Fig. 15(b), there is again a single high-overlap mode, which belongs to a one-dimensional sector, since it is the only product state that has the minimal possible value of $\langle \sum_i (-1)^{n_{0i}} n_i \rangle$. The driving amplitude is the largest energy scale ($\Delta_m = 6.36$).

TABLE II. Optimal driving parameters. $\mathbb{Z}_2$ (Néel), $\mathbb{Z}_3$ and $\mathbb{Z}_4$ are the states with an excitation on the every second, third and fourth site, respectively. $\mathbb{Z}_2\mathbb{Z}_3$ is $|\bullet\circ\bullet\circ\circ\bullet\circ\bullet\circ\ldots\circ\circ\bullet\circ\circ\rangle$ (alternating $\mathbb{Z}_2$ and $\mathbb{Z}_3$), while the randomly chosen state is $|\bullet\circ\bullet\circ\circ\circ\circ\circ\bullet\circ\circ\bullet\circ\circ\circ\circ\rangle$.

Initial state	Δ_0	Δ_m	ω	Floquet spectrum
$\mathbb{Z}_2$	−1.61	1.83	2.83	three arcs
$\mathbb{Z}_2$	0.45	5.89	2.16	multiple arcs
$\mathbb{Z}_3$	−0.26	4.14	2.24	one arc
$\mathbb{Z}_3$	0.70	5.43	1.82	multiple arcs
$\mathbb{Z}_4$	0.48	5.64	2.21	multiple arcs
$\mathbb{Z}_2\mathbb{Z}_3$	0.71	5.73	1.90	multiple arcs
random	0.60	6.36	2.33	multiple arcs

FIG. 15. Inhomogeneously driven random state $|\bullet\circ\bullet\circ\circ\circ\circ\circ\bullet\circ\circ\bullet\circ\circ\circ\circ\rangle$ ($\Delta_0 = 0.60$, $\Delta_m = 6.36$, $\omega = 2.33$). (a) Quantum fidelity. (b) Overlap of the initial state with all the Floquet modes. The color corresponds to $\langle \sum_i (-1)^{n_{0i}} n_i \rangle$ for each mode.

Finally, in Fig. 16 we scan the average fidelity cost function over the parameter space for the same randomly chosen state and fixed driving frequency $\omega = 2$. For comparison, in Fig. 16(a) we use the homogeneous driving protocol from Eq. (3). In this case, there are no significant peaks in the cost function, unlike for the Néel and polarized state in Fig. 1. However, as shown in Fig. 16(b), the inhomogeneous driving

FIG. 16. Average fidelity $\langle F(t) \rangle_t$ over time interval [0, 100] for a driven random state $|\bullet\circ\bullet\circ\circ\circ\circ\circ\bullet\circ\circ\bullet\circ\circ\circ\circ\rangle$, $\omega = 2$. (a) Homogeneous drive, Eq. (3). (b) Inhomogeneous drive, Eq. (B1).

scheme from Eq. (B1) results in a similar plot as those in Fig. 1. As for the polarized state, it contains only Type-2 peaks (no subharmonic response).

APPENDIX C: HIGH FREQUENCY EXPANSION

Here we calculate the effective Floquet Hamiltonian, which governs the stroboscopic dynamics for the three-step square pulse protocol in Eq. (8) under the assumption of high driving frequency ($T \ll 1$). To this end, we perform the expansion in powers of T using the Baker-Campbell-Hausdorff (BCH) series. We have numerically confirmed that higher frequency Type-I peaks can be well captured by a finite-order expansion. Motivated by this, we analytically calculate the Floquet Hamiltonian up to third order in BCH series.

We start by writing down the BCH series for the multiplication of three exponential matrices $e^z = e^x e^y e^w$, which gives the expansion of z as follows:

$$z = z^{(1)} + z^{(2)} + z^{(3)} + \cdots,$$
$$z^{(1)} = x + y + w,$$
$$z^{(2)} = \tfrac{1}{2}(-wx - wy + xw + xy + yw - yx),$$
$$\begin{aligned} z^{(3)} = \tfrac{1}{12}(&w^2x + w^2y + wx^2 - 2wxw - 2wxy \\ &+ wy^2 - 2wyw + 4wyx + x^2w \\ &+ x^2y + xw^2 - 2xwx - 2xwy + xy^2 \\ &+ 4xyw - 2xyx + y^2w + y^2x + yw^2 \\ &- 2ywx - 2ywy + yx^2 - 2yxw - 2yxy). \end{aligned} \quad \text{(C1)}$$

In fact, in our case $w = x$ [see Eq. (8)], which results in some simplifications,

$$z^{(1)} = 2x + y,$$
$$z^{(2)} = 0,$$
$$\begin{aligned} z^{(3)} &= \tfrac{1}{6}(-x^2y + xy^2 + 2xyx + y^2x - yx^2 - 2yxy) \\ &= \tfrac{1}{6}([[x, y], x] + [[x, y], y]), \end{aligned}$$
$$z^{(4)} = 0. \quad \text{(C2)}$$

In particular, all even order terms vanish ($z^{(2n)} = 0$).

We can now substitute $x = -iH_+ T/4$, $y = -iH_- T/2$, and $z = -iH_F T$, where

$$H_\pm = \Omega \sum_i P_{i-1} X_i P_{i+1} - (\Delta_0 \pm \Delta_m) \sum_i n_i. \quad \text{(C3)}$$

Now we have

$$e^{-iH_F T} = e^{-iH_+ \frac{T}{4}} e^{-iH_- \frac{T}{2}} e^{-iH_+ \frac{T}{4}},$$
$$\begin{aligned} -iH_F T = &\left(-2iH_+ \frac{T}{4} - iH_- \frac{T}{2}\right) \\ &+ \frac{1}{6}\left(\frac{iT^3}{32}[[H_+, H_-], H_+] + \frac{iT^3}{16}[[H_+, H_-], H_-]\right). \end{aligned} \quad \text{(C4)}$$

Using the expression for the commutator,

$$[H_+, H_-] = -2i\Omega\Delta_m \sum_i P_{i-1} Y_i P_{i+1}, \quad \text{(C5)}$$

after some algebra, we obtain

$$\begin{aligned} [[H_+, H_-], H_\pm] = &-4\Omega^2\Delta_m \sum_i P_{i-1} Z_i P_{i+1} \\ &-4\Omega^2\Delta_m \sum_i P_{i-1}(\sigma_i^+ \sigma_{i+1}^- + \sigma_i^- \sigma_{i+1}^+)P_{i+2} \\ &+2\Omega\Delta_m(\Delta_0 \pm \Delta_m) \sum_i P_{i-1} X_i P_{i+1}, \quad \text{(C6)} \end{aligned}$$

which finally leads to the expression Eq. (13) in the main text. We see from Eq. (C6) that, in addition to the PXP and detuning terms, two new terms are generated in the third-order expansion: a diagonal PZP term and an off-diagonal hopping term. The "time-crystal-like" dynamics from the Néel state is generated by the interplay of such terms. The resulting Hamiltonian is sufficiently local and captures the subharmonic fidelity revival quite well.

At higher frequencies, the agreement between BCH expansion and full dynamics under $H(t)$ is systematically improved. At lower frequencies, one needs to go higher order in the expansion to ensure a good agreement. We note that although new nonlocal terms (with support over larger clusters of sites) will proliferate at higher orders, the terms in Eq. (C6) will also occur repetitively, thus renormalizing their strength. For example, if we expand the high-amplitude expression of $H_F^{(1)}$
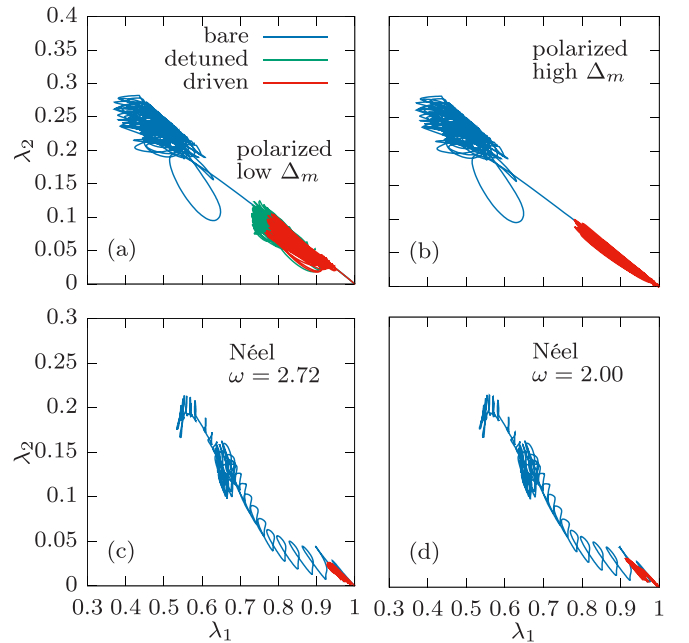

FIG. 17. Visualising the Hilbert space trajectory using the 2-site reduced density matrix eigenvalues. System size $N = 16$, without driving [$\Delta(t) = 0$, blue], with static detuning [$\Delta(t) = \Delta_0$, green], and with optimal cosine drive (red). (a) Polarized state, $\Delta_0 = 1.68$, $\Delta_m = -0.50$, $\omega = 3.71$. (b) Polarized state, $\Delta_0 = 0.64$, $\Delta_m = 7.55$, $\omega = 2.90$. (c) Néel state, $\Delta_0 = 1.15$, $\Delta_m = 2.67$, $\omega = 2.72$. (d) Néel state, $\Delta_0 = -1.17$, $\Delta_m = 4.81$, $\omega = 2.00$.

from Eq. (12) we get

$$\frac{\Delta_0}{2\Omega}g = \frac{\Delta_0}{\Delta_m^2 - \Delta_0^2}\left\{\left[1 + 2\frac{\sin\frac{(\Delta_m - \Delta_0)T}{4}}{\sin\frac{\Delta_0 T}{2}}\right]\Delta_m - \Delta_0\right\}$$

$$= 1 + \frac{\Delta_m T^2(3\Delta_0 - \Delta_m)}{96}$$

$$+ \frac{\Delta_m T^4\left(75\Delta_0^3 - 7\Delta_0^2\Delta_m - 15\Delta_0\Delta_m^2 + 3\Delta_m^3\right)}{92160}$$

$$+ \mathcal{O}(T^6). \tag{C7}$$

Note that the first two terms are exactly same as in Eq. (13). Thus to get a better Floquet effective Hamiltonian, one can just resum the terms in Eq. (13). Numerically, one can tune the coefficients of the terms in Eq. (13) manually to obtain a better matching between the fidelity dynamics calculated using H_F and $H(t)$. Ultimately, however, the BCH expansion is expected to diverge at lower frequencies, which is at odds with the numerics that shows the existence of long-lived subharmonic response at frequencies $\omega \sim 1$. We leave the interesting question how to adapt the BCH expansion to describe this nonperturbative regime for future work.

APPENDIX D: A DIFFERENT WAY OF VISUALISING THE HILBERT SPACE TRAJECTORY

In the main text, we analyzed the trajectory of a driven QMBS system in the Hilbert space by evaluating the average number of excitations of the two sublattices for the $|\mathbb{Z}_2\rangle$ initial state. This method is less useful for the $|0\rangle$ state since in this case the Hilbert space trajectory in just a diagonal line $\langle n_A \rangle = \langle n_B \rangle$. A more generic method for visualising the trajectory is to compute the reduced density matrix for a small subsystem,

e.g., ρ_2 for a 2-site subsystem, and plot its eigenvalues. Due to the PXP constraints, there are only three possible configurations for two sites (●○, ○○ and ○●), thus ρ_2 has three eigenvalues λ_i. However, only two of those are independent since $\mathrm{tr}(\rho_2) = 1$, which allows us to plot the trajectory in 2D.

The trajectories of the polarized state in two different optimal driving regimes can be observed in Figs. 17(a) and 17(b). Here we use the largest and the smallest eigenvalue of ρ_2 and compare the cases without driving (bare PXP model), with static detuning only, and with periodic driving. The polarized state is located at the (1,0) point (bottom right corner), since its reduced density matrix corresponds to a pure state ($\lambda_1 = 1$, $\lambda_2 = \lambda_3 = 0$). Similar to the Néel state, the driven trajectory approximately repeats the first part of the static trajectory. There are no revivals from the polarized state in the bare PXP model, so the trajectory at later times ends up in the region where all three eigenvalues are of approximately equal magnitudes, implying thermalization. In the low-amplitude regime, the static detuning alone is enough to produce revivals, as evidenced by the trajectory, which periodically returns to the vicinity of the initial state, while periodic driving further stabilizes the detuned trajectory, see Fig. 17(a). In the high-amplitude regime, the revivals are created purely by driving. In that case the driven trajectory is even more narrow and returns closer to the initial state, see Fig. 17(b).

For comparison, we use the same method to plot the trajectories for the Néel state in Figs. 17(c) and 17(d). In these two figures we use two different sets of driving parameters, one of which corresponds to the ideal trajectory with no loops in Fig. 9(c) and the other to a "one-loop" trajectory from Fig. 9(b). However, it is now much harder to see the difference between these two cases. In both cases the largest eigenvalue stays close to 1.

[1] M. Serbyn, D. A Abanin, and Z. Papić, Quantum many-body scars and weak breaking of ergodicity, Nat. Phys. **17**, 675 (2021).

[2] B. Sutherland, *Beautiful Models: 70 Years of Exactly Solved Quantum Many-Body Problems* (World Scientific, Singapore, 2004).

[3] R. Nandkishore and D. A. Huse, Many-body localization and thermalization in quantum statistical mechanics, Annu. Rev. Condens. Matter Phys. **6**, 15 (2015).

[4] D. A. Abanin, E. Altman, I. Bloch, and M. Serbyn, Colloquium: Many-body localization, thermalization, and entanglement, Rev. Mod. Phys. **91**, 021001 (2019).

[5] J. M. Deutsch, Quantum statistical mechanics in a closed system, Phys. Rev. A **43**, 2046 (1991).

[6] M. Srednicki, Chaos and quantum thermalization, Phys. Rev. E **50**, 888 (1994).

[7] M. Rigol, V. Dunjko, and M. Olshanii, Thermalization and its mechanism for generic isolated quantum systems, Nature (London) **452**, 854 (2008).

[8] S. Moudgalya, B. A. Bernevig, and N. Regnault, Quantum many-body scars and Hilbert space fragmentation: A review of exact results, Rep. Prog. Phys. **85**, 086501 (2022).

[9] H. Bernien, S. Schwartz, A. Keesling, H. Levine, A. Omran, H. Pichler, S. Choi, A. S. Zibrov, M. Endres, M. Greiner *et al.*, Probing many-body dynamics on a 51-atom quantum simulator, Nature (London) **551**, 579 (2017).

[10] D. Bluvstein, A. Omran, H. Levine, A. Keesling, G. Semeghini, S. Ebadi, T. T. Wang, A. A. Michailidis, N. Maskara, W. W. Ho *et al.*, Controlling quantum many-body dynamics in driven Rydberg atom arrays, Science **371**, 1355 (2021).

[11] W. Kao, K.-Yu Li, K.-Yu Lin, S. Gopalakrishnan, and B. L. Lev, Topological pumping of a 1D dipolar gas into strongly correlated prethermal states, Science **371**, 296 (2021).

[12] S. Scherg, T. Kohlert, P. Sala, F. Pollmann, B. Hebbe Madhusudhana, I. Bloch, and M. Aidelsburger, Observing non-ergodicity due to kinetic constraints in tilted Fermi-Hubbard chains, Nat. Commun. **12**, 4490 (2021).

[13] P. N. Jepsen, Y. K. Lee, H. Lin, I. Dimitrova, Y. Margalit, W. W. Ho, and W. Ketterle, Long-lived phantom helix states in Heisenberg quantum magnets, Nat. Phys. **18**, 899 (2022).

[14] S. Moudgalya, N. Regnault, and B. A. Bernevig, Entanglement of exact excited states of Affleck-Kennedy-Lieb-Tasaki models: Exact results, many-body scars, and violation of the strong

eigenstate thermalization hypothesis, Phys. Rev. B **98**, 235156 (2018).

[15] N. Shiraishi and T. Mori, Systematic Construction of Counterexamples to the Eigenstate Thermalization Hypothesis, Phys. Rev. Lett. **119**, 030601 (2017).

[16] D. K. Mark, C.-J. Lin, and O. I. Motrunich, Unified structure for exact towers of scar states in the Affleck-Kennedy-Lieb-Tasaki and other models, Phys. Rev. B **101**, 195131 (2020).

[17] N. O'Dea, F. Burnell, A. Chandran, and V. Khemani, From tunnels to towers: Quantum scars from Lie algebras and *q*-deformed Lie algebras, Phys. Rev. Research **2**, 043305 (2020).

[18] K. Pakrouski, P. N. Pallegar, F. K. Popov, and I. R. Klebanov, Many-Body Scars as a Group Invariant Sector of Hilbert Space, Phys. Rev. Lett. **125**, 230602 (2020).

[19] J. Ren, C. Liang, and C. Fang, Quasisymmetry Groups and Many-Body Scar Dynamics, Phys. Rev. Lett. **126**, 120604 (2021).

[20] M. Schecter and T. Iadecola, Weak Ergodicity Breaking and Quantum Many-Body Scars in Spin-1 XY Magnets, Phys. Rev. Lett. **123**, 147201 (2019).

[21] T. Iadecola and M. Schecter, Quantum many-body scar states with emergent kinetic constraints and finite-entanglement revivals, Phys. Rev. B **101**, 024306 (2020).

[22] K. Bull, I. Martin, and Z. Papić, Systematic Construction of Scarred Many-Body Dynamics in 1D Lattice Models, Phys. Rev. Lett. **123**, 030601 (2019).

[23] S. Chattopadhyay, H. Pichler, M. D. Lukin, and W. W. Ho, Quantum many-body scars from virtual entangled pairs, Phys. Rev. B **101**, 174308 (2020).

[24] N. Shibata, N. Yoshioka, and H. Katsura, Onsager's Scars in Disordered Spin Chains, Phys. Rev. Lett. **124**, 180604 (2020).

[25] S. Moudgalya, E. O'Brien, B. A. Bernevig, P. Fendley, and N. Regnault, Large classes of quantum scarred Hamiltonians from matrix product states, Phys. Rev. B **102**, 085120 (2020).

[26] F. M. Surace, G. Giudici, and M. Dalmonte, Weak-ergodicity-breaking via lattice supersymmetry, Quantum **4**, 339 (2020).

[27] Y. Kuno, T. Mizoguchi, and Y. Hatsugai, Flat band quantum scar, Phys. Rev. B **102**, 241115(R) (2020).

[28] O. Vafek, N. Regnault, and B. A. Bernevig, Entanglement of exact excited eigenstates of the Hubbard model in arbitrary Dimension, SciPost Phys. **3**, 043 (2017).

[29] D. K. Mark and O. I. Motrunich, *η*-pairing states as true scars in an extended Hubbard model, Phys. Rev. B **102**, 075132 (2020).

[30] S. Moudgalya, N. Regnault, and B. A. Bernevig, *η*-pairing in Hubbard models: From spectrum generating algebras to quantum many-body scars, Phys. Rev. B **102**, 085140 (2020).

[31] S. Moudgalya, B. A. Bernevig, and N. Regnault, Quantum many-body scars in a Landau level on a thin torus, Phys. Rev. B **102**, 195150 (2020).

[32] A. Hudomal, I. Vasić, N. Regnault, and Z. Papić, Quantum scars of bosons with correlated hopping, Commun. Phys. **3**, 99 (2020).

[33] H. Zhao, J. Vovrosh, F. Mintert, and J. Knolle, Quantum Many-Body Scars in Optical Lattices, Phys. Rev. Lett. **124**, 160604 (2020).

[34] J.-Y. Desaules, A. Hudomal, C. J. Turner, and Z. Papić, Proposal for Realizing Quantum Scars in the Tilted 1D Fermi-Hubbard Model, Phys. Rev. Lett. **126**, 210601 (2021).

[35] K. Pakrouski, P. N. Pallegar, F. K. Popov, and I. R. Klebanov, Group theoretic approach to many-body scar states in fermionic lattice models, Phys. Rev. Research **3**, 043156 (2021).

[36] G.-X. Su, H. Sun, A. Hudomal, J.-Y. Desaules, Z.-Yu Zhou, B. Yang, J. C. Halimeh, Z.-S. Yuan, Z. Papić, and J.-W. Pan, Observation of unconventional many-body scarring in a quantum simulator, arXiv:2201.00821.

[37] K. Lee, R. Melendrez, A. Pal, and H. J. Changlani, Exact three-colored quantum scars from geometric frustration, Phys. Rev. B **101**, 241111(R) (2020).

[38] P. A. McClarty, M. Haque, A. Sen, and J. Richter, Disorder-free localization and many-body quantum scars from magnetic frustration, Phys. Rev. B **102**, 224303 (2020).

[39] S. Ok, K. Choo, C. Mudry, C. Castelnovo, C. Chamon, and T. Neupert, Topological many-body scar states in dimensions one, two, and three, Phys. Rev. Research **1**, 033144 (2019).

[40] J. Wildeboer, A. Seidel, N. S. Srivatsa, A. E. B. Nielsen, and O. Erten, Topological quantum many-body scars in quantum dimer models on the kagome lattice, Phys. Rev. B **104**, L121103 (2021).

[41] F. M. Surace, P. P. Mazza, G. Giudici, A. Lerose, A. Gambassi, and M. Dalmonte, Lattice Gauge Theories and String Dynamics in Rydberg Atom Quantum Simulators, Phys. Rev. X **10**, 021041 (2020).

[42] D. Banerjee and A. Sen, Quantum Scars from Zero Modes in an Abelian Lattice Gauge Theory on Ladders, Phys. Rev. Lett. **126**, 220601 (2021).

[43] S. Biswas, D. Banerjee, and A. Sen, Scars from protected zero modes and beyond in $U(1)$ quantum link and quantum dimer models, SciPost Phys. **12**, 148 (2022).

[44] J.-Y. Desaules, D. Banerjee, A. Hudomal, Z. Papić, A. Sen, and J. C. Halimeh, Weak ergodicity breaking in the Schwinger model, arXiv:2203.08830.

[45] J.-Y. Desaules, A. Hudomal, D. Banerjee, A. Sen, Z. Papić, and J. C. Halimeh, Prominent quantum many-body scars in a truncated Schwinger model, arXiv:2204.01745.

[46] B. Buča, J. Tindall, and D. Jaksch, Non-stationary coherent quantum many-body dynamics through dissipation, Nat. Commun. **10**, 1730 (2019).

[47] J. Tindall, B. Buča, J. R. Coulthard, and D. Jaksch, Heating-Induced Long-Range *η* Pairing in the Hubbard Model, Phys. Rev. Lett. **123**, 030603 (2019).

[48] S. Sugiura, T. Kuwahara, and K. Saito, Many-body scar state intrinsic to periodically driven system, Phys. Rev. Research **3**, L012010 (2021).

[49] K. Mizuta, K. Takasan, and N. Kawakami, Exact Floquet quantum many-body scars under Rydberg blockade, Phys. Rev. Research **2**, 033284 (2020).

[50] B. Mukherjee, S. Nandy, A. Sen, D. Sen, and K. Sengupta, Collapse and revival of quantum many-body scars via Floquet engineering, Phys. Rev. B **101**, 245107 (2020).

[51] B. Mukherjee, A. Sen, D. Sen, and K. Sengupta, Dynamics of the vacuum state in a periodically driven Rydberg chain, Phys. Rev. B **102**, 075123 (2020).

[52] A. Haldar, D. Sen, R. Moessner, and A. Das, Dynamical Freezing and Scar Points in Strongly Driven Floquet Matter: Resonance vs Emergent Conservation Laws, Phys. Rev. X **11**, 021008 (2021).

[53] C. J. Turner, A. A. Michailidis, D. A. Abanin, M. Serbyn, and Z. Papić, Weak ergodicity breaking from quantum many-body scars, Nat. Phys. **14**, 745 (2018).

[54] C. J. Turner, A. A. Michailidis, D. A. Abanin, M. Serbyn, and Z. Papić, Quantum scarred eigenstates in a Rydberg atom chain: Entanglement, breakdown of thermalization, and stability to perturbations, Phys. Rev. B **98**, 155134 (2018).

[55] W. W. Ho, S. Choi, H. Pichler, and M. D. Lukin, Periodic Orbits, Entanglement, and Quantum Many-Body Scars in Constrained Models: Matrix Product State Approach, Phys. Rev. Lett. **122**, 040603 (2019).

[56] N. Maskara, A. A. Michailidis, W. W. Ho, D. Bluvstein, S. Choi, M. D. Lukin, and M. Serbyn, Discrete Time-Crystalline Order Enabled by Quantum Many-Body Scars: Entanglement Steering via Periodic Driving, Phys. Rev. Lett. **127**, 090602 (2021).

[57] P. Fendley, K. Sengupta, and S. Sachdev, Competing density-wave orders in a one-dimensional hard-boson model, Phys. Rev. B **69**, 075106 (2004).

[58] I. Lesanovsky and H. Katsura, Interacting Fibonacci anyons in a Rydberg gas, Phys. Rev. A **86**, 041601(R) (2012).

[59] B. Sun and F. Robicheaux, Numerical study of two-body correlation in a 1D lattice with perfect blockade, New J. Phys. **10**, 045032 (2008).

[60] B. Olmos, M. Müller, and I. Lesanovsky, Thermalization of a strongly interacting 1D Rydberg lattice gas, New J. Phys. **12**, 013024 (2010).

[61] E. J. Heller, Bound-State Eigenfunctions of Classically Chaotic Hamiltonian Systems: Scars of Periodic Orbits, Phys. Rev. Lett. **53**, 1515 (1984).

[62] C. J. Turner, J.-Y. Desaules, K. Bull, and Z. Papić, Correspondence Principle for Many-Body Scars in Ultracold Rydberg Atoms, Phys. Rev. X **11**, 021021 (2021).

[63] A. A. Michailidis, C. J. Turner, Z. Papić, D. A. Abanin, and M. Serbyn, Stabilizing two-dimensional quantum scars by deformation and synchronization, Phys. Rev. Research **2**, 022065(R) (2020).

[64] C.-Ju Lin, V. Calvera, and T. H. Hsieh, Quantum many-body scar states in two-dimensional Rydberg atom arrays, Phys. Rev. B **101**, 220304(R) (2020).

[65] V. Khemani, C. R. Laumann, and A. Chandran, Signatures of integrability in the dynamics of Rydberg-blockaded chains, Phys. Rev. B **99**, 161101(R) (2019).

[66] C.-Ju Lin, A. Chandran, and O. I. Motrunich, Slow thermalization of exact quantum many-body scar states under perturbations, Phys. Rev. Research **2**, 033044 (2020).

[67] I. Mondragon-Shem, M. G. Vavilov, and I. Martin, Fate of quantum many-body scars in the presence of disorder, PRX Quantum **2**, 030349 (2021).

[68] A. Pizzi, D. Malz, G. De Tomasi, J. Knolle, and A. Nunnenkamp, Time crystallinity and finite-size effects in clean Floquet systems, Phys. Rev. B **102**, 214207 (2020).

[69] D. Abanin, W. De Roeck, W. W. Ho, and F. Huveneers, A rigorous theory of many-body prethermalization for periodically driven and closed quantum systems, Commun. Math. Phys. **354**, 809 (2017).

Proposal for Realizing Quantum Scars in the Tilted 1D Fermi-Hubbard Model

Jean-Yves Desaules[●],[1] Ana Hudomal[●],[1,2] Christopher J. Turner[●],[1] and Zlatko Papić[●][1]
[1]*School of Physics and Astronomy, University of Leeds, Leeds LS2 9JT, United Kingdom*
[2]*Institute of Physics Belgrade, University of Belgrade, 11080 Belgrade, Serbia*

Motivated by recent observations of ergodicity breaking due to Hilbert space fragmentation in 1D Fermi-Hubbard chains with a tilted potential [Scherg *et al.*, arXiv:2010.12965], we show that the same system also hosts quantum many-body scars in a regime $U \approx \Delta \gg J$ at electronic filling factor $\nu = 1$. We numerically demonstrate that the scarring phenomenology in this model is similar to other known realizations such as Rydberg atom chains, including persistent dynamical revivals and ergodicity-breaking many-body eigenstates. At the same time, we show that the mechanism of scarring in the Fermi-Hubbard model is different from other examples in the literature: the scars originate from a subgraph, representing a free spin-1 paramagnet, which is weakly connected to the rest of the Hamiltonian's adjacency graph. Our work demonstrates that correlated fermions in tilted optical lattices provide a platform for understanding the interplay of many-body scarring and other forms of ergodicity breaking, such as localization and Hilbert space fragmentation.

Introduction.—Recently, there has been much interest in understanding how closed many-body quantum systems evolve in time when taken out of their equilibrium state. While many such systems rapidly return to their equilibrium state, in accordance with fundamental principles of quantum statistical mechanics [1], much of recent work has focused on systems that fail to do so as a consequence of ergodicity breaking [2,3], either due to the special mathematical structure known as integrability or very strong disorder which leads to (many-body) localization. Both of these paradigms of behavior are actively investigated in experiments on cold atoms, trapped ions, and superconducting qubits [4–7].

The inability of nonergodic systems to act as heat reservoirs for their smaller parts has been traditionally known to affect the entire spectrum of the system. Recently, however, there has been a flurry of interest in *weak* ergodicity breaking phenomena [8]. The latter refers to the emergence of a dynamically decoupled subspace within the many-body Hilbert space, in general without any underlying symmetry, spanned by ergodicity-breaking eigenstates. This behavior was first theoretically established in the Affleck-Kennedy-Lieb-Tasaki (AKLT) model [9,10], followed by the discovery of similar phenomenology in other nonintegrable lattice models [11–18], models of correlated fermions and bosons [19–25], frustrated magnets [26,27], topological phases of matter [28,29], and periodically driven systems [30–34]. In these examples, the ergodicity-breaking eigenstates are either explicitly embedded into a many-body spectrum via the mechanism due to Shiraishi and Mori [35], or they form a representation of an algebra [36–38].

A well-known example of weak ergodicity breaking in single-particle systems is the phenomenon of quantum scars in chaotic stadium billiards [39]. In this case, the particle's eigenfunctions exhibit anomalous concentration in the vicinity of an unstable periodic orbit in the classical limit $\hbar \to 0$ [40–42], leading to observable consequences in many physical systems [43–46]. In recent experiments on interacting Rydberg atom arrays [47], weak ergodicity breaking was observed via persistent revivals following the global quench of the system, prompting the name "quantum many-body scarring" [48–50] by analogy with stadium billiards [51,52]. Recently, quantum many-body scarring has been shown to occur in higher dimensions [53–55] and in the presence of certain kinds of perturbations [56–58] including disorder [59].

On the other hand, it has also been shown that ergodicity breaking can occur due to a fracturing of the Hilbert space into dynamically disconnected components [60–63]. This typically occurs by the interplay of local interactions with a higher-moment symmetry such as charge dipole conservation, which nontrivially intertwines spatial and internal symmetries. Recent work [64] has demonstrated that Hilbert space fragmentation can be experimentally realized via a magnetic field gradient applied to the Fermi-Hubbard (FH) model in a 1D optical lattice. Apart from offering a new platform to investigate the link between fragmentation and the so-called Stark many-body localization [65–67], an immediate question presents itself: can the tilted FH model realize quantum many-body scars?

In this Letter, we show that quantum many-body scars arise in the limit $U \approx \Delta \gg J$ in the tilted FH model, and that they can be detected using the quench from a specific

initial state at a different filling factor from the one considered in Ref. [64]. We derive an effective model for this setup, which can be mapped to a spinful generalization of the fractional quantum Hall effect on a thin torus [23], allowing for a practical experimental realization. While the phenomenology of quantum many-body scars is shown to be largely similar to their realization in Rydberg atom systems [47], including in particular an extensive set of eigenstates which violate the eigenstate thermalization hypothesis (ETH) [68,69], the origin of scars is different in the two systems and can be intuitively understood from a graph-theoretic viewpoint.

Large-tilt limit of the FH model.—The 1D FH model is given by the Hamiltonian

$$\hat{H} = \sum_{j,\sigma=\uparrow,\downarrow} -J\hat{c}_{j,\sigma}^{\dagger}\hat{c}_{j+1,\sigma} + \text{H.c.} + \Delta j\hat{n}_{j,\sigma} + U\sum_{j}\hat{n}_{j,\uparrow}\hat{n}_{j,\downarrow},$$

(1)

where $\hat{c}_{j,\sigma}^{\dagger}$ denotes the usual electron creation operator on site j with spin projection σ, $\hat{n}_{j,\sigma} \equiv \hat{c}_{j,\sigma}^{\dagger}\hat{c}_{j,\sigma}$, J and U are the hopping and on-site interaction terms, respectively. Tilt of the optical lattice is parametrized by Δ, which we take to be spin independent [64]. Note that tilting has the structure of a dipole term, $\sim j\hat{n}_j$. Below we impose open boundary conditions on the model in Eq. (1), and restrict to the electron filling factor $\nu = 1$, i.e., with $N/2$ fermions with spin $\uparrow$ and $N/2$ fermions with spin $\downarrow$ on a chain of N sites (assumed to be even). We also set $J = 1$ for simplicity. We label the Fock states using $\uparrow$ to denote a fermion with spin up and $\downarrow$ with spin down, while 0 stands for an empty site and $\updownarrow$ denotes a doublon.

We focus on the regime $\Delta \approx U \gg J$. In this case the sum of the dipole moment and the number of doublons is effectively conserved. The dominant contribution to the Hamiltonian (using a Schrieffer-Wolff transformation at first order [70]) is then given by

$$\hat{H}_{\text{eff}} = -J\sum_{j,\sigma}\hat{c}_{j,\sigma}^{\dagger}\hat{c}_{j+1,\sigma}\hat{n}_{j,\bar{\sigma}}(1 - \hat{n}_{j+1,\bar{\sigma}}) + \text{H.c.}$$
$$+ (U - \Delta)\sum_{j}\hat{n}_{j,\uparrow}\hat{n}_{j,\downarrow}.$$

(2)

In this effective Hamiltonian, hopping to the left (which decreases the total dipole moment by 1) is only allowed if it increases the number of doublons by the same amount ($\bar{\sigma}$ denotes opposite spin from σ).

The action of the Hamiltonian Eq. (2) within the $\nu = 1$ sector fragments the Hilbert space beyond the simple conservation of $U + \Delta$. In this work we focus on the largest connected component, which is the one containing the state with alternating $\uparrow$ and $\downarrow$ fermions. In addition to the symmetries of the full model in Eq. (1), i.e., SU(2) spin symmetry and spin reversal [71], the Hamiltonian Eq. (2) projected to the largest sector has an additional symmetry
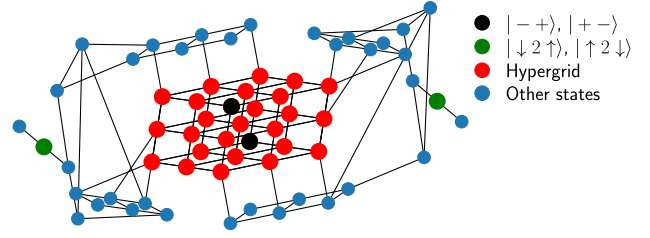

FIG. 1. Adjacency graph of the effective model in Eq. (2) for $N = 6$. Red vertices denote the states belonging to the hypergrid, with the black vertices corresponding to $|-+\rangle$, $|+-\rangle$ states defined in the text. Green vertices are the isolated states $|\downarrow 2\uparrow\rangle$, $|\uparrow 2\downarrow\rangle$ which live on the tails of the graph. For this graph, the hypergrid contains 27 vertices out of 63.

related to spatial inversion and particle-hole exchange [72]. After resolving these symmetries, we find the level statistics parameter $\langle r \rangle$ [73] to be close to 0.53 for all symmetry sectors with large numbers of states ($\gtrsim 10^3$) [72]. From these values which coincide with the Wigner-Dyson statistics [74], we expect the model in Eq. (2) to be chaotic. We next outline an intuitive approach for identifying many-body scars in this model.

Embedded hypergrid subgraph.—A practical diagnostic of quantum many-body scars is the existence of weakly correlated states which undergo robust revivals under quench dynamics, while the majority of other initial states thermalize fast and do not display revivals. In the Rydberg-blockaded chains [47], the reviving Néel state of atoms is the densest configuration compatible with the blockade constraint, and it is an extremal vertex of the Hamiltonian adjacency graph [48]. In this graph each vertex corresponds to a basis state, and two vertices are connected by an edge if the Hamiltonian matrix element between their respective basis states is nonzero. We next show, by examining the adjacency graph of the model in Eq. (2), that we can identify a subgraph, weakly coupled to the rest of the Hilbert space, which contains the reviving initial states and leaves a strong imprint on the scarred eigenstates. This leads to a transparent manifestation of scarring in the original Fock basis, in contrast with Rydberg atoms. In the latter case, the subspace which is weakly coupled to the rest of the Hilbert space has a much more complicated structure, leading to the wave function spreading across the entire adjacency graph [56] before refocusing onto the Néel state.

In Fig. 1 we plot the adjacency graph of the Hamiltonian in Eq. (2) for a small system. For the effective model in Eq. (2), it is possible to gauge away the fermionic minus signs [72], resulting in an unweighted, undirected graph. As the Hamiltonian Eq. (2) (for $U = \Delta$) has no diagonal elements and the spectrum is symmetric around zero, all product states are effectively in the infinite temperature ensemble and are expected to thermalize quickly. As we confirm numerically below, there are two important exceptions.

First, as highlighted in red color in Fig. 1, there is a regular subgraph which has the form of the hypergrid—a Cartesian product of line graphs (in our case, of length 3), i.e., the hypergrid is isomorphic to an adjacency graph of a free spin-1 paramagnet. This mapping can be understood by looking at the state $|\downarrow\uparrow\downarrow\uparrow\downarrow\uparrow\ldots\rangle$. Each cell of two sites can take the values $- := \downarrow\uparrow$, $2 := \updownarrow 0$ or $+ := \uparrow\downarrow$, leading to a three level system. Note that the configuration $0\updownarrow$ is omitted, as doublons can only be formed by hopping to the left. On the other hand, hopping between two neighboring cells will break this mapping and take the system out of the hypergrid subgraph. Inside the hypergrid, we identify two states for which the cell alternates between $-$ and $+$. These are the state $|-+\rangle := |-+-+\ldots\rangle = |\downarrow\uparrow\uparrow\downarrow\uparrow\uparrow\downarrow\ldots\rangle$ and its spin-inverted partner, $|+-\rangle = |+-+-\ldots\rangle := |\uparrow\downarrow\downarrow\uparrow\uparrow\downarrow\downarrow\uparrow\ldots\rangle$. The states $|-+\rangle$ and $|+-\rangle$ for $N = 6$ are shown in black color in Fig. 1. These two states are the only corners of the hypergrid (state with only $+$ and $-$ cells) with no edges going out of it. As we show below, either of these states shows persistent oscillations in quench dynamics, undergoing robust state transfer to their spin-inverted counterpart. While other corners of the hypergrid also show revivals, they are much smaller in amplitude and decay faster due to the leakage out of this substructure. The second example of a reviving state is $|\downarrow 2\uparrow\rangle := |\downarrow\downarrow\ldots\downarrow\updownarrow 0\uparrow\uparrow\ldots\uparrow\rangle$ (and its spin-reversed partner $|\uparrow 2\downarrow\rangle$), which is situated on a tail-like structure of length 3 (independent of system size) with minimal connectivity to the rest of the Hilbert space (green points in Fig 1). Similar tail-like structures occur in constrained spin models [75].

Many-body scarred dynamics and eigenstates.—Having identified candidate states for revivals, we now scrutinize their quench dynamics using large-scale exact diagonalization simulations of the effective model in Eq. (2). Making use of various symmetries present in the model, we have been able to exactly simulate dynamics for up to $N = 22$ electrons. For convenience, the simulations were performed in the spin representation of the model [72].

Figure 2(a) shows the time dependence of the entanglement entropy $S_{\text{ent}}(t)$ when the system is quenched from various initial product states, such as $|-+\rangle$, $|\downarrow 2\uparrow\rangle$ and a few randomly chosen product states. S_{ent} is defined as the von Neumann entropy of the reduced density matrix for one half of the chain. In all cases, entropy grows linearly in time, consistent with thermalization of the system. However, the coefficient of linear growth is visibly different for $|-+\rangle$ and $|\downarrow 2\uparrow\rangle$ states, and it is smaller than that of random states, indicating nonergodic dynamics. The long-time value of the entropy is also different for the $|-+\rangle$ state [72], hinting that the wave function is still not completely spread into the whole Hilbert space. The hallmark of many-body scars is the oscillations superposed on top of the linear growth, as seen in the scarred dynamics in Rydberg atom chains [48]. Rapid
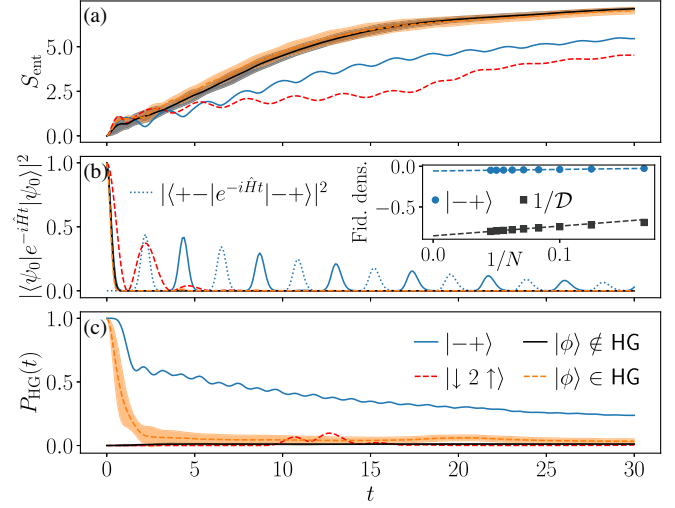

FIG. 2. Dynamics in the effective model Eq. (2) for $N = 18$ for $|-+\rangle$, $|\downarrow 2\uparrow\rangle$ and randomly chosen initial states. (a) Entanglement entropy S_{ent} for an equal bipartition of the system. Entropy grows linearly in time for all states, consistent with thermalizing dynamics, but it shows oscillations due to many-body scarring. $|\phi\rangle \notin$ HG and $|\phi\rangle \in$ HG denote the average over 10 random product states outside or within the hypergrid, respectively, and the shading represents standard deviation. (b) Fidelity dynamics for the same initial states as in (a). Inset shows the finite-size scaling of the fidelity density $1/N \ln |\langle\psi_0|e^{-i\hat{H}t}|\psi_0\rangle|^2$ at the first revival for $|-+\rangle$ state, demonstrating a value much higher than $1/N \ln(1/\mathcal{D})$ (with $\mathcal{D}$ the dimension of the Hilbert space), expected for a random state. Blue dotted line shows the amplitude of state transfer between $|-+\rangle$ and $|+-\rangle$ states. (c) Probability to remain within the hypergrid over time is much higher for $|-+\rangle$ than other states.

growth of entropy at short times is a consequence of the bipartition being located in the middle of a two-site effective cell.

Entropy oscillations mirror those of the wave function return probability, $|\langle\psi_0|e^{-i\hat{H}t}|\psi_0\rangle|^2$, in Fig. 2(b). For the isolated state $|\downarrow 2\uparrow\rangle$, only a single revival is clearly visible as the return probability decays rapidly once the wave function leaks out of the tail of the graph. Because of the low connectivity of the tail, the first revival is still visible on the scale of Fig. 2(b). The revival time can be accurately estimated by assuming the tail is completely disconnected, leading to the period $\pi/\sqrt{2}$. In contrast, the state $|-+\rangle$ displays several revivals with the sizable weight of the wave function $\sim 40\%$ returning to its initial value. The fidelity density, $1/N \ln |\langle\psi_0|e^{-i\hat{H}t}|\psi_0\rangle|^2$, shown in the inset, converges as $1/N$ to a value of -0.058. In contrast, the inverse Hilbert space dimension, $\mathcal{D}^{-1}$, expected for a random state leads to a fidelity density of -0.855—an order of magnitude higher. The scarred dynamics in this case can be visualized as the state bouncing within the hypergrid between $|-+\rangle$ and its partner $|+-\rangle$, illustrated by the dotted line in Fig. 2(b). From the hypergrid analysis, we expect the revival period to be $\sqrt{2}\pi$, coming from the 2π
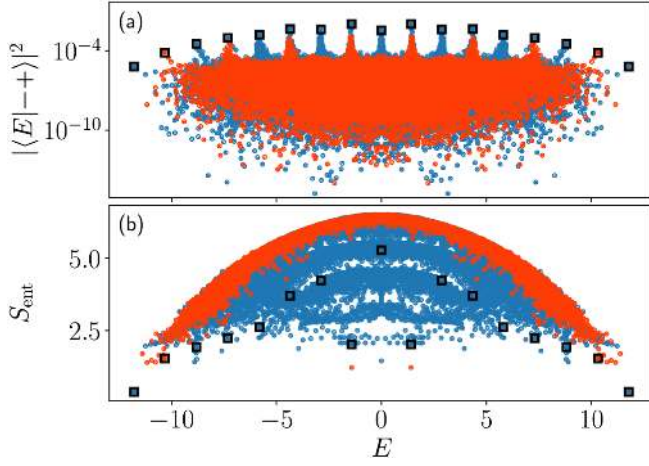
FIG. 3. Eigenstate properties of the effective model Eq. (2). (a) Overlap of eigenstates with the $|-+\rangle$ state as a function of their energy E. (b) Entanglement entropy S_{ent} of the eigenstates. Data is for system size $N = 16$. Red dots correspond to eigenstates with total spin $S = 1$, while the blue ones mark all other spin values. The squares indicate the eigenstates sitting at the top of each tower of states. These towers have an energy separation of approximately $\sqrt{2}$, as expected for the spin-1 hypergrid.

FIG. 4. (a) Occupation imbalance in the full model [in Eq. (1)] with $N = 12$ for various values of $U = \Delta$ for the initial state $|-+\rangle$, and for $U = \Delta = 6$ for the initial states $|\phi_0\rangle = |\uparrow\downarrow\uparrow\downarrow \cdots \uparrow\downarrow\rangle$ (within the hypergrid) and $|\phi_1\rangle = |\downarrow\updownarrow 0\uparrow\updownarrow 0\updownarrow 0\downarrow\updownarrow 0\uparrow\rangle$ (outside of it). (b) $U - \Delta$ phase diagram showing the scarring regime near the diagonal (dashed line). The colour scale represents the value of the first peak of the imbalance for $N = 12$.

period of free precession and the spin-1 matrix elements $\sqrt{2}$. This prediction closely matches the revival period observed in Fig. 2(b).

The importance of the hypergrid for scarred dynamics is illustrated in Fig. 2(c) which plots the probability to remain in the hypergrid, $P_{\text{HG}}(t) = \langle\psi_0|e^{i\hat{H}t}\hat{P}_{\text{HG}}e^{-i\hat{H}t}|\psi_0\rangle$, where $\hat{P}_{\text{HG}}$ is the projector onto the subspace spanned by product states belonging to the hypergrid. For the initial state $|-+\rangle$, we observe that the wave function remains concentrated inside the hypergrid, even at late times. This is in stark contrast with the PXP model which describes a chain of Rydberg atoms in the blockade regime [56], where the wave function spreads across the entire graph by the time it undergoes the first revival. Furthermore, even at the first revival peak the fidelity is lower than P_{HG}. This shows that the wave function does not exactly return to itself but gets more spread even within the hypergrid. Finally, for this initial state after a long time P_{HG} converges to a non-zero value which is higher than expected from the relative size of the hypergrid in the Hilbert space [72], hinting that the subgraph could have additional structure that prevents states from leaking out. The fact that this long-time value is much lower for random states in the hypergrid than for $|-+\rangle$ confirms that this is not simply due to low connectivity between the hypergrid and the rest of the Hilbert space, but that the special eigenstates indeed play an important role.

Properties of eigenstates of the model Eq. (2) are summarized in Fig. 3. The projection of eigenstates onto the $|-+\rangle$ state, shown in panel (a), displays prominent tower structures reminiscent of other scarred models [13,48]. The existence of towers implies that eigenstates tend to
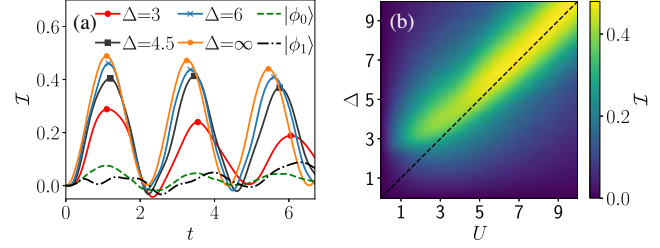
concentrate around certain energies in the spectrum, causing an ETH violation. The separation between the towers is approximately $\Delta E \approx \sqrt{2}$, as expected from the embedded hypergrid. Note that the eigenstates have been classified according to the conserved total value of spin S; in contrast, the $|-+\rangle$ state is not an eigenstate of $\mathbf{S}^2$. One can show that for this state, $\langle\mathbf{S}^2\rangle = N/2$, thus $|-+\rangle$ is predominantly supported by $S = 1$ and $S = 2$ eigenstates at the given system size. The $S = 1$ eigenstates are indicated by red points in Fig. 3.

Similar violation of the ETH can be seen in the large spread in entanglement entropy of eigenstates in Fig. 3(b), showing that eigenstates of similar energy have very different amounts of entanglement. Part of this spreading, however, can be attributed to the eigenstates belonging to different spin sectors S, giving rise to multiple bands that do not fully overlap at the system size shown in Fig. 3(b) [72]. The distribution of entropy in the $S = 1$ sector [red points in Fig. 3(b)] is relatively narrow apart from two "outliers" shown at energy $E \approx \pm\sqrt{2}$, which sit at the top of the tower for their sector in Fig. 3(a). The states at the top of each tower are indicated by squares, but unlike the PXP model [56] these states are not well separated from other states in the same tower.

Experimental implications.—The effective model studied above is exact for $U = \Delta \to \infty$. For experimental realizations, it is important to ascertain that the same physics persists for accessible values of U, Δ and that it can be detected using local measurements. We demonstrate this in Fig. 4 for the full model in Eq. (1) focusing on the regime $U, \Delta < 10$. Panel (a) shows the dynamics of imbalance on the even and odd sublattices, $\mathcal{I} = (N_o - N_e)/(N_o + N_e)$, where $N_{e/o}$ is the total number of fermions on the even or odd sites. The imbalance is bounded between -1 and 1. We see robust oscillations in $\mathcal{I}$ with the frequency matching half the wave function revival frequency in Fig. 2(b). The amplitude of the imbalance revival remains close to the infinite-limit value for $U = \Delta \gtrsim 6$. As further evidence that the hypergrid is the cause of nonergodicity, we devised a local perturbation

which effectively disconnects the hypergrid, leading to the improvement of revivals in the full model [72].

Conclusions and discussion.—We have proposed an experimental realization of quantum many-body scars in the regime $U = \Delta$ of the tilted FH model. We have identified product states $|-+\rangle$, $|+-\rangle$ at filling factor $\nu = 1$ which give rise to scarred dynamics and reveal towers of ergodicity-breaking many-body eigenstates, allowing us to investigate the interplay of many-body scarring with other facets of weak ergodicity breaking such as localization and Hilbert space fragmentation. In addition to the filling factor $\nu = 1$, we have also studied the filling $\nu = 1/2$ used in Ref. [64]. In the latter case, taking the large-tilt limit $\Delta \gg U, J$ and using a Schrieffer-Wolff transformation up to third order, we found analogous signatures of scars [72], provided we neglect the diagonal terms in the effective Hamiltonian. Under these assumptions, the resulting model can be viewed as a spinful generalization of the fractional quantum Hall effect on a thin torus [23]. By contrast, the approach presented here for $\nu = 1$ is considerably simpler as it allows us to conveniently eliminate the undesirable diagonal terms.

Statement of compliance with EPSRC policy framework on research data: This publication is theoretical work that does not require supporting research data.

[1] C. Gogolin and J. Eisert, Equilibration, thermalisation, and the emergence of statistical mechanics in closed quantum systems, Rep. Prog. Phys. **79**, 056001 (2016).

[2] R. Nandkishore and D. A. Huse, Many-body localization and thermalization in quantum statistical mechanics, Annu. Rev. Condens. Matter Phys. **6**, 15 (2015).

[3] D. A. Abanin, E. Altman, I. Bloch, and M. Serbyn, Colloquium: Many-body localization, thermalization, and entanglement, Rev. Mod. Phys. **91**, 021001 (2019).

[4] T. Kinoshita, T. Wenger, and D. S. Weiss, A quantum Newton's cradle, Nature (London) **440**, 900 (2006).

[5] M. Schreiber, S. S. Hodgman, P. Bordia, H. P. Lüschen, M. H. Fischer, R. Vosk, E. Altman, U. Schneider, and I. Bloch, Observation of many-body localization of interacting fermions in a quasirandom optical lattice, Science **349**, 842 (2015).

[6] J. Smith, A. Lee, P. Richerme, B. Neyenhuis, P. W. Hess, P. Hauke, M. Heyl, D. A. Huse, and C. Monroe, Many-body localization in a quantum simulator with programmable random disorder, Nat. Phys. **12**, 907 (2016).

[7] B. Chiaro *et al.*, Direct measurement of non-local interactions in the many-body localized phase, arXiv:1910.06024.

[8] M. Serbyn, D. A. Abanin, and Z. Papić, Quantum many-body scars and weak breaking of ergodicity, arXiv:2011.09486.

[9] D. P Arovas, Two exact excited states for the $S = 1$ AKLT chain, Phys. Lett. A **137**, 431 (1989).

[10] S. Moudgalya, N. Regnault, and B. A. Bernevig, Entanglement of exact excited states of Affleck-Kennedy-Lieb-Tasaki models: Exact results, many-body scars, and violation of the strong eigenstate thermalization hypothesis, Phys. Rev. B **98**, 235156 (2018).

[11] M. Schecter and T. Iadecola, Weak Ergodicity Breaking and Quantum Many-Body Scars in Spin-1 XY Magnets, Phys. Rev. Lett. **123**, 147201 (2019).

[12] T. Iadecola and M. Schecter, Quantum many-body scar states with emergent kinetic constraints and finite-entanglement revivals, Phys. Rev. B **101**, 024306 (2020).

[13] K. Bull, I. Martin, and Z. Papić, Systematic Construction of Scarred Many-Body Dynamics in 1D Lattice Models, Phys. Rev. Lett. **123**, 030601 (2019).

[14] S. Chattopadhyay, H. Pichler, M. D. Lukin, and W. Wei Ho, Quantum many-body scars from virtual entangled pairs, Phys. Rev. B **101**, 174308 (2020).

[15] N. Shibata, N. Yoshioka, and H. Katsura, Onsager's Scars in Disordered Spin Chains, Phys. Rev. Lett. **124**, 180604 (2020).

[16] S. Moudgalya, E. O'Brien, B. A. Bernevig, P. Fendley, and N. Regnault, Large classes of quantum scarred Hamiltonians from matrix product states, Phys. Rev. B **102**, 085120 (2020).

[17] F. Maria Surace, G. Giudici, and M. Dalmonte, Weak-ergodicity-breaking via lattice supersymmetry, Quantum **4**, 339 (2020).

[18] Y. Kuno, T. Mizoguchi, and Y. Hatsugai, Flat band quantum scar, Phys. Rev. B **102**, 241115(R) (2020).

[19] O. Vafek, N. Regnault, and B. Andrei Bernevig, Entanglement of exact excited eigenstates of the Hubbard model in arbitrary dimension, SciPost Phys. **3**, 043 (2017).

[20] D. K. Mark, C.-J. Lin, and O. I. Motrunich, Unified structure for exact towers of scar states in the Affleck-Kennedy-Lieb-Tasaki and other models, Phys. Rev. B **101**, 195131 (2020).

[21] D. K. Mark and O. I. Motrunich, η-pairing states as true scars in an extended Hubbard model, Phys. Rev. B **102**, 075132 (2020).

[22] S. Moudgalya, N. Regnault, and B. A. Bernevig, η-pairing in Hubbard models: From spectrum generating algebras to quantum many-body scars, Phys. Rev. B **102**, 085140 (2020).

[23] S. Moudgalya, B. A. Bernevig, and N. Regnault, Quantum many-body scars in a Landau level on a thin torus, Phys. Rev. B **102**, 195150 (2020).

[24] A. Hudomal, I. Vasić, N. Regnault, and Z. Papić, Quantum scars of bosons with correlated hopping, Commun. Phys. **3**, 99 (2020).

[25] H. Zhao, J. Vovrosh, F. Mintert, and J. Knolle, Quantum Many-Body Scars in Optical Lattices, Phys. Rev. Lett. **124**, 160604 (2020).

[26] K. Lee, R. Melendrez, A. Pal, and H. J. Changlani, Exact three-colored quantum scars from geometric frustration, Phys. Rev. B **101**, 241111(R) (2020).

[27] P. A. McClarty, M. Haque, A. Sen, and J. Richter, Disorder-free localization and many-body quantum scars from magnetic frustration, Phys. Rev. B **102**, 224303 (2020).

[28] S. Ok, K. Choo, C. Mudry, C. Castelnovo, C. Chamon, and T. Neupert, Topological many-body scar states in dimensions one, two, and three, Phys. Rev. Research **1**, 033144 (2019).

[29] J. Wildeboer, A. Seidel, N. S. Srivatsa, A. E. B. Nielsen, and O. Erten, Topological quantum many-body scars in quantum dimer models on the kagome lattice, arXiv:2009.00022.

[30] B. Buča, J. Tindall, and D. Jaksch, Non-stationary coherent quantum many-body dynamics through dissipation, Nat. Commun. **10**, 1730 (2019).

[31] J. Tindall, B. Buča, J. R. Coulthard, and D. Jaksch, Heating-Induced Long-Range η Pairing in the Hubbard Model, Phys. Rev. Lett. **123**, 030603 (2019).

[32] S. Sugiura, T. Kuwahara, and K. Saito, Many-body scar state intrinsic to periodically driven system, Phys. Rev. Research **3**, L012010 (2021).

[33] K. Mizuta, K. Takasan, and N. Kawakami, Exact Floquet quantum many-body scars under Rydberg blockade, Phys. Rev. Research **2**, 033284 (2020).

[34] B. Mukherjee, S. Nandy, A. Sen, D. Sen, and K. Sengupta, Collapse and revival of quantum many-body scars via Floquet engineering, Phys. Rev. B **101**, 245107 (2020).

[35] N. Shiraishi and T. Mori, Systematic Construction of Counterexamples to the Eigenstate Thermalization Hypothesis, Phys. Rev. Lett. **119**, 030601 (2017).

[36] K. Pakrouski, P. N. Pallegar, F. K. Popov, and I. R. Klebanov, Many-Body Scars as a Group Invariant Sector of Hilbert Space, Phys. Rev. Lett. **125**, 230602 (2020).

[37] J. Ren, C. Liang, and C. Fang, Quasi-Symmetry Groups and Many-Body Scar Dynamics, Phys. Rev. Lett. **126**, 120604 (2021).

[38] N. O'Dea, F. Burnell, A. Chandran, and V. Khemani, From tunnels to towers: Quantum scars from Lie algebras and q-deformed Lie algebras, Phys. Rev. Research **2**, 043305 (2020).

[39] E. J. Heller, Bound-State Eigenfunctions of Classically Chaotic Hamiltonian Systems: Scars of Periodic Orbits, Phys. Rev. Lett. **53**, 1515 (1984).

[40] E. J. Heller, Wavepacket dynamics and quantum chaology, in *Chaos and Quantum Physics*, Vol. 52 (North-Holland, Amsterdam, 1991).

[41] G. G. de Polavieja, F. Borondo, and R. M. Benito, Scars in Groups of Eigenstates in a Classically Chaotic System, Phys. Rev. Lett. **73**, 1613 (1994).

[42] D. A. Wisniacki, F. Borondo, E. Vergini, and R. M. Benito, Localization properties of groups of eigenstates in chaotic systems, Phys. Rev. E **63**, 066220 (2001).

[43] S. Sridhar, Experimental Observation of Scarred Eigenfunctions of Chaotic Microwave Cavities, Phys. Rev. Lett. **67**, 785 (1991).

[44] P. B. Wilkinson, T. M. Fromhold, L. Eaves, F. W. Sheard, N. Miura, and T. Takamasu, Observation of 'scarred' wavefunctions in a quantum well with chaotic electron dynamics, Nature (London) **380**, 608 (1996).

[45] D. Wintgen and A. Hönig, Irregular Wave Functions of a Hydrogen Atom in a Uniform Magnetic Field, Phys. Rev. Lett. **63**, 1467 (1989).

[46] F. J. Arranz, F. Borondo, and R. M. Benito, Scar Formation at the Edge of the Chaotic Region, Phys. Rev. Lett. **80**, 944 (1998).

[47] H. Bernien, S. Schwartz, A. Keesling, H. Levine, A. Omran, H. Pichler, S. Choi, A. S. Zibrov, M. Endres, M. Greiner, V. Vuletic, and M. D. Lukin, Probing many-body dynamics on a 51-atom quantum simulator, Nature (London) **551**, 579 (2017).

[48] C. J. Turner, A. A. Michailidis, D. A. Abanin, M. Serbyn, and Z. Papic, Weak ergodicity breaking from quantum many-body scars, Nat. Phys. **14**, 745 (2018).

[49] W. Wei Ho, S. Choi, H. Pichler, and M. D. Lukin, Periodic Orbits, Entanglement, and Quantum Many-Body Scars in Constrained Models: Matrix Product State Approach, Phys. Rev. Lett. **122**, 040603 (2019).

[50] C. J. Turner, J.-Y. Desaules, K. Bull, and Z. Papić, Correspondence Principle for Many-Body Scars in Ultracold Rydberg Atoms, Phys. Rev. X **11**, 021021 (2021).

[51] S. Choi, C. J. Turner, H. Pichler, W. Wei Ho, A. A. Michailidis, Z. Papić, M. Serbyn, M. D. Lukin, and D. A. Abanin, Emergent SU(2) Dynamics and Perfect Quantum Many-Body Scars, Phys. Rev. Lett. **122**, 220603 (2019).

[52] K. Bull, J.-Y. Desaules, and Z. Papić, Quantum scars as embeddings of weakly broken Lie algebra representations, Phys. Rev. B **101**, 165139 (2020).

[53] A. A. Michailidis, C. J. Turner, Z. Papić, D. A. Abanin, and M. Serbyn, Stabilizing two-dimensional quantum scars by deformation and synchronization, Phys. Rev. Research **2**, 022065(R) (2020).

[54] C.-J. Lin, V. Calvera, and T. H. Hsieh, Quantum many-body scar states in two-dimensional Rydberg atom arrays, Phys. Rev. B **101**, 220304(R) (2020).

[55] D. Bluvstein, A. Omran, H. Levine, A. Keesling, G. Semeghini, S. Ebadi, T. T. Wang, A. A. Michailidis, N. Maskara, W. Wei Ho, S. Choi, M. Serbyn, M. Greiner, V. Vuletic, and M. D. Lukin, Controlling quantum many-body dynamics in driven Rydberg atom arrays, Science **371**, 1355 (2021).

[56] C. J. Turner, A. A. Michailidis, D. A. Abanin, M. Serbyn, and Z. Papić, Quantum scarred eigenstates in a Rydberg atom chain: Entanglement, breakdown of thermalization, and stability to perturbations, Phys. Rev. B **98**, 155134 (2018).

[57] V. Khemani, C. R. Laumann, and A. Chandran, Signatures of integrability in the dynamics of Rydberg-blockaded chains, Phys. Rev. B **99**, 161101(R) (2019).

[58] C.-J. Lin, A. Chandran, and O. I. Motrunich, Slow thermalization of exact quantum many-body scar states under perturbations, Phys. Rev. Research **2**, 033044 (2020).

[59] I. Mondragon-Shem, M. G. Vavilov, and I. Martin, The fate of quantum many-body scars in the presence of disorder, arXiv:2010.10535.

[60] V. Khemani, M. Hermele, and R. Nandkishore, Localization from Hilbert space shattering: From theory to physical realizations, Phys. Rev. B **101**, 174204 (2020).

[61] S. Pai and M. Pretko, Dynamical Scar States in Driven Fracton Systems, Phys. Rev. Lett. **123**, 136401 (2019).

[62] S. Moudgalya, A. Prem, R. Nandkishore, N. Regnault, and B. A. Bernevig, Thermalization and its absence within Krylov subspaces of a constrained Hamiltonian, arXiv:1910.14048.

[63] P. Sala, T. Rakovszky, R. Verresen, M. Knap, and F. Pollmann, Ergodicity Breaking Arising from Hilbert Space Fragmentation in Dipole-Conserving Hamiltonians, Phys. Rev. X **10**, 011047 (2020).

[64] S. Scherg, T. Kohlert, P. Sala, F. Pollmann, Bharath H M, I. Bloch, and M. Aidelsburger, Observing non-ergodicity due to kinetic constraints in tilted Fermi-Hubbard chains, arXiv:2010.12965v1.

[65] M. Schulz, C. A. Hooley, R. Moessner, and F. Pollmann, Stark Many-Body Localization, Phys. Rev. Lett. **122**, 040606 (2019).

[66] E. van Nieuwenburg, Y. Baum, and G. Refael, From Bloch oscillations to many-body localization in clean interacting systems, Proc. Natl. Acad. Sci. U.S.A. **116**, 9269 (2019).

[67] R. Yao and J. Zakrzewski, Many-body localization of bosons in an optical lattice: Dynamics in disorder-free potentials, Phys. Rev. B **102**, 104203 (2020).

[68] J. M. Deutsch, Quantum statistical mechanics in a closed system, Phys. Rev. A **43**, 2046 (1991).

[69] M. Srednicki, Chaos and quantum thermalization, Phys. Rev. E **50**, 888 (1994).

[70] S. Bravyi, D. P. DiVincenzo, and D. Loss, Schrieffer-Wolff transformation for quantum many-body systems, Ann. Phys. (Amsterdam) **326**, 2793 (2011).

[71] F. H. L. Essler, H. Frahm, F. Göhmann, A. Klümper, and V. E. Korepin, *The One-Dimensional Hubbard Model* (Cambridge University Press, Cambridge, England, 2005).

[72] See Supplemental Material at http://link.aps.org/supplemental/10.1103/PhysRevLett.126.210601 for additional details on symmetries of the model and on the effect of the hypergrid on the Hilbert space.

[73] V. Oganesyan and D. A. Huse, Localization of interacting fermions at high temperature, Phys. Rev. B **75**, 155111 (2007).

[74] M. Lal Mehta, *Random Matrices* (Elsevier, New York, 2004), Vol. 142.

[75] N. Pancotti, G. Giudice, J. Ignacio Cirac, J. P. Garrahan, and M. Carmen Bañuls, Quantum East Model: Localization, Nonthermal Eigenstates, and Slow Dynamics, Phys. Rev. X **10**, 021051 (2020).

Letter   Editors' Suggestion

Fractional chiral hinge insulator

Anna Hackenbroich,[1,2] Ana Hudomal [ORCID],[3,4] Norbert Schuch,[1,2,5,6] B. Andrei Bernevig,[7] and Nicolas Regnault [ORCID][7,8]

[1]*Max-Planck-Institute of Quantum Optics, Hans-Kopfermann-Straße 1, 85748 Garching, Germany*
[2]*Munich Center for Quantum Science and Technology, Schellingstraße 4, 80799 München, Germany*
[3]*Institute of Physics Belgrade, University of Belgrade, 11080 Belgrade, Serbia*
[4]*School of Physics and Astronomy, University of Leeds, Leeds LS2 9JT, United Kingdom*
[5]*Faculty of Physics, University of Vienna, Boltzmanngasse 5, 1090 Wien, Austria*
[6]*Faculty of Mathematics, University of Vienna, Oskar-Morgenstern-Platz 1, 1090 Vienna, Austria*
[7]*Joseph Henry Laboratories and Department of Physics, Princeton University, Princeton, New Jersey 08544, USA*
[8]*Laboratoire de Physique de l'Ecole normale supérieure, ENS, Université PSL, CNRS, Sorbonne Université,
Université Paris-Diderot, Sorbonne Paris Cité, Paris 75005, France*

We propose and study a wave function describing an interacting three-dimensional fractional chiral hinge insulator (FCHI) constructed by Gutzwiller projection of two noninteracting second-order topological insulators with chiral hinge modes at half filling. We use large-scale variational Monte Carlo computations to characterize the model states via the entanglement entropy and charge-spin fluctuations. We show that the FCHI possesses fractional chiral hinge modes characterized by a central charge $c = 1$ and Luttinger parameter $K = 1/2$, like the edge modes of a Laughlin $1/2$ state. The bulk and surface topology is characterized by the topological entanglement entropy (TEE) correction to the area law. While our computations indicate a vanishing bulk TEE, we show that the gapped surfaces host an unconventional two-dimensional topological phase. In a clear departure from the physics of a Laughlin $1/2$ state, we find a TEE per surface compatible with $(\ln \sqrt{2})/2$, half that of a Laughlin $1/2$ state. This value cannot be obtained from topological quantum field theory for purely two-dimensional systems. For the sake of completeness, we also investigate the topological degeneracy.

I. INTRODUCTION

Strong interactions in condensed-matter systems can lead to fascinating emergent phenomena. In two-dimensional (2D) systems, strong interactions may lead to the emergence of topological order (TO), such as that experimentally observed in the fractional quantum Hall effect. Features of TO in two dimensions include a nontrivial ground state degeneracy on certain surfaces and the appearance of itinerant excitations with fractional quantum numbers and braiding statistics. It has long been an active field of study to extend this rich physics to three-dimensional (3D) strongly interacting systems, where the emergent physics can be even more diverse, including systems with fractonic excitations [1,2]. Whereas many microscopic models based on interacting spin systems have been proposed to exhibit TO in three dimensions, such as the 3D toric code [3] and 3D Kitaev models [4–7], and there are treatments of 3D fractional topological insulators using effective field theory [8,9], there is a scarcity of electronic or realistic examples that could be experimentally relevant.

Among the 3D electronic topological insulators (TIs), an entirely new class was recently discovered: Certain TIs protected by crystalline symmetries, now dubbed higher-order TIs [10–25], possess a much richer bulk-boundary correspondence than conventional, or first-order, TIs. For example, a 3D chiral hinge insulator (CHI) exists whose gapped surfaces are connected by gapless chiral hinge modes [12]. Higher-order

TIs in two and three dimensions have been experimentally observed in materials [26], mechanical [27], acoustic [28,29], photonic [30–33], and electrical [34,35,38] systems. Two-dimensional higher-order TIs have also been studied in the strongly interacting regime [36,37].

In this Letter, we provide a first stepping stone in the realization of a full-fledged electronic 3D fractional TI by building a 3D fractional chiral hinge insulator (FCHI) model wave function. Indeed, the hinge modes of the noninteracting CHI are of the same nature as the edge modes of a Chern insulator, two copies of which at fractional filling and with strong interactions form a fractional Chern insulator (FCI) hosting fractional quantum Hall physics [39–41]. Therefore, we may speculate that under similar conditions the FCHI will also display nontrivial topology with fractionalized excitations at least at the hinges or surfaces.

Numerical computations and especially exact diagonalizations for interacting electronic systems in three dimensions are notoriously difficult due to the spatial dimensionality. To partially circumvent this challenge, we will rely on a model wave function, a fruitful approach for TO, to capture the FCHI. This approach has been extensively applied in the realm of the fractional quantum Hall effect [42,43] and FCIs [44]. In order to define the FCHI wave function, we will make use of Gutzwiller projection, a systematic method to construct interacting model wave functions starting from copies of noninteracting ground states. Large-scale variational Monte Carlo

(MC) simulations then allow us to analyze this wave function for bigger system sizes than possible with other methods.

To probe the topological content of the wave function, we will study the entanglement entropy (EE), which can be evaluated in MC simulations [44–48] and follows an area law with characteristic subleading corrections [49]. In two dimensions there are logarithmic corrections for gapless edge modes [50–52] which along with the constant topological entanglement entropy (TEE) correction to the bulk area law [53,54] provide information on the system's topology. In three dimensions, corrections to the bulk area law include the TEE and possible size-dependent corrections for fractonic systems and layered constructions [55–57]. In particular, we study the hinge modes in an open system and show that they are fractionalized excitations characterized by a central charge $c = 1$ and Luttinger parameter $K = 1/2$, like the FCI edge modes. Next, we study the TEE of the bulk system and that of the gapped surfaces. Whereas our computations indicate a vanishing bulk TEE, we show that the gapped surfaces host a nontrivial two-dimensional topological phase with a TEE per surface compatible with half that of a Laughlin 1/2 state. For completeness, we then study the linear independence of different interacting wave functions obtained by changing the boundary conditions for the underlying fermions.

II. MODEL WAVE FUNCTION

We consider an interacting model wave function obtained by Gutzwiller projection of the ground state of a noninteracting 3D second-order TI with chiral hinge modes. The CHI model is described by a local Hamiltonian for spinless fermions with four sites per unit cell [12] [see Fig. 1(a) for a sketch of the model]. The ground state $|\psi\rangle$ of the CHI model lies at filling $\nu = 1/2$ of the lattice. With open boundary conditions (OBC) in the x and y directions, each of the four hinges of the CHI parallel to the z axis supports a single chiral mode localized at the hinge. Each hinge mode corresponds to a free bosonic mode with central charge $c = 1$ and Luttinger parameter $K = 1$ akin to the edge modes of a Chern insulator [58]. Since the CHI model is noninteracting, it does not have TO or a nontrivial ground state degeneracy with periodic boundary conditions (PBC).

In order to define the interacting model wave function $|\Psi\rangle$, we take two copies $|\psi_s\rangle$ of the ground state of the CHI model at half filling, to which we assign different values $s \in \{\uparrow, \downarrow\}$ of a spinlike degree of freedom. The interacting wave function is obtained as the Gutzwiller projection

$$|\Psi\rangle = P_G[|\psi_\uparrow\rangle \otimes |\psi_\downarrow\rangle] \tag{1}$$

of the product of the two noninteracting wave functions. With $\hat{n}_{s,i}$ denoting the particle number operator for fermions of spin s on the lattice site i, the Gutzwiller projection operator is expressed as

$$P_G = \prod_i (1 - \hat{n}_{\uparrow,i} \hat{n}_{\downarrow,i}). \tag{2}$$

It forbids simultaneous occupancy of any lattice site i by both a particle with spin $\uparrow$ and a particle with spin $\downarrow$. Therefore, it simulates the effect of a very large on-site Hubbard interaction. Since each copy of the ground state of the CHI model has
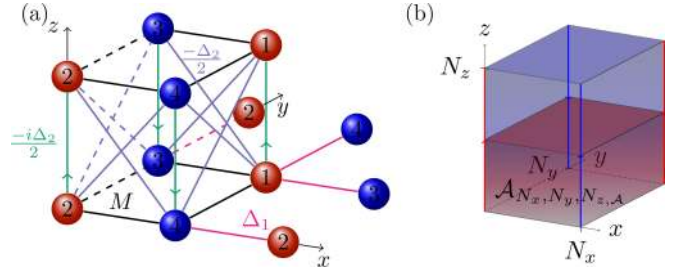

FIG. 1. (a) Local real-space model for a 3D second-order TI with chiral hinge states. The Hamiltonian is defined on a cubic lattice with a unit cell of four sites lying in the xy plane. In this plane, sites in the same unit cell are connected by a nearest-neighbor hopping M marked by black lines ($-M$ for dashed black lines). In the xy plane, sites in adjacent unit cells are connected by a nearest-neighbor hopping Δ_1 marked by violet lines ($-\Delta_1$ for dashed violet lines). In the z direction, adjacent unit cells are connected by a real next-nearest-neighbor hopping $-\Delta_2/2$ marked by light blue lines ($\Delta_2/2$ for dashed light blue lines). In addition, there is a purely imaginary nearest-neighbor hopping between adjacent unit cells in the z direction with a value of $-i\Delta_2/2$ in the direction of the green arrows. We study the model for parameter values $M = \Delta_1 = \Delta_2 = 1$, where the correlation length is close to its minimal value [58]. (b) Three-dimensional system with OBC and N_x, N_y unit cells in the x, y directions and periodic boundaries and N_z sites in the z direction. The subsystem $\mathcal{A}_{N_x,N_y,N_{z,\mathcal{A}}}$ consists of N_x, N_y unit cells in the x, y directions and $N_{z,\mathcal{A}}$ unit cells in the z direction.

a filling $\nu_{\psi_\uparrow} = \nu_{\psi_\downarrow} = 1/2$, the Gutzwiller projection enforces that the interacting wave function lies at filling $\nu_\Psi = 1/2$ with exactly one particle per lattice site (each lattice site having a spin degree of freedom which can take two values). Hence, charge fluctuations are completely frozen, and the only relevant degree of freedom in the interacting wave function is the spin s.

III. CHARACTERIZATION OF HINGE MODES

With OBC in the x and y directions, the interacting model wave function $|\Psi\rangle$ is expected to possess one gapless chiral mode at each of the four hinges parallel to the z axis, inherited from the hinge modes of the noninteracting CHI. Like the edge modes of chiral topologically ordered phases in two dimensions, we expect the hinge modes of $|\Psi\rangle$ to be described by a chiral conformal field theory (CFT). Moreover, since $|\Psi\rangle$ is interacting, we expect its hinge CFT to be possibly different from the trivial free-boson CFT describing the hinge modes of the noninteracting CHI.

In order to characterize the chiral hinge modes, we adapt the methods that were previously employed for 2D chiral phases [51,52,59] to the 3D setting: We study the second Rényi entropy $S^{(2)}$ and spin fluctuations of $|\Psi\rangle$, in focusing on the critical contributions stemming from the *physical* hinges. We evaluate these observables for the interacting wave function $|\Psi\rangle$ in large-scale MC simulations using the SWAP-operator technique [60] with sign-problem refinement [58,61].

We consider the geometry sketched in Fig. 1(b): a total system with $N_x \times N_y \times N_z$ unit cells, OBC in the xy plane, and PBC in the z direction to ensure that the only gapless excitations are the four hinge states. We consider a series of
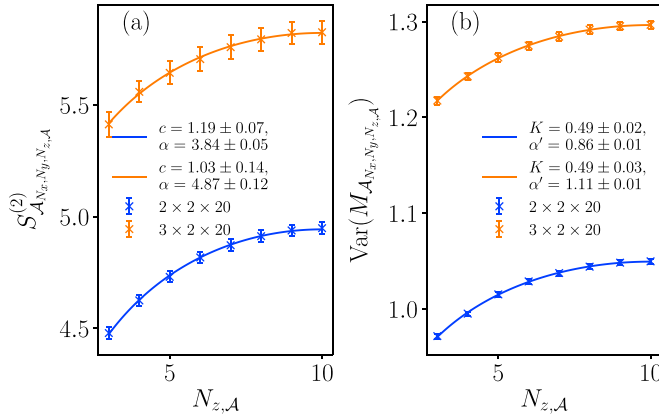
FIG. 2. Second Rényi entropy and spin fluctuations of the interacting model wave function $|\Psi\rangle$ for a series of subsystems $\mathcal{A}_{N_x,N_y,N_{z,\mathcal{A}}}$ [58]. We plot MC data obtained for two different systems sizes $2 \times 2 \times 20$ (in blue) and $3 \times 2 \times 20$ (in orange). (a) Scaling of the second Rényi entropy, fit to the prediction of Eq. (3). (b) Scaling of the spin fluctuations, fit to the prediction of Eq. (6).

subsystems $\mathcal{A}_{N_x,N_y,N_{z,\mathcal{A}}}$ with N_x, N_y unit cells in the x, y directions and $N_{z,\mathcal{A}} \in \{1,\dots,N_z-1\}$ unit cells in the z direction, marked in red in Fig. 1(b). $\mathcal{A}_{N_x,N_y,N_{z,\mathcal{A}}}$ bisect each of four physical hinge modes into a part of length $N_{z,\mathcal{A}}$ contained in $\mathcal{A}_{N_x,N_y,N_{z,\mathcal{A}}}$ and the remaining part outside of the subsystem. Hence, we expect that the EE and spin fluctuations with respect to $\mathcal{A}_{N_x,N_y,N_{z,\mathcal{A}}}$ will contain signatures from the hinges.

Specifically, if the hinge modes are described by a chiral CFT with central charge c, the second Rényi entropy $S^{(2)}$ of $|\Psi\rangle$ with respect to $\mathcal{A}_{N_x,N_y,N_{z,\mathcal{A}}}$ for different $N_{z,\mathcal{A}}$ at fixed N_x and N_y is expected to scale as

$$S^{(2)}_{\mathcal{A}_{N_x,N_y,N_{z,\mathcal{A}}}}(N_{z,\mathcal{A}}) = \alpha + 4 \times S^{(2)}_{\text{crit}}(N_{z,\mathcal{A}}; N_z). \quad (3)$$

Here, α is a constant independent of $N_{z,\mathcal{A}}$. It includes the area law contributions from the virtual surfaces at $z = 0, N_{z,\mathcal{A}}$ which scale proportional to $N_x N_y$ and are therefore independent of $N_{z,\mathcal{A}}$ in the thermodynamic limit, and any potential corner contributions. In Eq. (3),

$$S^{(2)}_{\text{crit}}(N_{z,\mathcal{A}}; N_z) = \frac{c}{8} \ln\left[\frac{N_z}{\pi} \sin\left(\frac{\pi N_{z,\mathcal{A}}}{N_z}\right)\right] \quad (4)$$

is the second Rényi entropy of a periodic one-dimensional chiral critical mode with central charge c and total system size N_z restricted to a single interval of length $N_{z,\mathcal{A}}$ [50]. The factor of 4 in Eq. (3) takes into account the four hinge modes, which contribute equally to the EE.

The scaling of the second Rényi entropy of $|\Psi\rangle$ as computed from MC is shown in Fig. 2(a) for two different system sizes, $2 \times 2 \times 20$ and $3 \times 2 \times 20$. For computational reasons, we choose N_x and N_y to be much smaller than N_z [58]. Due to the short correlation length of the CHI, equal to one lattice spacing [58], we may expect that the characteristic parameters approach their thermodynamic limit even for small N_x, N_y. The logarithmic scaling from the hinge states is clearly visible, and numerical values for c and α can be extracted by fitting the data to Eq. (3). The numerical value for the central charge is $c = 1.19 \pm 0.07$ for $2 \times 2 \times 20$ and $c = 1.03 \pm 0.14$ for $3 \times 2 \times 20$. This provides strong evidence

that the hinge modes of the interacting model wave function $|\Psi\rangle$ are described by a chiral free-boson CFT with central charge $c = 1$.

Free-boson CFTs with $c = 1$ are characterized by their Luttinger parameter K. For such Luttinger liquids, the variance of the U(1) current integrated over a subsystem scales proportionally to the EE, where the proportionality constant allows the extraction of K [59]. Since charge fluctuations are completely frozen in the wave function $|\Psi\rangle$, the relevant U(1) symmetry stems from the spin degree of freedom, and we need to consider the fluctuations of the number $M_{\mathcal{A}}$ of particles with spin $\uparrow$ in a subsystem $\mathcal{A}$. Concretely, we consider the variance

$$\text{Var}\left(M_{\mathcal{A}_{N_x,N_y,N_{z,\mathcal{A}}}}\right) \equiv \left\langle M^2_{\mathcal{A}_{N_x,N_y,N_{z,\mathcal{A}}}}\right\rangle - \left\langle M_{\mathcal{A}_{N_x,N_y,N_{z,\mathcal{A}}}}\right\rangle^2, \quad (5)$$

which is expected to scale as [59]

$$\text{Var}\left(M_{\mathcal{A}_{N_x,N_y,N_{z,\mathcal{A}}}}\right) = 2\frac{K}{\pi^2} \ln\left[\frac{N_z}{\pi} \sin\left(\frac{\pi N_{z,\mathcal{A}}}{N_z}\right)\right] + \alpha' \quad (6)$$

with the Luttinger parameter K and a constant α' independent of $N_{z,\mathcal{A}}$.

The scaling of the spin fluctuations in the wave function $|\Psi\rangle$ as computed from MC is shown in Fig. 2(b) for two different system sizes, $2 \times 2 \times 20$ and $3 \times 2 \times 20$. Remarkably, even for these small sizes, the numerical value for K extracted by fitting the data to Eq. (6) is $K = 0.49 \pm 0.02$ for $2 \times 2 \times 20$ and $K = 0.49 \pm 0.03$ for $3 \times 2 \times 20$. This provides strong evidence that the Luttinger parameter for the chiral hinge modes of the interacting higher-order TI is $K = 1/2$, similar to the edge modes of a FCI.

IV. TOPOLOGICAL DEGENERACY AND TOPOLOGICAL ENTANGLEMENT ENTROPY

In two dimensions, fractionalized excitations such as those of the edge modes of an FCI are an indication of bulk TO. Above, we showed that the FCHI has fractional hinge modes. It is therefore natural to investigate whether it also possesses nontrivial topology in the bulk and on the surfaces. Two-dimensional topologically ordered systems are characterized by a nonzero TEE and a nontrivial topological degeneracy on surfaces with a genus greater than zero. In three dimensions, TEE and topological degeneracy remain important signatures of nontrivial topology. We now study these signatures for the FCHI model.

a. Topological entanglement entropy. In order to compute the TEE of the FCHI, we use the Kitaev-Preskill construction [53] extended to 3D systems [55]. As sketched in Fig. 3(a), the system is divided into four regions, $\mathcal{A}$, $\mathcal{B}$, $\mathcal{C}$, and $\mathcal{D}$, which are translation invariant in the z direction and whose cross sections with the xy plane form the pattern required for the usual 2D Kitaev-Preskill cut. The EE of these regions and their unions can be collected into the linear combination

$$-\gamma = S^{(2)}_{\mathcal{ABC}} - S^{(2)}_{\mathcal{AB}} - S^{(2)}_{\mathcal{BC}} - S^{(2)}_{\mathcal{AC}} + S^{(2)}_{\mathcal{A}} + S^{(2)}_{\mathcal{B}} + S^{(2)}_{\mathcal{C}}, \quad (7)$$

which cancels all contributions from the virtual surfaces and hinges. The remaining quantity, denoted γ, could contain two contributions, $\gamma = \gamma_{3D} + N_z \gamma_{2D}$. The constant γ_{3D} is the 3D TEE [55]. $\gamma_{2D} N_z$ would occur for layered constructions of 2D
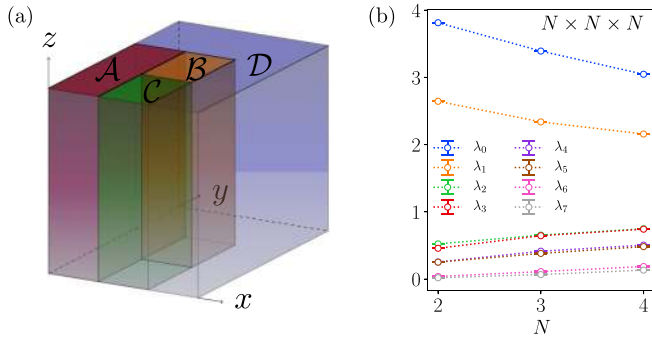
(a)

(b)

FIG. 3. (a) Subsystems $\mathcal{A}$, $\mathcal{B}$, $\mathcal{C}$, and $\mathcal{D}$ for the extraction of the bulk TEE using a Kitaev-Preskill cut. Note that the subsystems are translation invariant in the z direction. (b) Scaling of the eigenvalues λ_i with $i = 0, \ldots, 7$ of the overlap matrix $\mathcal{O}$ of the FCHI on the isotropic three-torus with $N \times N \times N$ unit cells.

topological orders perpendicular to the z direction with 2D TEE γ_{2D} [55] or in some fractonic systems [1,2].

We have computed γ for the FCHI on the three-torus in large-scale variational MC computations. For the geometry sketched in Fig. 3(a), we were able to study the FCHI with $3 \times 3 \times 2$ unit cells, for which we found $\gamma = -0.08 \pm 0.04$, and with $3 \times 3 \times 3$ unit cells, for which we found $\gamma = -0.06 \pm 0.11$. In both cases, the subsystem $\mathcal{A}$ is of size $1 \times 2 \times N_z$ unit cells, and the subsystems $\mathcal{B}$ and $\mathcal{C}$ are of size $1 \times 1 \times N_z$ unit cells [62]. Because of the intrinsic anisotropy of the FCHI, we also considered a second geometry obtained by rotating the subsystems in Fig. 3(a) along the y axis such that they are translation invariant in the x direction while leaving the insulator unchanged. Here, we computed γ for a system of $2 \times 3 \times 5$ unit cells [63] and found $\gamma = -0.009 \pm 0.102$. All these values are consistent with $\gamma = 0$ (up to small finite-size effects for $3 \times 3 \times 2$) *irrespective* of the orientation of the cut. We stress that γ is several orders of magnitude smaller than any of the EEs appearing in Eq. (7), excluding the existence of both a nonvanishing 3D TEE γ_{3D} and a nonzero γ_{2D}.

Since we have not been able to find any clear signature of a true nontrivial bulk topology, we now probe the nature of the gapped surfaces perpendicular to the x direction [64]. Since the vertical hinges host fractionalized one-dimensional modes like those of an FCI, we may speculate that the vertical surfaces host some nontrivial TO [65]. To characterize it, we compute γ according to Eq. (7) for the geometry obtained by rotating the subsystems in Fig. 3(a) as described above, OBC in the x direction, and PBC in the y and z directions. We have performed this computation for a system with $2 \times 3 \times 5$ unit cells and found $\gamma = 0.31 \pm 0.16$ [66]. Since the same computation with PBC in x yields a vanishing result for γ as discussed above, this nonzero value is due entirely to the two surfaces at $x = 0$ and $x = N_x - 1$ and confirms that the vertical surfaces host a nontrivial 2D TO. Indeed, each surface contributes with $\gamma_{\text{FCHI}}^{2D} = \gamma/2$ to the TEE. The value of $\gamma_{\text{FCHI}}^{2D}$ is consistent with $(\ln\sqrt{2})/2$, a clear departure from the TEE of a single 2D FCI in the Laughlin 1/2 phase.

b. Topological degeneracy. In order to study the topological degeneracy of the FCHI we closely follow a well-known approach established for 2D projected wave functions such as

the FCI. On the 2D torus, one defines four interacting wave functions by choosing PBC or antiperiodic boundary conditions (APBC) for the underlying fermions in each direction of the torus. For the FCI, these four states yield two linearly independent wave functions, as expected in the phase of the Laughlin wave function with filling $\nu = 1/2$ [58].

For the FCHI, we consider eight independent ansatz states on the 3D torus obtained by Gutzwiller projection of the noninteracting CHI wave function with PBC or APBC in each direction. The ground state degeneracy is then given by the rank of an eight-dimensional overlap matrix $\mathcal{O}$ containing the normalized overlaps of these ansatz states [58]. Note that the topological degeneracy could, in principle, be larger than 8. In such a case, the rank of the overlap matrix considered here would still be, at most, 8, and our approach would fail to measure the full ground state degeneracy.

We have studied the topological degeneracy of the FCHI on isotropic three-tori with $N \times N \times N$ unit cells up to $N = 4$ using variational MC simulations [58]. The results are shown in Fig. 3(b). For these system sizes, we observe a separation of the eigenvalues of the overlap matrix $\mathcal{O}$ into a group of two larger eigenvalues and a group of six smaller eigenvalues. However, there is no clear trend indicating that the former would converge to a finite value and the latter to zero in the thermodynamic limit. The finite-size effects due to the numerical limitation to small system sizes therefore do not allow us to draw clear conclusions about the asymptotic topological degeneracy from these results.

Since we have observed a nontrivial surface topology from the TEE, we want to investigate whether these modes contribute a topological degeneracy. For that purpose, we have also studied the degeneracy of the FCHI with OBC in the x direction, meaning each surface mode is defined on a 2D torus. In this geometry, four ansatz states are generated by changing the boundary conditions for the underlying CHI in the two periodic directions. We have found behavior very similar to the full-PBC case, namely, two larger eigenvalues but no clear evidence of a reduction of the bulk degeneracy in the thermodynamic limit [58]. Finally, we mention that we have also analyzed the topological degeneracy for very anisotropic three-tori with N_z much larger than $N_x = N_y$. An extensive discussion is given in the Supplemental Material [58].

V. DISCUSSION AND CONCLUSION

We have studied a model wave function for a 3D chiral hinge insulator with strong interactions at fractional band filling using extensive MC simulations. By studying the EE and spin fluctuations in an open geometry, we showed that the hinges host fractional gapless modes which have the same characterization as the edge modes of an FCI in the Laughlin 1/2 phase. We have also studied the system's topology through the topological degeneracy and the TEE. While the results for the topological degeneracy remain inconclusive due to the small number of numerically accessible system sizes, our results point to the absence of a bulk TEE. However, we found clear signatures of a nontrivial 2D topological order on the vertical surfaces. Interestingly, the TEE contribution per surface is consistent with $\gamma_{\text{FCHI}}^{2D} = (\ln\sqrt{2})/2$, in other words

half of the TEE of an FCI. This result cannot be explained using a quantum dimension since a TEE of $(\ln\sqrt{2})/2$ would correspond to a total quantum dimension $2^{1/4}$, whereas any nontrivial total quantum dimension has to be larger than or equal to $\sqrt{2}$. This suggests the emergence of a highly unconventional surface topology *that cannot be realized in a strictly 2D system*, with a nontrivial relation to the hinge modes [65]. In this Letter, we have restricted our analysis to the gapped surfaces and their gapless edges. It would be highly interesting, but very numerically challenging, to consider the top and bottom surfaces, which host single Dirac cones in the noninteracting CHI. Their fate in the interacting system is yet unknown and beyond the scope of the present work, but it should be the focus of further study.

[1] R. M. Nandkishore and M. Hermele, Annu. Rev. Condens. Matter Phys. **10**, 295 (2019).

[2] M. Pretko, X. Chen, and Y. You, Int. J. Mod. Phys. A **35**, 2030003 (2020).

[3] C. Castelnovo and C. Chamon, Phys. Rev. B **78**, 155120 (2008).

[4] S. Ryu, Phys. Rev. B **79**, 075124 (2009).

[5] I. Mondragon-Shem and T. L. Hughes, J. Stat. Mech. (2014) P10022.

[6] S. Mandal and N. Surendran, Phys. Rev. B **79**, 024426 (2009).

[7] N. C. Randeep and N. Surendran, Phys. Rev. B **98**, 125136 (2018).

[8] J. Maciejko, X.-L. Qi, A. Karch, and S.-C. Zhang, Phys. Rev. Lett. **105**, 246809 (2010).

[9] B. Swingle, M. Barkeshli, J. McGreevy, and T. Senthil, Phys. Rev. B **83**, 195139 (2011).

[10] W. A. Benalcazar, B. A. Bernevig, and T. L. Hughes, Science **357**, 61 (2017).

[11] W. A. Benalcazar, B. A. Bernevig, and T. L. Hughes, Phys. Rev. B **96**, 245115 (2017).

[12] F. Schindler, A. M. Cook, M. G. Vergniory, Z. Wang, S. S. Parkin, B. A. Bernevig, and T. Neupert, Sci. Adv. **4**, eaat0346 (2018).

[13] Z. Song, Z. Fang, and C. Fang, Phys. Rev. Lett. **119**, 246402 (2017).

[14] J. Langbehn, Y. Peng, L. Trifunovic, F. von Oppen, and P. W. Brouwer, Phys. Rev. Lett. **119**, 246401 (2017).

[15] S. Parameswaran and Y. Wan, Physics **10**, 132 (2017).

[16] E. Khalaf, Phys. Rev. B **97**, 205136 (2018).

[17] M. Geier, L. Trifunovic, M. Hoskam, and P. W. Brouwer, Phys. Rev. B **97**, 205135 (2018).

[18] L. Trifunovic and P. W. Brouwer, Phys. Rev. X **9**, 011012 (2019).

[19] Y. You, T. Devakul, F. J. Burnell, and T. Neupert, Phys. Rev. B **98**, 235102 (2018).

[20] A. Rasmussen and Y.-M. Lu, Phys. Rev. B **101**, 085137 (2020).

[21] S. A. A. Ghorashi, X. Hu, T. L. Hughes, and E. Rossi, Phys. Rev. B **100**, 020509(R) (2019).

[22] O. Dubinkin and T. L. Hughes, Phys. Rev. B **99**, 235132 (2019).

[23] Y. X. Zhao, Y. Lu, and S. A. Yang, arXiv:2005.14500.

[24] Y. You, J. Bibo, and F. Pollmann, Phys. Rev. Research **2**, 033192 (2020).

[25] B. Kang, W. Lee, and G. Y. Cho, Phys. Rev. Lett. **126**, 016402 (2021).

[26] F. Schindler, Z. Wang, M. G. Vergniory, A. M. Cook, A. Murani, S. Sengupta, A. Y. Kasumov, R. Deblock, S. Jeon, I. Drozdov, H. Bouchiat, S. Guéron, A. Yazdani, B. A. Bernevig, and T. Neupert, Nat. Phys. **14**, 918 (2018).

[27] M. Serra-Garcia, V. Peri, R. Süsstrunk, O. R. Bilal, T. Larsen, L. G. Villanueva, and S. D. Huber, Nature (London) **555**, 342 (2018).

[28] H. Xue, Y. Yang, F. Gao, Y. Chong, and B. Zhang, Nat. Mater. **18**, 108 (2019).

[29] X. Ni, M. Weiner, A. Alú, and A. B. Khanikaev, Nat. Mater. **18**, 113 (2019).

[30] S. Mittal, V. V. Orre, G. Zhu, M. A. Gorlach, A. Poddubny, and M. Hafezi, Nat. Photon. **13**, 692 (2019).

[31] A. E. Hassan, F. K. Kunst, A. Moritz, G. Andler, E. J. Bergholtz, and M. Bourennane, Nat. Photon. **13**, 697 (2019).

[32] B.-Y. Xie, G.-X. Su, H.-F. Wang, H. Su, X.-P. Shen, P. Zhan, M.-H. Lu, Z.-L. Wang, and Y.-F. Chen, Phys. Rev. Lett. **122**, 233903 (2019).

[33] Y. Yang, Z. Jia, Y. Wu, R.-C. Xiao, Z.-H. Hang, H. Jiang, and X. C. Xie, Sci. Bull. **65**, 531 (2020).

[34] C. W. Peterson, W. A. Benalcazar, T. L. Hughes, and G. Bahl, Nature (London) **555**, 346 (2018).

[35] S. Imhof, C. Berger, F. Bayer, J. Brehm, L. W. Molenkamp, T. Kiessling, F. Schindler, C. H. Lee, M. Greiter, T. Neupert, and R. Thomale, Nat. Phys. **14**, 925 (2018).

[36] K. Laubscher, D. Loss, and J. Klinovaja, Phys. Rev. Research **1**, 032017(R) (2019).

[37] K. Laubscher, D. Loss, and J. Klinovaja, Phys. Rev. Research **2**, 013330 (2020).

[38] M. Serra-Garcia, R. Süsstrunk, and S. D. Huber, Phys. Rev. B **99**, 020304(R) (2019).

[39] D. N. Sheng, Z.-C. Gu, K. Sun, and L. Sheng, Nat. Commun. **2**, 389 (2011).

[40] T. Neupert, L. Santos, C. Chamon, and C. Mudry, Phys. Rev. Lett. **106**, 236804 (2011).

[41] N. Regnault and B. A. Bernevig, Phys. Rev. X **1**, 021014 (2011).

[42] R. B. Laughlin, Phys. Rev. Lett. **50**, 1395 (1983).

[43] G. Moore and N. Read, Nucl. Phys. B **360**, 362 (1991).

[44] Y. Zhang and A. Vishwanath, Phys. Rev. B **87**, 161113(R) (2013).

[45] J. Shao, E.-A. Kim, F. D. M. Haldane, and E. H. Rezayi, Phys. Rev. Lett. **114**, 206402 (2015).

[46] Y. Zhang, T. Grover, and A. Vishwanath, Phys. Rev. B **84**, 075128 (2011).

[47] J. Pei, S. Han, H. Liao, and T. Li, Phys. Rev. B **88**, 125135 (2013).

[48] J. Wildeboer and N. E. Bonesteel, Phys. Rev. B **94**, 045125 (2016).

[49] M. Srednicki, Phys. Rev. Lett. **71**, 666 (1993).

[50] P. Calabrese and J. Cardy, J. Phys. A **42**, 504005 (2009).

[51] V. Crépel, N. Claussen, B. Estienne, and N. Regnault, Nat. Commun. **10**, 1861 (2019).

[52] V. Crépel, N. Claussen, N. Regnault, and B. Estienne, Nat. Commun. **10**, 1860 (2019).

[53] A. Kitaev and J. Preskill, Phys. Rev. Lett. **96**, 110404 (2006).

[54] M. Levin and X.-G. Wen, Phys. Rev. Lett. **96**, 110405 (2006).

[55] T. Grover, A. M. Turner, and A. Vishwanath, Phys. Rev. B **84**, 195120 (2011).

[56] H. Ma, A. T. Schmitz, S. A. Parameswaran, M. Hermele, and R. M. Nandkishore, Phys. Rev. B **97**, 125101 (2018).

[57] H. He, Y. Zheng, B. A. Bernevig, and N. Regnault, Phys. Rev. B **97**, 125102 (2018).

[58] See Supplemental Material at http://link.aps.org/supplemental/10.1103/PhysRevB.103.L161110 for the additional information on our numerical methods, benchmarks on a two-dimensional fractional Chern insulator and the non-interacting three-dimensional chiral hinge insulator, and additional results for the topological degeneracy of the three-dimensional model.

[59] B. Estienne and J.-M. Stéphan, Phys. Rev. B **101**, 115136 (2020).

[60] M. B. Hastings, I. González, A. B. Kallin, and R. G. Melko, Phys. Rev. Lett. **104**, 157201 (2010).

[61] Y. Zhang, T. Grover, and A. Vishwanath, Phys. Rev. Lett. **107**, 067202 (2011).

[62] We recall that the number of physical sites for these subsystems is $2 \times 4 \times N_z$ and $2 \times 2 \times N_z$, respectively.

[63] We recall that the number of physical sites in this case is $4 \times 6 \times 5$. Thus, although $N_x = 2$, the PBC along x are nontrivial. Here, subsystem $\mathcal{A}$ is of size $2 \times 2 \times 2$ unit cells, and subsystems $\mathcal{B}$ and $\mathcal{C}$ are of size $2 \times 1 \times 2$ unit cells.

[64] We could alternatively choose those perpendicular to the y direction.

[65] A. Tiwari, M.-H. Li, B. A. Bernevig, T. Neupert, and S. A. Parameswaran, Phys. Rev. Lett. **124**, 046801 (2020).

[66] Here, the statistical error bar is a conservative estimate, in particular much larger than the remaining fluctuations in the mean of the MC computations [58]. We stress that our conservative error bar confirms a nontrivial TEE smaller than $\ln\sqrt{2}$ per surface.